Structure, morphology, optical, mechanical and magnetic properties of 3d transition metal doped ZnO RF-sputtered thin films.

A thesis submitted for the award of degree of

Doctor of Philosophy

By

VENKAIAH MALAPATI

School of Physics

University of Hyderabad

Hyderabad-500046

INDIA

May 2013

CONTENTS

CHAPTER 1

Introduction

The materials like ZnO, ZnS, SnO_2 are interesting class of II-VI semiconductor compounds. These materials with wide band gaps exhibit efficient emitting properties in the blue to ultra-violet (UV) spectral range and are likely to replace material like GaN in light emitting laser diodes [1]. Regardless of the similarities, each of the II-VI semiconductors demonstrates their unique novel physical properties. The band gaps of these compounds have a major influence on the properties like optical absorption, electrical conductivity and index of refraction. Semiconductors with the direct band gaps in opto-electronics are advantageous over indirect band gap semiconductors, as they do not require phonons to satisfy the wave vector conservation. Most of the II-VI semiconductors are found to be direct band gap semiconductors and have been dominating the optical field for short range wavelength applications such as light emitting diode (LEDs) and ultraviolet photo detectors [2].

These compounds crystallize, mostly in the cubic (Zinc blende) or hexagonal (wurtzite) structure. The structural characteristics of Wurtzite can be illustrated by zinc sulfide (ZnS) wherein number of alternating planes composed of tetrahedrally coordinated S^{2-} and Zn^{2+} ions, are stacked alternatively along the c-axis. ZnS with band gap of 3.6 eV [3] displays a high refractive index and high transmittance in the visible range which makes it a strong candidate for opto-electronic devices. Most of the group-II-VI binary compound semiconductors crystallize in either cubic zinc-blende or hexagonal wurtzirte structure where each ion is surrounded by four cations at the corners of tetrahedron, and vice versa. This tetrahedral coordination is typical of sp^3covalent bonding, but these materials also have a substantial ionic character. ZnO is II-VI compound semiconductor whose iconicity resides at borderline between covalent and ionic semiconductor. The crystal structure shared by ZnO wurtzite (*B*4), zinc blende (*B*3) and rocksalt (*B*1), at ambient conditions, thermodynamically stable phase is wurtzite [4].

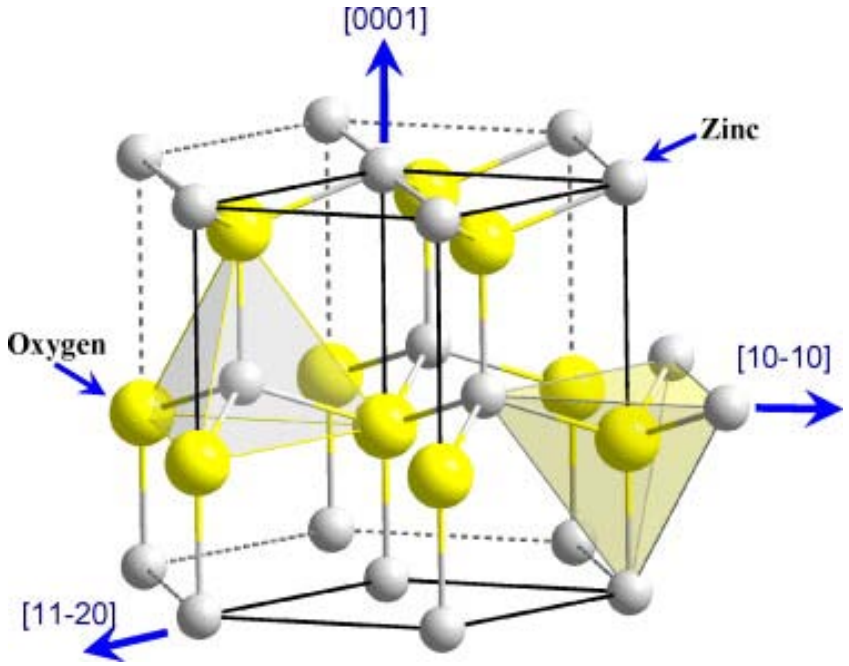

Figure 4: Wurtzite hexagonal crystal structure of ZnO

1.1 Historical developments of ZnO-based semiconductors:

Although, research focusing on ZnO dates back to 1930's, but advantages in thin films growth technology have made possible many advances in ZnO material engineering using appropriate dopant to tailor its properties for the indentified applications. Thin films are always advantageous over their bulk counterpart for device applications. ZnO have found several technological applications owing to its wide band gap and piezoelectric properties.

Also, its charge carrier concentration can be controlled by incorporating different dopants to exhibit insulating, semiconductor or conducting behavior. Initially focus was on the use of ZnO thin films only for transparent conducting layers for solar cell to allow visible light from the sun to the device for efficient collection of charge carriers. Due to its wide band gap (3.3 eV) the harmful UV radiations from sun were absorbed by ZnO to save the underlying device and increase its life time [5]. In 1990's the effect of external dopants like aluminum (Al) in ZnO film resulted in greater electrical conductivity. This aspect of ZnO was later found to be very useful for making high quality transparent conducting electrodes for photovoltaic devices like solar cells [6]. The ZnO thin films have found prominent use in the area of surface acoustic wave (SAW) devices [7] and micro-

electromechanically systems (MEMS). Piezoelectric nature of ZnO and its high coupling coefficient in thin film form have been mostly utilized in these devices.

ZnO itself is *n*-type semiconductor. Recently major emphasis has been put to obtain *p*-type semiconducting films [8]. If robust *p*-type conductivity can be obtained in ZnO film then the prospects of its future applications in homo-junction optoelectronic devices like emitting diodes, lasers, and transparent thin films transistors (TTFTs) are very bright. Several groups reported the fabrication of *p*-type ZnO thin films using various techniques and different dopants, but reproducibility is a major concern. The observation of exitonic lasing in ZnO thin films and nanostructures at room temperature, at a very low threshold power (24 $kWcm^{-2}$) further triggered research interest in ZnO for ultraviolet light emitting devices (UV-LED) [9, 10]. ZnO in this respect is superior because of its wide band gap (3.3 eV) and a large exitonic binding energy (60 meV) compared to GaN (25 meV). Its high radiation hardness to MeV proton irradiation [11] is found useful for space applications, and its large thermal conductivity makes it an ideal material for shorter wavelength devices(such as UV photon detector) and thus finds applications in automotive industry, astronomy, environmental monitoring, military areas and exploration [12, 13]. In recent years, a rich assembly of ZnO nanostructures has been synthesized having various shapes including nanowire, nanorods, nanocombs, nanohelixes, nanorings, nanoflowers, nanoparticles etc. have added a new dimension for potential applications in flat panel displays, field emission sources, gas sensors, UV detectors, UV laser and switches, such one or two dimensional structures are ideal systems for understanding the transport phenomenon of the confined charges and are being exploited for developing new generation of nano- devices with high performance.

1.2 Review of work on undoped and 3d TM doped ZnO thin films:

There has been great deal of interest in zinc oxide (ZnO) semiconductor materials lately, as seen from the surge of relevant number of publications. The interest in ZnO is fueled by its unique optoelectronic applications owing to its wide band gap (E_g ~3.3eV at 300K). Some optoelectronic applications of ZnO overlap with that of GaN, another wide band gap semiconductor (E_g ~3.7 eV at 300K). The growth of ZnO thin films has been studied utilizing growth techniques such as magnetron sputtering [68, 69], chemical vapor deposition and PLD [14]. Latter attempts led to high-quality ZnO single crystal films

prepared by rf magnetron sputtering [15] and other growth techniques allowing a fine control over the procedure, such as molecular beam epitaxy (MBE) [16,17], pulsed laser deposition [18], metal organic chemical-vapor deposition (MOCVD) [19] of the structural, optical and mechanical properties of the ZnO thin films grown by different techniques. One of the most popular growth techniques for early ZnO investigation was sputtering (dc sputtering, RF magnetron sputtering, and reactive sputtering). As compared to sol gel and chemical-vapor deposition [20, 21] the magnetron sputtering was a preferred method because of its low cost, simplicity, and low operating temperate [22]. Post deposition annealing also has been used to relieve the stress and improves the structure and optical properties of the sputtered film [23-24].

The optical properties of a semiconductor are connected with both intrinsic and extrinsic effects. Intrinsic transitions take place between the electrons in the conduction band and holes in the valence band, including exitonic effects due to the Coulomb interactions. Exitons are classified in to free and bound exitons. ZnO has a strong potential for various short-wavelength optoelectronic device applications. In order to attain the potential offered by ZnO, both high-quality *n*- and *p* type ZnO are indispensible. However, difficulty in bipolar carriers doping (both *n* and *p* types) is a major obstacle as seen in other wide-band-gap semiconductors such as GaN, ZnS, ansZnTe [25-32]. Unipolar doping has not been a surprising issue in wide band-gap semiconductors: ZnO, GaN, ZnS and ZnSe are easily doped to *n*-type, while *p*-type is difficult. Generally, 3*d* transition-metal ions (some spices of magnetic ions i.e. ions bearing the net magnetic moment) are substituted for the cations of the host semiconductors. As a consequence, the electronic structure of the substituted 3*d* transition-metal impurities in semiconductors influenced by two competing factors: strong 3*d* host hybridization and strong Coulomb interaction between 3*d*-3*d* electrons, as specifically shown for the Mn-doped systems the hybridizations between the transition metal 3*d* and the host valance band gives rise to the magnetic interaction between the localized 3*d* spins and carriers in the host valance band [33]. Assuming that ZnO can be made ferromagnetic by doping with transition metals such as Mn, Fe, Cr, Co etc., or when spin injecting contacts to ZnO can be found, the material would be suitable for spin FETs. Several groups have fabricated (Zn, TM) O [TM= Mn, [34, 35, 36-41] Fe [42]] films by different techniques. Although there is a great deal of controversy and discrepancy about actual ferromagnetic Curie temperature

and the source ferromagnetism in transition-metal-doped ZnO films found in various reports, T_c values above the room temperature are reported [43].

The theory by Dietl et al [44] assumes that the ferromagnetic correlation among the Mn ions, which provide the spin after substituting the group II or III site, are mediated by the holes from the shallow acceptors. The model suggest that tha carrier –mediated ferromagnetism in *n*-type material may be observed only at low temperatures with shallow donor, while higher temperatures for *p*-type materials (>300K for p-type GaN and ZnO) are predicted.

In addition to the prediction of Dietl*et al*., ferromagnetism in magnetic –ion-doped ZnO has been theoretically investigated by *ab initio* calculations based on the local density approximation by Sato and Katamaya-Yoshida [45-47].Again, the results suggest that ferromagnetic ordering of Mn is favored when medicated by holes. The transition from the antiferromagentic state to ferromagnetic state took place as the holes were introduced, but no transition was found by n-type doping. However, for V, Cr, Fe, Co and NI dopants, ferromagnetic ordering in ZnO predicted to occur without the need for additional charge carriers. Analyzing the density of states, it was suggested that the ferromagnetism originated from completion between the ferromagnetic double-exchange interaction and the antiferromagetic super exchange interaction. Notice that ferromagnetism becomes weaker for Fe-, Co- and Ni-doped ZnO with increasing hole concentration. The stability of the ferromagnetic states for 3d transition-metal-doped ZnOfor no additional carrier doping. It was also found that the ferromagnetic state was ground state for V, Cr, Fe, Co, and Ni in ZnO. As a conclusion, acceptor-doped (Zn, Mn) O and ZnO doped with other 3d transition metals were proposed as candidates of ferromagnetism.

The critical step in designing modern optoelectronic devices is the realization of band-gap engineering to create barrier layers and quantum well in devices heterostructres. In order to realize such optoelectronic devices, two important requirements should satisfied: *p*-type doping of ZnO as discussed previously, and the other is modulation of the band-gap. The spin of electron is hence used in hard-disk technology, yet the challenge that remains is developing a spintronics devices out of semiconductors, which could make the logical elements in the computers function on the principle of measuring the spin state of electrons and not whether current is on or off.

Applications of zinc oxide (ZnO) are numerous. The dielectric properties of humidity sensors based on Li2O-ZnO [48] have been investigated at frequencies from 1Hz to 1MHz at room temperature. The resistivity was found to be dependent significantly on the relative humidity levels. The mechanism for this behavior is related to adsorption of water molecules at grain surfaces [49], especially at the Li sites, with hydrogen bonds between adjacent layers of molecular water forming at progressively higher humidity levels. The electronic conduction happens through, primarily, proton hopping. Among the tetrahedrally bonded semiconductors, ZnO has the highest piezoelectric tensor [67, 50]. In hexagonal wurtzite phase the piezoelectric tensor has three independent components which characterize the full piezoelectric tensor [51]. The polarization induced along the c-axis at zero electric field by a uniform strain in the basal plane or along the c axis is measured. It was found [52] that the piezoelectric constant is strongly sensitive to both temperature and stress. This arises due to a strong hybridization between the O 2p and Zn 3d electrons which itself strongly dependent on bond lengths.

1.3 Objectives of present work:

The general objectives of the present work are to investigate the structure, morphology, optical, mechanical and magnetic properties of undoped and 3d TM doped ZnO thin films with different processing conditions like, working gas, films thickness and effect of substrate in argon, oxygen and nitrogen gas environment. The structure of this work is as follows. First, basics of spintronics are introduced through more pedagogical than chronological approach. The physics of diluted magnetic semiconductors with their spin-dependent properties as potential goldmine of materials for applications in spintronics is discussed subsequently. Zinc oxide, the host material for this thesis work. The aim of this thesis work is to present a systematic study of novel materials, based on a wide band gap zinc oxide, ZnO, that have potential application in spin electronics -spintronics. ZnO, is a material with ubiquitous applications in piezoelectric transducers, varistors and as transparent electrodes.

The Specific Objectives

- To synthesize the thin films of un-doped and 3d TM (= Mn, Fe and co-doped) ZnO thin films by rf-magnetron sputtering.

- To study the structure, morphology, optical, mechanical and magnetic properties of undoped and 3d TM doped ZnO thin films by rf-magnetron sputtering as function of working gas pressure of argon and oxygen gas environment.
- To study the structure, morphology, optical, mechanical and magnetic properties of undoped and 3d TM doped ZnO thin films by rf-magnetron sputtering as function of films thickness in argon, oxygen and nitrogen gas environment.
- To study the structure, morphology, optical, mechanical and magnetic properties of undoped and 3d TM doped ZnO thin films by rf-magnetron sputtering as function of films substrates on in argon, oxgen and nitrogen gas.

1.4 Thesis organization

The thesis has been organized in six chapters as follows

Chapter 1 includes the literature survey and the brief review of work on ZnO doped and 3d doped thin films. The objectives of present work are also listed in this chapter.

Chapter 2 contains the details of the experimental techniques used in the present study. The chapter includes synthesis of target material by solid state reaction and RF-magnetron sputtering for thin films deposition.

Chapter 3 describes the structural, morphological and compositional properties of the as deposited thin film samples.

Chapter 4 presents the optical properties of un-doped and Mn, Fe doped ZnO thin films.

Chapter 5 contains the mechanical properties of the thin films deposited on quartz and silicon substrates.

Chapter 6 deals with the magnetic studies of various undoped and doped ZnO thin films.

The main results and conclusions are summarized at the end of the thesis.

References

[1] J.Gutowski,H.Heinke, D.Hommel and Peter michler, *Phy.sta.sold b***229** (2002) 1.

[2] Shujinakumura, S.J.Pearton, Gerhard Fasol*The blue laser diode* (1997) 368p.

[3] N.R.Pawaskar, S.D.Sathaye, M.M.Bhadbhade, K.R.Patil, *Materials Research Bulletin,* **37**1539.

[4] Ozugure et al J.Appl.Phys, **98** (2005) 041301.

[5] Tadatsugu Minami, Hirotoshi Sato, ShinzoTakata, Takashi Mouri, *Jpn. J. Appl. Phys*.**31** (1992) pp. L1106.

[6]Byeong-Yun Oh, Min-Chang Jeong, Tae-Hyoung Moon, Woong Lee, Jae-Min Myoung, *J. Appl. Phys***99** 124505.

[7] F.S. Hickernell, J.W. Brewer,*Appl.Phys.Lett***21** 389.

[8] S.J.Pearton et.al. *J. Appl. Phys***93** 1.

[9] Qian Huang etal.*Science*, **294** (2001) 870.

[10] Y.G. Wanga, S.P. Laua, X.H. Zhangb, H.H. Hngc, H.W. Leea, S.F. Yua, B.K. Tay, *Journal of Crystal Growth***259** (2003) 335.

[11] F.D. Auret, S.A. Goodman, G. Myburg, S.E. Mohney J.M. de Lucca, *Materials Science and Engineering B***82** (2001) 102.

[12] Fernando Monroy , Manuel Aira, Jorge Domínguez, FuencislaMariño, *European Journal of Soil Biology***39** (2003) 13.

[13] A. Ohtomo, H. Kimura, K. Saito, T. Makino, Y. Segawa, H. Koinuma, M. Kawasaki, *Journal of Crystal Growth***214-215** (2000) 284.

[14] R. D. Visputee*t al.*, Appl. Phys. Lett. **73** (1998) 348.

[15] K.-K. Kim, J.-H.Song, H.-J.Jung, W.-K.Choi, S.-J.Park, and J.-H.Song, J. Appl. Phys. **87** (2000) 3573.

[16] P. Fons, K. Iwata, S. Niki, A. Yamada, and K. Matsubara, J. Cryst. Growth **201** (1999) 627.

[17] Y. Chen, D. M. Bagnall, H.-J.Koh, K.-T.Park, K. Hiraga, Z.-Q. Zhu, and T. Yao, J. Appl. Phys. **84** (1998) 3912.

[18] R. D. Visputee*t al.*, Appl. Phys. Lett. **73** (1998) 348.

[19] Y. Liu, C. R. Gorla, S. Liang, N. Emanetoglu, Y. Lu, H. Shen, and M.

Wraback, J. Electron. Mater.**29** (2000) 69.

[20] S. K. Tiku, C. K. Lau, and K. M. Lakin, Appl. Phys. Lett. **36** (1980) 318.

[21] V. Srikant, V. Sergo, and D. R. Clarke, Appl. Phys. Lett. **16** (1995) 439.

[22] J. L. Vossen, Phys. Thin Films **9** (1977) 1.

[23] R. J. Lad, P. D. Funkenbusch, and C. R. Aita, J. Vac. Sci. Technol. **17** (1980) 808.

[24] K. Ozaki and M. Gomi, Jpn. J. Appl. Phys., Part 1 **41** (2002) 5614.

[25] M. K. Ryu, S. H. Lee, M. S. Jang, G. N. Panin, and T. W. Kang, J. Appl. Phys. **92** (2002) 154.

[26]G. F. Neumark, Phys. Rev. Lett. **62** (1989) 1800.

[27] D. J. Chadi, Phys. Rev. Lett. **72** (1994) 534.

[28] S. B. Zhang, S.-H. Wei, and A. Zunger, Phys. Rev. Lett. **84** (2000) 1232.

[29] T. Minami, H. Sato, H. Nanto, and S. Takata, Jpn. J. Appl. Phys., Part 2 **24** (1985) L781.

[30] S. B. Zhang, S.-H.Wei, and A. Zunger, J. Appl. Phys. **83** (1998) 3192.

[31] D. B. Laks, C. G. Van de Walle, G. F. Neumark, and S. T. Pantelides, Appl. Phys. Lett. **63** (1993) 1375.

[32] C. Weisbuch and B. Vinter, *Quantum Semiconductor Structures* _Academic, San Diego, 1991.

[33] J. K. Furdyna, J. Appl. Phys. **64** (1998) R29.

[34] K. Ueda, H. Tabata, and T. Kawai, Appl. Phys. Lett. **79** (2001) 988.

[35] P. Sharma *et al.*, Nat. Mater. **2** (2003) 673.

[36] K. Ando, H. Saito, Z. Jin, T. Fukumura, M. Kawasaki, Y. Matsumoto, and H. Koinuma, J. Appl. Phys. **89** (2001) 7284.

[37] T. Fukumura, Z. Jin, A. Ohtomo, H. Koinuma, and M. Kawasaki, Appl. Phys. Lett. **75** (1999) 3366.

[38] T. Fukumura, Z. Jin, M. Kawasaki, T. Shono, T. Hasegawa, S. Koshihara, and H. Koinuma, Appl. Phys. Lett. **78** (2001) 958.

[39] S. W. Jung, S.-J.An, G.-C. Yi, C. U. Jung, S.-I. Lee, and S. Cho, Appl.

Phys. Lett. **80** (2002) 4561.

[40] D. P. Norton, S. J. Pearton, A. F. Hebard, N. Theodoropoulou, L. A. Boatner, and R. G. Wilson, Appl. Phys. Lett. **82** (2003) 239.

[41] Y. M. Kim, M. Yoon, I.-W. Park, Y. J. Park, and J. H. Lyou, Solid State Commun.**129** (2004) 175.

[42] Z. Jin *et al.*, Appl. Phys. Lett. **78** (2001) 3824.

[43] S. J. Pearton, W. H. Heo, M. Ivill, D. P. Norton, and T. Steiner, Semicond. Sci. Technol. **19** (2004) R59.

[44] T. Dietl, H. Ohno, F. Matsukura, J. Cibert, and D. Ferrand, Science **287** (2000) 1019.

[45] K. Sato and H. Katayama-Yoshida, Jpn. J. Appl. Phys., Part 2 **39** (2000) L555.

[46] K. Sato and H. Katayama-Yoshida, Physica B **308–310** (2001) 904.

[47] K. Sato and H. Katayama-Yoshida, Semicond.Sci. Technol. **17** (2002) 367.

[48] Costa, M. E. V., Mantas, P. Q., and Baptista, J. L. *Sensors and Actuators B-Chemical*
27(1-3) (1995) 312.

[49] Joanni, E. and Baptista, J. L. *Sensors and Actuators B-Chemical* **17(1)** (1993) 69.

[50] Dalcorso, A., Posternak, M., Resta, R., and Baldereschi, A. *Physical Review B* **50(15)** (1994) 10715.

[51] Nye, J. F. *Physical Properties of Crystals*. Clarendon, Oxford, (1975).

[52] Hill, N. A. and Waghmare, U. *Physical Review B* **62(13)**(2000) 8802.

CHAPTER 2

Thin film preparation and Characterization

This chapter deals with the experimental techniques used for thin film deposition and property measurements.

2.1 Sputter target preparation method:

Solid state reaction, probably the most widely used method for the preparation of polycrystalline solids (i.e. powders) is the direct reaction, in the solid state, of mixture of solid starting materials. Solids do not usually react together at room temperature over normal time scales and it is necessary to heat them to much higher temperatures, often 1000 to 1500^0C, in order for reaction to occur at an appreciable rate. This shows that both thermodynamic and kinetic factors are important in solid state reaction; thermodynamic considerations show whether or not a particular reaction should occur by considering the rate at which the reaction occurs.

The method of target preparation plays a very important role in determining the chemical composition, structural, optical and magnetic properties of diluted magnetic semiconductors (DMS) of un-doped and Mn, Fe, co-doped ZnO target prepared by ceramic method (Solid state reaction). The final ceramic target used as sputter target. Various deposition methods have been used for deposition of thin films, out of them sputtering is the most widely used technique because of its high rate of deposition, uniformity and large area deposition. In this thesis we have used the RF-magnetron sputtering for thin film preparation. In order to appreciate why solid state reaction takes place with difficulty and only at higher temperatures, consider the reaction of two crystals of ZnO and MnO_2 which are intimate contact shared faces

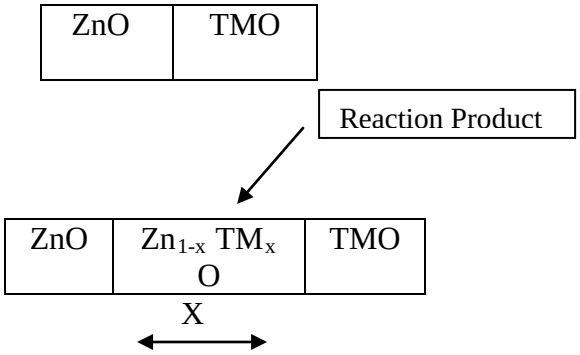

Figure 2.1: Reaction mechanism in sintering process

The most widely used method for the preparation oxide ceramic target is by the reaction of solid components in the correct molar portion at elevated temperature over a long period. The preparation of materials by this method requires the care to avoid excess quantity of reagents as the method involves treatment of the whole lattice and the materials cannot be purified after the synthesis [1].

The $Zn_{1-x}TM_xO$ ceramic targets were prepared using the standard solid-state reaction technique. Stoichiometric amounts of ZnO (99.999%), MnO_2 (99.99%) and Fe_2O_3 (99.99%). For TM= Mn and Fe respectively were calcinated at 400^0C for 4 hrs about 2-3 times with intermediate grinding to get proper mixing. The final powder was pressed into pellets of 2-inch diameter which are to be used as sputter targets suitable for sputter gun. These pellets were sintered at different sintering temperatures of 600, 700 and 900^0C for 12 hrs and were slow cooled are to be used as sputter targets.

2.1.1 Experimental procedure

Solid state reactions are so rarely discussed in text books so it is worthwhile to give details of experimental procedure involved. A typical procedure is outlined in the following, using the synthesis of oxides.

Reagents. For the synthesis of oxide powders, these should be dried thoroughly prior to weighing, by heating at high temperature, e.g. 200 to 800^0C, for few hours. Fine grained material should be used, if possible in order to maximize surface area and hence the reaction rate.

Mixing. After the reactants have been weighed out in the required amounts, they are mixed quantities together. Manual mixing of small quantities (≤ g total), can be done with

an agate mortar and pestle. Agate is preferable to, for example porcelain since it is hard, unlikely to contaminate the mixture and, with its smooth, non-porous surface, is easy to clean afterwards. For quantities much larger than ~20g, manual mixing is very tedious since normal-sized mortars cannot cope with the large quantities of material; mixing must be done in batches. In such cases, mechanical mixing may be better, using a ball mill, and may take several hours.

Heat treatment. The heating programme to be used depends on the form and reactivity of the reactants, refractory materials and is unlikely to react together to any significant degree below 1200 to 1300^0C. The first stage of reaction must be the decomposition of the oxysalt and the mixture should be heated first at appropriate temperatures for few hours are so that decomposition occurs in a controlled manner. If this stage is omitted and the mixture is heated directly at higher temperatures, the decomposition may occur very vigorously and may cause the sample to spit out of the container. In order to speed up the reaction rates, it would perhaps better that the obvious approach is to raise the temperatures high as possible [2]

2.2 Film deposition Techniques

Different types of deposition methods are discussed in the following:

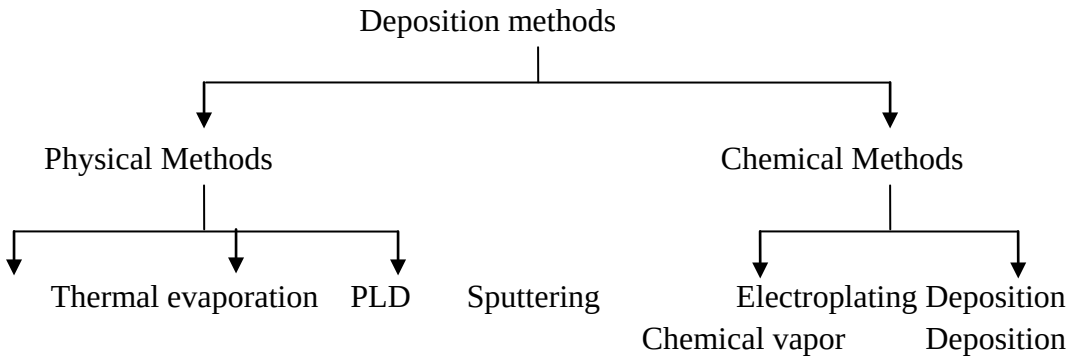

Figure 2.2: Thin film deposition methods

Figure 2.2 summarizes the main preparation methods for thin film process. Different techniques have been used by researchers for the preparation of dilute magnetic semiconductor thin films. These include Chemical vapor deposition (CVD), magnetron sputtering, laser ablation, thermal evaporation, screen planting, ion beam deposition and

ion implantation. Semiconducting thin films can be prepared by chemical vapor deposition (CVD) or physical vapor deposition (PVD) techniques. In both CVD and PVD methods, one of the most critical deposition factors is the kinetic energy of the vapor phase particle, which can generally be divided according to the range of typically reported energies [3,4,5], into three regimes.

1. Thermal regime (0~0.3 eV), in which particles have low energy. Techniques within this range include chemical vapor deposition and thermal evaporation;
2. Mediate regime (1~ 100 eV), in which particles have energies ranging from the bonding strength to lattice penetration threshold. Techniques within this range include sputtering deposition and arc vapor deposition;
3. Implantation regime (>100 eV), in which particle energies are well able to cause surface penetration and implantation. Techniques within this range are ion implantation.

2.2.3 Sputtering

Sputtering is a Physical Vapor Deposition (PVD) process, which etches material from a ceramic target [6]. The physical sputtering (Sputtering) process. It involves the physical (not thermal) vaporization of atoms from a surface by momentum transfer from the bombarding energetic atomic sized particles. The energetic particles usually ions of gaseous material accelerated in the electric field. Sputtering was first observed by Grove in 1858 using von Guericke-type oil-sealed piston vacuum pumps [7]. When solid surface is bombarded with energetic particles such as accelerated ions, surface atoms of the solid are scattered backward due to collisions between the surface atoms and the energetic particles as illustrated in Figure 2.5. This phenomenon is called back-sputtering, or simply sputtering, this technique has become one of the most versatile techniques in the thin films technology for preparing thin solid films of almost any material. Some of the main advantages of sputtering as a thin film preparation techniques are (1) a high uniformity of thickness of the deposited films, (2) good adhesion to the substrate, (3) better reproducibility of the films, (4) ability of the deposit to maintain stoichiometry of the original target composition, and (5) relative simplicity of the thickness control [8].

2.2.3.1. Sputtering compounds

Many compounds have chemical bonds that are stronger than those of the elements and thus have a lower sputter yield than the elements. For example, the sputter yield of TiO_2 is about one tenth that of titanium. Compound generally sputter by preferentially losing the some of the more volatile constituent of the molecule (i.e., oxygen from TiO_2) so the sputtering surface is generally enriched in the less volatile constituent. Often some of the lighter and more volatile species are lost in the transport between the target and the substrate or there is a less than unity reaction probability with the more condensable species on the surface of the depositing material. This leads to a loss of stoichiometry in the deposited film compared to the target material. This loss is often made-up by some degree of reactive deposition.

In sputtering, targets composed of several materials with greatly differing electronegitivities, such as the oxides, may have significant number of negative ions sputtered and accelerated away from the cathodic target. These high energy ions can then be bombard on the growth material, causing sputtering and other bombardment effects. The negative ions can completely re-sputter the depositing material. To avoid this effect, the substrates can be mounted in-an off axis potential or negative bias can be applied to the substrate [7].

2.2.3.2 Sputtering process

The sputtering process can be summarized as follows [9]: an external potential is applied from an outside power source, charging the target with high negative voltage (3 to 5 kV). A gas is introduced into the vacuum chamber between the target and the grounded substrate and chamber wall. The large potential difference causes the ionization of introduced gas in the high electric field that forms *plasma.*

The ionization results in a negatively charged electron and positively charged ion pairs, whereas the plasma itself retains net neutral charge. Positively charged ions are attracted to the negatively charged target and accelerated by electric filed, resulting in a collision with the target material. When an ion approaches the surface of a solid (target), one or the entire following phenomenon may occur (figure2.5) [10].

- The ion may be reflected, probably being neutralized in the process.
- The impact of the ion may cause the target to eject an electron, usually referred to as a *secondary electron.*
- The ion impact may become buried in the target. This is the phenomenon of *ion implantation.*
- The ion impact may also be responsible for some structural rearrangements in the target material.
- The ion impact may set up a series of collisions between atoms of the target, possibly leading to the ejection of one of the neutral atoms from the material by *momentum transfer*. The ejection process is known as *sputtering.* The sputtered atoms leave the target surface with relatively high energies (~ 10 eV) compared to evaporation atoms (~ 0.1 eV). This ejected flux of target atoms, which has a main direction, is then transported through the space towards the substrate where they condense and form a thin film [11].

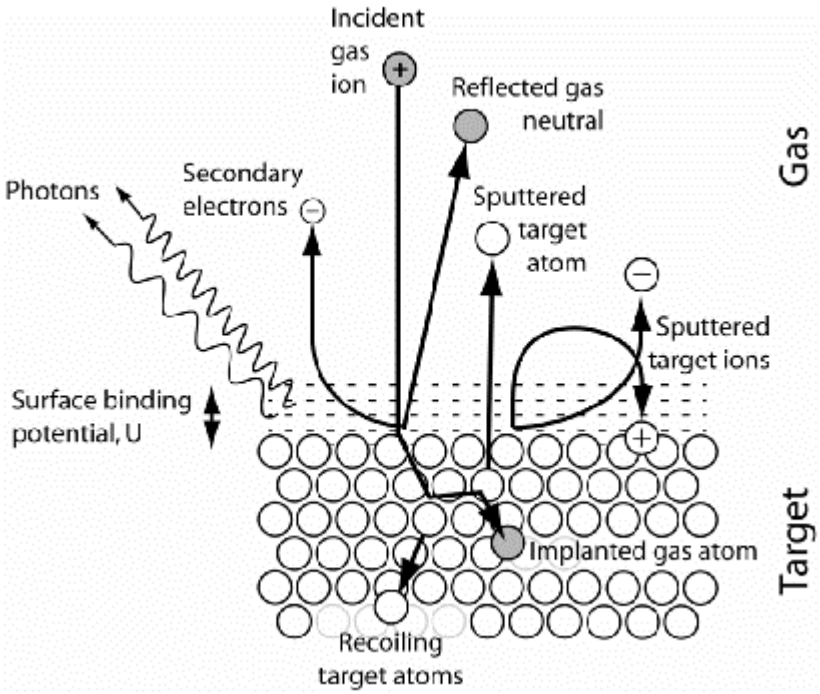

Figure 2.5 Schematic view of the physical sputtering process [12]

The average number of the atoms ejected from the surface per incident ion is called the *sputtering yield* [13]. The sputtering yield, S depends on many factors, such as the mass and the energy of the incident particles; the mass and the binding energy of the sputtered atoms; the crystallinity of the target; etc. and can be described as [13,14]:

$$S = const\,(E_{ion} - E_{thers}) = const \times e\,(V_p - V_{dc} - V_{thers}) \qquad (2.1)$$

where E_{ion} is the energy of the incident ion, $E_{thers} = 8U_s \left[\frac{M_1}{M_2}\right]^{2/5}$ is the threshold energy

V_p is the plasma potential, V_{dc} is the dc voltage on the target (discharge voltage), U_s is the surface potential barrier and M_1 and M_2 are the mass number of the ion and the target, respectively.

The deposition rate R is proportional to the sputtering yield S, and I (1-γ), with I the discharge current and γ the secondary electron emission coefficient [15].

$$R = const \times SI\,(1-\gamma) \qquad (2.2)$$

The principle of *momentum transfer* used to deposit material has made the sputtering technique very attractive. Using this technique, it is easy to deposit materials which could not be easily deposited using other deposition techniques. This includes even refractory materials.

Depending on the gas pressure and the distance between substrate and target the flux will be more or less scattered by the gas. The average distance an atom can travel before a collision called the *mean free path (λ)*. The mean free path λ can be estimated through [12].

$$\lambda = \frac{kT_g}{\sqrt{2\pi P_g d_g^2}} \qquad (2.3)$$

where k is the Boltzmann constant, T_g and P_g the gas temperature and pressure respectively, and d_g the diameter of the gas molecule (d_{Ar} = 0.364 nm). During the sputtering process, the films surface is ion bombarded. Because of the high-energy state of plasma, sputtered particles have enough energy to migrate on the films surface which can densify the growing film by enhancing the surface atom mobility [16]. In addition, ion bombardment of the growing film can restrict the grain growth and permit the formation of nanocrystalline grown in the film [17]. The size and crystallographic orientation of grains can be controlled by the energy of bombarding ions [13].

2.2.3.3 Effect of magnetic field (Magnetron sputtering)

The ionization efficiency improved by using a magnetic field parallel to the cathode surface and thus retaining the primary electron motion to the vicinity of the cathode [18]. These electrons thus trapped move inside the orbit gain a higher mean free path and collisionally scatter before reaching the anode. Consequently magnetron sputtering requires a lower gas pressure to sustain the plasma compared to that of the diode sputtering technique. Reduced scattering and increased electron usage efficiency leads to a better deposition rate and reduced applied voltage to sustain plasma in this technique. Besides these advantages, this technique has the disadvantage of the discharge being swept to one side by the E × *B* force [6]. This is avoided by using the cylindrical cathodes that allow these drift currents to close on themselves.

On the basis of the type of magnets used, magnetron sputtering is classified into different categories like cylindrical magnetron, hollow cathodes, cylindrical post, cylindrical hallow and planar magnetrons [3].

2.2.3.4 Film growth

Thin film formation includes the process of nucleation and growth. During the earliest stage of films formation, a sufficient number of vapor atoms or molecules condense and establish a permanent residence on the substrate. There are three basic growth modes [3]. (1) Island mode (or Volmer- Weber), (2) layer by layer mode (or Frank-van der Merwe), and (3) mixed mode (Stranski- Krastanov), which are illustrated schematically in Figure 2.6. Island growth occurs when the smallest stable clusters nucleate on the substrate and grow in three dimensions to form an island. This island growth happens when atoms and molecules in the films are more strongly bound to each other than to the substrate. Many systems of materials on insulators, alkali halide crystals, and graphite are good examples of this growth mode.

The opposite characteristics are displayed during the layer growth. In the layer growth mode, the atoms are more strongly bound to the substrate than to each other. The first complete monolayer is then covered with somewhat less tightly bound second layer, providing the decrease in binding energy is continuous toward the bulk crystal value. The layer growth mode is sustained. The most important example of this growth mode involves single crystal epitaxial growth of semiconductor films. The layer plus island or mixed growth mechanism is an intermediate combination of both above mentioned

modes. In this case, after forming one or several monolayers, subsequent layer growth becomes unfavorable and an island is formed. The growth of DMS films prepared using sputtering system could be attributed to the third mode.

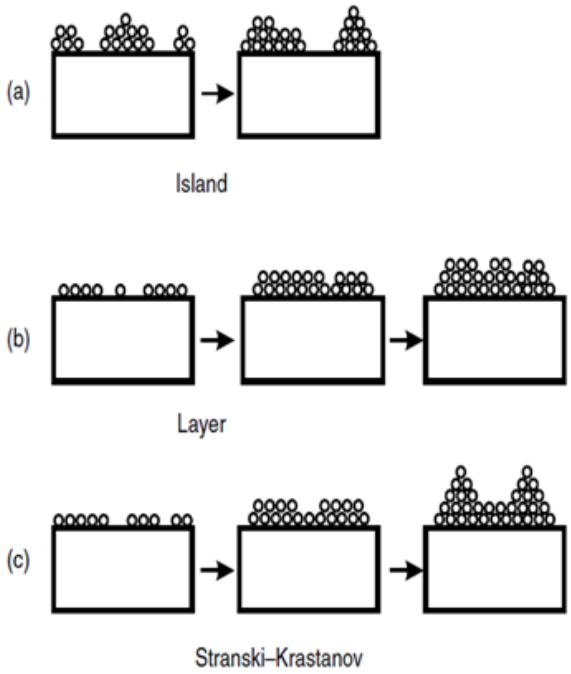

Figure 2.6 Modes of growth of films (a) Volmer-Weber island growth (b) Frank-Vander Merwe layer growth and (c) Stranski-Krastanov layer plus island growth (mixed) [19].

2.2.3.5 Film microstructure

The most important parameters which influences the final grain structure of a vapor-deposited film for a given material are substrate temperature and growth flux. The growth flux is a quantity that represents the mass or volume flow rate onto the growth surface. In general, increasing the rate of deposition tends to promote formation of a finer scale microstructure, while increasing the substrate temperature tends to promote a coarser microstructure or single crystal growth [16]. Polycrystalline films are commonly described in terms of their grain structure, which is usually understood to include some measure of grain size, grain boundary morphology (typical grin shape), and film texture (distribution of crystallographic orientations). Thornton [18] proposed a four zone model which is illustrated in Figure 2.7. In zone1, tapered or fibrous grains and voided boundaries from where the structure is influenced by the shadowing effect and by the roughness of the substrate surface on which deposition is made. The transition zone is marked by dense grain boundary arrays and a film with a high dislocation density.

Columnar grains evolve in zone 2, where the evolution of the structure is aided by surface diffusion process. The transition from surface diffusion to bulk diffusion, as well as recrystallization and grain growth lead to the formation of an equipped grain structure in zone 3. As a general trend similar structures evolve at higher temperatures in sputtered films as compared to evaporated films [17, 19-21].

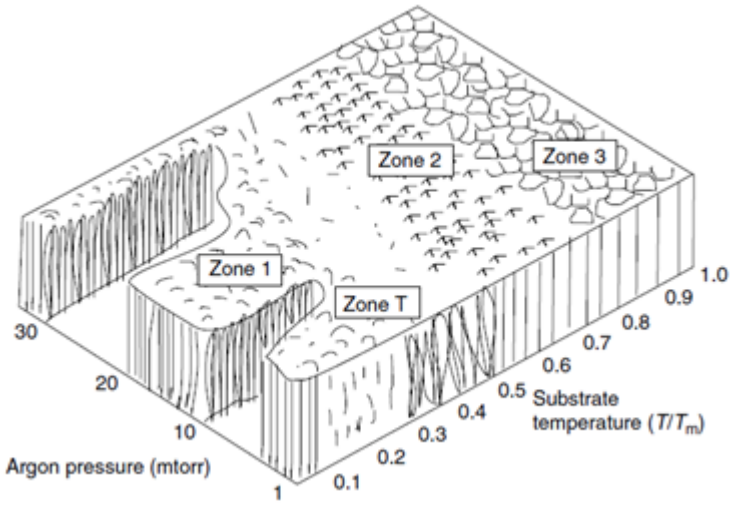

Figure 2.7 Structural evolution of polycrystalline films as a function of substrate temperature and argon gas pressure, following the four-zone model of Thornton [19].

2.2.3.6 Deposition Equipment (Sputtering system)

Grove's (1852) observation of metal deposits on the walls of discharge tube emanating from the electrodes is the precursor for the use of sputtering in the deposition of thin films [19]. Sputtering is a type of Physical Vapor Deposition (PVD) as it uses the principle of momentum transfer to remove neutral atoms from a target. Several sputtering systems are proposed for thin- film deposition including dc diode, rf diode, magnetron, and ion-beam sputtering. The simplest model is the dc-diode sputtering system. The dc-sputtering system is composed of a pair of planar electrodes. One of the cathodes is covered with target materials to be deposited. The substrates are placed on the anode. The sputtering chamber is filled with sputtering gas, typically argon gas at 5 Pa (4×10^{-2} Torr). The glow discharge is maintained under the application of dc voltage between the electrodes. In the dc sputtering system, the target is composed of metal since the glow discharge (current flow) is maintained between the metallic electrodes. The schematic diagram of the dc-sputtering system is shown in Figure 2.8.

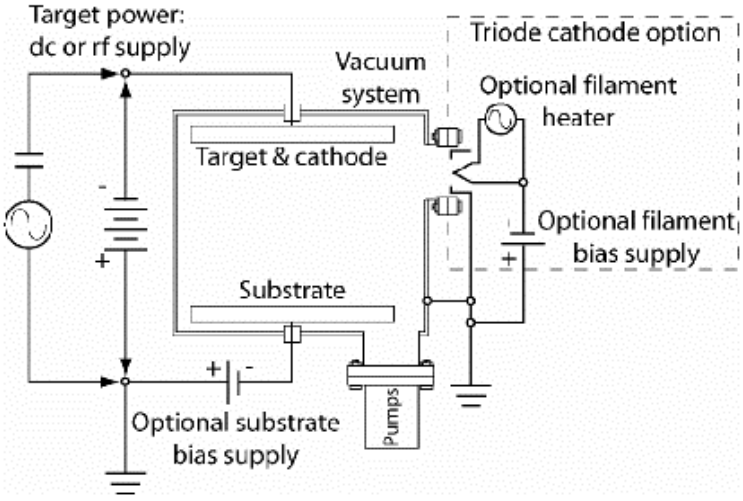

Figure 2.8: Schematic showing the basic features of a dc- sputtering deposition [18]

By simple substitution of an insulator for the metal target in the dc sputtering discharge system, the sputtering discharge cannot be sustained because of the immediate build up of surface charge positive ions on the front side of insulator. To sustain the glow discharge with the insulator target, rf voltage is supplied to the target. This system is called rf-diode sputtering. In the rf-sputtering system, the thin films of the insulator are sputtered directly from the insulator target.

RF sputtering makes it possible for the dielectric material to be sputtered relatively low voltages. However, due to the inherent difficulty of passing current through a dielectric, sputtering rates for oxides are extremely slow and inefficient. Magnetron sputtering helps alleviate this problem by introducing a magnetic field in addition to the usual electric field present in the plasma as demonstrated in Figure 2.9. This helps to confine electron motion to the target area, improving plasma intensity and thus the deposition rate. The fact that the plasma is more confined to the area between the target and substrate, efficiency by reducing the amount of material wasted during deposition.

In magnetron sputtering, a magnetic field is superposed on the cathode and glow discharge, which is parallel to the cathode surface. The electrons in the glow discharge show cylindrical motion, and the center of the orbit drifts in the direction of **E×B** with the drift velocity of E/B, where E and B denote the electric field in the discharge and the superposed transverse magnetic field, respectively.

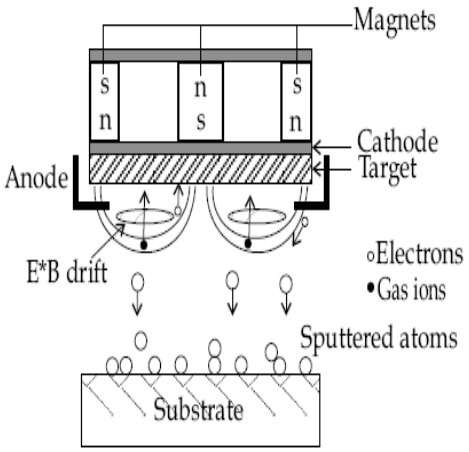

Figure 2.9: Simplified cross-section of a Sputtering system.

The magnetic field is oriented such that these drift paths for electrons from a closed loop. This electron trapping effect increases the collision rate between the electrons and the sputtering gas molecules. This enables one to lower the sputtering system, the magnetic field increase the plasma density which leads to increase in the current density at the cathode target. Due to the gas's low working pressure, the sputtered particles travel the discharge space without collisions, resulting in a higher deposition rate.

When a reactive gas species such as oxygen or nitrogen is introduced into the chamber, thin films of compounds (i.e., oxide or nitrides) are deposited by the sputtering of the appropriate metal targets [22]. This technique is known as *reactive sputtering* may be used either in dc or rf mode. Reactive sputtering is used, in practice, for the high-rate deposition of insulating metal oxide films. In these glow-discharge systems, sputtering gas molecules, during thin-films growth, irradiated the sputtered films. This causes the inclusion of the gas molecule in the sputtered films [23].

In a plasma magnetron, the magnetic flux on the cathode surface is terminated to the magnetic core as shown in the Figure 2.10 (a). The magnetron is called a *balanced* magnetron shown in Figure 2.10 (b), the magnetron is called an *unbalanced* magnetron.

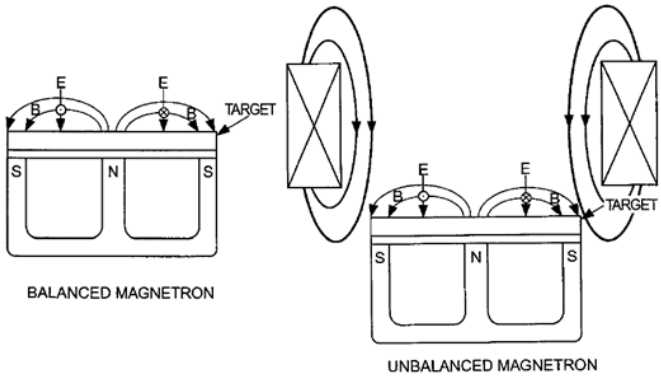

Figure 2.10: (a) Balanced (Left) and (b) Unbalanced magnetron sputtering (Right) [3].

2.2.3.7 RF-Magnetron Sputtering System

DMS films were deposited by employing TORR R300 rf-magnetron sputtering system as shown in figure 2.11. The deposition equipment is composed of two 2-inch planar high performance water cooled magnetrons, a stainless steel chamber, high vacuum system, switch cabinet, a heated rotatable substrate holder, etc. The equipment as provision of cooling water supply to cathode, power supply and turbo pump. The schematic diagram of the construction of the sputtering system is displayed in Figure 2.12.

(a)

(b) (c) (d)

Figure 2.11: (a) Sputtering System used in this work (*Torr International, Inc, USA*) and Plasma colors of (b) Argon, (c) Oxygen and (d) Nitrogen gases during the deposition process.

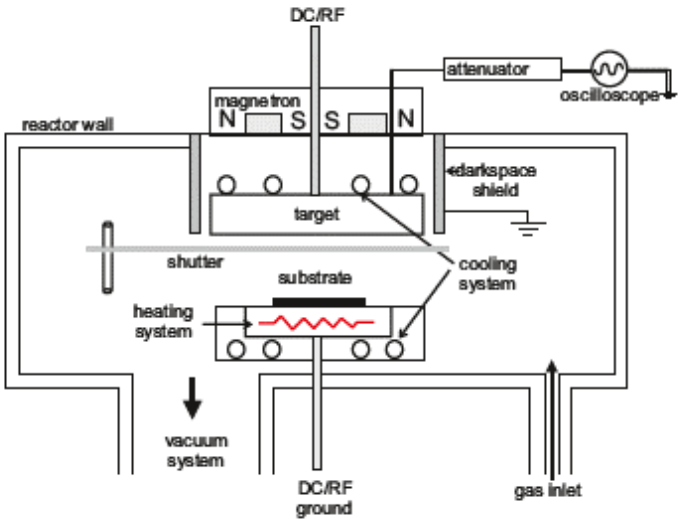

Figure 2.12: Schematic diagram of the sputtering system with magnetron [24]

The material to be deposited (target) acts as the cathode and is connected to a negative voltage RF power supply. The substrate is placed on a substrate holder and could be grounded, floating, biased, heated, cooled, or could be a combination of these. The substrates are exactly below the target which makes 15^0 with the normal to the substrate. This set up placed inside a vacuum system is pumped down and maintained at high vacuum. An inert gas like Argon is introduced into the system as a medium for glow discharge. This is because an inert gas like argon has its meta-stable energy greater than its first ionization potential which helps in producing a sufficient supply of ions for self-sputtering. When this glow discharges are initiated, ions with high kinetic energy strike the cathode (target) resulting in sputtering. The main parts of the deposition system are elaborated as follows.

1. Process Chamber

The sputtering chamber used to deposit the DMS oxide films is made up of electro-polished stainless steel chamber of dimensions 16 inch × 16 inch. These materials are non corrosible, non-magnetic, easy to weld and clean, highly malleable and have good out-gassing characteristics. The process chamber contains feed-throughs for power, waterlines (for supplying cooling water to the sputter guns and crystal monitor), thermocouple, gas lines and other purposes. Rubber O-rings act as a vacuum sealant between the feed-throughs and the chamber. The chamber contains a rotatable substrate holder around a central axis supported by an external motor connected to the chamber through one of the feed-throughs. It also contains two rf sputtering guns above the substrate holder. The typical base pressure that could be maintained using this setup is in the 10^{-3} Torr range. The sputtering system used to deposit the films for our work is made by TORR Company, USA. Figure 2.11 depicts the vacuum chamber used to deposit the ferrite films.

2. Vacuum System

The vacuum inside a sputtering chamber is created and maintained using a pumping assembly. There are various factors that are to be considered when choosing a pumping system. The pumping rate, ultimate pressure that can be achieved, ability to handle gas loads and potential for oil contamination for the pump are some of them. The pumping system used in this work is a combination of rotary vane pump (Varian DS 302) for roughing the system to a pressure of 10^{-3} Torr and a Varian turbo-molecular pump (300 l/s) for maintaining a high vacuum inside the system. This pump has the capability to pump the system down to a pressure in the microtorr range. The vacuum system is also composed of choke (for reducing the volume flow rate during sputtering) and a full range compact pressure sensor.

3. Source and RF-Sputtering power supply

The system is attached with two 2-inch Angstrom Science magnetron guns, each with innovative integral shutter shielded for depositing metals and dielectric target materials. The guns are at a tilt angle and focus at the center of the substrate stage. The guns are retractable up to 6 inch while keeping the focal point the same. The electrical systems of rf sputtering for DMS deposition involves an rf generator operated at 13.56 MHz, an rf switching control, an rf selector switch and two matchboxes (Figure 2.13). The output of

the rf generator is up to 300 W. Figure 2.09 shows the sputtering cathode with cross-sectional schematic diagram of planar magnetron sputter gun. It consists of target, backing plate, target holder, ground shield, permanent magnet, pole piece, ceramic insulator and cooling water inlet. The entire gun is oriented ~15° from the substrate normal and 5-6 cm center to center distance of the target to the surface. The electrical connections show how the target is isolated from the grounding shield which is at common ground with the substrate stage via the chamber walls.

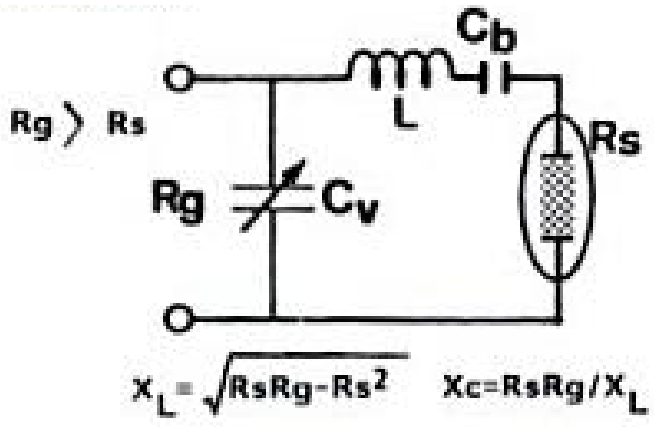

Figure 2.13: A typical “L” matching network used on an RF diode sputtering system [25].

Further attachments

1. Substrate heater

The substrates are heated using quartz lamp heating arrangement to heat the sample stage up to 400 °C. The temperature is controlled and maintained digitally through a PID controller on front panel using a thermocouple as a sensor.

2. Pressure gauges

Deposition pressure is one of the most important parameter that could affect the properties of the film. A full range combination cold cathode and pirani gauge measuring from 760 to 10^{-8} Torr is provided.

3. Mass flow controller

There are two mass flow controllers with shutoff valves for Argon and Oxygen. A unique gas shower ring is provided inside the chamber for uniform gas distribution during the sputtering process.

4. RF Power supply

The RF power supply is capable of delivering up to 300W. The RF supply is with an auto matching network in order to minimize the reflected power. Both the total and reflected power is shown digitally on displays.

2.2.3.8 Experimental Procedure

1. Target preparation

The source for the material to be deposited, the sputtered target, is a 2-inch ferrite ceramic target matching the size of the sputter gun. The targets are made of fine powders of ZnO (99.999%), MnO_2 (99.999%) and Fe_2O_3 (99.999%) of *Sigma Aldrich* make. The powders grounded and calcinated at 400^0C for 3 hrs and re-grounded after getting the proper phase formation of the resultant powder was pressed into pellet of 2-inch diameter by hydraulic press and was sintered at 700-900^0C. Slow cooling rate was maintained for cooling the target. The final target was loaded into the sputter gun for thin film deposition.

2. Substrate cleaning

All the films were deposited on glass and quartz substrates. The substrates were subjected to a sequential cleaning process before being loaded for deposition. The substrates were rinsed in following distilled water to remove the dust particles. They are then cleaned with acetone to remove any organic impurities followed by a subsequent cleaning with isopropyl alcohol. The substrates were ultrasonically cleaned with distilled water. Complete drying is achieved by hot air dryer at 40°C for 30 minutes.

3. In order to produce an edge for the thickness measurement by a profilometer, a glass slide was fixed on the glass substrate before coating and removed later together with the material deposited on top of it.

4. The substrates are loaded onto a circular stainless steel substrate holder. This set up is then mounted on the rotary sample holder assembly. This rotary assembly aids in placing the substrate exactly under the DMS target.

5. Chamber evacuation

The vacuum chamber was evacuated down to a base pressure of 2×10^{-6} mTorr prior to the deposition.

6. The gun shutter to the DMS target is opened. The RF power to the sputtering gun is turned on and the target was pre-sputtered for 10 min in chosen Argon, Oxygen, Nitrogen and gases.

7. The substrate was brought under the target and kept in this position for the entire sputtering process.

8. The films were deposited for different time durations.

9. The optimized sputter parameters were listed in the table below.

Table.1 Experimental parameters use for the thin film deposition in this thesis work.

	Experimental parameters
Substrates	Glass, Quartz and Silicon
Base pressure	1×10^{-6} mTorr
Working gas pressure	5, 8, 12 and 15mTorr
S-T distance	85 mm
RF power	40, 60, 80 and 100W
Working gas	Argon, Oxygen and Nitrogen
Deposition duration (min)	30, 60, 90 and 120

2.3 Characterization techniques

The characterization of materials requires obtaining information about the spatial arrangement of the atoms and identifying precisely which atoms occupy which particular sites in the crystal structure. It also includes the specifications of imperfections, impurities, in homogeneities, and so on. Often, it involves measuring some particular electronic or optical properties. This chapter includes the deposition of DMS films and

the physical principles of a set of tools that have been used to characterize the prepared samples with details of the experimental procedure. Some tools produce pictures of the material in the real space. These include the field-emission scanning electron microscope (FE-SEM) and the atomic force microscope (AFM). Other complementary tools take pictures in momentum space or wave-vector space rather than in real space such as x-ray diffraction (XRD).

Additional tools provide information about the dynamical response of a material. Included among the numerous techniques available in frequency space are the optical spectroscopes: infrared, visible, and ultraviolet and micro Raman spectroscopy. There are spectroscopic techniques in which both the electrons and photons play a significant role. Included among the spectroscopic tools we have extensively used in this study. The experimental techniques employed for the characterization of as deposited DMS films used in this work as follows.

1. X-ray diffraction (XRD) (θ-2θ scan)
2. Field emission scanning electron microscopy (FE-SEM)
3. Energy dispersive X-ray spectroscopy (EDS)
4. Thickness measurement (Surface profilometer)
5. Atomic force microscopy (AFM)
6. Uv-Vis spectrophotometer
7. Nano-indentation
8. Vibrating sample magnetometer (VSM)

2.3.1 X-Ray Diffraction (XRD) (θ-2θ Scan)

X-ray diffraction (XRD) is a powerful technique used for analyzing the structure, geometry, and phase identification of unknown materials. It can be used on single crystal materials or for the determination of preferred orientation, defects, and stresses in thin films as well as polycrystalline materials [13]. XRD is based on the scattering of x-rays from crystal. Scattering is defined as the deflection of either waves or particles randomly as a result of collisions. In the case of x-ray radiation, the waves are scattered by electrons surrounding atoms. The total scattering of a system is the combination of the scattered from an individual atom in the solid summed over the contribution of all related in the lattice [14].

Diffraction effect is observed when electromagnetic radiation impinges on periodic structures whose geometrical variations on the length scale of the wave length of the radiation. The interatomic distances in crystals and molecules amount to 0.15-0.4 nm which correspond in the electromagnetic spectrum with the wavelength of x-rays having photon energies between 3 and 8 keV. Accordingly, phenomena like constructive and destructive interference become observable when crystalline and molecular structures are exposed to x-rays. When a monochromatic x-ray radiation is incident upon the sample, a part of the radiation is scattered from the sample atoms and the constructively interferes when certain conditions are satisfied. This phenomenon is known as diffraction of x-rays (Figure 2.14) and the condition is known as the Bragg law [26].

$$n\lambda = 2d_{hkl} \sin\theta \qquad (2.4)$$

where n is order of diffracting grating,

λ wave length of x-rays used.

Two incident rays are scattered from two atomic planes of the crystal. The difference of two rays is equal to the double product of the inter-atomic plane distance d_{hkl} and the sin function of the incident angle θ. The Bragg law says that if the path difference equals an integer of the incident x-ray wavelength then the constructive interference of the diffracted beam occurs and a sharp diffraction peak can be observed.

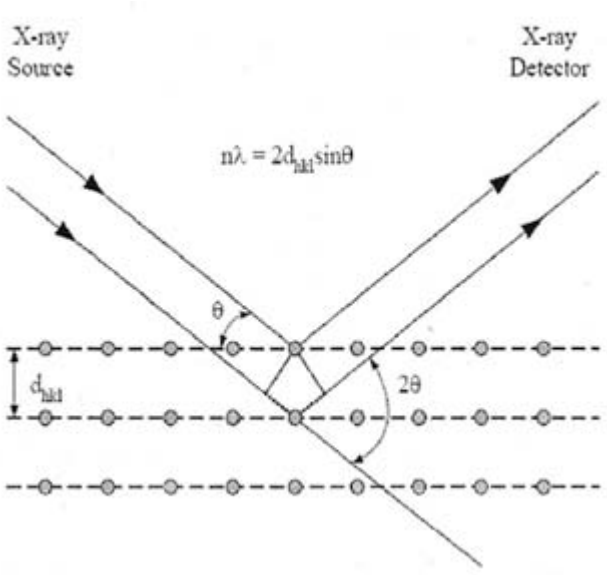

Figure 2.14: Reflection of X-rays from different atomic planes illustrating Bragg's law [26].

The key components of a modern diffractometer include a monochromatic radiation source, sample stage (gonimeter), radiation detection system, enclosure, and safety features. One of the most common configurations is the θ-θ upright. This type of diffractometer has a movable detector and x-ray source, rotating about the circumference of a circle centered on the surface of a flat powder specimen.

Figure 2.15 shows the beam path schematically. The intensity of the diffracted beam is measured directly by an electronic solid-state detection system. The scattered x-rays dissipate energy by generating electron-hole pairs in the detector. The electronic system converts the collected charge into voltage pulses. The electronics counts the number of pulses per unit of time, and this number is directly proportional to the intensity of the x-ray beam entering the detector.

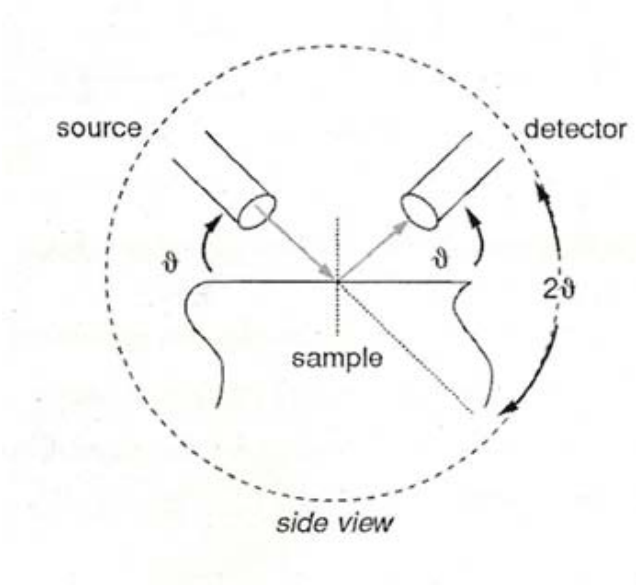

Figure 2.15: Schematic of θ-θ upright configuration where the source and detector each move at a constant rate of θ relative to the sample. So that they move to 2θ, relative to one another [27].

The XRD technique used to characterize powders of single crystal as well as polycrystalline materials. The material of interest is grounded to produce a fine randomly oriented powder, with each particle in the powder consisting of small single crystals or an aggregate of crystals 10 μm or less. The powder is placed into a recess of a plastic sample holder and leveled flat in the sample holder with a straight edge.

This sample is irradiated by monochromatic X-rays, which will be diffracted according to Bragg's law. In our experiment we have used X' Pert Philips PW 1730 diffractometer with Cu-K_α source (λ = 0.15406 nm) and with Co-K_α (λ = 0.17898 nm)

Inel XRG 3000 France. The diffraction intensity is measured continuously during a detector scan of 2θ, coupled to a specimen rotation of θ as shown in Figure 2.16. The recorded results are presented in the form of a diffractrogram where I, is the intensity, plotted as a function of 2θ. The recorded results are then compared with theoretical calculation and literature.

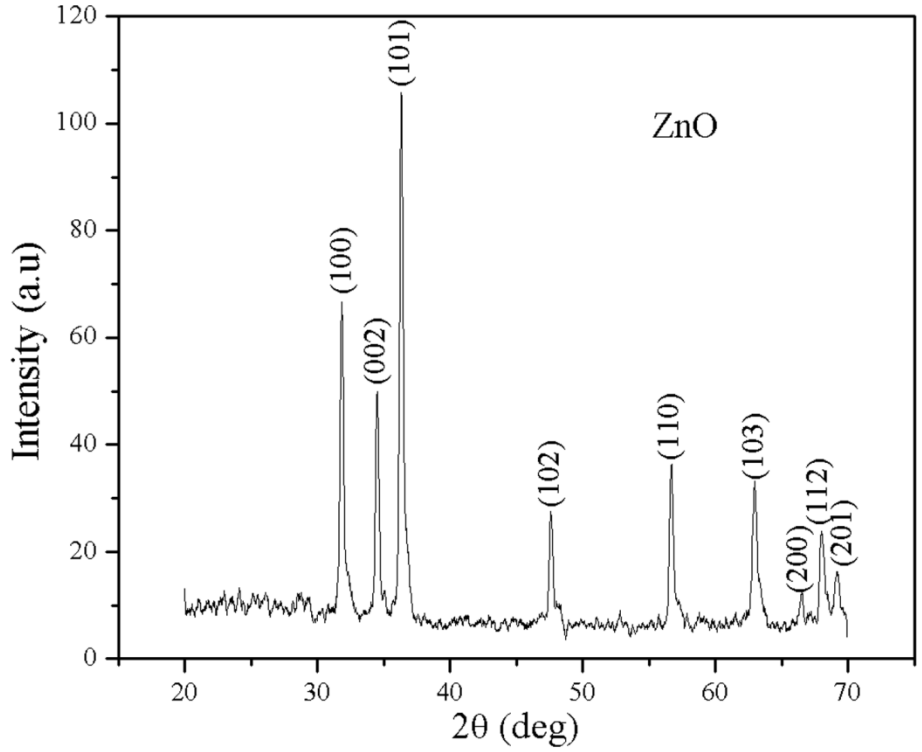

Figure 2.16: XRD patterns of the ZnO powder obtained in this work.

The diffraction data were fitted with a lorentzian function to determine the location of each peak 2θ (Figure 2.17). Using Bragg's law, the interplanar lattice spacing, d_{hkl}, was calculated. The variation of the average lattice spacing, i.e. the slight shift of the (hkl) peak position, in the direction normal to the plane of the films gives strain on the films; it is either compressive or tensile. The strain on films is calculated using the following formula:

$$Strain\ (\%) = \frac{\Delta d}{d} \times 100 \qquad (2.5)$$

Where d is lattice spacing. A characteristic shift towards lower angles compared to the reflex of ideal crystals indicates a lattice expansion. The broadening due to strain (ε) can be written as $\Delta\beta$ = -ε tanθ where ε = $\frac{\Delta d}{d}$. The XRD line width and particle size are

connected through the Scherrer equation [29], $D = \frac{0.9\lambda}{\beta_1 \cos\theta}$ where, D is particle diameter, λ the wavelength of the x-ray radiation and β_1 a measure of the broadening of diffraction line due to size effect.

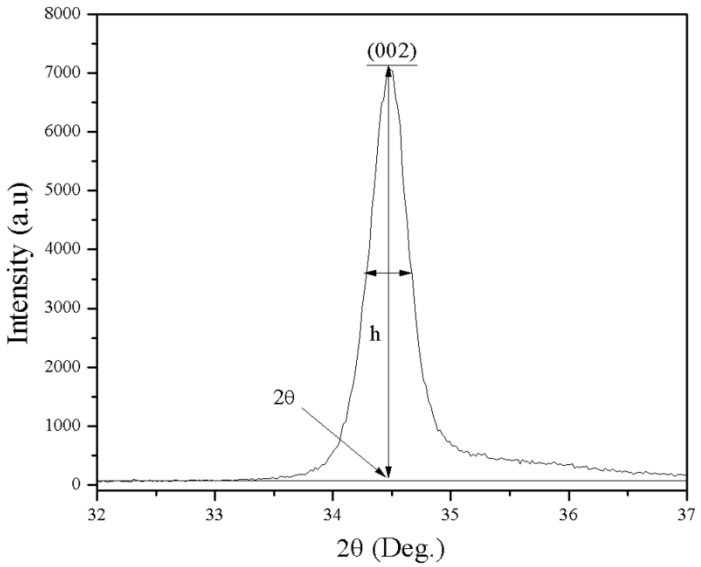

Figure 2.17: The (002)-reflex of XRD for $Zn_{0.95}Mn_{0.05}O$ films in nitrogen atmosphere obtained in this work.

Now, if both, the effect of "particle-size broadening" and "strain-broadening" is taken into consideration, then the total broadening (β) can be expressed as follows [28], using the Williamson-Hall relation

$$\beta = \beta_1 + |\Delta\beta| = \frac{\lambda}{D\cos\theta} + \varepsilon \tan\theta \qquad (2.6)$$

$$\frac{\beta\cos\theta}{\lambda} = \frac{1}{D} + \frac{\varepsilon\sin\theta}{\lambda}$$

where β is the full width at half maxima (FWHM) of the XRD peaks of the sample, D is the effective particle size and ε is the effective strain. A plot of $\frac{\beta\cos\theta}{\lambda}$ vs. $\frac{\sin\theta}{\lambda}$ will be a straight line, slope of which will give the estimation of the effective strain, whereas the intercept on $\frac{\beta\cos\theta}{\lambda}$ axis will carry the information of the particle size.

Usually, the polycrystalline sample is such that crystal aggregates orientations may deviate widely from complete randomness, which is said to possess texture. In general the recorded reflected intensities of different orientation are usually normalized and

compared with those tabulated peak positions and heights of the slandered powder diffractograms.

2.3.2 Field Emission Scanning Electron Microscopy (FESEM)

Field emission scanning electron microscope (FESEM) [29], is a scanning probe microscope technique to observe the small structures (as small as 1 nanometer = one billion of a millimeter) on the surface of the materials. FESEM works with electrons (particles with negative charge) instead of light. These electrons are liberated from field emission source. The object is scanned by electrons according to a zig-zag pattern. The electrons are liberated from field emission source and accelerated in a high electric field gradient. Within the high vacuum column these so-called primary electrons are focused and deflected by electronic lenses to produce a narrow scan beam that bombards the object. As a result secondary electrons are emitted from each spot on the object. A detector catches the i.e secondary electrons and produces an electronic signal. This signal is amplified and transformed to a video scan image that can be saved and processed further. In standard electron microscope electrons are mostly generated by heating a tungsten (W) filament by means of a current to attain temperature of about 2800^0C. Sometimes electrons are produced by a crystal of lanthanum hexaboride (LaB_6) that is mounted on the tungsten filament. This modification results in a higher electron density in the beam and better resolution than with conventional device. In a field emission (FE) scanning electron microscope, no heating but so-called “cold” source is employed. An extremely high thin and strong tungsten needle (tip diameter 10^{-7}-10^{-8} m) functions as a cathode in front of primary and secondary anode. The voltage between cathode and anode is of the order of 05 to 30 KV. Because the electron beam produced by FE source is 1000 times smaller than in a standard microscope, the image quality is markedly better. As field emission necessitates an extreme vacuum (10^{-8} Torr) in the column of microscope, a device is present that regularly decontaminates the column of electron source by a current flash. In contrast to a conventional tungsten filament, a FE tip has theoretically for a life time, provided the vacuum is maintained stable.

Working mechanism:

The electron beam is focused by the electro-magnetic lenses (condenser lens, scan coils, stigmator coils and objective lens) and the apparatus in the column to a tiny sharp spot.] as shown schematically in the figure 2.18

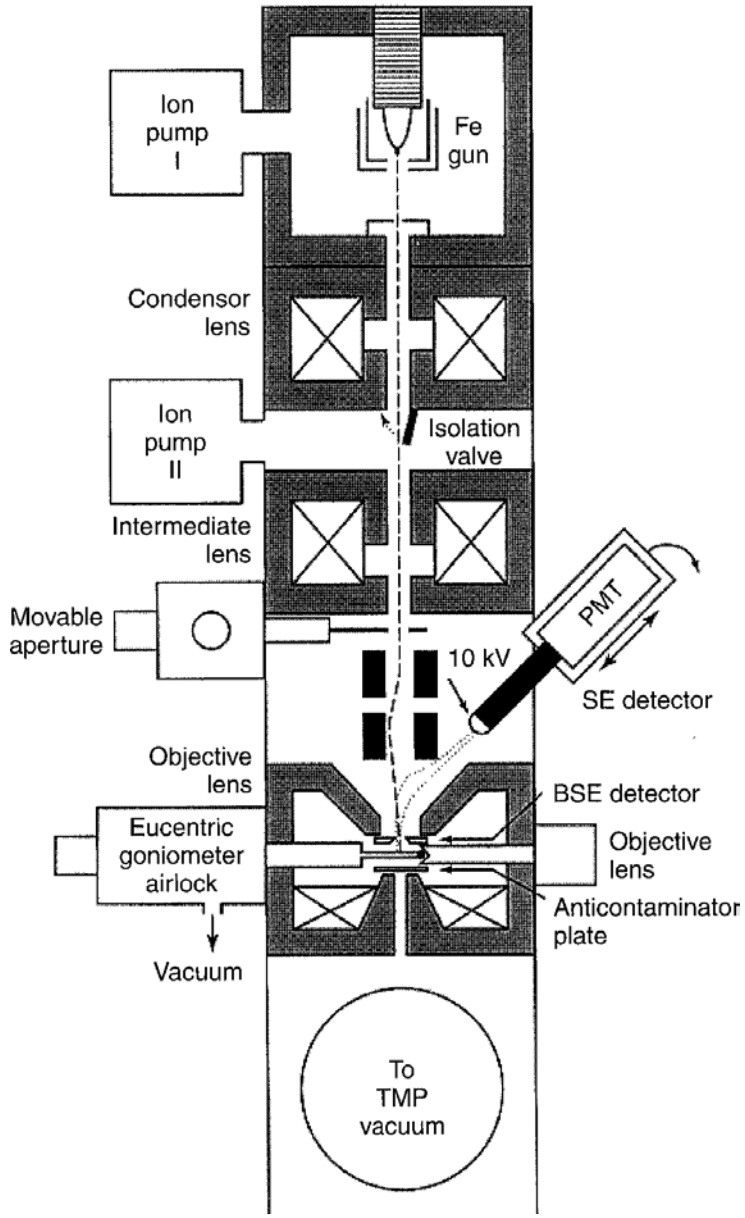

Figure 2.18: A typical view of In-Lens FE-SEM [30].

1. Condenser lens

The current in the condenser determines the diameter of the beam: low current results in a small diameter, a higher current in a larger beam. A narrow beam has the advantage that the resolution is better, but the signal to noise ratio is worse. The situation is reversed when the beam has a larger diameter. The condenser lens consists of two parts.

2. *Scan coils*

   The scan coils deflect the electron beam over the sample according to zig-zag pattern. The formation of a image on the monitor occurs in synchrony with this scan moment. The scan velocity determines the refreshing rate on the screen and the amount of noise in the image (rapid scan = rapid refreshing = low signal = much noise: see SCANMODE in the virtual FESEM). Scan coils often consists of upper and lower coils, which prevent the formation of circular shadow at lower magnification.

3. *The objective lens*

   The objective lens is the lowest lens in the column. The objective focuses the electron beam on the object. A short working distance (= object in the higher position, that is closer to the objective lens) the objective lens needs apply a greater force to deflect the electron beam. The shortest working distance produces the smallest beam diameter and hence the best resolution, but the poorest depth of field, (The depth of field indicates which range in the vertical direction in the object can still be visualized sharply).

4. *The stigmator coils*

   The stigmator coils are utilized to correct irregularities in the x and y deflections of the beam to obtain a perfectly round-shape beam. When the beam is not in circular, but ellipsoidal, the images looks blurred and starched.

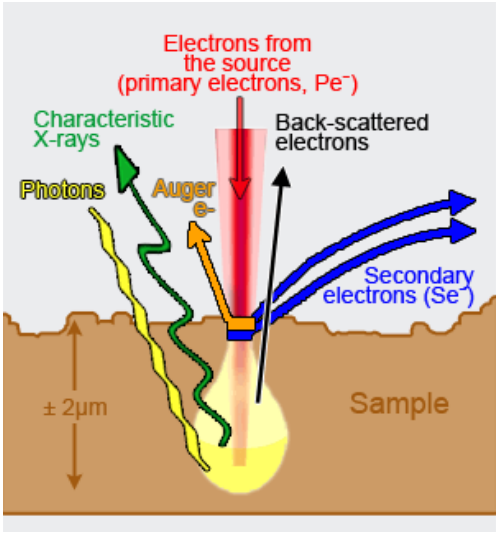

Figure: 2.20 Electron bombardments onto the sample surface.

2.3.3 Energy dispersive X-ray spectroscopy (EDS)

As already seen in the FE-SEM, the bombardment of a specimen with an electron beam leads to the generation of x-rays. These can be used to determine the elemental composition of different regions or features within the specimen [31].

Basically, electrons in the inner shells of an atom are ejected and the atom is ionized. The exited atom returns to its stable state by emitting an electron in one of its outer shells releasing its excess energy in the form of x-rays and filling the hole. The emitted x-rays have a characteristic energy for the shells involved in the activity and are characteristics of the given element. They may be used to gain chemical information about the specimen [32].

The x-rays can be detected by Si-crystal which produces electrical pulses with amplitude proportional to the energy of the incoming photon. The pulse amplitude are measured and then stored in a multi-channel analyzer where each channel corresponds to a certain interval of pulse heights. A spectrum is then plotted showing the number of counts per energy channel. Peaks which form at certain energy levels in the spectrum can be identified and are proportional to the element(s) present within the specimen with that x-ray energy. The concentration of a given element can be determined by carrying out a quantitative analysis. A typical EDS spectrum after collection is shown in the Figure 2.21.

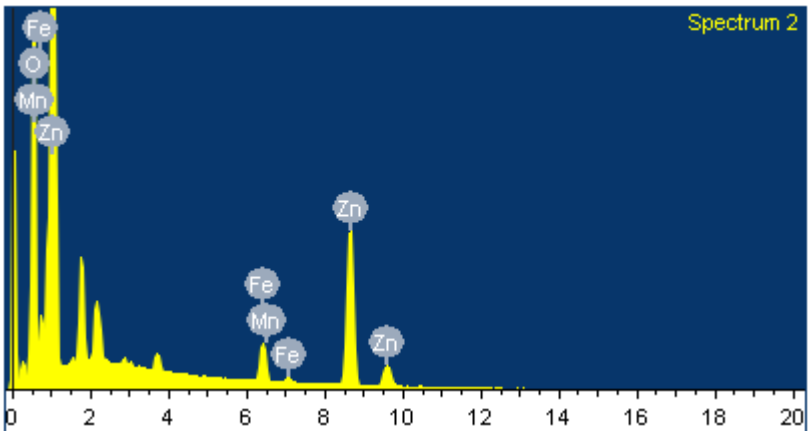

Figure 2.21: Typical EDS spectrum obtained from $Zn_{0.925}Mn_{0.025}Fe_{0.05}O$ films.

2.3.4 Profilometry

Insulating thin films are semitransparent, thus can be easily measured using optical techniques such as spectrophotometer and ellipsometry [13]. The thickness of the films in this work was measured by a profilometer, with a vertical resolution of 5Å. Profilometry

describes a class of techniques for measuring the surface topography. The general operating technique is shown in Figure2.22.

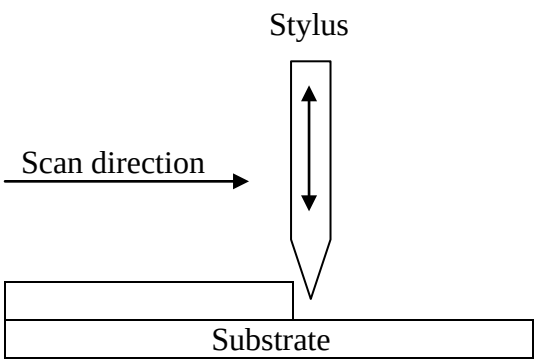

Stylus profilometer

Figure 2.22: Operating Concept for Stylus surface profilometer.

A mechanical diamond tip stylus is scanned across the film surface in a straight line and height is recorded. Several measurements per sample were preformed to average over variation in the film thickness. The probe generates a measurable signal response, typically electrostatic or the deflections of a laser signal, proportional to the change in height of the sample surface. These results are in a direct contour trace of the sample surface with primary limitations on resolution attributed to the scratching of the film surface, substrate roughness, and vibration during measurement [13]. Stylus based profilometers can be accurate to a resolution of roughly 1 nm. The primary drawback to the profilometry is that a step must be patterned into the film to allow for the measurement of the film thickness. For the purpose of this study, the thickness measurement of ferrite films was performed using surface stylus profilometer (Ambios tech model XP-1). The samples were particularly masked in order to obtain a step height between the glass substrates and the films. The thickness of DMS thin films was measured at three different positions and was averaged.

2.3.5 Atomic Force Microscopy (AFM)

Atomic force microscope (AFM) [33], a non-destructive analytical technique, can be used to visualize the surface morphology and roughness of films samples with a resolution down to the atomic level. One of the major advantages of this technique is that the images obtained directly correspond to the surface profile. It is therefore possible to extract quantities such as

the concentration of particles, particle size, particle size distribution and surface roughness or terrace step height about the surface from the image. AFM images were obtained by scanning a probe needle over a rectangular area of the surface.

Different Scanning probe microscope (SPM) scanning modes can be classified by the forces that they monitor and the distance between the tip and sample surface over which the forces operates as shown in Figure 2.23. There are three primary possible operational modes contacts, intermittent contact or non-contact modes [34]. In contact AFM mode an AFM tip makes soft physical contact with the sample where a constant normal force, typically in the nN-range, is maintained via regulation loop. The net force measured is the sum of the attractive and repulsive forces. On the other hand, in the non-contact mode the influence of the force gradient between probe and surface on a vibrating cantilever is utilized to measure the topography. The tip-sample separation is large, typically between 1 and 100 nm. In contrast to the contact mode, the non-contact mode is less destructive. The net force detected is the attractive force between the tip and the sample [35, 36]. With intermittent contact or trapping mode, the probe is oscillated close to the surface where it repeatedly comes into and out of contact with the surface.

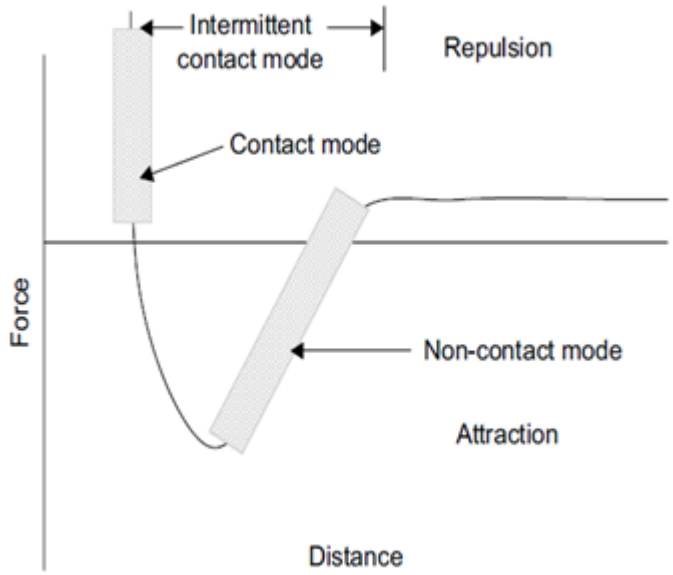

Figure 2.24: A Typical force-distance curve experienced by a probe tip as it approaches a surface [36].

Working principle of AFM

The image is produced [36] by dragging a vibrating cantilever, a weak interaction force exist between the tip and the films surface that causes the tip to deflect from its equilibrium

position, resulting in an amplitude change and a phase shift. A laser beam is reflected off the back of the cantilever and is detected with a split position sensitive photodiode and onto a piezoelectric transducer. The degree of deflection of the tip can be measured by using this piezoelectric transducer together with a feedback loop. By adjusting the tip height during a scan so that there is no loss of vibration amplitude, a profile of the surface and topographic image can be obtained. Simplified block diagram of the atomic force microscope is shown in Figure 2.26.

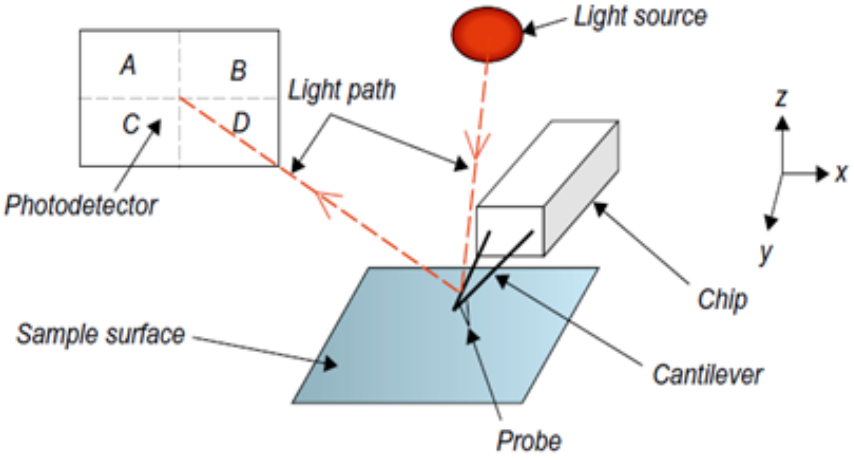

Figure 2.26: Schematic diagram of an atomic force microscope, AFM. (36)

The resolution of the system is determined by the diameter of the tip and it is routinely possible to achieve nm-order spatial resolution. The lateral resolution is of the order of a few nanometers while resolution in the vertical direction is better than 0.1 nm.

Two surface roughness quantities are commonly determined by AFM: average roughness (RA) and root-mean-square roughness (RMS). For N measurements of height z and average height z of the scanned area, the average roughness is the mean deviation of the height measurements

$$V = -na\frac{dB}{dt} \qquad RA = \frac{1}{N}\sum_{i=1}^{N}\left|Zi - Z\right| \tag{2.7}$$

and the root-mean-square roughness is the standard deviation

$$RMS = \left[\frac{1}{N}\sum\nolimits_{i=1}^{N}\left(zi - z\right)^2\right]^{1/2} \tag{2.8}$$

2.3.6 Optical transmittance

The transmission spectra of the films were recorded on a UV-Vis-NIR spectrophotometer (JASCO –V570 & V670). The spectrophotometer features an all-reflecting double monochromator optical system. The components are coated with silica for durability. Holographic gratings are used in the monochromator for the ultra-violet, visible light and near infrared range.

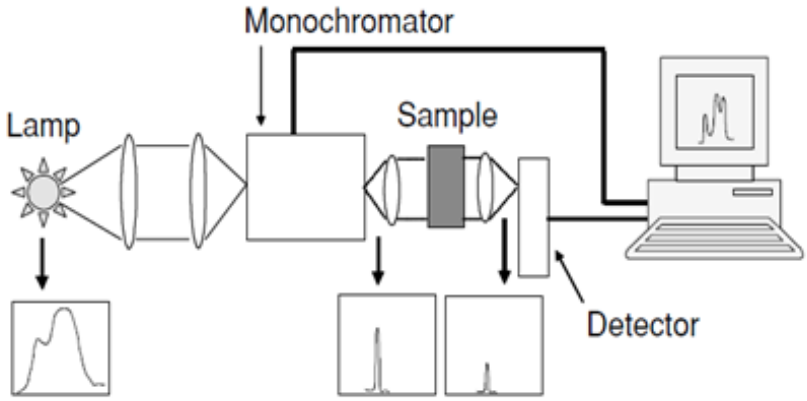

Figure 2.27: Schematic diagram of the UV-Vis-NIR double beam spectrophotometer [37]

Figure 2.27 is a schematic diagram illustrating the operation of a spectrometer. Basically, the instrument has two radiation sources that cover the full operating wavelength of spectrometer from 190 nm to 3000 nm, a monochromator that is responsible for passing monochromatic light to the sample, and two photo detectors for measuring the transmittance at different wavelength regions. The deuterium lamp and halogen lamp are the two radiation sources. The later is in charge of the wavelength in the visible to near infrared region, i.e. from 300 nm to 3300 nm, while the other is in charge of those wavelengths from 185 nm to 350 nm.

The monochromator uses reflection gratings and entrance-and-exit slits to pass monochromatic light to the sample. The transmittance of the monochromatic light that passed through the sample is measured by a photomultiplier operating in the ultraviolet and visible region and lead sulfide (PbS) detector operating in the near region. One thing to note here is that all transmittance values shown by the instrument are in relative terms. It shows what percentage of light, from 0% to 100% gets transmitted through the sample with respect to another parallel and unobstructed reference beam.

Reflectivity spectra provide similar and complementary information to the transmission and absorption measurements. For instance, absorption coefficients corresponding to the fundamental absorption are as high as $10^5 – 10^6$ cm^{-1} , so that they can only be measured by using thin sample (thin films). In these cases, the reflectivity spectra R(ν) can be very advantageous, as they manifest the singularities caused by the absorption process but with the possibility of using bulk samples [38,39]. The reflectivity at each frequency is defined by $R = I_R/I_0$ where I_R is the reflected intensity.

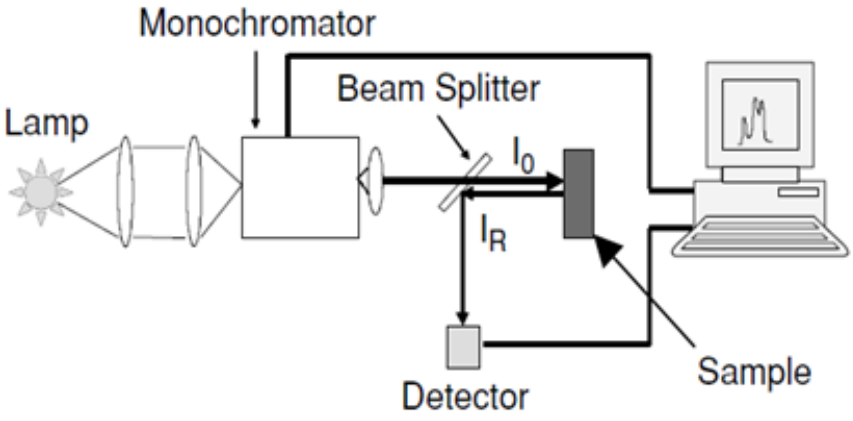

Figure 2.29: An experimental arrangement used to measure direct reflectivity spectra [37]

Reflectivity spectra can be registered in two different modes [39]: *direct reflectivity* and *diffuse reflectivity*. Direct reflectivity measurements are made with well-polished samples a normal incidence. Diffuse reflectivity is generally used for unpolished or powdered samples. For direct reflectivity measurements (Figure 2.29), a monochromatic light (produced by a lamp and a monochromator) is passed through a semitransparent lamina (the beam splitter). This lamina deviate the light reflected in the sample toward a detector.

2.3.7 Nano-indentation studies

Indentation testing [40] is a simple method that consists essentially of touching the material of interest whose mechanical properties such as elastic modulus and hardness are unknown. The technique has its origin in Mohs' hardness scale of 1822 in which materials that are able to leave a permanent scratch in another were ranked hard materials that are harder with diamond assigned the maximum value of 10 on the scale. The establishment of the Brinell, Knoop, Viockers, and Rock well tests all fallow from a refinement of the method of indenting one material with another. Nanoindentation is simply an indentation test in which the length of the scale of the penetration is measured in nanometers (10^{-9} m) rather than microns (10^{-6}

m) or millimeters (10^{-3} m), the later being common in conventional hardness tests. A part from the displacement scale involved, the distingubush feature of most nanoindetation testing is the indirect measurement of the contact area-that is the area of contact between the indenter and specimen. In, conventional indentation tests, the area of contact is calculated from direct measurements of the dimensions of the residual impression left in the specimen surface upon the removal of the load. In, nanoindentation tests, the size of the residual impression is of the order of microns and too small to be conventionally measured directly. Thus, it is customary to determine the area of contact by measuring the depth of penetration of the indenter into the specimen surface. This, together with the known geometry of the indenter, provides an indirect measurement of contact area at full load. For, this reason nanoindentation tainting can be considered a special case of the more general terms: depth-sensing indentation (DSI) or instrumented indentation testing (IIT).

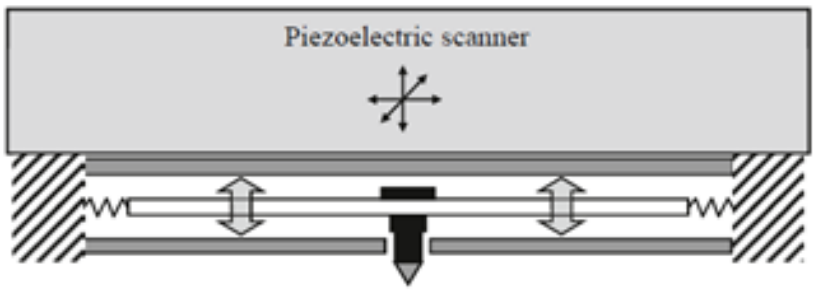

Figure 2.33: Combined sensor actuator of the Hystron instruments is based on the electrostatic attraction as the load actuator [41]

It is not only hardness that is of interest to materials scientist. Indentation techniques can also be used to calculate elastic modulus, strain hardness exponent, fracture toughness (for brittle materials), and viscoelastic properties. How can such a wide variety of properties to be extracted from such a simple test, which in many respects, can be considered a “non-destructive” test method. The maximum depth of penetration for a particular load, together with the slope of unloading curve measured at the tangent to the data point at maximum load, lead to a measure of both hardness and elastic modulus of the specimen material. In some cases, it is possible to measure elastic modulus from not only the unloading portion, but also the loading portion of the curve.

There has been considerable recent interest in the mechanical characterization of thin films systems and small volume of materials using depth-sensing indentation test with either of spherical or pyramidcal indenters. Usually, the principal goal of such testing to

extract elastic modulus and hardness of the specimen material from experimental regarding of the indenter load and depth of penetration. These reading give indirect measure of the area of the contact at full load, from which the mean contact pressure, and thus hardness, may be estimated. The test procedure for both spheres and pyramidal indenters, usually involves an elastic-plastic loading sequence fallowed by an unloading. The validity of results for hardness and modulus depends largely upon the analysis procedure used to process raw data. Such procedures are connected not only with the extraction of modulus and hardness, but also with correcting the data for various systematic errors that have been indentified for this type of testing. The forces involved are usually in the micronewton (10^{-6} N) range and are measured with and are measured with a resolution of few nanonewtons (10^{-9} N). The depths of penetration are on the order of nanonewtons (10^{-9} N).

2.3.8 Vibrating Sample Magnetometer (VSM)

The vibrating sample magnetometer (VSM) is a basic instrument which was developed in 1956 by S.Foner and Van Oosterhart for characterization of the magnetic materials [42]. The VSM method is based on Faraday's law, which states that emf will be generated in a coil when there is a change in the flux going through the coil [43]. When a material is placed within a uniform magnetic field a vibrator mechanism vibrates the sample in the magnetic field. This causes the sample to undergo sinusoidal and creates a change in the magnetic flux, which is detected by pickup coils as an induction voltage. For a coil with n turns of a cross sectional area a, the emf (V) is related to dB/dt, given as [44]

$$V = -na\frac{dB}{dt} \qquad (2.9)$$

Since $\Delta B = \mu_0 M$, when we place a magnetic sample into the coil, this relationship becomes

$$V = -na\mu_0 \frac{M}{dt} \qquad (2.10)$$

The output measurement displays the magnetic moment M as a function of the field H. A schematic of the VSM system shown in Figure2.34. It has a pair of electromagnets that generates a DC magnetic field, and pick up coil that acquires the sample signals. When a sample has a net magnetization, it produces magnetic flux in its vicinity. During VSM measurements, the sample is mechanically vibrated (up and down) at a fixed frequency (generally 82 Hz). This vibration produces a flux change, which generates an AC voltage

proportional to the magnetic moment of the sample in the pick-up coil. A lock-in amplifier is then used to measure the voltage. The AC signal picked up by the coil is proportional to the frequency and amplitude of the sinusoidal motion and the total magnetic moment of the sample at the applied magnetic field.

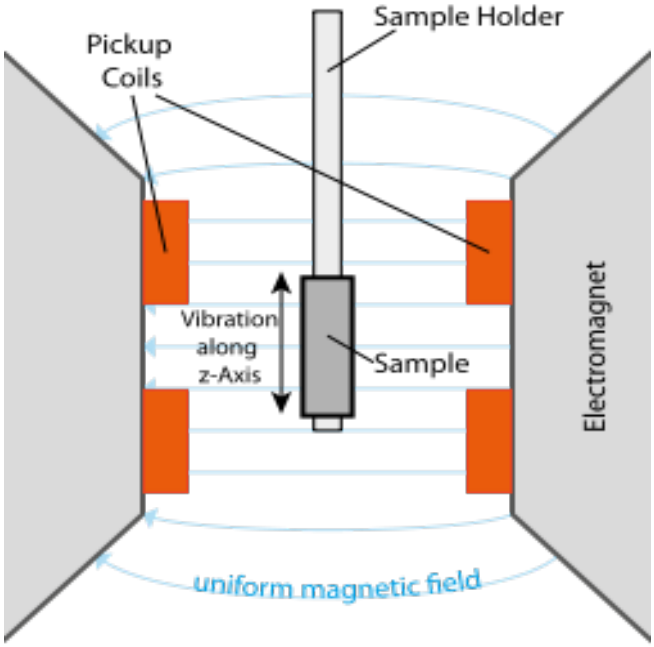

Fig 2.34: Vibrating Sample Magnetometer or VSM (Schematic)

The frequency and amplitude of the sinusoidal motion are held constant, which is controlled by a capacitor (reference signal generator). By feeding the signal from the pick-up coils and the reference signal into a demodulator, the magnetic moment of the sample is extracted [45]. The system is calibrated with a magnetic material with a known saturation magnetization, e.g. Ni. A hall probe was used in order to determine the values of the applied field. Using the computer interface, the magnetic field and the signal proportional to the magnetic moment can be simultaneously recorded (hysteresis loop). The magnetic moment determined by VSM is given in terms of the basic electromagnetic unit (or, emu), which can be related to the magnetization, susceptibility, and Bohr magnetron. VSM provides a fast and easy technique for the measurement of the magnetic properties of a material [42]. The sensitivity of VSM manufactured by Lake Shore is in the range of 10^{-6} emu which is sufficiently accurate for the samples used in this dissertation.

References

[1] S.E. Dann, *Reaction and characterization of solids,* The Royal society of Chemistry, Great Britain (2000).

[2] A. R. West, *Solid State Chemistry and its Applications*, John Wiley & Sons (Asia) Pvt.Ltd (2003).

[3] K. Wasa, M. Kitabatake and H. Adachi, *Thin film material technology*: Sputtering of Compound materials, William Andrew, New York (2004).

[4] A. A.Voevodin and M. S. Donley, *Surf.Coat.Technol*. **82** (1996) 199-213.

[5] S. Zhang and N. Ali, *Nanocomposite thin films and coatings*, Imperial College Press, London (2007).

[6] R. A. Powell and S. M. Rossnagel, *PVD for Microelectronics*: Sputter Deposition Applied to Semiconductor Manufacturing, Academic Press, San Diego (1999).

[7] D. M. Mattox, *Hand book of Physical Vapor Deposition Processing*, Noyes Pub.Ltd New Jersey (1998).

[8] J.George, *Preparation of thin films*, Marcel Deckker, Newyork (1992).

[9] J. A. Thornton and J. E. Green, *Sputter Deposition Process*, In: R.F. Bunshah, (ed.), Deposition technologies for films and coating, 2nd ed. Noyes, New Jersey, (1994).

[10] B. Champman, *Glow discharge processes*: Sputtering and Plasma etching, Wiley, New York (1980).

[11] R. F. Bunshah, (ed.), *Deposition technologies for films and coatings*, 2nd ed. Noyes Publications, New Jersey, (1994).

[12] A. Rockett, *The material science of semiconductors*, Springer, New York, (2008).

[13] M. Ohring, *The material Science of Thin films* 2nd ed.Academic Press, San Diego, USA (2002).

[14] M. Birkholz, P. F. Fewster and C.Genze, *Thin films Analysis by X-ray Scattering*, Wiley-VCH Germany (2009).

[15] K. Ellmer, J. Phys.D: Appl.Phys.33 (2000) R17-R32

[16] J. E. Mahan, *Physical vapor deposition of thin films*, John Wiley & Sons, New York (2000).

[17] L. B. Freund and S. Suresh, Thin film materials: Stress, Defect Formation and surface Evaluation, (2003).

[18] K. Seshan, *Hand book of thin films deposition process and techniques*, 2nd ed. Noyes, New Jersey (2002).

[19] K. S. Sree Harsha, *Principle of Physical Vapor Deposition of Thin films*, Elsevier (2006).

[20] A. Thornton, *Annual Rev. Mater. Sci.* 7(1977) 239-260.

[21] C. V. Thompson, Annual Rev. Mater. Sci. 30(2000) 159-190.

[22] D. Depla and S. Mahieu and J. E. Green. Sputter Deposition Process, In: Ed. P.M. Martin, Hand book of deposition technologies for films and coatings, 3rd ed.Elseveir, USA (2010).

[23] D. Depla and S. Maheiu, *Reactive Sputter Deposition*, Springer-Verlag, Berlin, Heideberg (2008).

[24] G. Franz., *Low pressure plasmas and microstructuring technology*, Springer-Verlag, Berlin, Heiedeberg (2009) P-377.

[25] K. Wasa and S. Hayakawa, *Hand book of sputter deposition technology: Principles, Technology and applications*, Noyes publications, USA (1992).

[26] B. D. Culity and S. R. Stock, Elements of X-Ray Diffraction, 3rd Ed.,Pretice Hall, New Jersey, USA (2001).

[27] T. L. Alford, L.C. Feldman and J.W.Mayer, *Fundamentals of Nanoscale Film Analysis*, Springer, New York (2007).

[28] A. I. Gusev and A. A. Rempel, *Nanocrystalline materials*, Cambridge Intern.Sci.Pub. (2004).

[29] Geert- Jan Janssen, *Huub Geurts, Inc*.

[30] James Pawley *et al*, *Scanning* **19** 324 (1997).

[31] W. Zhou and Z. L. Wang,Ed., *Scanning microscopy for nanotercnology*, Springer, New York (2006).

[32] A. J. Garatt-Reed and D.C. Bell, *Energy –Dispersive X-Ray Analysis in Electron microscope*, BIOS Scientific, Oxford, UK (2003).

[33] W. R. Bowen and N.Hilal, *Atomic force microscopy in progressing engineering*, Elsevier, UK (2009).

[34] A R Clarke and CN Eberhardt, *Microscopy techniques for materials science*, Wood head, CRC, England (2002).

[35] K. S. Birdi, *Scanning probe microscopes: applications in science and technology*, CRC press, Florida USA (2003).

[36] H. S. Nalwa, ED., *Advances in surface science*, Academic press, San Diego (2001).

[37] J. G.Sole, L. E. Bausa and D.Jaque, *An introduction to the optical spectroscopy of inorghanic solids*, John Wiley, New Hersey (2005).

[38] H. Kuzumany, *Solid-State Spectroscopy*, Springer-Verlang Berlin Heidelberg (2009).

[39] M. Fox, *Optical properties of solids*, Elesver, USA (2004).

[40] Anthony C. Fischer-Cripps, *Nanoindentation*, 3rd Ed. Springer, New York (2011).

[41] Hystron Corporation. Inc, Minneapolis, USA.

[42] B. D. Cullity and C.D. Graham, *Introduction to magnetic materials*, 2nd ed. IEEE, New Jersey (2009).

[43] H. Zijilstra, *Experimental methods in magnetism*, North-Holland publishing, Amsterdam (1967).

[44] K. H. J. Buschow and F.R.de Boer, *Physics of magnetism and magnetic materials*, Kluwer Academic, New York (2004).

[45] F. Fiorillo, *Measurement and characterization magnetic materials*, Elsevier, Amsterdam (2004).

Chapter 3

Structure and morphological studies

In this chapter the detailed structural and morphological characterization of un-doped and 3d TM ion doped ZnO thin films deposited by rf-magnettron sputtering are presented. The important feature of current work is the investigation of biaxial stress and strain and other strucutral parameters of various deposited films.

This chapter is divided into three sections including effect of working gas pressure, film thickness and substrate material on the structure and morphology of the films. These studies would help in optimizing the deposition parameters to obtain films of desired structure and morphology.

(i) Thin films of Un-doped ZnO

Thin films of un-doped ZnO thin films were depsited on quartz substrate by rf mageron sputtering in argon gas environment. The sputtering deposition conditions were kept at working gas pressure of 12 mTorr, sputter duration 60 min and substrate to target diastance at 80 mm. The rf power was changed from 40 – 100 W. Figure 3.1 shows the XRD pattern of the as deposited films of ZnO. The films shows hexagonal wurtzite structure with (002) orientation along c-axis. The thichness of the film increases and orientation of the film along (002) direction improves with increases in rf power.

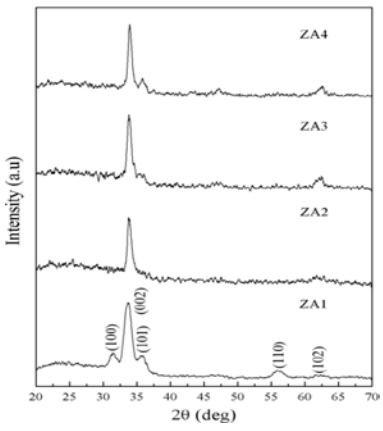

Fig 3.1: XRD pattern of as-sputtered films of different film thickness at argon working pressure of 12 mTorr.

Table 3.1: Structural parameters of as-sputtered ZnO films with different partial pressure.

Sputter power (Watt)	40	60	80	100
Thickness(nm)	360	707	910	1066
Grain size (nm) (SEM)	135±5	86±5	45±5	145±5
Roughness (nm) (AFM)	1.20	1.01	1.23	1.85

(b) Microstructure and surface morphology (FE-SEM)

The FE-SEM images of ZnO films of various thicknesses are shown in Figure.3.2. The grain size initial decreases with increase in power (thickness) of the film. It increases as the power is increased to 100 W.

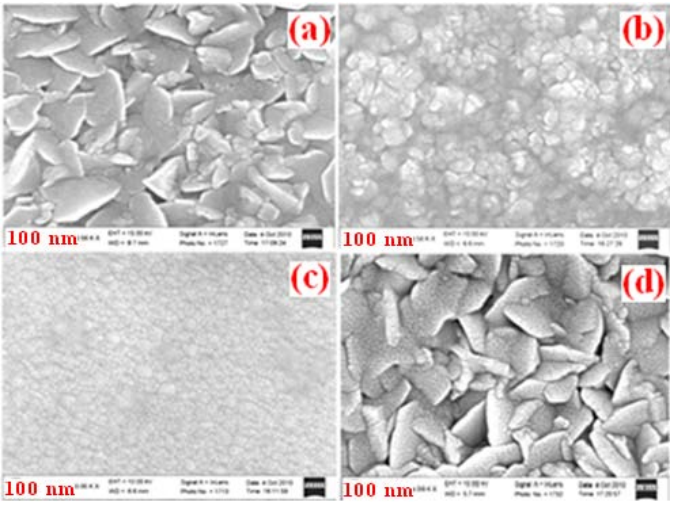

Fig 3.2: FE-SEM micrographs of as-sputtered films of different film thickness at argon working pressure of 12 mTorr

(c) Atomic force microscpe (AFM)

The atomic force microscope (AFM) images of ZnO films deposited at various film thicknesses are shown in Figure 3.3. The films have bigger grains at 100 W of power in support with FE-SEM data. The root mean square (RMS) values vary between 1.0 – 1.8 nm with homogeneous structure.

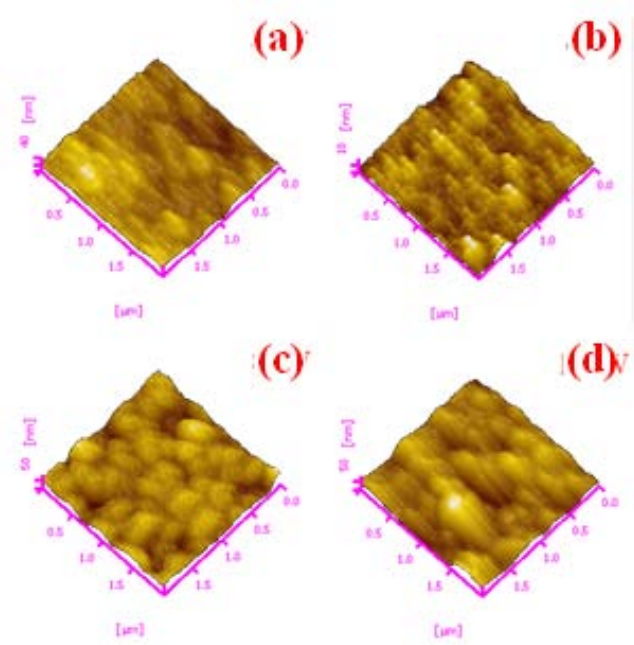

Fig 3.3: AFM images of as-sputtered films of different film thickness at argon working pressure of 12 mTorr.

For comparison purpose all the films were deposited using 100 W of rf power. Keeping the rf power same the effect of working gas pressure, film deposition duration (thickness) and substrate material on the structure and morphology of the film is studied.

3.1 Effect of working gas Pressure

Thin films of un-doped and Mn, Fe and Mn-Fe co-doped ZnO thin films were depsoited on glass and quartz substrates by rf-magnetron sputtering with working gas partial pressure of argon and oxygen gas environment as variable parameter.

3.1.1 Argon gas environment

The argon gas has advantage over other gases like oxygen and nitrogen that it gives high sputter yield and thicker fims can be deposited in a short interval of time. Thin films were deposited on glass and quartz substrates with the argon partial pressure in the range 9-18 mTorr. The sputter parametrs i.e RF power at 100 W, deposition duration 60 min, substrate – target distance at 8.5 cm and substrate temperature at room temperature were kept constant except the argon gas partial pressure.

3.1.1.1 Un-doped ZnO

The XRD pattern of the as deposited ZnO films shown in figure 3.4 reveals the influence of working gas pressure on the structure. The xrd pattern indicates the films to be polycrystalline with a hexagonal structure. As the working gas pressure increases the intensity of (002) peak increases indicating the increasing preferred orientation with the c-axis perpendicular to the substrate. From the peak position of the (002) peak, the grain size, the full width at half maximum (FWHM), interplanar distance *d*, stress σ, strain ε_z and the crystal lattice constant *c* are calculated.

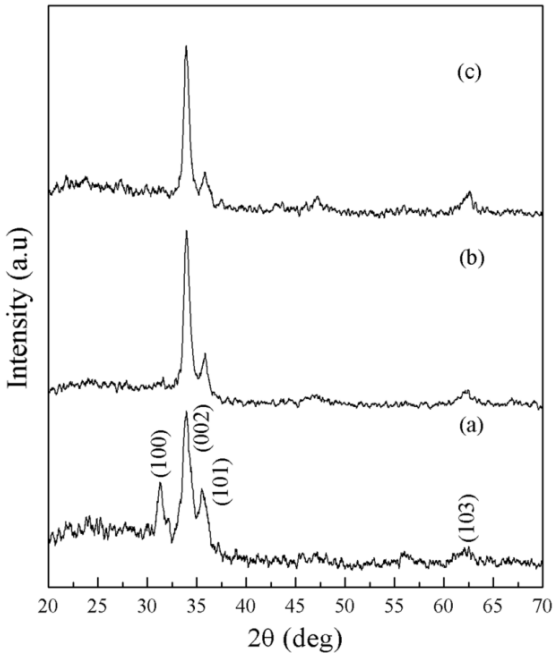

Fig 3.4: XRD patterns of as-sputtered films of (a) 9.7, (b) 13 and (c) 18 mTorr of argon working gas pressure.

Fig.3.1 also shows that as the gas pressure increases the diffraction peaks become sharper, their intensity is enhanced and peak position changes. This trend means that the residual stress is generated in the film during the deposition process [5]. The strain in the ZnO films along the c-axis perpendicular to substrate is given by the following equation [6].

$$\varepsilon_z(\%) = \frac{c - c_0}{c_0} \times 100 \qquad (3.1)$$

Where *c* is the lattice parameter of the ZnO film, c_0 (5.2066 Å) is the unstrained lattice parameter of ZnO [6]. The values of strain for 9, 13 and 18 mTorr thin films are given intable.1. The strain can be positive (tensile) or negative (compressive). The residual stress (σ) in ZnO films can be expressed as [7]

$$\sigma = \frac{2c_{13}^2 - c_{13}(c_{11} + c_{12})}{2c_{13}} \times \frac{c - c_0}{c_0} \qquad (3.2)$$

Here c_{ij} are the elastic stiffness constants for single crystal ZnO (c_{11} = 208.8 GPa, c_{33} = 213.8 GPa, c_{12} = 119.7 GPa and c_{13} = 104.2 GPa [8]). The residual stress with increasing the thickness increases. The values of the residual stress for 9, 13 and 18 mTorr thin films are given in the table 1. If the stress is positive, the biaxial stress is tensile; if the stress is negative, the biaxial stress is compressive [9]. The residual stress of the as deposited thin films is tensile.

The crystal size of ZnO thin films with different working pressure were calculated using the Scherer's formula [10, 11]

$$D = \frac{0.9\lambda}{\beta \cos\theta} \; D = \frac{0.9\lambda}{\beta \cos\theta} \qquad (3.3)$$

Where λ= 1.5418Å and β is FWHM were determined from the broadening of the ZnO line.The crystal lattice constant c and the interplanar distance d of the diffracting planes were indentified using the Bragg's equation nλ = 2dsinθ, where n is the order if the diffracted beam, λ is the wavelength of x-ray and θ is the angle between the incoming x-ray and the normal of the diffracting plane. The value of (002) peak position, peak intensity, FWHM, grain size and the crystalline quality increased with the increase of film thickness. No significant changes in the values of c and d were observed with the change of film thickness. The thickness of the film is highest at 13 mTorr. The decrease in thickness wih further increase in gas pressure can be due to back-sputtering from the film surface at gas pressure. The structural parameters of the as deposited ZnO films are listed in table 3.2.

Table 3.2: Structural parameters of as-sputtered ZnO films with different partial pressures.

Working gas Pressure (mTorr)	9	13	18
Thickness(nm)	738	1067	882
2θ (˚)	33.98	34	33.97
Crystallite size, D (nm) (XRD)	11±3	14±3	14±3
Relative Peak intensity	46.98	83.75	65.51
FWHM (˚)	0.764	0.614	0.590
Grain size (nm) (SEM)	122±5	111±5	124±5
Roughness (nm) (AFM)	12.33	10.58	12.96
c (nm)	0.527	0.527	0.527
d (nm)	0.264	0.263	0.264
Strain, ε_z (%)	1.262	1.205	1.291
Stress, σ ($\times 10^9$ Pa)	-2.939	-2.805	-3.006

3.1.1.1.2 Microstructure and surface morphology (FE-SEM)

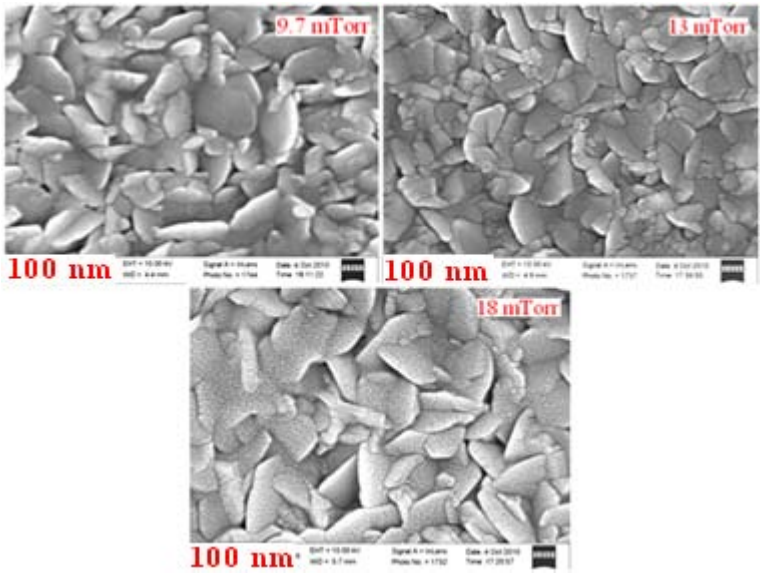

Fig 3.5: FE-SEM micrographs of as-sputtered films of argon working gas pressure of (a) 9.7, (b) 13 and (c) 18 mTorr.

The FESEM micrographs of the surface of ZnO films deposited in various argon gas environment. All the micrographs reveal the presence of large grains throughout the polycrystalline matrix. In the case of 13 mTorr films, however, the grain sizes are less than that of 9 and 18 mTorr films of working gas pressure. The grain sizes are in the

range 111-122 nm. The films deposited under 13 mTorr pressure have the bigger grains surrounded by smaller grains of size ~40 nm. The increase in gas pressure favors the nucleation of oriented grains which explains the increase in 002 peak intensity (figure 1). The intensity of (002) orientation may is effected by the growth direction of ZnO grains [13].

3.1.1.1.3 Atomic force microscope (AFM)

The AFM images of the as deposited films shown (figure 3.6) in the scan area of 2μm× 2μm by non -contact mode of AFM. The films show the roughness values in range of ~13 nm. The higher roughness in the films is attributed to the high rate of deposition and possibility of forming the island growth films in argon gas environment. The average grain size values estimated from the AFM have similar range with that of FESEM micrographs of thin films

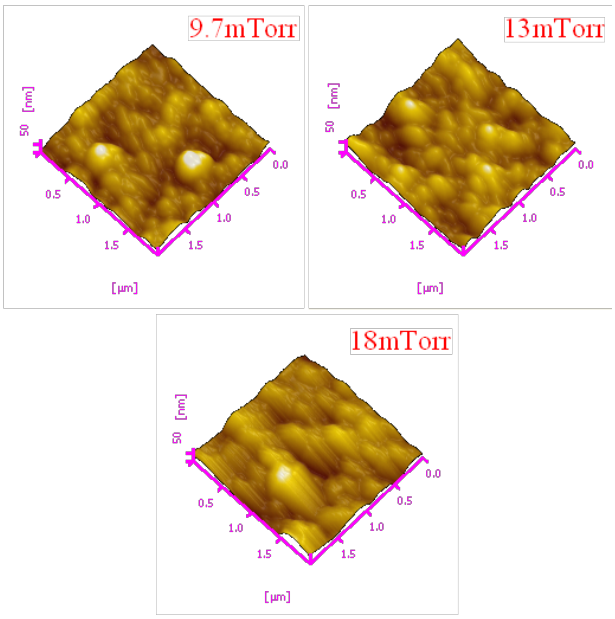

Fig 3.6: AFM images of as-sputtered films of argon working gas pressure of (a) 9.7, (b) 13 and (c) 18 mTorr.

3.1.1.2 $Zn_{0.95}Mn_{0.05}O$

The experimental data on the thin films of $Zn_{0.95}Mn_{0.05}O$ deposited onto quartz substrates in argon gas environment at room temperature by rf-magnetron sputtering are presented below.

1.2.1 X-ray analysis

Fig 3.7 shows the XRD pattern of thin films deposited in argon environment. As gas pressure increases the 2θ values shift to higher angles indicating that the films have compressive stress. The intensity of (002) peak decreases and (100) and 9101) peaks emerge with increase in the argon gas pressure. The orientation of the film detoeriots with increase in working gas pressure. The thickness of film is highest at 5 mTorr of gas pressure. The present data shows that the oriented and thickest films can be obtained at low gas pressure. This is in contrast with the result on undoped films. The Mn doping helps in getting oriented films at low gas pressure.

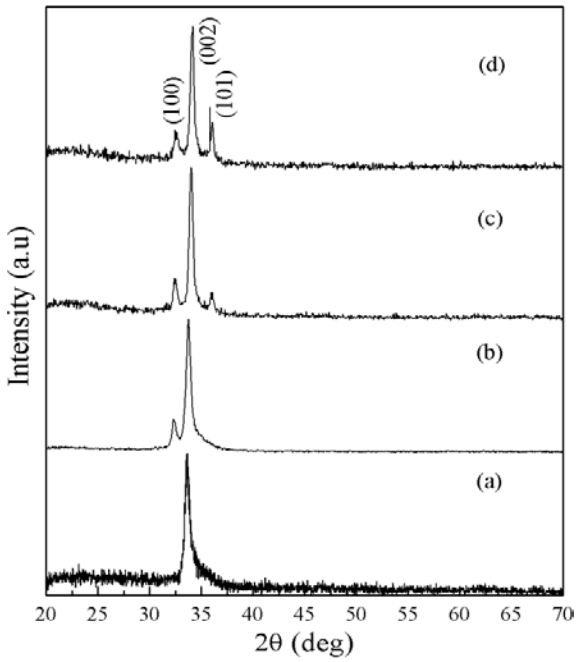

Fig 3.7: XRD pattern of as-sputtered films of argon working gas pressure of (a) 5, (b) 8, (c) 12 and (d) 15 mTorr.

The structural parameters estimated from XRD data are listed in the table.3.3. All the films show the residual stress negative indicating that the films have compressive the stress and these values are decreases with increase in the argon pressure. These values are higher compared to undoped films. This shows that Mn ion doping in ZnO causes more residual stress in the films.

Table 3.3: Structural parameters of as-sputtered $Zn_{0.95}Mn_{0.05}O$ films with different partial pressures.

Working gas pressure (mTorr)	5	8	12	15
Thickness(nm)	1003	924	895	807
2θ (˚)	33.66	33.56	34.02	34.12
Crystallite size, D (nm) (XRD)	33±3	33±3	42±3	46±3
Relative Peak intensity	166.35	1968.44	739.14	530.1
FWHM (˚)	0.497	0.501	0.394	0.359
Grain size (nm) (SEM)	28±5	68±5	98±5	62±5
Roughness (nm) (AFM)	0.70	5.88	5.18	6.70
c (nm)	0.532	0.534	0.527	0.525
d (nm)	0.266	0.267	0.263	0.263
Strain, ε_z (%)	2.211	2.488	1.149	0.847
Stress, σ ($\times 10^9$ Pa)	-5.147	-5.792	-2.676	-1.972

3.1.1.2.2 Microstructure and surface morphology (FE-SEM)

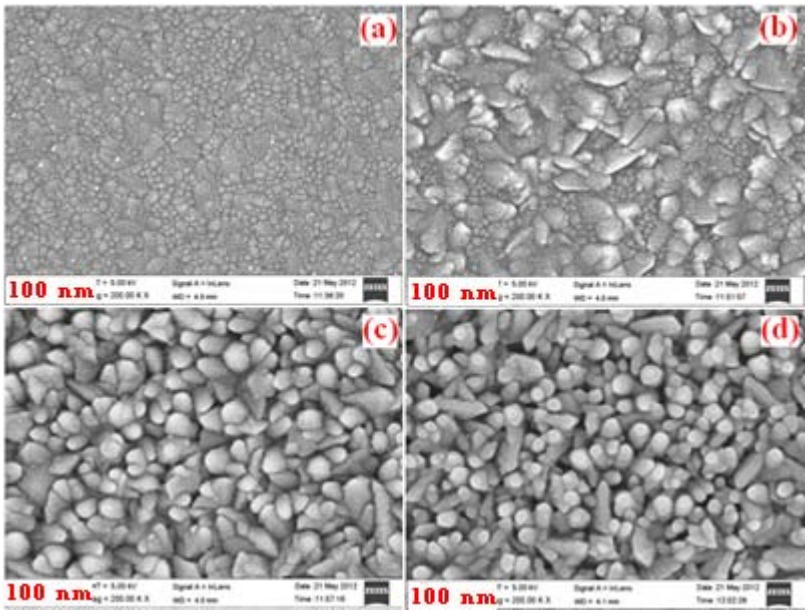

Fig 3.8: FE-SEM micrographs of as-sputtered films of argon working gas pressure of (a) 5, (b) 8, (c) 12 and (d) 15 mTorr.

The FESEM micrographs of as deposited thin films of $Zn_{0.95}Mn_{0.05}O$ with different working gas pressure are shown in figure 3.8. The grain size initially increases and then

decreases as pressure increases. The grains are growing in near elliptical to circular shapes and the films have dense texture with mixed grain sizes of small and bigger grains.

3.1.1.2.3 Atomic force microscope (AFM)

AFM images of as deposited thin films of Mn5% doped ZnO are shown in figure 3.9 as function of argon gas pressure. The micrographs show the formation of dense structure with increase in the gas pressure. The roughness is high for films deposited at 8 mTorr of argon gas pressure and RMS values for as deposited films are listed in the table 3.2. The grain growth for 8 mTorr gas pressure deposited films has columnar structure compare to other films with peak to valley height ~ 8 nm. The AFM images are in accordance with FESEM micrographs in terms of grain sizes and texture of the films.

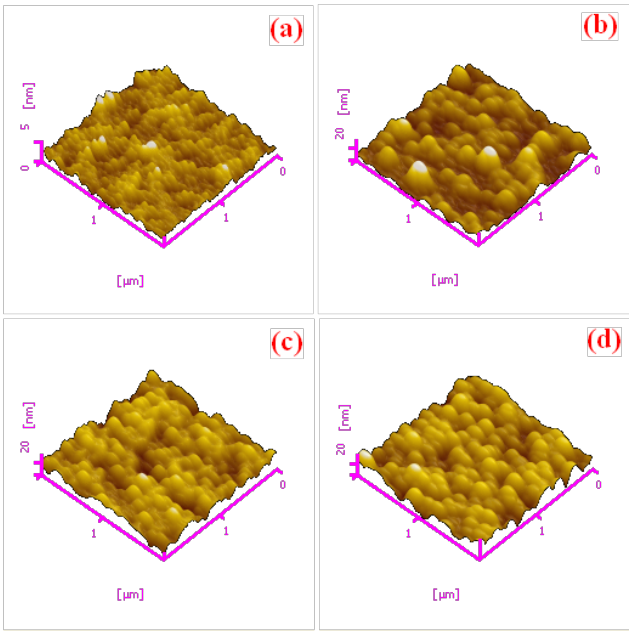

Fig 3.9: AFM images of as-sputtered films of argon working gas pressure of (a) 5, (b) 8, (c) 12 and (d) 15 mTorr.

3.1.1.3 $Zn_{0.95}Fe_{0.05}O$

The experimental data on the thin films of $Zn_{0.95}Fe_{0.05}O$ were deposited onto quartz substrates in argon gas environment at room temperature by variying the argon working gas pressure from 5-15 mTorr by keeping the other parameters constant as listed above.

3.1.1.3.1 X-ray analusis

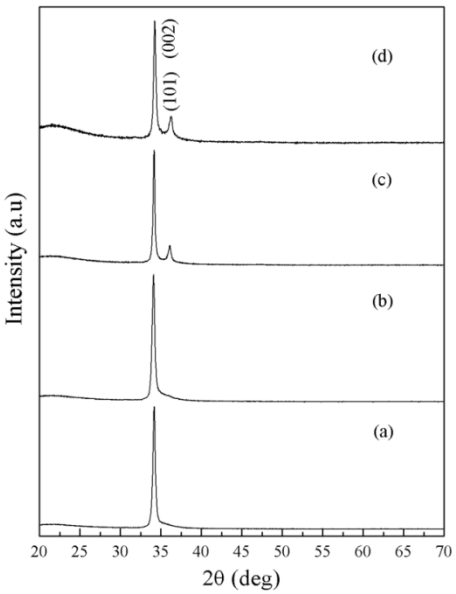

Fig 3.10: XRD pattern of as-sputtered films of argon working gas pressure of (a) 5, (b) 8, (c) 12 and (d) 15 mTorr.

The XRD patterns of the $Zn_{0.95}Fe_{0.05}O$ films were measured, as shown in the figure 3.10. The peaks appears at 2θ = 34.18, 34.10, 34.17 and 34.26, which are corresponds to the (002) direction of ZnO hexagonal wurtzite structure. It is easy to find that the all films are single phase with c-axis preferred orientation and that no evidence of any other secondary phases and impurities of Fe element are detected. Meanwhile, as the argon pressure increases, the position of the $Zn_{0.95}Fe_{0.05}O$ peak moves to higher angles expect the films deposited at 8 mTorr of working gas pressure, such as Fe doped ZnO[14] show the consistent shift of 2θ towards the lower angles. From the above and XRD results, suggest that Fe^{2+} ions have successfully substituted for the Zn^{2+} ions in the ZnO lattice free from clusters such as FeO and Fe_2O_3. Moreover, as the Fe concentration increases in the films, the full width at half maximum of the (002) diffraction peak is found to be narrowing and the intensity is decreases gradually. This presumably due to the ionic radius of Fe^{2+} is known to be larger than that of Zn^{2+} by about 5% so that the lattice disorder and strain induced by the substitution of Fe^{2+} for Zn^{2+} [15,16], The strain (%) in the films initially increased with argon pressure and decreased with increase in the pressure. The films have biaxial stress is compressive, and the values are listed in table 3.4.

Table 3.4: Structural parameters of as-sputtered $Zn_{0.95}Fe_{0.05}O$ films with different partial pressures.

Working gas pressure (mTorr)	5	8	12	15
Thickness(nm)	837	785	746	705
2θ (˚)	34.18	34.10	34.17	34.26
Crystallite size, D (nm) (XRD)	47±3	45±3	63±3	56±3
Relative Peak intensity	31989.24	27385.39	16666.66	8961.51
FWHM (˚)	0.354	0.372	0.264	0.298
Grain size (nm) (SEM)	50±5	48±5	70±5	77±5
Roughness (nm) (AFM)	5.71	3.60	9.57	5.61
c (nm)	0.524	0.525	0.524	0.523
d (nm)	0.262	0.263	0.262	0.261
Strain, ε_z (%)	0.688	0.918	0.715	0.448
Stress, σ ($\times 10^9$ Pa)	-1.602	-2.138	-1.665	-1.044

3.1.1.3.2 Microstructure and surface morphology (FE-SEM)

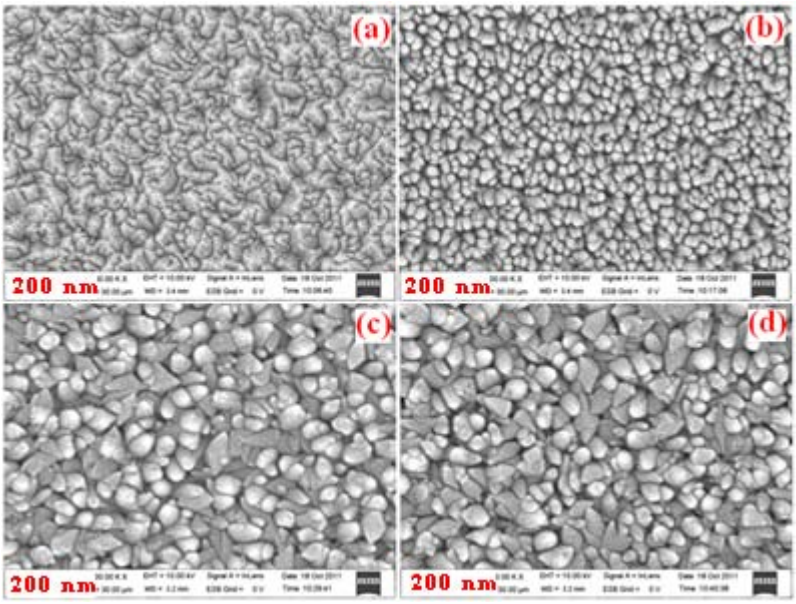

Fig 3.11: FE-SEM micrographs of as-sputtered films of argon working gas pressure of (a) 5, (b) 8, (c) 12 and (d) 15 mTorr.

Now we can get a conclusion that the crystalline quality of the films gets better and grain size decreases with substitution of Fe in the films which can be demonstrated by FESEM

micrographs, as shown in the figure 3.11. It is obvious that the particle size decreases with increase in Fe concentration. The lower pressure deposited films have bigger grains with increase it is decreasing. As the amount of Fe increases in the films granular particles increases with increasing the Fe dopant in the ZnO films. The elemental composition of as deposited films was recorded by employing the EDS measurements. The figure 3.11 shows the spectra taken from the films deposited at higher working gas pressure. The stoichiometric ratios of the elements are nearly the composition of target material.

3.1.1.3.3 Atomic force microscpe (AFM)

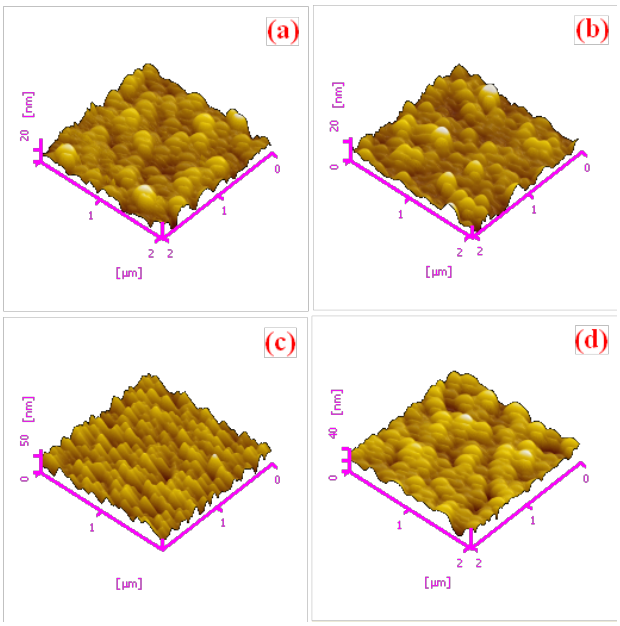

Fig 3.12: FE-SEM micrographs of as-sputtered films of argon working gas pressure of (a) 5, (b) 8, (c) 12 and (d) 15 mTorr.

Figure 3.12 shows the non-contact mode AFM images of $Zn_{0.95}Fe_{0.05}O$ thin films. The roughness values estimated from AFM micrographs are listed in table 3.4. The films deposited at 12 mTorr pressure have high roughness values than the other films. The micrographs show the formation of dense structure with increase in gas pressure Similar results were obtained by Gao et.al. [17] for Fe doped ZnO thin films deposited by DC magnetron sputtering. The AFM micrographs show the spherical shape of grains except for the films deposited at 12 mTorr of gas pressure. The AFM images are in accordance

with FESEM micrographs in terms of grain sizes and texture of the films and suggest that the surface quality of ZnO thin film improved when doped with Fe.

3.1.1.4 $Zn_{0.925}Mn_{0.025}Fe_{0.05}O$

Thin films of $Zn_{0.925}Mn_{0.025}Fe_{0.05}O$ deposited onto quartz substrates in argon gas environment at room temperature by varying the argon working gas pressure from 5-15 mTorr. Other parameters were kept constant.

3.1.1.4.1 X-ray analysis

Fig.3.13 shows the XRD patterns of the as-sputtered $Zn_{0.925}Mn_{0.025}Fe_{0.05}O$ thin films at different working gas pressure. XRD lines for all the samples have been indentified as coming from wurtzite structured ZnO (space group $P6_3mc$) with (002) orientation along c-axis only: no peak from Fe2O3 or MnO2 was found. M. Chakrabarti et.al. [18] have shown that there is no indication of secondary phase after the bulk samples of Fe doped ZnO were fired by at 490ºC.

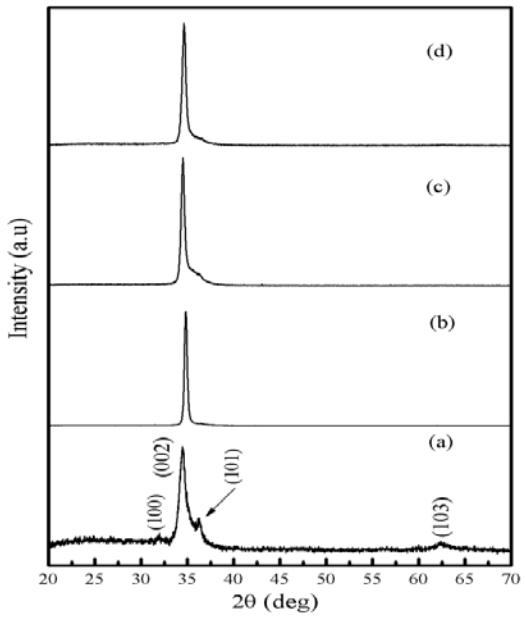

Fig 3.13: XRD pattern of as-sputtered films of argon working gas pressure of (a) 5, (b) 8, (c) 12 and (d) 15 mTorr.

The strcutural parameters obtained from XRD data are listed in table 3.5. These results alos suggest that the doping does not change the wurtzite strucutre. The films deposited at 8 mTorr of working gas pressure show high crysttalinity than other films with crystallite

value ~ 48 nm with high peak intensity. The residual stress for this film is high ~ 2.571 GPa compared to other films The films show tensile (positve) stress at all working gas pressure.

Table 3.5: Structural parameters of as-sputtered $Zn_{0.925}$ $Mn_{0.025}Fe_{0.05}O$ films with different partial pressures.

Working gas pressure (mTorr)	5	8	12	15
Thickness(nm)	1112	1330	1344	1280
2θ (˚)	34.48	34.82	34.50	34.63
Crystallite size, D (nm) (XRD)	25±3	48±3	41±3	37±3
Relative Peak intensity	760.52	20475.38	8271.64	4429.82
FWHM (˚)	0.656	0.344	0.401	0.445
Grain size (nm) (SEM)	10± 5	86± 5	89± 5	91± 5
Roughness (nm) (AFM)	6.28	6.22	13.22	5.30
c (nm)	0.520	0.515	0.519	0.518
d (nm)	0.260	0.257	0.260	0.259
Strain, ε_z (%)	-0.160	-1.105	-0.232	-0.577
Stress, σ ($\times 10^9$ Pa)	0.372	2.571	0.539	1.343

3.1.1.4.2 Microstructure and surface morphology (FE-SEM)

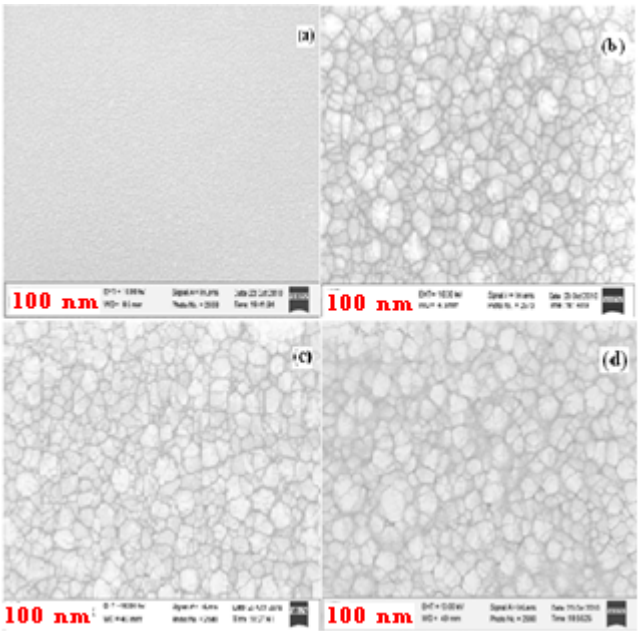

Fig 3.14: FE-SEM micrographs of as-sputtered films of argon working gas pressure of (a) 5, (b) 8, (c) 12 and (d) 15 mTorr.

The field emission scanning electron microscope (FE-SEM) micrographs of Zn0.925Mn0.025Fe0.05O thin films at various woking pressure are shown in figure 3.14. The grain size increases with increase in working gas pressure indicating that higher sputter yield increases higher growth fromation. The bigger grains are surrounded by smaller grains of ~ 15 nm. The compositional analysis shows the presence of Mn and Fe elements in the films with reasonable conecntrtions.

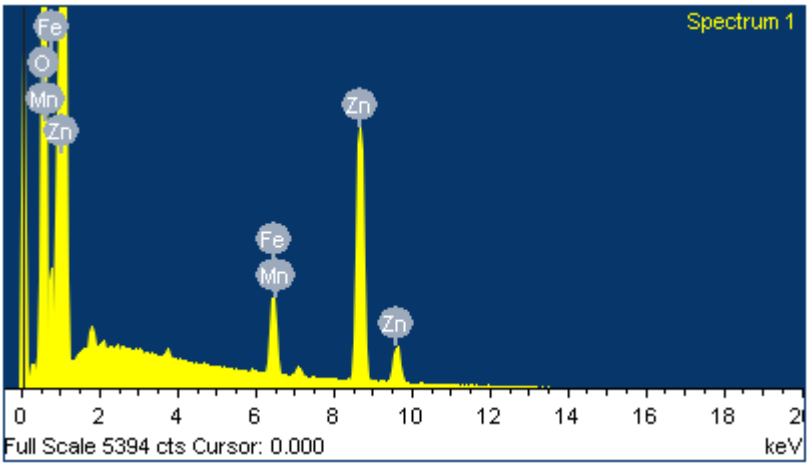

Fig 3.15: E-DAX spectra of as-sputtered film at argon working gas pressure.

3.1.1.4.3 Atomic force micorscope (AFM)

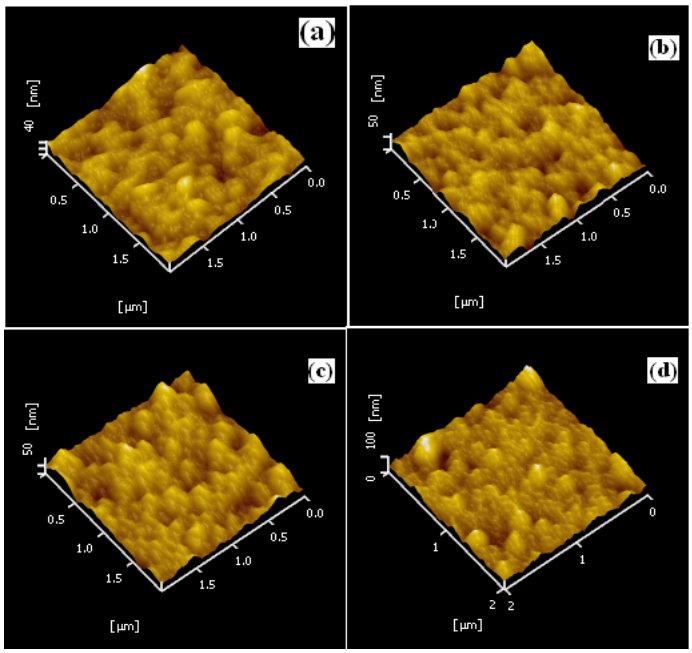

Fig 3.16: FE-SEM micrographs of as-sputtered films of argon working gas pressure of (a) 5, (b) 8, (c) 12 and (d) 15 mTorr.

Figure 3.16 shows the non-contact mode AFM images of $Zn_{0.925}Mn_{0.025}Fe_{0.05}O$ thin films. The roughness values estimated from AFM micrographs are listed in table 3.5. The AFM micrographs show the dense structure with increase in the pressure. The films deposited at 12 mTorr pressure have higher roughness values of 13.22 nm than the other deposited films. The AFM images are in accordance with FESEM micrographs in terms of grain sizes and texture of the films.

3.1.2 Oxygen gas environment

Thin films of un-doped and Mn5%, Fe5% and Mn.Fe co-doped ZnO films have been deposited onto quartz substretes under diffrent oxygen gas partial pressure from 7-13 mTorr. The othe sputter parametrs were kept same as mentioned above.

3.1.2.1 Un-doped ZnO

The pure un-doped ZnO thin films were deposited for 1hr on un-heated and un-rotating quartz substrates.

3.1.2.1.1 X-ray anaylsis

The X-ray diffraction patterns of ZnO thin films (figure 3.17) deposited under oxygen pressure of 7-18 mTorr are characteristic of a crystallized phase of wurtzite type [19]. The (002) reflection becomes more prominent, indicating an oriented growth along c-axis perpendicularly to the substrate surface, with increase in gas pressure. These results are similar to other reported studies dealing with the growth of Zinc oxide thin films obtained by r.f. sputtering and other deposition techniques [20 - 23].

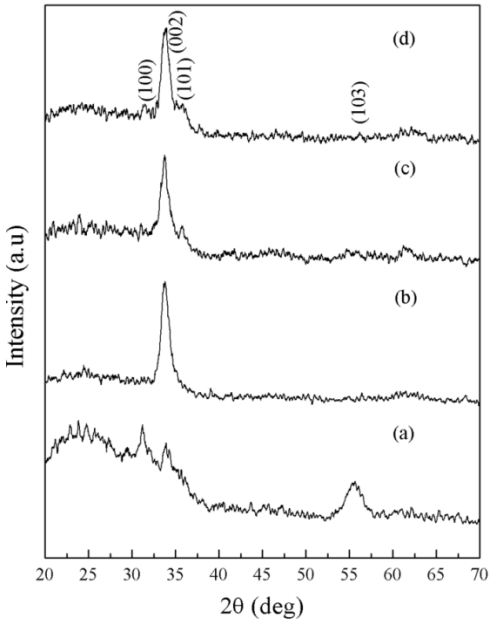

Fig 3.17: XRD pattern of as-sputtered films of oxygen working gas pressure of (a) 7, (b) 9, (c) 13 and (d) 18 mTorr.

Ttable 3.5 lists various structure parameters estimated from xrd data. The intensity of (002) peak decreases while its FWHM increases with increase in oxygen pressure. Zhang et.al [12] reported that for the PLD deposited films intensity of (002) increases and FWHM decreases with increase in oxygen pressure. There is slight shift in peak position towards higher angles are due to tensile stress.

Table 3.6: Structural parameters of as-sputtered ZnO films with different partial pressures

Working gas pressure (mTorr)	7	9	11	13
Thickness(nm)	840	1014	842	708
Grain size (nm) (SEM)	121±5	126±5	124±5	68±5
Roughness (nm) (AFM)	2.85	2.15	4.75	5.35

3.1.2.1.2 Microstructure and surface morphology (FE-SEM)

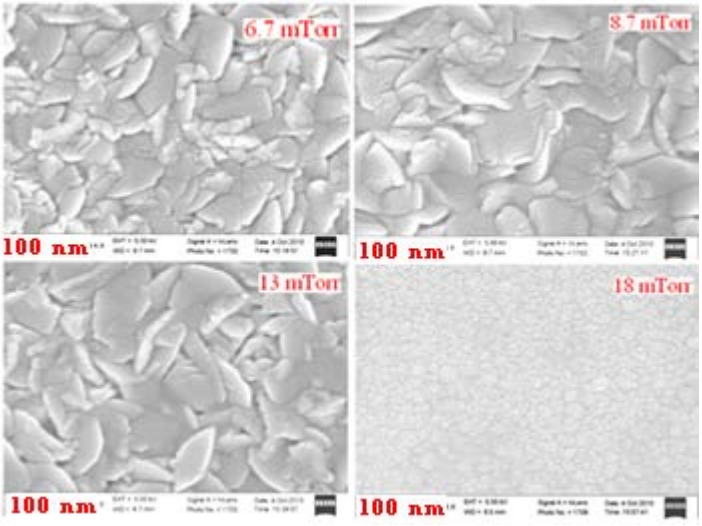

Fig 3.18: FE-SEM of as-sputtered films of oxygen working gas pressure of (a) 7, (b) 9, (c) 13 and (d) 18 mTorr.

The FESEM micrographs of ZnO films at various oxygen partial pressures are shown in Figure 3.18. The films show grain size is weaky dependent when the oxygen partial pressure is in the range 7-13 mTorr. The grain size decreases sharply as gas pressure increases to 18 mTorr. The films deposited at 18 mTorr of oxygen pressure show different structure unlike other films. This behavior might be due to high oxygen deficiency in film. In contrast to our results E.M. Bachari et.al [20] reported mixed dense and columnar structure normal to surface of the substrate.

3.1.2.1.3 Atomic force microscope (AFM)

The surface morphology of ZnO films is strongly dependent on the oxygen pressure when the substrate temperature and rf power are fixed. The surface morphology of ZnO films is investigated through AFM measurements. The results are shown in the Fig. 3.19. The surface roughness of ZnO films increases with increase in oxygen pressure. This tendency is similar to PLD deposited films reported earlier [12].

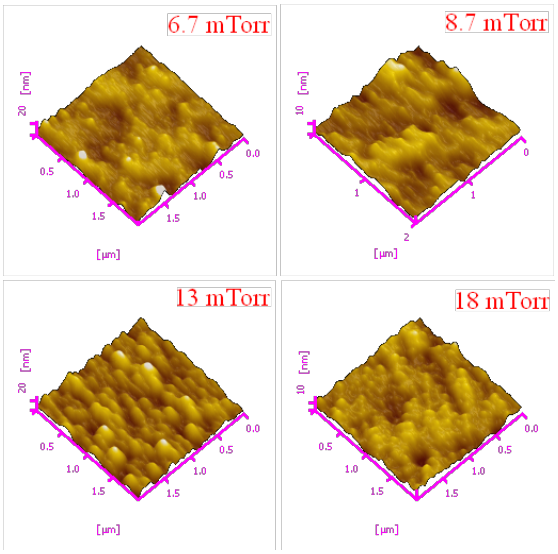

Fig 3.19: AFM images of as-sputtered films of oxygen working gas pressure of (a) 7, (b) 9, (c) 13 and (d) 18 mTorr.

3.1.2.2 $Zn_{0.95}Mn_{0.05}O$

3.1.2.2.1 X-ray analysis

The XRD patterns of Mn-doped ZnO as deposited films at various oxygen partial pressures are shown in Figure 3.20. All diffraction peaks correspond to ZnO without any trace of Mn oxides segregation in the film. There is no preferential growth or orientation of the films. The films can classified as mixture of disordered and amorphous phases. It is hard to conclude from the XRD patterns whether the Mn oxides exist as nanocrystalline or amorphous state.

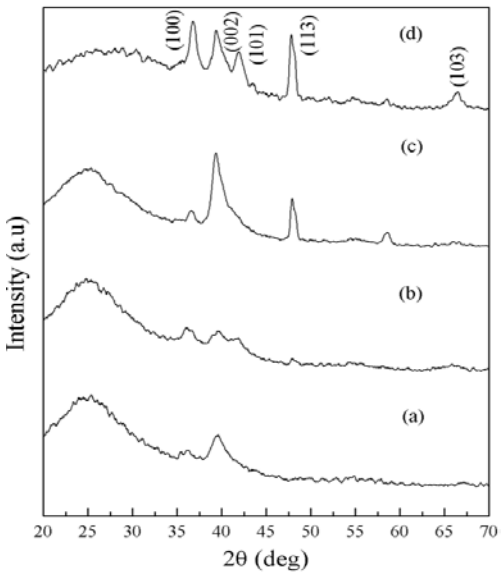

Fig 3.20: XRD pattern of as-sputtered films of oxygen working gas pressure of (a) 7, (b) 9, (c) 11 and (d) 13 mTorr.

Table 3.7: Structural parameters of as-sputtered $Zn_{0.95}Mn_{0.05}O$ films with different partial pressure.

Working gas pressure (mTorr)	7	9	11	13
Thickness(nm)	398	450	405	424
Grain size (nm) (SEM)	12±5	22±5	37±5	52±5
Roughness (nm) (AFM)	1.56	2.64	1.62	4.18

3.1.2.2.2 Microstructure and surface morphology (FE-SEM)

Figure 3.21 display the FE-SEM images of $Zn_{0.95}Mn_{0.05}O$ films for different oxygen partial pressures. From FESEM micrographs show dense structure in the film and the grain size increases with increase in oxygen pressure from 33 to 52 nm. The average grain size and surface roughness values are listed in table 3.7.

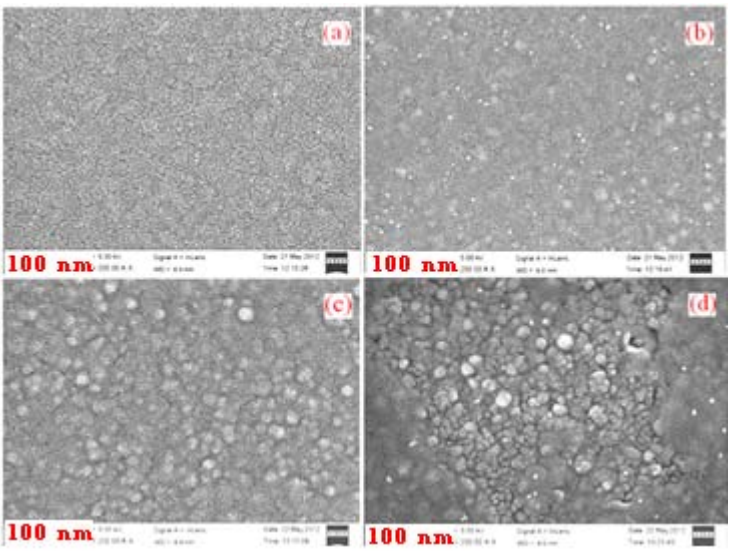

Fig 3.21: FE-SEM micrographs of as-sputtered films of oxygen working gas pressure of (a) 7, (b) 9, (c) 11 and (d) 13 mTorr.

3.1.2.2.3 Atomic force microscope (AFM)

The atomic force microscope (AFM) images of $Zn_{0.95}Mn_{0.05}O$ thin films deposited at various oxygen partial pressures are shown in Figure 3.22. The surface roughness of the

films is low except for the film deposited at 13 mTorr gas pressure. This might be due to excess oxygen trapped in the films. The increase in roughness (oxygen pressure during deposition) is leading to the increase in crystallinity.

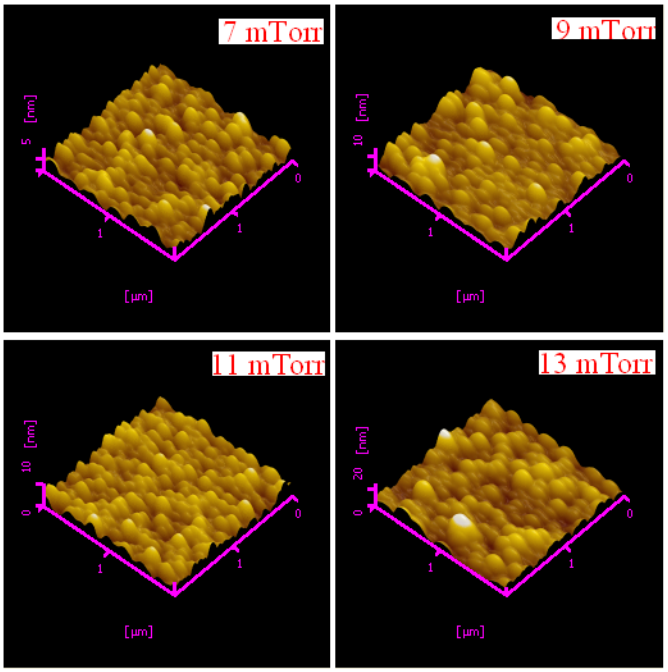

Fig 3.22: FE-SEM micrographs of as-sputtered films of oxygen working gas pressure of (a) 7, (b) 9, (c) 11 and (d) 13 mTorr.

3.1.2.2 $Zn_{0.95}Fe_{0.05}O$

The X-ray diffraction of $Zn_{0.95}Fe_{0.05}O$ films deposited at various working gas pressures in oxygen environment are shown in Figure 3.23. There is no preferential growth or orientation of the films. The films can classified as mixture of disordered and amorphous phases. The xrd peaks intensity increases with increase in gas pressure indicating evolution of crysttaline phase from the disordered and amorphous phases.

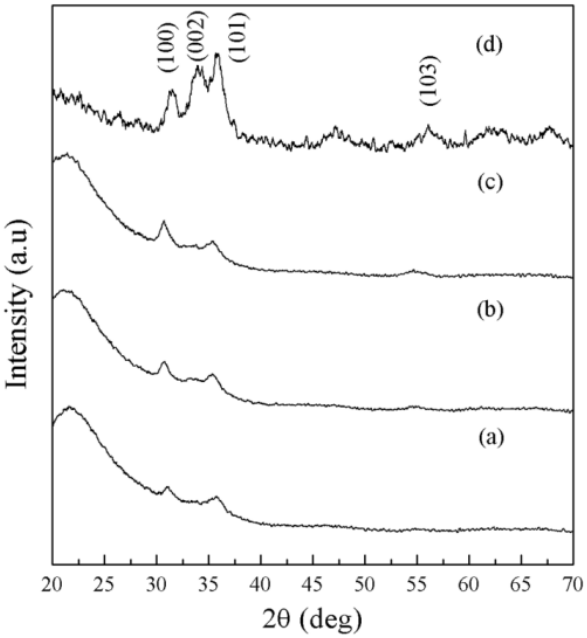

Fig 3.23: XRD pattern of as-sputtered films of oxygen working gas pressure of (a) 7, (b) 9, (c) 11 and (d) 13 mTorr.

Table 3.8: Structural parameters of as-sputtered $Zn_{0.95}Fe_{0.05}O$ films with different partial pressure.

Working gas pressure (mTorr)	7	9	11	13
Thickness(nm)	305	737	940	1234
Grain size (nm) (SEM)	16± 5	22± 5	38± 5	41± 5
Roughness (AFM)	1.05	4.84	6.64	4

3.1.2.2.2 Microstructure and surface morphology (FE-SEM)

Figure 3.24 display the FE-SEM images of $Zn_{0.95}Fe_{0.05}O$ films for different oxygen partial pressures. The grain size increases with increase in oxygen pressure. The average grain size and surface roughness values are listed in table 3.8.

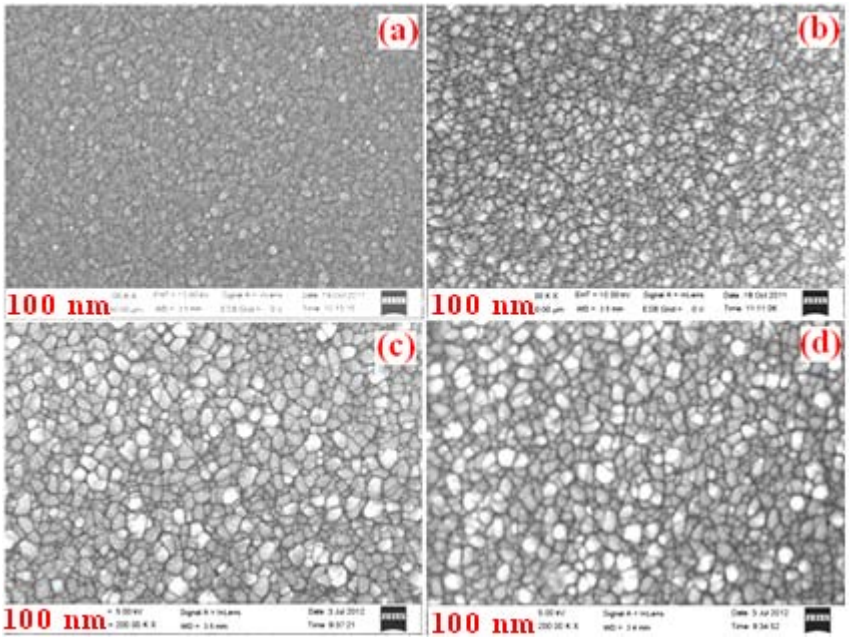

Fig 3.24: FE-SEM micrographs of as-sputtered films of oxygen working gas pressure of (a) 7, (b) 9, (c) 11 and (d) 13 mTorr.

3.1.2.2.3 Atomic force microscpe (AFM)

The atomic force microscope (AFM) images of $Zn_{0.95}Fe_{0.05}O$ thin films deposited at various oxygen partial pressures are shown in Figure 3.25. The roughness of the film increases with increase in gas pressure upto 11 mTorr followed by a decrease as gas pressure is increased to 13 mTorr. These results are in agreement with Fe doped ZnO by DC magnetron sputtering reported in reference [17].

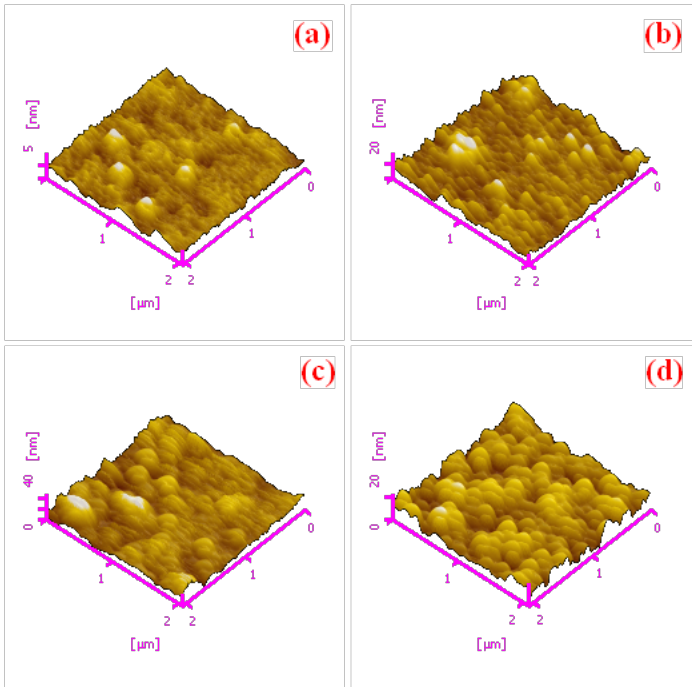

Fig 3.25: AFM images of as-sputtered films of oxygen working gas pressure of (a) 7, (b) 9, (c) 11 and (d) 13 mTorr.

3.1.2.3 $Zn_{0.925}Mn_{0.025}Fe_{0.05}O$

The X-ray diffraction of Mn and Fe codoped doped ZnO films deposited at various oxygen gas presure environment are shown in Figure 3.26. The XRD pattern show films have crystallize in hexagonal wurtzite phase with (002) orientation along *c*-axis penducular to the substrate base plane. As we can from (Figure 3.27) the (002) peak is evalvuating with increase in oxyggen pressure indicating excess oxygen gas pramoting the film growth perpendicular to substrate this may might be due to decrease in surface free energy along (002) plane. The crystallite (D) value for 9 mTorr films is less about 6 nm and average crystallite values range from 6- 65 nm. The films deposited at 13 mTorr show compressive (negative) stress and rest of the films show tensile (positve) stress. The detailed structural parameters are lited in Table. 3.9. The stress and strain (%) values show inverse behavior for as deposited films.

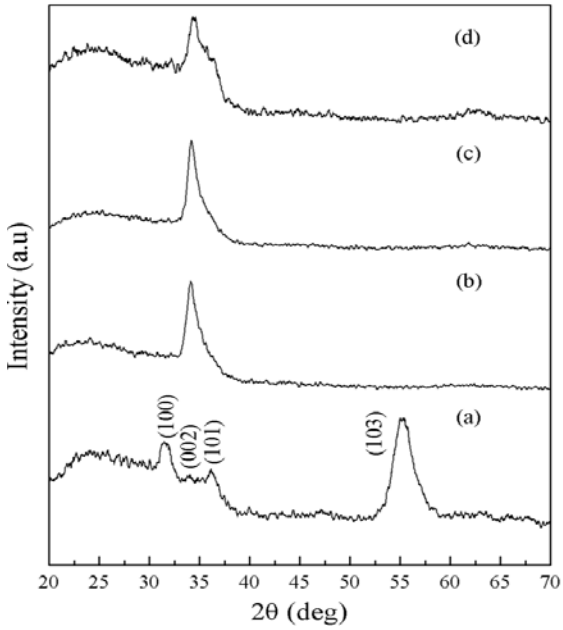

Fig 3.26: XRD pattern of as-sputtered films of oxygen working gas pressure of (a) 7, (b) 9, (c) 11 and (d) 13 mTorr.

Table 3.9: Structural parameters of as-sputtered $Zn_{0.925}$ $Mn_{0.025}Fe_{0.05}O$ films with different partial pressure.

Working gas pressure (mTorr)	7	9	11	13
Thickness(nm)	726	716	681	801
Grain size (nm) (SEM)	13±5	18±5	36±5	62±5
Roughness (nm) (AFM)	6.70	1.92	1.65	3.70

3.1.2.3.2 Microstructure and surface morphology (FE-SEM)

Field emission scanning electron microscope (FE-SEM) images of Mn, Fe doped ZnO films at various oxygen partial pressures are shown in Figure.3.27. From FE-SEM micrographs we can see that the grain size is increasing with increase in oxygen pressure are in the range of 26 to 60 nm. The lower pressure deposited films show smoother surface whereas high pressure deposited films show rough surface with increase size could be due to excess will produce oxygen deficiency in the films. The presence of Mn and Fe elements in ZnO host matrix was confirmed by EDS spectra.

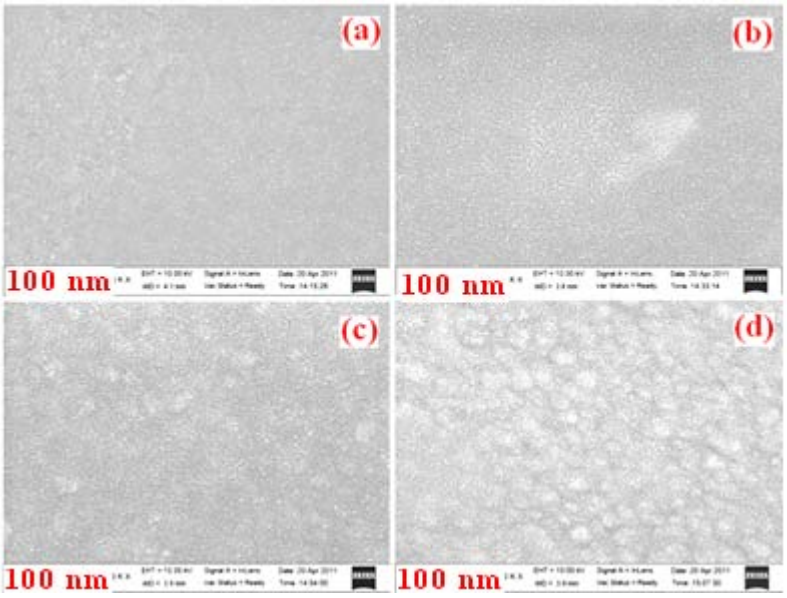

Fig 3.27: FE-SEM images of as-sputtered films of oxygen working gas pressure of (a) 7, (b) 9, (c) 11 and (d) 13 mTorr.

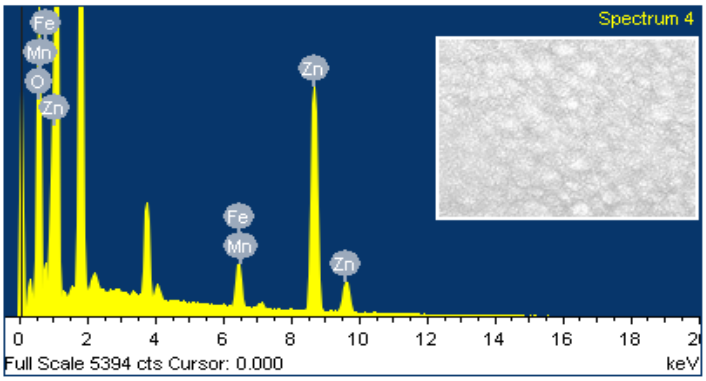

Fig 3.28: E-DAX spectra of as-sputtered films at oxygen working gas pressure 13 mTorr.

3.1.2.3.3 Atomic force microscope (AFM)

The atomic force microscope (AFM) images of Mn, Fe doped ZnO films deposited at various oxygen partial pressures are shown in Figure 3.29. The root mean square (RMS) values decreases with increase in gas presuree.

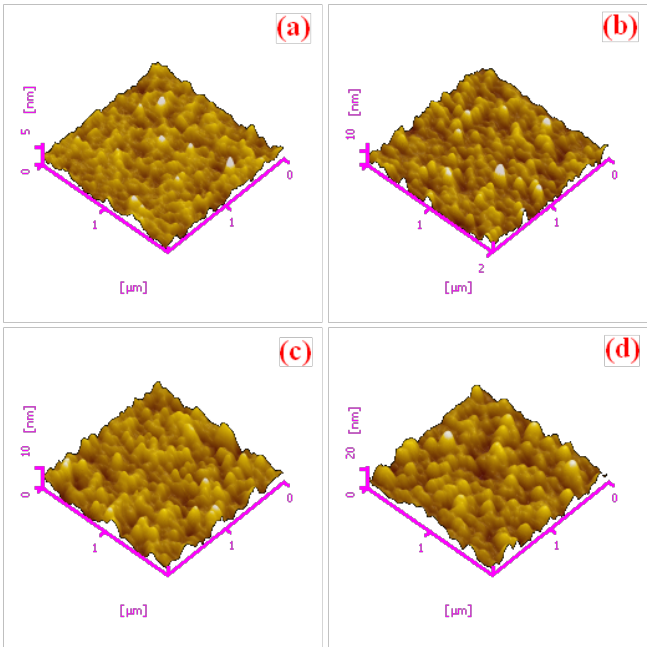

Fig 3.29: AFM images of as-sputtered films of oxygen working gas presure of (a) 7, (b) 9, (c) 11 and (d) 13 mTorr.

3.2 Effect of film thickness

The film thickness can be changed either by changing the deposition duration keeping other deposition parametrs same. Thin films of un-doped and Mn, Fe and Fe ,Mn co-doped ZnO thin films were depsoited onto quartz substrates by rf-magnetron sputtering in argon and nitrogen gas environment as function of rf power and deposition duration (film thickness) by keeping all other deposition conditions same as stated earlier.

3.2.1 Argon gas environment

3.2.1.1 $Zn_{0.95}Mn_{0.05}O$

Thin films of $Zn_{0.95}Mn_{0.05}O$ ceramic target have been depsited onto quartz substrate by rf mageron sputtering in argon gas environment. The sputter duration varied from 30 to 120 min by keeping the other deposition conditions constant i.e. working gas pressure 12 mTorr, rf power 100 W substrate – target distance 85 mm. The thickness increases from 634 to 2861 nm with increase in deposition duration.

3.2.1.1.1 X-ray analysis

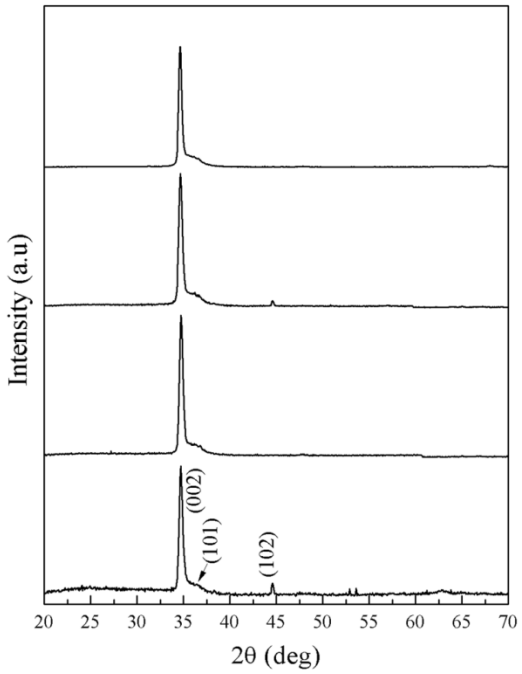

Fig 3.30: XRD pattern of as-sputtered films of $Zn_{0.95}Mn_{0.05}O$ at different film thickness of argon working pressure.

Fig. 3.30 shows the XRD plots for films deposited in Ar – environment for different thicknesses. All the as deposited films show preferential orientation along the c-axis (normal to the substrate base plane). With the increase in thickness the orientation along (0 0 2) direction improves and corresponding 2θ value shifts towards lower value compared to that of ZnO, indicating that the films are in a state of uniform stress [2 - 4]. The imperfection of the crystallites and the mismatch of the ionic radii of the substituent ions in the host matrix can lead to internal stress. The stress in the films first increases and then decreases with increase in film thickness value presumably due to increase in preferential orientation of the film.

Table 3.10: Structural parameters of as-sputtered $Zn_{0.95}Mn_{0.05}O$ films with different films thickness in argon environment.

Deposition duration (min)	30	60	90	120
Thickness(nm)	634	1404	1906	2861
2θ (˚)	34.72	34.76	34.69	34.65
Crystallite size, D (nm) (XRD)	43±3	42±3	41±3	47±3
Relative Peak intensity	2127.26	5267.96	5826.54	18538.48
FWHM (˚)	0.390	0.395	0.406	0.352
Grain size (nm) (SEM)	85±5	124±5	136±5	204±5
Roughness (nm) (AFM)	5.05	2.48	6.44	4.23
c (nm)	0.516	0.516	0.517	0.517
d (nm)	0.258	0.258	0.258	0.259
Strain, ε_z (%)	-0.854	-0.938	-0.747	-0.650
Stress, σ ($\times 10^9$ Pa)	1.988	2.184	1.739	1.515

3.2.1.1.2 Microstructure and surface morphology (FE-SEM)

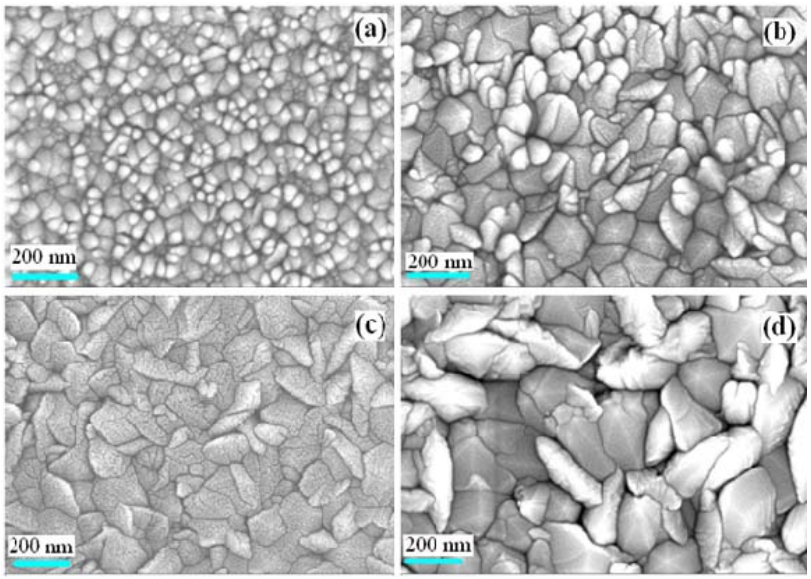

Fig 3.31: FE-SEM micrographs of as-sputtered films of $Zn_{0.95}Mn_{0.05}O$ at different film thickness of argon working gas pressure.

Fig. 3.31 shows the FESEM images of the films. With increasing thickness of films the spread in the sizes of the grains decreases i.e. the grains sizes become more homogeneous [27]. Films deposited for shorter durations contain agglomerates varying from 90 to 130nm with smaller grain of sizes 30 – 70 nm dispersed non- uniformly around them.

With increase in deposition duration these agglomerates grow in size to ranges of 120 – 160 nm and are comparatively uniformly spread with a fewer grains of the size in the range 20 – 50nm spread around them. Growth of the grains is attributed to the greater nucleation of the increased amount of sputtered atoms due to longer film deposition duration, which have sufficient kinetic energy for surface mobility and consequent diffusion [28]. Larger agglomerates may also form due to larger grain boundary movement [29]**.** Whereas, the heterogeneity in the films maybe due to the grain boundary mobilities which occur due to the influence of the dopant on the grain boundary transport [30]. The composition of the films obtained by EDS spectra is close to the starting composition.

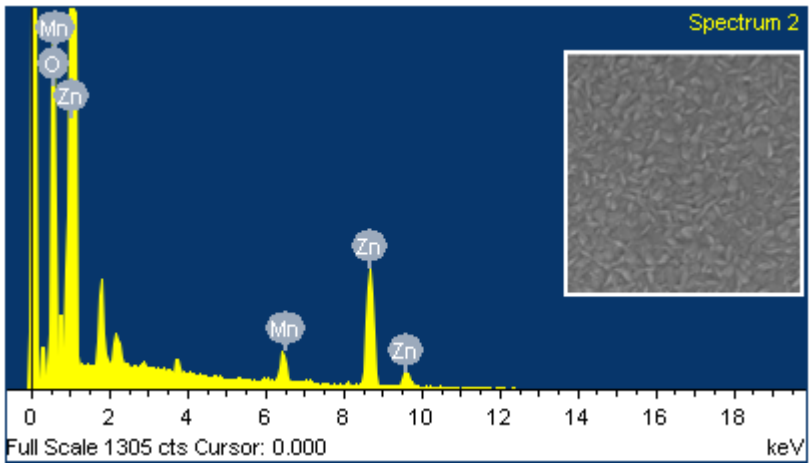

Fig 3.32: E-DAX spectra of as-sputtered films of $Zn_{0.95}Mn_{0.05}O$ at film thickness 2861 nm of argon working gas pressure.

3.2.1.1.3 Atomic force microscope (AFM)

Surface morphology of the films is examined using the AFM. The film images are shown in fig. 3.33. The images present grains of varying sizes and irregular grain boundaries. The average grain size is estimated to vary between ~90 and 130nm for films deposited for shorter durations and ~120 and 160 nm for films deposited for longer durations. The surface roughness (rms) of the films varies between ~ 4 and 8nm, while the average

roughness (R_a) varies between ~3 and 6nm.The Peak to Valley (P-V) height of the films lies in the range of ~30 to 60nm which is estimated from the line profile analysis. The density of protrusions decrease while the size of it increases with increase in duration of film coat, indicating better homogeneity and uniform growth being promoted with longer duration of film coating. This hints at the coalescing of sputtered material with deposition time. If atoms or clusters at the surface obtain sufficient activation energy to diffuse, the protrusions may grow in an island like manner absorbing activated atoms or clusters and diffusing them from adjacent protrusions leading to grain growth due to coalescence [3]. Reduction in the average roughness suggests the smoothening of the films with a relative decrease in the difference of the peak to valley height observed in the AFM studies [31]. It is observed that films with larger grains do not necessarily possess rougher surfaces. This is because of the growth and coalescing of grains in all directions.

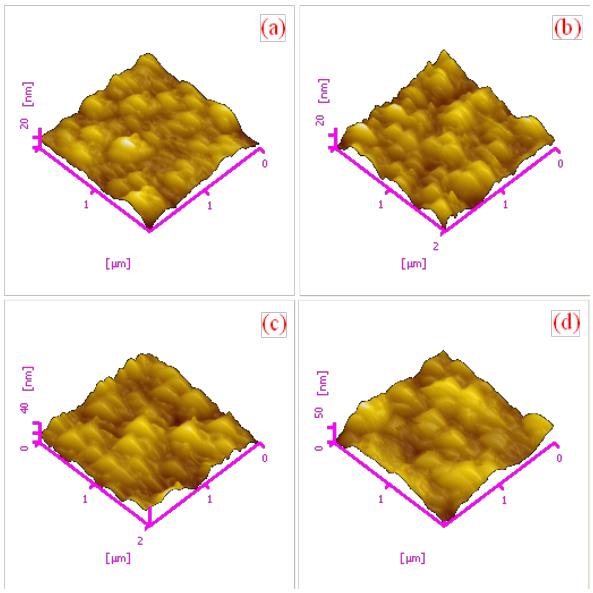

Fig 3.33: AFM images of as-sputtered films of $Zn_{0.95}Mn_{0.05}O$ at different film thickness of argon working gas pressure.

3.2.1.2 $Zn_{0.95}Fe_{0.05}O$

3.2.1.2.1 X-ray analysis

Fig. 3.34 shows the XRD plots for films of different thicknesses deposited in Ar – environment. The single phase formation of the films is confirmed from the plots. That the films have a hexagonal wurtzite structure is confirmed by prominent peak at (0 0 2). It is worth noting that all the films are oriented along the c-axis, normal to the substrate base plane, even without any kind of post deposition processing. The peak position corresponding to the (0 0 2) reflection shifts towards higher 2θ values compared to bulk ZnO. The shift towards higher angles shows that films have tensile (positive) stress, where E.S.Tuzemen et.al reported for ZnO films [5]. The imperfection of the crystallites and the mismatch of the ionic radii of the substituent ions in the host matrix can lead to internal stress. With increasing of films thickness a slight decrease from 0.530 to 0.524 nm of the c-value, indicating reduction along the c – axis is observed. But the change in stress is comparatively insignificant.

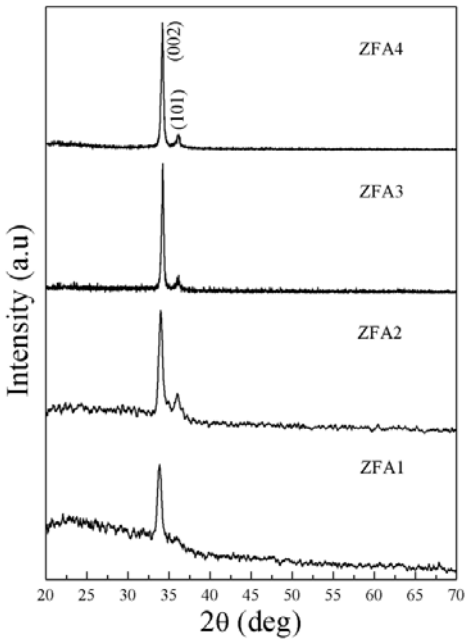

Fig 3.34: XRD pattern of as-sputtered films of $Zn_{0.95}Fe_{0.05}O$ at different film thickness of argon working gas pressure. .

Table 3.11: Structural parameters of as-sputtered $Zn_{0.95}Fe_{0.05}O$ films with different films thickness.

Sputter duration (mins)	30	60	90	120
Thickness(nm)	305	737	940	1234
2θ (˚)	33.83	33.98	34.22	34.18
Crystallite size, D (nm) (XRD)	30±3	32±3	58±3	50±3
Relative Peak intensity	274.27	2622.02	9784.38	14956.98
FWHM (˚)	0.553	0.521	0.282	0.332
Grain size (nm) (SEM)	24± 5	38± 5	44± 5	82± 5
Roughness (nm) (AFM)	8.05	9.57	7.68	6.54
c (nm)	0.530	0.527	0.524	0.524
d (nm)	0.265	0.264	0.262	0.262
Strain, ε_z (%)	1.698	1.262	0.573	0.687
Stress, σ ($\times 10^9$ Pa)	-3.954	-2.939	-1.335	-1.600

3.2.1.2.2 Microstructure and surface morphology (FE-SEM)

Fig. 3.35 shows the FESEM images of the films. With increasing thickness of films the grain size is increasing gradually. The bigger grains size increases from 23 to 84 nm, with smaller grain of 10 – 40 nm sizes dispersed non- uniformly around them. Growth of the grains is attributed to the greater nucleation of the increased amount of sputtered atoms due to longer durations, which have sufficient kinetic energy for surface mobility and consequent diffusion [28]. Larger agglomerates may also form due to larger grain boundary movement [29]**.** Whereas, the heterogeneity in the films maybe due to the grain boundary mobilities which occur due to the influence of the dopant on the grain boundary transport [30]. The Presence of Mn element in the film is confirmed by EDS spectra.

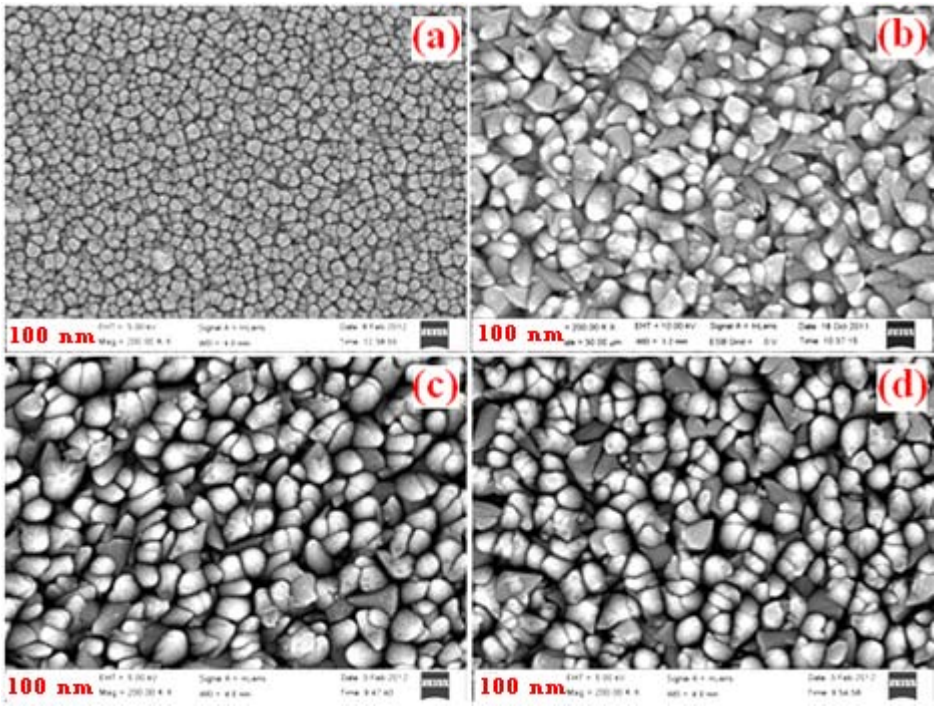

Fig 3.35: AFM images of as-sputtered films of $Zn_{0.95}Fe_{0.05}O$ at different film thickness of argon working gas pressure.

3.2.1.2.3 Atomic force microscope (AFM)

Surface morphology of the films examined using the AFM is shown in fig. 3.36. The images present grains of varying sizes and irregular grain boundaries. The average grain size is estimated to increase from ~17 to 68 nm for films deposited at various thicknesses, which are in agreement with FE-SEM data. The surface roughness (rms) of the films varies between ~6.5 and 9.5 nm, while high roughness is obtained for 60 min deposited films and we can see from (Figure 3.41) the films with 737 nm show peak to valley height high about 30 nm. The density of protrusions decrease while the size of it increases with increase in duration of film coat, indicating better homogeneity and uniform growth being promoted with longer duration of film coating. This hints at the coalescing of sputtered material with deposition time. If atoms or clusters at the surface obtain sufficient activation energy to diffuse the protrusions may grow in an island like manner absorbing

activated atoms or clusters and diffusing them from adjacent protrusions leading to grain growth due to coalescence [3]. Reduction in the average roughness suggests the smoothening of the films with a relative decrease in the difference of the peak to valley height observed in the AFM studies [31]. It is observed that films with larger grains do not necessarily possess rougher surfaces. This is because of the growth and coalescing of grains in all directions.

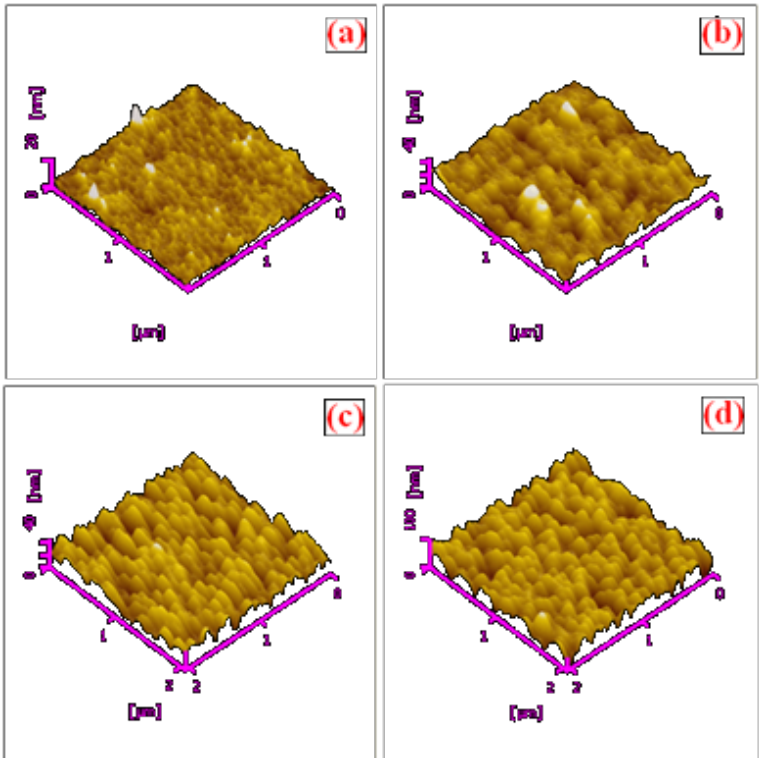

Fig 3.36: AFM images of as-sputtered films of $Zn_{0.95}Fe_{0.05}O$ at different film thickness of argon working gas pressure.

3.2.1.3 $Zn_{0.925}Mn_{0.025}Fe_{0.05}O$

Thin films of Mn, Fe co-doped ZnO ceramic were deposited onto quartz substrate by rf mageron sputtering in argon gas environment from 15 to 40 min by keeping the other deposition conditions constant.

3.2.1.3.1 X-ray analysis

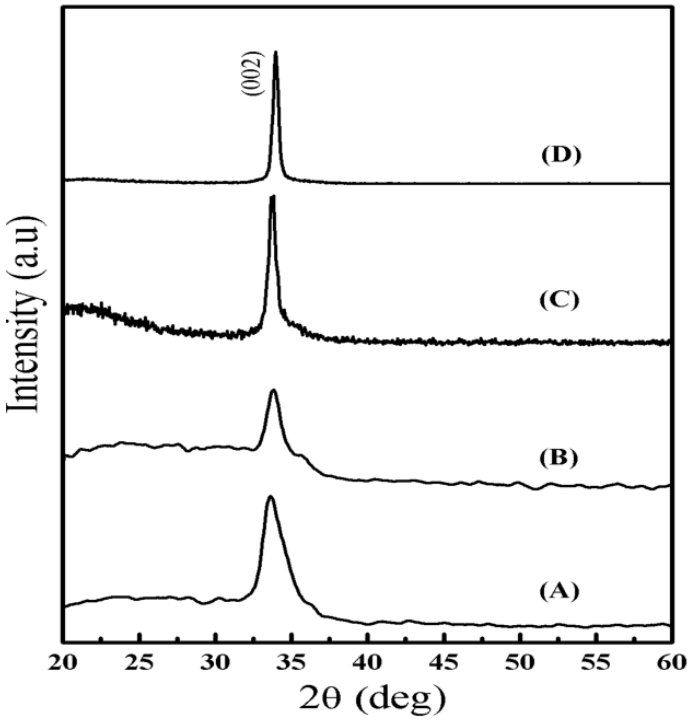

Fig 3.37: AFM images of as-sputtered films of $Zn_{0.95}$ $Mn_{0.025}Fe_{0.05}O$ at different film thickness of argon working gas pressure.

Figure.3.37.Shows the XRD patterns of the as-sputtered Mn-Fe doped ZnO thin films at different time durations from 15-40 min. as deposited films show the wurtzite structure with (002) plane oriented along the c-axis normal to the substrate plane. The crystallinity is increased with increase in thickness, which shows the film thickness increase promotes the film growth perpendicular substrate plane. The peak position of the films shifted to higher 2θ values as thickness of the films increases is attributed that the films have tensile stress. From XRD we can see there are no secondary phase presented in the film within the detection limit indicates that the Mn^{2+}/Mn^{3+} or Fe^{2+}/Fe^{+} replaces the Zn^{2+} in host semiconducting matrix. The average crystallite size (D), lattice parameter (*c*) and other parameters of the films were estimated from XRD data listed in table 3.12. The crystallite size is increased with increase in thickness of the films with better orientation of the films high crystallinity.

Table 3.12: Structural parameters of as-sputtered $Zn_{0.95}$ $Mn_{0.025}Fe_{0.05}O$ films with different films thickness.

Deposition duration (min)	15	20	30	40
Thickness(nm)	365	385	595	645
2θ (˚)	33.77	33.81	33.75	33.97
Crystallite size, D (nm) (XRD)	12±3	17±3	31±3	40±3
Relative Peak intensity	245	135	598	3635
FWHM (˚)	1.386	0.949	0.531	0.413
Grain size (nm) (SEM)	55±5	38±5	18±5	26±5
Roughness (RMS) (nm)	1.5	7.4	3.1	4.9
c (nm)	0.530	0.529	0.531	0.527
d (nm)	0.265	0.265	0.265	0.264
Strain, ε_z (%)	1.867	1.748	1.944	1.302
Stress, σ ($\times 10^9$ Pa)	-4.346	-4.069	-4.525	-3.032

3.2.1.3.2 Microstructure and surface morphology (FE-SEM)

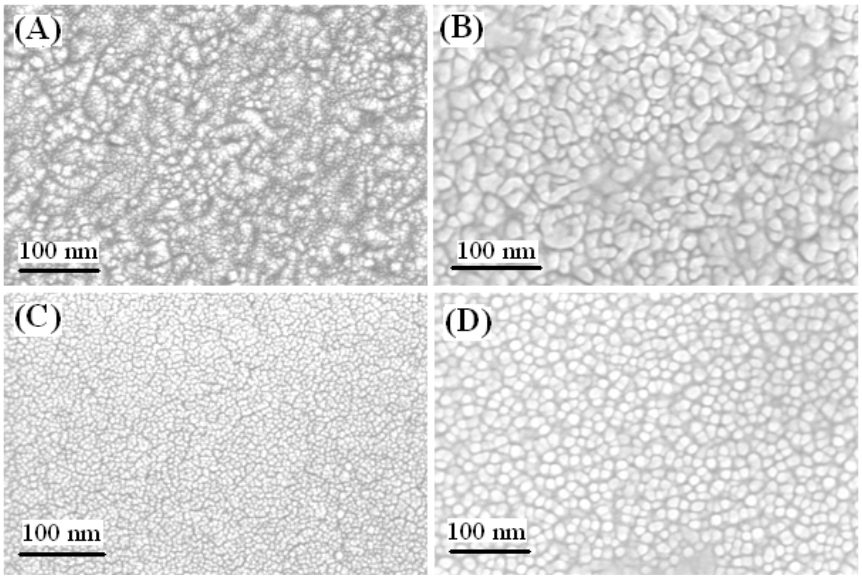

Fig 3.38: FE-SEM micrographs of as-sputtered films of $Zn_{0.95}Mn_{0.025}Fe_{0.05}O$ at different film thickness of argon working gas pressure.

Figure 3.38 displays field emission scanning electron microscope (FE-SEM) micrograph of the films at varies films thickness. It can be seen that the topography of the films with homogeneous spread of grains decreasing with increase in films thickness. The average grain size of deposited films varies in the range of 105 – 55 nm. The presence of Mn, Fe elements in ZnO matrix was confirmed by EDS spectra.

3.2.1.3.3 Atomic force micorscope (AFM)

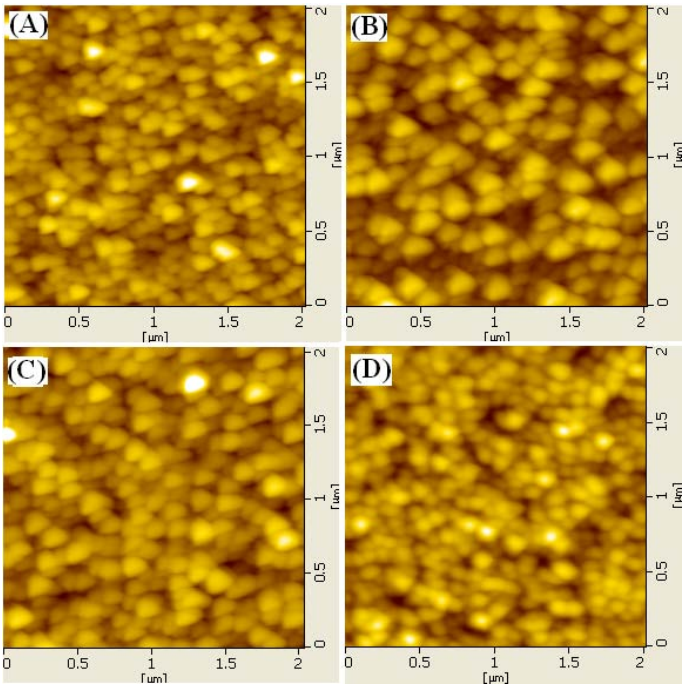

Fig 3.39: AFM images of as-sputtered films of $Zn_{0.95}$ $Mn_{0.025}Fe_{0.05}O$ at different film thickness of argon working gas pressure.

Figure 3.39 shows AFM images from which the nanocrystalline nature with uniform spread of grains is evident. The thicker film exhibit a dense microstructure compared with those of lower thickness. The root mean square (RMS) of the ranges 1.5 – 7 nm indicating films have smooth surface.

3.2.2 Nitrogen gas environment

Thin films Mn and Fe doped ZnO films were deposited on quartz substretes as a function of film thickness (time duration) in nitrogen gas environment. The nitrogen gas partial pressure was kept at 12 mTorr.

3.2.2.1 $Zn_{0.95}Mn_{0.05}O$

Figure.3.40 shows the XRD plots for films deposited in N_2 – environment for different durations. The peak at (0 0 2) confirms the hexagonal wurtzite structure of the films. The as deposited films are oriented along the c-axis, normal to the substrate base plane. Though the 2θ values are close to 34.4^0 that of unstressed bulk ZnO [2], the peak

gradually shifts to lower angle with increase in the duration of film deposition. This indicates that the films deposited in N_2 environment contain either Mn ions in the lower valence state, which have larger ionic radius than that of Zn^{2+} or nitrogen enters in the lattice in place of oxygen. With increasing duration of deposition the c-

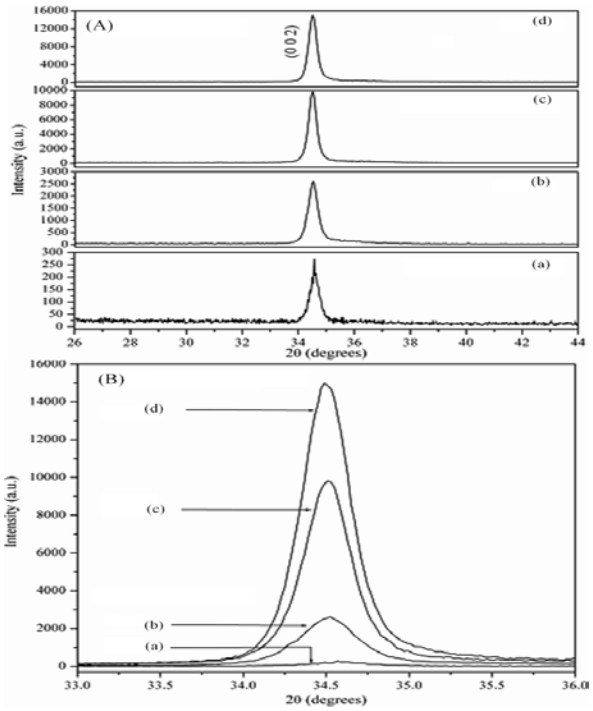

Fig 3.40: XRD pattern of as-sputtered films of $Zn_{0.95}Mn_{0.05}O$ at different film thickness of nitrogen working gas.

axis parameter increases from 5.99 to 6.68 A^o. This may be attributed to the substitution of oxygen atom by N_2, or the O^{2-} by N^{3-} ion as the radius of nitrogen is larger than that of oxygen, resulting in the (002) diffraction peak shifting to a lower angle [32].

The crystal lattice constant c and the interplanar distance of the diffracting planes d were indentified using the Bragg's equation $n\lambda = 2d\sin\theta$, where n is the order if the diffracted beam, λ is the wavelength of x-ray and θ is the angle between the incoming x-ray and the normal of the diffracting plane. The values of peak position, peak intensity, FWHM, grain size and the crystalline quality increased with the increase of film thickness. No significant changes in the values of c and d were observed with the change of film thickness.

Table 3.13: Structural parameters of as-sputtered $Zn_{0.95}$ $Mn_{0.05}O$ films with different films thickness in nitrogen environment.

Deposition duration (min)	30	60	90	120
Thickness(nm)	398	957	1346	1650
2θ (˚)	34.41	34.53	34.51	34.5
Crystallite size, D (nm) (XRD)	36±3	42±3	51±3	48±3
Relative Peak intensity	274.27	2622.02	9784.38	14956.98
FWHM (˚)	0.462	0.390	0.324	0.340
Grain size (nm) (SEM)	23± 5	37± 5	55± 5	84± 5
Roughness (nm) (AFM)	3.36	3.18	4.40	5.10
c (nm)	0.521	0.519	0.519	0.520
d (nm)	0.260	0.260	0.259	0.259
Strain, ε_z (%)	0.035	-0.303	-0.247	-0.218
Stress, σ ($\times 10^9$ Pa)	-0.080	0.704	0.574	0.509

3.2.2.1.2 Microstructure and surface morphology (FE-SEM)

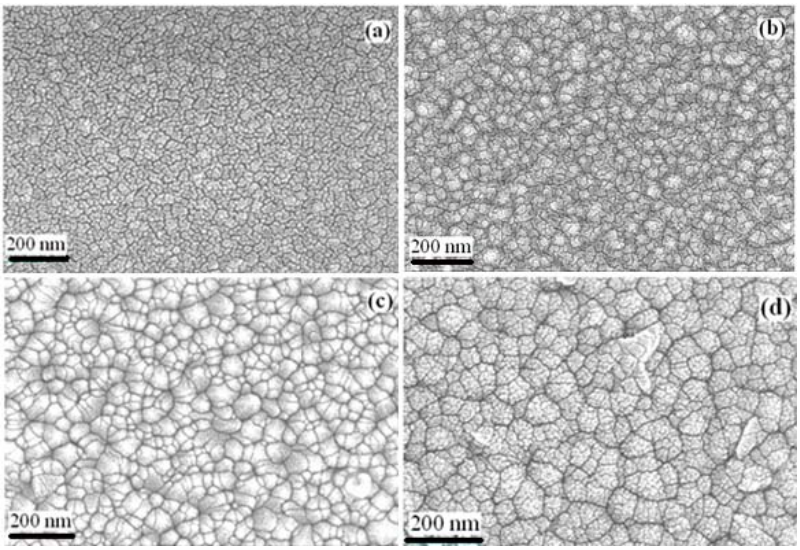

Fig 3.41: FE-SEM micrographs of as-sputtered films of $Zn_{0.95}$ $Mn_{0.05}O$ at different film thickness of nitrogen working gas.

Figure 3.41 shows the FESEM images of the films. Films deposited for shorter duration possess bigger grains of size ranging from 40 to 70nm and smaller grains (dispersed non- uniformly around the bigger grains) of sizes 15 – 30 nm. While the films

deposited for longer durations have these agglomerates grow in size to 80 – 130 nm with more uniform spread and fewer grains of the size 20 – 50 nm spread around them. The change in the size of the grains with change in the duration of deposition can be due to the incorporation of nitrogen in the ZnO host lattice and/or because of some of nitrogen atoms get located in grain boundary regions and prevent the grain growth because of the difference of atomic radii of zinc and nitrogen atoms [33, 34], thereby leading to a larger spread in the grain size.

3.2.2.1.3 Atomic force microscope (AFM)

The AFM images of the films are shown in fig. 3.42. The average grain size is estimated to be 90 -110 nm and 130 -160 nm for thinner and thicker films respectively. These values are greater than the size of grains estimated from the FESEM images. The root mean square (rms) and average roughness value varies in the range 3 – 5 nm and 2-4nm respectively. The peaks to valley height (P–V) values are in the range 20 - 50nm. The 3 – dimensional images show improved homogeneity and uniform growth as the thickness of the film increases.

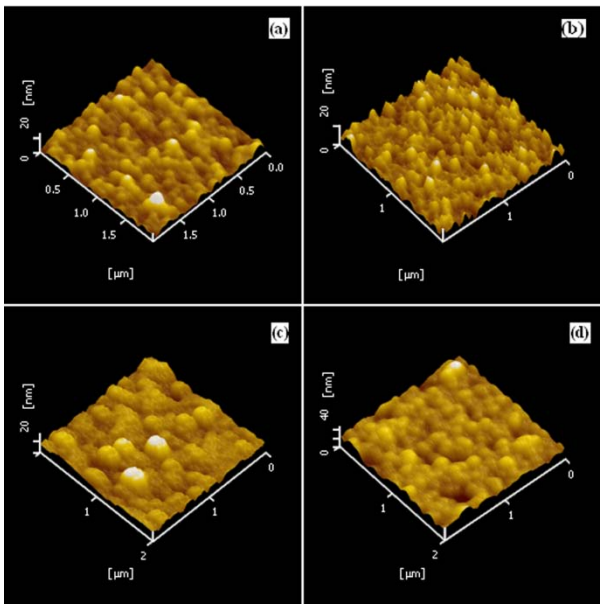

Fig 3.42: AFM images of as-sputtered films of $Zn_{0.95}Mn_{0.05}O$ at different film thickness of nitrogen working gas.

3.2.2.2 $Zn_{0.95}Fe_{0.05}O$

Figure.3.43 shows the XRD plots for films deposited in N_2 – environment for different durations (thickness). The peak at (0 0 2) confirms the hexagonal wurtzite structure of the

films. The as deposited films are oriented along the c-axis, normal to the substrate base plane. The 2θ values are shift towards higher angles above the value 34.4^0 of unstressed bulk ZnO [2]. The crystallite (D) of the films increases with increase in film thickness shows the films are growing in nanocrystalline single crystals.

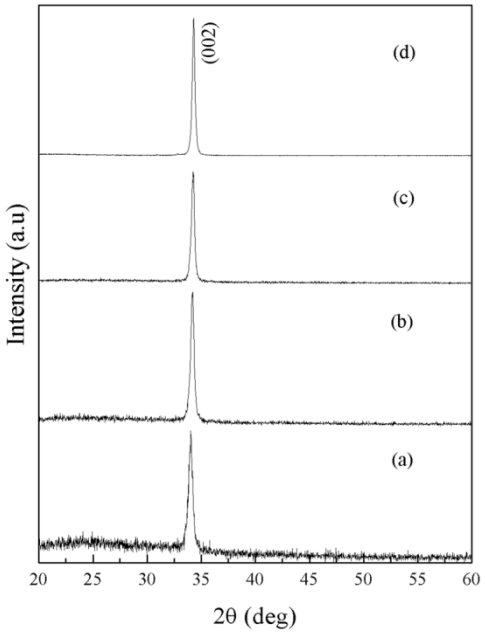

Fig 3.43: XRD pattern of as-sputtered films of $Zn_{0.95}Fe_{0.05}O$ at different film thickness of nitrogen working gas.

. The lattice parameter (*c*) shows increase trend with film thickness attributes the films elongation along the *c*- axis perpendicular substrate base plane and structural parameters obtained by XRD data are listed in Table 3.14. The peak (002) orientation except the other planes show film growth promotes the growth perpendicular to substrate indicates that the films deposited in N_2 environment contain either Fe ions in the lower valence state, which have larger ionic radius than that of Fe^{2+} or nitrogen enters in the lattice in place of oxygen. With increasing duration of deposition the c- axis parameter decreases from 0.527 to 0.522 nm.

The quality of films was determined by the $Zn_{0.95}Fe_{0.05}O$ thin film thickness.Fig.3.43 also shows that as the film thickness increases the diffraction peaks become shaper, their intensity is enhanced and its location changes. The films show the residual compressive (negative) stress is generated during the deposition process. No

significant changes in the values of c and d were observed with the change of film thickness

Table 3.14: Structural parameters of as-sputtered $Zn_{0.95}$ $Fe_{0.05}O$ films with different films thickness.

Deposition duration (min)	30	60	90	120
Thickness(nm)	312	588	684	850
2θ (˚)	34.02	34.18	34.24	34.30
Crystallite size, D (nm) (XRD)	38±3	45±3	48±3	55±3
Relative Peak intensity	218	533	930	5468
FWHM (˚)	0.434	0.364	0.341	0.302
Grain size (nm) (SEM)	28±5	36±5	42±5	48±5
Roughness (nm) (AFM)	1.97	3.18	3.75	3.63
c (nm)	0.527	0.524	0.523	0.522
d (nm)	0.263	0.262	0.262	0.261
Strain, ε_z (%)	1.157	0.692	0.520	0.350
Stress, σ ($\times 10^9$ Pa)	-2.694	-1.610	-1.212	-0.814

3.2.2.2.2 Microstructure and surface morphology (FE-SEM)

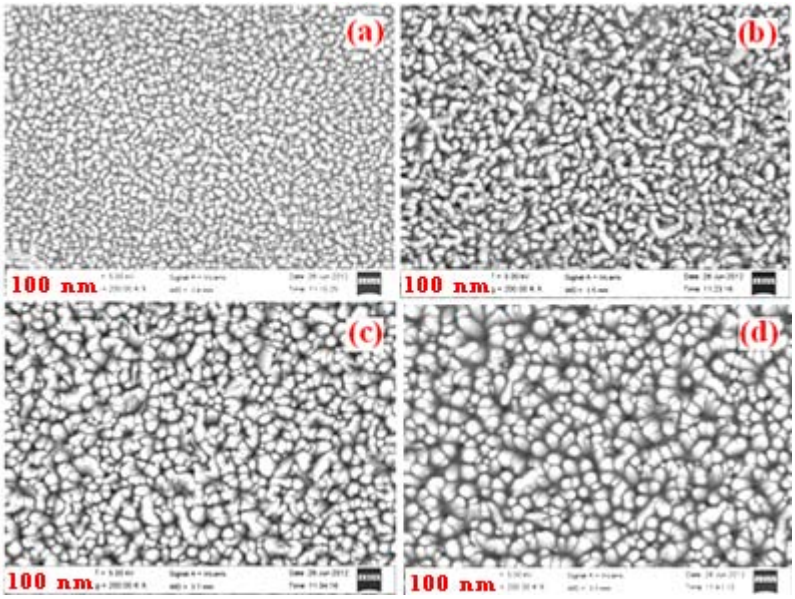

Fig 3.44: FE-SEM micrographs of as-sputtered films of $Zn_{0.95}$ $Fe_{0.05}O$ at different film thickness of nitrogen working gas.

Figure 3.44 shows the FESEM images of as sputtered films of $Zn_{0.95}Fe_{0.05}O$ ceramic target in nitrogen gas environment at various time durations. The grain size is increasing with increasing in film thickness in the range of 38 to 62 nm with nominal change. The films show homogeneous dense microstructure for all the films with film thickness. The EDS spectra confirm the presence of Fe element in ZnO matrix.

3.2.2.2.3 Atomic force microscope (AFM)

The AFM images of $Zn_{0.95}F_{0.05}eO$ films at various film thicknesses in nitrogen gas environment are shown fig. 3.45. The films with thickness 850 nm high peak to valley height ~ 15 nm and also the root mean square (rms) has higher value the films. The average RMS values vary from 1.9 to 3.75 nm indicates that the films have smooth surface. The peaks to valley height (P–V) values are in the range 10 – 15 nm. The 3 – dimensional images show improved homogeneity and uniform growth as the thickness of the film increases.

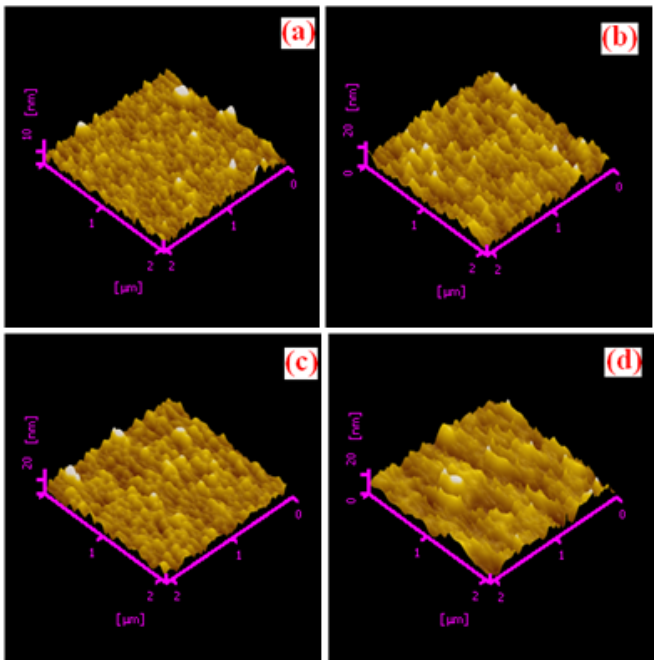

Fig 3.45: AFM images of as-sputtered films of $Zn_{0.95}$ $Fe_{0.05}O$ at different film thickness of nitrogen working gas.

3.3 Effect of Substrates

Thin films of Mn, Fe and Mn-Fe doped ZnO have been deposited onto Si (100) substratre by rf sputtering in argon gas environment by keeping the sputter parameters as base pressure 1×10^{-6} Torr, working gas pressure 12 mTorr, sputter duration 60 min and substrate to target diatcvnce 75 mm were maintained during the deposition. The Si (100) doen't have significant role on stuctural properties of as deposited thin films.

3.3.1 Films on silicon substretes

Figure 3.46 shows the X-ray diffraction of Mn, Fe indidual and co-doped ZnO films on to Si (100) substrate. From the XRD we can see that the films are crystallize in hexagonal wurtzite structure with promnet (002) peak along *c*-axis. From the XRD data it is clear indication that no secondary phase of MnO_2 or Fe_2O_3 expect the ZnO peaks this could be due to both Mn^{2+}, Fe^{2+} or Fe^{3+} replacing Zn^{2+} site in host ZnO matrix. The detailed structurural parameters obtained from XRD data are listed in Table 3.15. The lattice paramer (*c*) for Mn, Fe co-doped film show high than the Mn, Fe indidual dopant this beahavior may be attributed that varion in ionic radi of Mn and Fe in ZnO matrix. The films show compressive (negative) residual stress with dopant are in the range of -1.78 to-4.28.

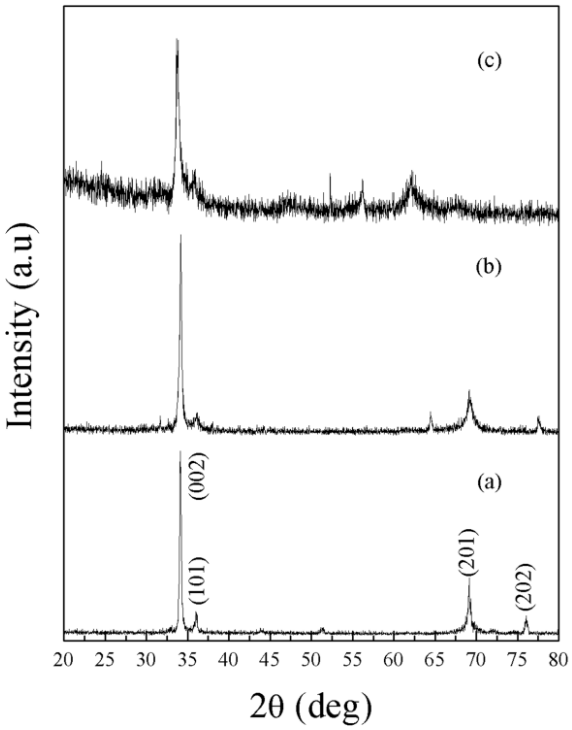

Fig 3.46: XRD pattern of as-sputtered films of Mn, Fe co-doped ZnO thin films on silicon substrates in argon gas environment.

Table 3.15: Structural parameters of as-sputtered films of Mn and Fe co-doped ZnO thin films on silicon substrates in argon gas environment.

	Mn5%	Fe5%	Mn2.5%+Fe5%
Thickness(nm)	510	458	521
2θ (˚)	34.13	34.15	33.78
Crystallite size, D (nm) (XRD)	32±3	28±3	21±3
Relative Peak intensity	333	267	127
FWHM (˚)	0.259	0.290	0.388
Grain size (nm) (SEM)	85±5	63±5	55±5
Roughness (nm) (AFM)	6.4±2	6.8±2	5.2±2
c (nm)	0.525	0.525	0.530
d (nm)	0.263	0.262	0.265
Strain, ε_z (%)	0.844	0.764	1.837
Stress, σ ($\times 10^9$ Pa)	-1.965	-1.779	-4.277

3.3.2 Microstructure and surface morphology (FE-SEM)

Figure 3.47 shows the FE-SEM micrographs of Mn, Fe indidual and co-doped ZnO films. It is clear evident from FE-SEM images the nancrystallinity with homogeneous dense microstrucuture. The average grain sizes are not varied much with dopnat in the range of 111 to 122 nm, the smaller grains about 40-60 nm are surrounded by bigger grains with grain sizes 80- 110 nm. The elemental composition of Mn, Fe in ZnO host matrix confirmed by our EDS spectra.

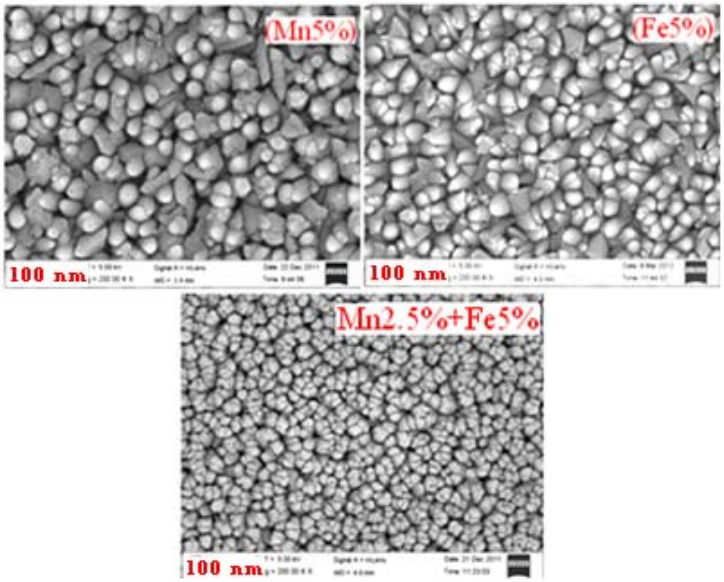

Fig 3.47: FE-SEM micrographs of as-sputtered films of Mn, Fe co-doped ZnO thin films on silicon substrates in argon gas environment.

3.3.3 Atomic force micorscope (AFM)

The non-contact modes of atomic force microscope (AFM) microstructural images are shown in Figure 3.48. The 3- dimensional images (Figure 3.53) of un-doped ZnO film show root mean square (RMS) has nominal changes with dopant is about 5.2 – 6.8 nm. The AFM image of Fe doped ZnO films has high value this might be due to the nature of dopant in the ZnO film.

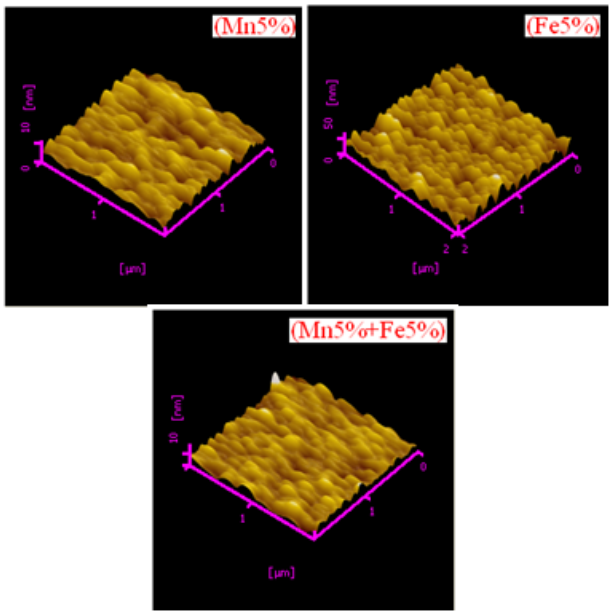

Fig 3.48: AFM micrographs of as-sputtered films of Mn, Fe co-doped ZnO thin films on silicon substrates in argon gas environment.

The gas pressure mainly determines the atomic kinetic energy when rf power and substrate temperature are fixed. It is reported that the (002) orientation has the lowest surface energy among all orientations [13-15]. Therefore, at a relatively high gas pressure, adatoms on the surface can move quickly to look for the lowest energy sites and form the low energy structure, which lead to improvement of the film crystalinity. When the (002) peak shows the weakest intensity and small area, this means the crystalline quality is degraded. For one hand, the kinetic energy of the atoms in plasma is decreased by collision with the ambient gas. The energy decreases of atoms reduce the possibility of adatoms to look for the lowest energy position and form low energy structure. For the other hand, the collision between the atoms in plasma and ambient gas results in the formation of thinnest film. So the crystalline quality degraded. Therefore, it is important that an optimum gas pressure should be chosen in the experiment.

Conclusions

- The detailed structural and morphological studies conducted on Mn, Fe and Mn and Fe co-doped ZnO thin films has revealed that the microstructure and preferential orientation of the as-deposited films strongly depend on the deposition

gas environment , gas pressure , duration of deposition (thickness) , dopant nature and type of substrate.

- All the as- deposited films show hexagonal wurtzite structure.
- The as- deposited films in argon and nitrogen gas environment show the hexagonal wurtzite structure with highly oriented with (002) plane along *c* – axis.
- The preferential orientation of the as –deposited film can be controlled by adjusting the gas pressure and doping with Mn or Fe. The (002) orientation can be improved for the undoped films and Mn-Fe co doped films by increasing the gas pressure. Whereas for the Mn and Fe doped films highly oriented films along (002) direction can be obtained at low gas pressure.
- The increase in gas pressure leads to decrease in thin film thickness because of back sputtering process.
- The films deposited in oxygen gas environment are disordered in nature and are not found to be stable.
- The average grain size increases with films thickness from 40- 80 nm in argon gas compared to nitrogen gas deposited films
- The films deposited in argon gas show bigger grain size compared to films deposited in oxygen or nitrogen gas atmosphere. This could be due high rate of deposition in argon gas.
- Thin films of un-doped and Mn, Fe doped ZnO show films have compressive (negative) stress for both argon and oxygen gases.
- The crystal structure of the films improved as a function of film thickness for Mn and Fe doped ZnO films with preferred orientation in (002) plane along *c*-axis perpendicular to substrate base plane.
- The Mn doped ZnO films have tensile (positive) stress, where as un-doped and Fe doped films show compressive (negative) stress.

- The films deposited in argon gas for different dopants have high values of residual stress (σ) in the range of – 4.525 – 2.184 GPa than films in oxygen gas.
- The films deposited on Si (100) show higher lattice parameters (*c*) than the films on quartz substrate.
- The crystallite (D) size is lower (2 – 21 nm) for films on Si (100) substrate. Whereas for films on quartz substrate it is in the range 15- 45 nm. This could be due to lattice mismatch and surface properties of substrate material.
- The residual stress (σ) of the films is compressive (negative) for all the as deposited films.

References

[1] K. Wasa, M. Kitabatake, and H. Adachi, *Thin Films Material Technology: Sputtering of Compound Materials*, William Andrew, USA, (2004).

[2] JCPDS powder diffraction File No. 36-1451.

[3] X. Zi-Qiang, D. Hong, L. Yan, C. Hang, Mater. Sci. Semicond. Process **9** (2006) 132.

[4] Y.G. Wang, S.P. Lau, H.W. Lee, S.F. Yu, B.K. Tay, X.H. Zang, K.Y. Tse, H.H. Hng,

J.

Appl. Phys. **94** (2003) 1597.

[5] Ebru Senadim, Tuzemen Sitkl Eker, Hamide Kavak, Ramazan Esen, Appled Surface Science **255** (2009) 6195-6199.

[6] H.C. Ong, A.X.E. Zhu, G.T. Du, Appl. Phys. Lett. **80** (2002) 941.

[7] C. Wang, P. Zhang, J. Yue, Y. Zhang, L. Zheng, Physica B **403** (2008) 2235.

[8] B.D. Cullity, Elements of X-ray Diffractions, Addison-Wesley, Reading, MA, 1978.

[9] C. Li, X.C. Li, P.X. Yan, E.M. Chong, Y. Liu, G.H. Yue, X.Y. Fan, Appl. Surf. Sci. **253**
(2007) 4000.

[10] L. Sagalowicz, G.R. Fox, J. Mater. Res. **14** (5) (1999) 1876.

[11] G. Sanon, R. Rup, A. Mansingh, Thin Solid Films **190** (1990) 287.

[12] Z.G. Zhang, F. Zhoua, X.Q. Weib, M. Liub, G. Sunb, C.S. Chenb, C.S. Xueb, H.Z. Zhuangb, B.Y. Manb *Physica E* **39** (2007) 253.

[13] F.K. Shan, B.C. Shin, S.W. Jang, Y.S. Yu, *J. Eur. Ceram. Soc*. **24** (2004) 1015.

[14] A.J.Chen, X M Wu, Z.D.Sha, L. J. Zhuge, Y.D.Meng, *J.Phys D: Appl.Phys* **39** (2006) 4762.

[15] X.M. Fan, J.S. Lian, Z.X. Guo, H.J. Lu, *Appl. Surf. Sci*. **239** (2005) 176.

[16] M. Sultan, R.Singh (2009) *J.Phys.D : Appl.Phys*. **42** (2009)115306.

[17] Fei Gao, Xiao Yan Liu, Li Yun Zhneg, Mei Xia LI, Yong Mei Bai, Juan Xie, *J.Cryt.Grow.* (In Press) (2013)

[18] M. Chakrabarti, S. Dechoudhury, D. Sanyal, T. Kundu Roy, D. Bhowmick, A Chakrabarti, *J.Appl.Phys.D: Appl.Phys* **41** (2008) 135006.

[19] R.W.G. Wyckoff, *Crystal Structures*, Vol.1, Interscience, New York (1960) P.19.

[20] E.M. Bachari, G.Baud, S.Ben Amor, M.Jacquet, *Thin.Solid.Films* **348** (1999) 165.

[21] E. Jacobshon, D. Shechtman, *Mater.Res.Soc.Symp.Proc*, **242** (1992) 779.

[22] S.B.Krupanidhi, M.Sayer, J.Appl.Phys, 56 (1984) 3308.

[23] L.J.Meng, M.P. dos Santos, *Thin. Solid. Films*, **250** (1994) 26.

[24] Li-Wei Wang, Zheng Zu, Fu-jun Zhang, Su-ling Zhao, Li-fang Lu, Inter. J. Min.Metll.Matr **17** (2010) 475.

[25] N. Fujimura, T. Nishihara, S. Goto, J. Xu, and T. Ito, *J. Cryst. Growth*, **130** (1993) 269.

[26] Patterson A L (1939) Phys.Rev **56** (1939) 978.

[27] O. Lupan, T. Pauporte, L. Chow, B. Viana, F. Pelle, L.K. Ono, B. Roldan Cuenya, H.

Heinrich, Appl. Surf. Sci. 256 (2010) 1895.

[28] L. Bentes, R. Ayouchi, C. Santos, R. Schwarz, P. Sanguino, O. Conde, M. Peres, T.

Monteiro, O. Teodoro Superlattices Microstruct. 42 (2007) 152.

[29] Wei Gao, Zhengwei Li, Ceram. Int. 30 (2004) 1155.

[30] J.C. Lodder, T. Wielinga, J. Worst, Thin Solid Films 101 (1983) 61.

[31] J. Han, P.Q. Mantas, A.M.R. Senos, J. Eur. Ceram. Soc. 20 (2000) 2753.

[32] V.A.L Roy, A.B.Dijurinic, H. Liu, X.X. Zhang, Y.H. Leung, M.H. Xie, J.Gao, H.F.Lui, C.Surya, *Appl. Phys.Lett.* **84** (2004) 756.

[33] Redfield D, Phys. Rev. 130 (1963) 914.

[34] Shinho Cho Current Applied Physics 10 (2010) S443.

Chapter 4

Optical Properties

This chapter presents the detailed optical properties of un-doped and 3d TM ion doped ZnO thin films deposited by rf-magnettron sputtering. The optical constans like refrative index (n), optical band gap (Eg) , Urbach energy and extinction coefficient (k) etc are estimated from the experimental optical data on the as deposited thin films. The chapter is divided into three sections: effect of working gas pressure, film thickness and substrate material on the optical properties of thin films.

The optical properties of thin films are of significant importance, in both basic and applied research. The wide use of thin films in optical devices requires a good knowledge of such properties. The optical behavior of a thin film is a function of its interaction with electromagnetic radiation. Possible interactive phenomena are reflection, transmission and absorption of the incident light onto the surface of the thin film. When light proceeds from one medium to another medium (e.g. from air into a thin film), some of the light radiation will be reflected at the interface between the media, some may be transmitted through the medium, and some will absorbed within if the material of thin films is absorbing (metal or semi metal) [1]. The principle of conservation of energy determines that for any light radiation-matter interaction, the intensity I_0 of the incident beam on the surface of the thin film at a particular wavelength must equal the sum of intensities of he reflected, transmitted, and absorbed beams, denoted I_R, I_T, and I_A, respectively, i.e.,

$$I_0 = I_R + I_T + I_A \qquad (4.1)$$

An alternate form is

$$R + T + A = 1 \qquad (4.2)$$

Where R, T, and A represent the reflectance (I_R/I_0), transmittance (I_T/I_0), and absorbance (I_A/I_0), respectively. The sum of these macroscopic quantities which are usually known as

the optical properties of the thin films must equal unity since the incident radiant flux at one wavelength is distributed totally between reflected, transmitted, and absorbed intensity.

For a complete understanding of the optical behavior of thin film, a good knowledge of the structure of thin film is also necessary. The optical properties of thin films depend on the deposition methods, microstructure, the impurity concentration, the annealing temperature and on the surface morphology of the films. The propagation of light through a medium is quantified by the complex refractive index (n^*) where $n^* = n-ik$. The real part n which determines the velocity of light in the medium is called the refractive index and the imaginary part, k, excitation coefficient is related to the absorption coefficient by the equation: $k= \alpha\lambda/ 4\pi$.

4.1 Optical parameters

The optical constants of thin films could be measured experimentally by several methods including reflection or/and transmittance, spectrophotometry, interferometry, transmittance data (envelope), and ellipsometry. There are a number of methods that can be used for the routine determination of the wavelength dependent complex refractive index of thin films, using simple spectrophotometric equipment [3].

4.1.1 Reflection-Transmission (RT) Method

In the reflection –transmission (RT) method, the film is illuminated by unpolarized radiation, and the intensities of reflected and transmitted beams are measured as a function of wavelength. The photometric measurements of reflectance *R* and transmittance *T* at normal incidence are recognized as the most suited for determining the optical constants *n* and *k* of a thin films materials over a wide wavelength range. The result from this method is sensitive to film surface properties. For normal incidence, the reflection coefficient, *r*, is obtained as [2]

$$\alpha h\nu = A\left(h\nu - E_g\right)^q \; r = \frac{1-n^*}{1+n^*} = \frac{1-n+ik}{1+n-ik} \qquad (4.3)$$

The reflectance R is then defined by

$$R = |r| = \left|\frac{1-n+ik}{1+n-ik}\right| = \frac{(1-n)^2 + k^2}{(1+n)^2 + k^2} \qquad (4.4)$$

$$T = (1\text{-}R)^2 \exp(-\alpha d) \qquad (4.5)$$

These two relations offer a convenient method for determining the optical constants from the *R* and *T* data on the same film.

4.1.2 Envelope method

The envelope method was proposed by Manifacier et al [4] and developed by Swanepoel [5] for transmission measurements to evaluate films thickness and optical constants such as refractive index n, excitation coefficient k, and absorption coefficient α from transmission spectra. This method is based on the use of the extremes of the interference fringes of transmission spectrum for calculation the refractive index and film thickness in both weak absorption region and transparent region.

The envelopes are constructed by curve fitting to connect the maxima(T_M) and minima (Tm). Consider the optical system consist of thin film deposited onto thick, finite transparent quartz substrates. The homogeneous film thickness d and complex refractive index n= n-ik, where, n is the refractive index and k the excitation coefficient, which can be expressed in terms of the absorption coefficient a by the equation: $k = \alpha\lambda/4\pi$. The thickness of the substrate is several order magnitude larger than d and its index refraction is n_s. The system is surrounded by air with refractive index $n_0 = 1$. Taking all the multiple reflections at the three interfaces into account (air (n_0)/film (n_f)/thick transparent substrate (n_s)/air (n_0)), it can be shown that in the case of $k^2 << n^2$ the expression for the transmittance T for normal incidence is given by [5]

$$T = \frac{Ax}{B - CxCos\theta + Dx^2} \qquad (4.6)$$

Where $A = 16n^2n_s$, $B = (n+1)^3(n+n_s^2)$, $C = 2(n^2-1)(n^2 - n_s^2)$,

$D = (n-1)^3(n-n_s^2)$, $\varphi = 4\pi nd/\lambda$ and $x = \exp(-\alpha d)$

The extreme of the interference fringes can be obtained from equation (4.6) by setting the interference condition cosφ +1 for maxima T_M and cos φ = -1 for minima T_m and can be written as

$$\left\{\begin{array}{l} T_M = \dfrac{Ax}{B - Cx + Dx^2} \\ T_m = \dfrac{Ax}{B - Cx + Dx^2} \end{array}\right\} \qquad (4.7)$$

The interference maxima T_M and T_m can be considered to be a continuous function of the λ and experimentally determined by the envelopes as shown in figure 4.7

From the two new formulae (4.7) the optical constants can be derived (Next section)

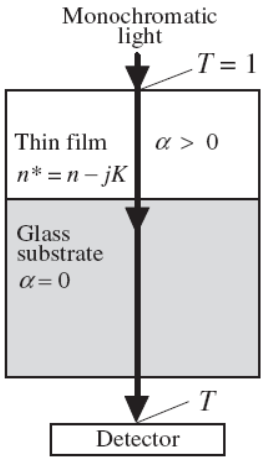

Figure 4.1: Schematic sketch of the typical behavior of light passing through a thin film on a substrate with normal incident [8].

(a) Film thickness

The thickness (d) of the films can be determined from the interference fringes of the transmission data by calculation the refractive index of the thin film corresponding to two adjacent maxima (or minima) given as $n(\lambda_1)$at λ_1 and $n(\lambda_2)$ at λ_2 [6,7]

$$d = \frac{\lambda_1 \lambda_2}{2(n(\lambda_1)\lambda_2 - n(\lambda_2)\lambda_1)} \qquad (4.8)$$

Where $n(\lambda_1)$ and $n(\lambda_2)$ are the refractive indexes in two consecutive maxima (or minima) and λ_1 and λ_2 the corresponding wavelengths. Thickness measurements made by a

surface stylus profilometer can be carried out to cross check the results obtained by the method employing only transmission spectra T (λ).

(b) Refractive index

According to Swanpeol's method [5], the refractive index, n, values calculated from the transmission spectra of the film. A typical transmission spectrum at normal incidence has two spectral regions: the region of weak and medium absorption region, a first approximation of the real part of the refractive index n of the films can be calculated by the following expression:

$$n = \left[N + \sqrt{N^2 - n_s^2} \right]^{1/2} \qquad (4.9)$$

Where

$$N = 2n_s \left[\frac{T_M - T_m}{T_M T_m} \right] + \frac{n_s^2 + 1}{2}$$

Where T_M and T_m are the transmission maximum and the corresponding minimum at certain wavelength, λ, and n_s is the refractive index of the substrate used (for glass n_s = 1.52, for quartz n_s = 1.46)

(c) Absorption and excitation coefficients

The absorption coefficient (α) can be evaluated from the transmission spectra using the relation [11] as follows

$$x = \exp(-\alpha d), \ \alpha = -\frac{1}{d} \ln[x] \qquad (4.10)$$

Where d is the film thickness and x is absorbance

in the region of weak and medium absorption, parameter x is given by:

$$x = \frac{E_M - \left[E_M^2 - \left(n^2 - 1\right)^3 \left(n^2 - n_s^4\right) \right]^{1/2}}{\left(n-1\right)^3 \left(n - n_s^2\right)} \qquad (4.11)$$

where

$$E_M = \frac{8n^2 n}{T_M} + \left(n^2 - 1\right)\left(n - n_s^2\right)$$

In the region of strong absorption the interference fringes disappear and the absorption coefficient (α) can be calculated from the relation:

$$\alpha = -\frac{1}{d}\ln\left(\frac{(n+1)^2\left(n+n_s^2\right)}{16n^2 n_s}T\right)$$

$$\alpha = -\frac{1}{t}\ln(T) \qquad (4.12)$$

Where T is transmittance of the films in the strong absorption region, *t* is thickness of the film.

The extinction coefficient, k, is calculated using the relation

$$k = \frac{\alpha\lambda}{4\pi} \qquad (4.13)$$

The low value of the extinction coefficient (order of 10^{-2}) is a qualitative indication of good surface smoothness of the films.

4.1.3 Optical band gap

When an incoming photon with energy, E = hυ is absorbed, it can interact with one of four types of carriers: inner shell electrons, valance electrons, free carriers, or electrons trapped by localized impurities and other defect [2]. The fundamental absorption process can occurs when a valance electron is promoted to higher energy state (e.g. conduction band). The optical band *Eg* for the films can be estimated from absorption coefficient α using the Tauc relation [12].

$$\alpha h\nu = A\left(h\nu - E_g\right)^q \qquad (4.13)$$

Where A is a constant depends on the transition probability, (hυ) is energy of incident photon and (q) is an index that characterizes the optical absorption process and is theoretically equal to 2, 1/2 and 3 or 3/2 for allowed indirect, direct and forbidden indirect or forbidden direct electronic transition responsible for the reflection respectively [13].

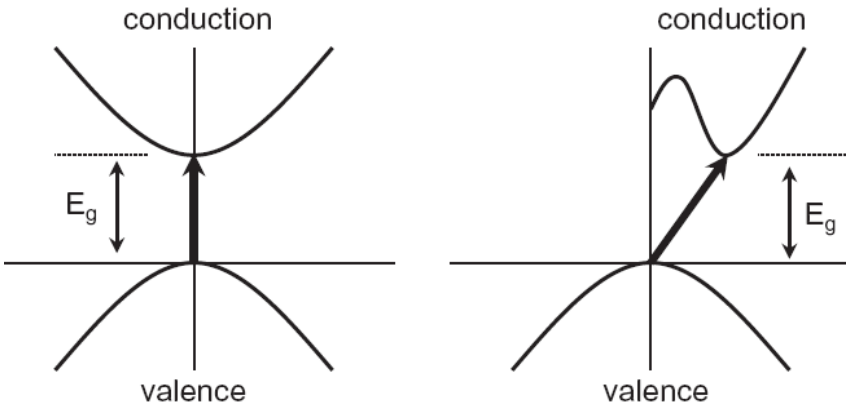

Figure 4.2: Direct (left) and indirect (right) band gap transition [14]

A direct transition occurs when the valance band maximum and the conduction band minimum are at the zone center where k = 0 in the brillioun zone, and an indirect one occurs when the conduction band minimum does not occur at k = 0, but rather at some other value of k which is usually at the zone edge or close to it (figure 4.2) [14]. For a direct transition, a photon with energy hυ can be absorbed promoting a valance band electron to the conduction band, creating electron-hole pair. This process involves a two body collision (electron and photon) accompanied by strong light absorption, whereas for an indirect transition between two bands with different wave vectors, both kinetic energy and potential energy of an electron must be changed , which requires the assistance of photon. Hence, this process involves a three-body collision (electron, photon and phonon) and relatively weak light absorption [14, 15]

The band gap energy, E_g of the thin films can be obtained by extrapolation the linear portion of the plot of $(\alpha h\alpha)^2$ and $(\alpha h\upsilon)^{1/2}$ against hυ to $(\alpha h\upsilon)^2 = 0$ for direct and indirect band gap respectively [16].

4.1.4 Urbach Energy tails and its effect on band gap:

Urbach energy (tail) is a energy between band tails below the band edges and this tail (Urbach) can originate from disorder of perfect crystal, e.g. from defects or doping and the fluctuation of electronic energy bands due to lattice vibrations [17]. Modification of band structure which may be due to introduction of defects in a material can be established by determining the material Urbach energy before and after the defects are

introduced. Urbach energy gives a measure of structural disorder in a material [18]. The formula for determination of Urbach energy is as follows [19]:

$$(\alpha h\nu) = \alpha_0 \exp(\frac{h\nu}{E_U}) \qquad (4.17)$$

where α absorption coefficient, E_U Urbach energy

The Urbach energy (E_U) values change inversely with optical band gap [17, 20]. Some defects were formed during the growth of the film and these defects produce localized states in the films. Thus, increase in width of the localized states leads to decrease in optical band gap [21].

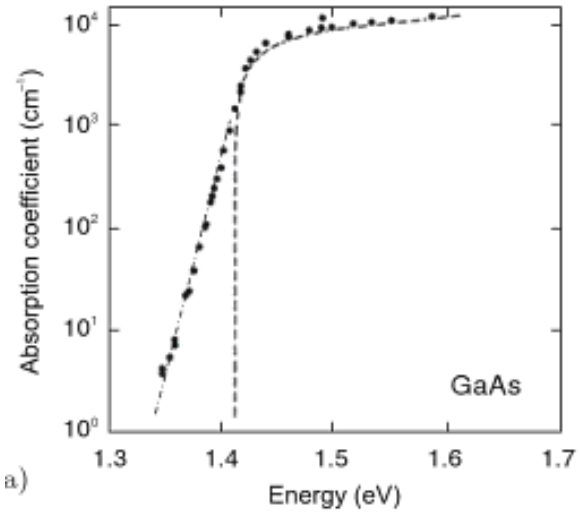

Figure 10: The exponential below the band gap called Urbach tail (dash-dotted line) [21]

4.1.5 Band gap from reflection spectra

The reflectivity of an interface is defined as the ratio of the reflected energy to the incident energy. For the films of high thickness the intensity of reflected beam [22]

$$\ln[(R_{\max} - R_{\min}) / R - R_{\min}], \quad I = I_1 + I_2 \exp(-2\alpha t) \qquad (4.18)$$

Where I_1 is reflection from upper surface of the film and I_2 exp (-2αt) is reflection from inner surface. So

$$I_1 = I_{\min} \tag{4.19}$$

From eqs (4.18) and (4.19) we can write

$$I_1 = I_{\min} + I_2 \exp(-2\alpha t)$$

$$I_1 - I_{\min} = I_2 \exp(-2\alpha t)$$

Taking logarithm

$$\ln(I_1 - I_{\min}) = \ln(I_2) - 2\alpha t \tag{4.20}$$

In order to find out ln (I_2) consider the region where α = 0, there $I = I_{max}$ or

$$\ln(I_{\max} - I_{\min}) = \ln(I_2) \tag{4.21}$$

Using eqs (4.20) & (4.21)

$$\ln(I - I_{\min}) = \ln(I_{\max} - I_{\min}) - 2\alpha t$$

$$2\alpha t = \left(\frac{(I_{\max} - I_{\min})}{(I - I_{\min})}\right)$$

$$2\alpha t = \left(\frac{(R_{\max} - R_{\min})}{(R - R_{\min})}\right) \tag{4.22}$$

Where R is reflectance is given by $R=I/I_0$

For a direct band gap material, the absorption coefficient is give in eqn (4.16)

I_{min} is estimated by the fall in reflection spectra of the film. From eqn (4.22) and (4.16) it is clear that there is proportionality relation between $\ln[(R_{\max} - R_{\min})/R - R_{\min}]$ and α where R_{max} and R_{min} are the maximum and minimum reflectance in reflectance spectra and R is the reflectance for any intermediate energy of photon recorded by V-675 Uv-vis Spectrophotometer. As in the case of absorption spectra, we plot a graph between $(\alpha h\nu)^2$ (as ordinate) and hν (as abscissa), a straight line to $(\alpha h\nu)^2 = 0$ axis gives the values of

direct band gap. Similarly here we plot a graph between hν (as abscissa) nad the square of $\ln[(R_{max} - R_{min}) / R - R_{min}]$. As the ordinate we can get the band gap of semiconductor.

(i) Thin films of un-doped ZnO

The RT transmission spectra of un-doped ZnO thin films at various film ticknesses in argon gas are shown figure 4.42. The films show high transmission in the visible range about 87-89 (%). These results are in spport with ZnO film at various film thickness [32]. With increase in film thickness, the transmittance of the film decreased due to thickness effect. From the plots, we can see the interfernce frings are increasing with increase in film thickness the average film thickness varies from 360- 1066 nm.

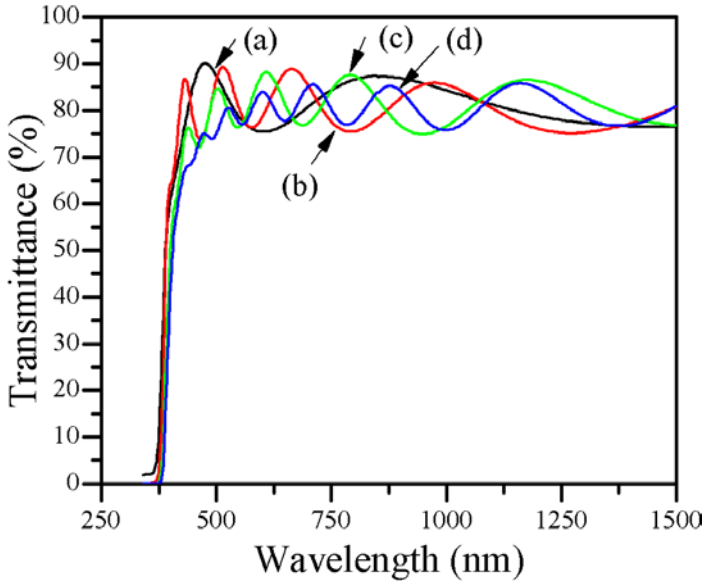

Fig 4.42: RT transmission spectra of Un-doped ZnO films at various film thicknesses of (a) 360, (b) 707, (c) 910 and (d) 1066 nm of argon gas environment.

Fig 4.43 show the $(\alpha h\nu)^2$ vs hν plot of un-doped ZnO films at different film thicknesses in argon gas environment. To determine the optical band gap *Eg* we used Tuac et.al.'s relation [12]. The optical energy band gap of the films have abrupt values with film thickness unlike the results obtained on PFCVAD deposited ZnO films [32]. The energy gap values are varied from 3.21 – 3.26 eV as a function of film thickness.

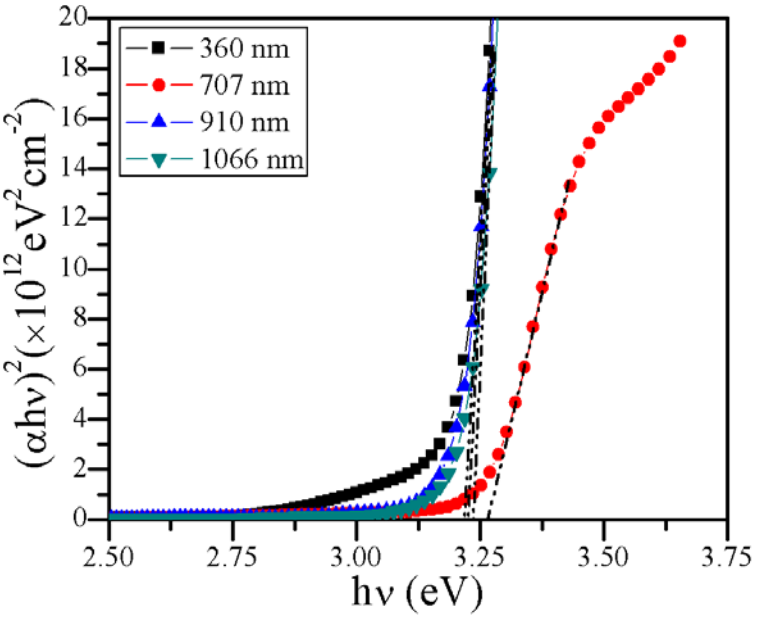

Fig 4.43: Estimated direct band gap of Un-doped ZnO films at various film thicknesses of (a) 360, (b) 707, (c) 910 and (d) 1066 nm of argon gas environment.

Table 4.9: Optical parameters of ZnO films at various film thicknesses.

Power (Watt)	Thickness (nm)	T (%)	Band gap (eV)	UE (eV)	RI (n)	β (eV)
40	360	89	3.21	0.159	1.494	0.091
60	707	89	3.26	0.144	1.495	0.095
80	910	87	3.22	0.097	1.494	0.142
100	1066	88	3.23	0.094	1.493	0.145

Fig 4.44 shows the ln(α) vs hν plot of un-doped ZnO films at various film thickness of argon gas environment. The Urbach energy is decreasing with film thickness. The Urbach energy and stiffness factor (β) values at various working gas pressure are listed in Table 4.9.

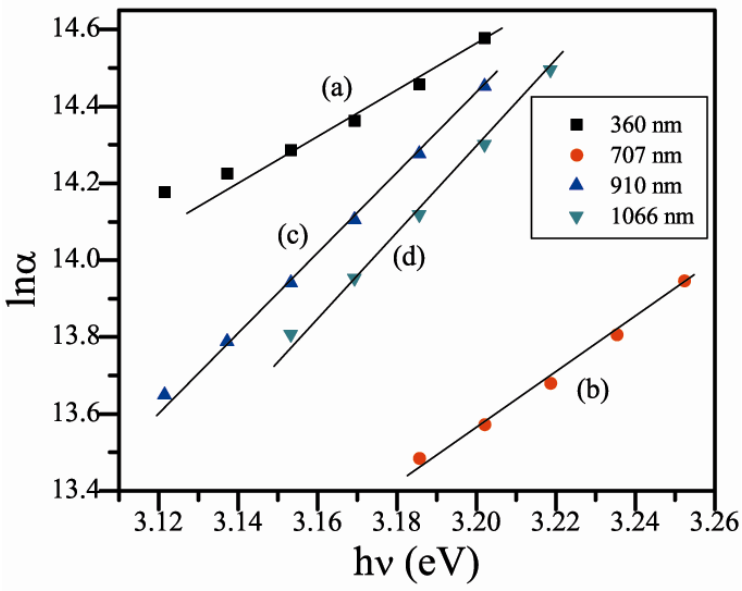

Fig 4.44: ln (α) vs hν plot of Un-doped ZnO films at various film thicknesses in argon gas environment.

Fig 4.45 show the refractive index (n) as a function of wavelength (nm) of ZnO films at various gas pressures of argon environment. There is no change refractive index with wavelength, the values with working gas pressure ranges from 1.493 – 1.495.

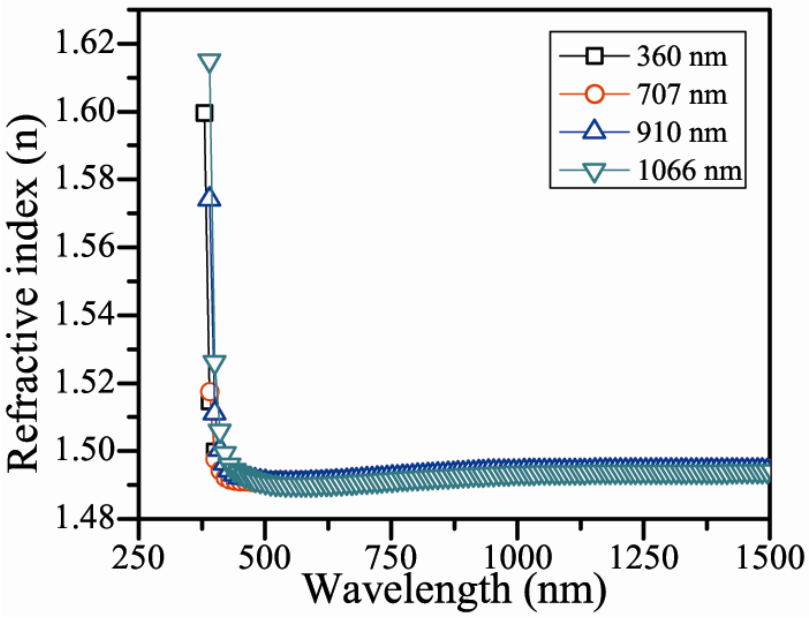

Fig 4.45: Refractive index (n) vs Wavelength (nm) plot of Un-doped ZnO films at various film thicknesses in argon gas environment.

Figure 4.46 shows the dependence of the extinction coefficient (*k*) on wavelength, λ, for the films deposited with different film thicknesses in argon environment. The extinction coefficient sligthly effected by the change in film thickness. From the plot, it is clear that except the films deposited at low thickness about 360 nm had a lower extinction coefficient (i.e more transmission) than those deposited at high film thicknesses in argon environment. This behavior probabily due to lower porasity of the films depositede in oxygen gas atmosphere. This factor plays a singnificant role in optical absoption process. The variation of extinction coefficient can be related to the variation of transmission. As the film thickness increases, the transmittance decreases and results in decrease in the extinction coefficient.

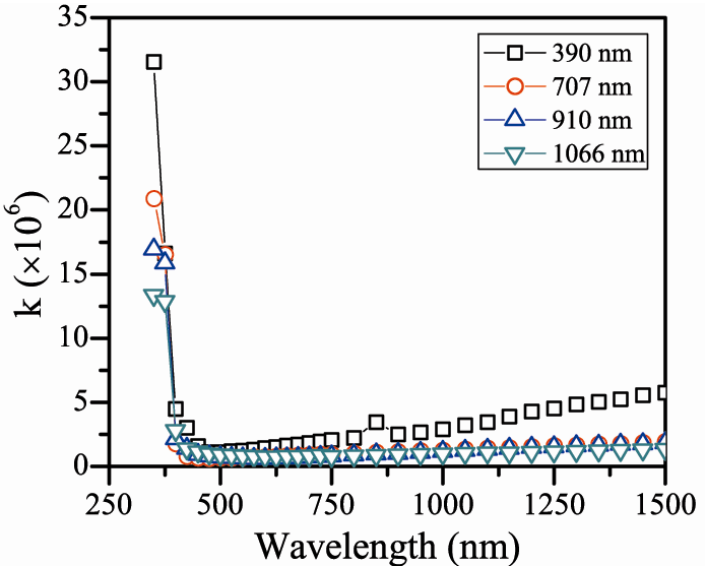

Fig 4.46: Extinction coefficient (k) vs wavelength (λ) of Un-doped ZnO films at various film thicknesses of argon gas environment.

4.2 Effect of working gas Pressure

The un-doped and Mn, Fe and Mn-Fe co-doped ZnO thin films were deposited on quartz substrates by rf-magnetron sputtering with working gas pressure in the range 5 -18 mTorr. The sputter parameters were kept constant i.e 100W power, 60 min time sputter duration, substrate-target distance 8 cm and the base pressure 1×10^{-6} Torr.

4.2.1 Argon gas environment

The room temperature transmission spectra for various films are shown in this section. The argon gas has an advantage over other inert gases like oxygen and nitrogen, as it gives the high sputter yield and homogenious films onto substrate material.

4.2.1.1 Un-doped ZnO

The RT transmission spectra of un-doped ZnO thin films is shown in figure 4.1. The films are highly transperent about70-85 (%) in the visible range of electromagnnetic spectrum. The films show more number of fringes in the spectra indicating higher thickness of the films and this gives rise to multiple constructive interference between air –film-substrate-film. The film tickness varies between 731- 1037 nm.

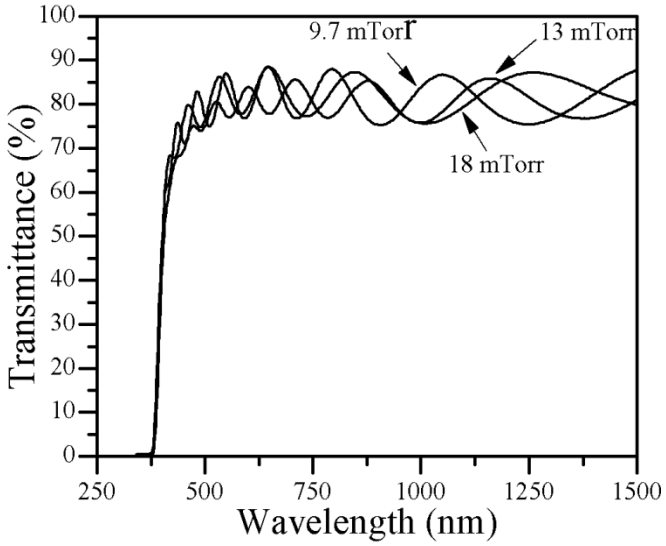

Fig 4.1: RT transmission spectra of un-doped ZnO films at various partial pressures of (a) 9.7, (b) 13 and (c) 18 mTorr of argon gas environment.

Fig 4.2 shows the estimated direct band gap of un-doped ZnO films at different partial pressures of argon gas environment. The direct band gap (*Eg*) was estimated by assuming a direct transition between valance and conduction bands by Tauc [12] relation. The *Eg* is determined by extrapolating straight line portion of spectrum to $\alpha h\nu = 0$. The films deposited for low working gas pressure show high band gap values than other gas pressure of argon.

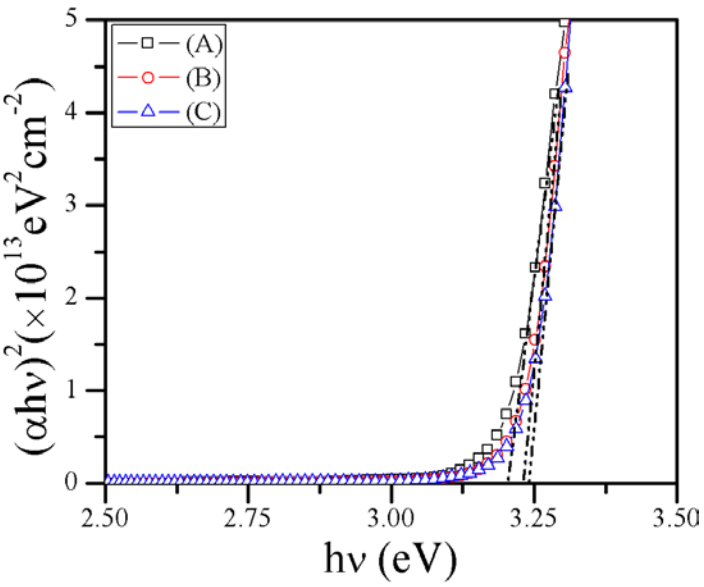

Fig 4.2**:** Estimated direct band gap of un-doped ZnO films at various partial pressures (a) 9.7, (b) 13 and (c) 18 mTorr of argon environment.

Table 4.1: Optical parameters of Un-doped ZnO films at various working gas pressure.

Press (mTorr)	Thickness (nm)	T (%)	Band gap (eV)(±0.01)	UE (eV)	RI (n)	β (eV)
9.7	738	89	3.20	0.255	1.495	0.054
13	1067	85	3.22	0.306	1.494	0.044
18	882	88	3.24	0.348	1.493	0.039

Fig 4.3 show the ln(α) vs hν plot of un-doped ZnO films at various gas pressures of argon environment. The Urbach energy is increasing with increase in argon pressure indicating presence of impurity bands in between valance and conduction with increasing in gas pressure. The increase in Urbach energy will give reduction in band gap. The optical parameters extracted from transmission spectra are listed in Table 4.1.

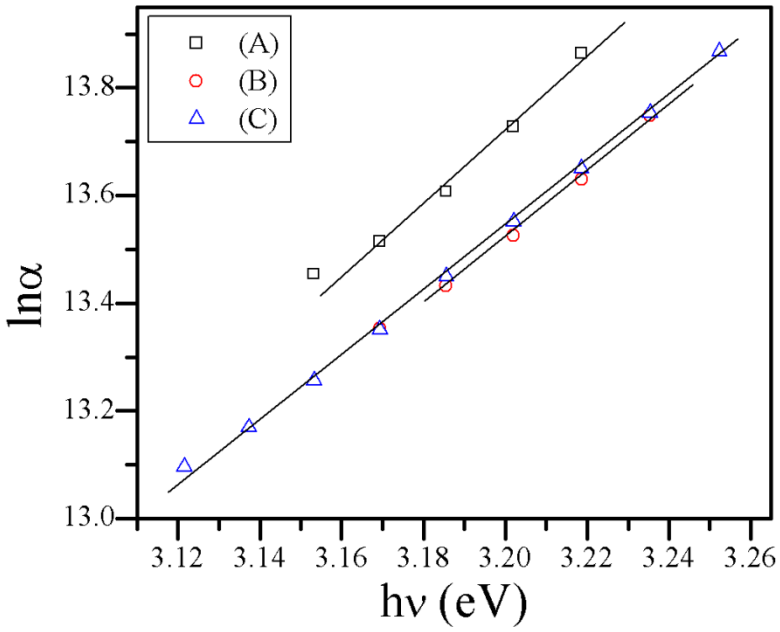

Fig 4.3**:** lnα vs hν plot of un-doped ZnO films at various partial pressures (a) 9.7, (b) 13 and (c) 18 mTorr of argon environment.

Fig 4.4 show the refractive index (n) as a function of wavelength (nm) for un-doped ZnO films at various gas pressures of argon environment. The refractive index has no change with wavelength it is Linear A function of wavelength (nm) is good agreement previously reported data of ZnO films [23]. The results obtained by Nanda Shakti et.al [24] showed the refractive index n unaffected by heat treatment on ZnO films. The index of refraction at different working gas pressure are in the ranges from 1.495 – 1.493.

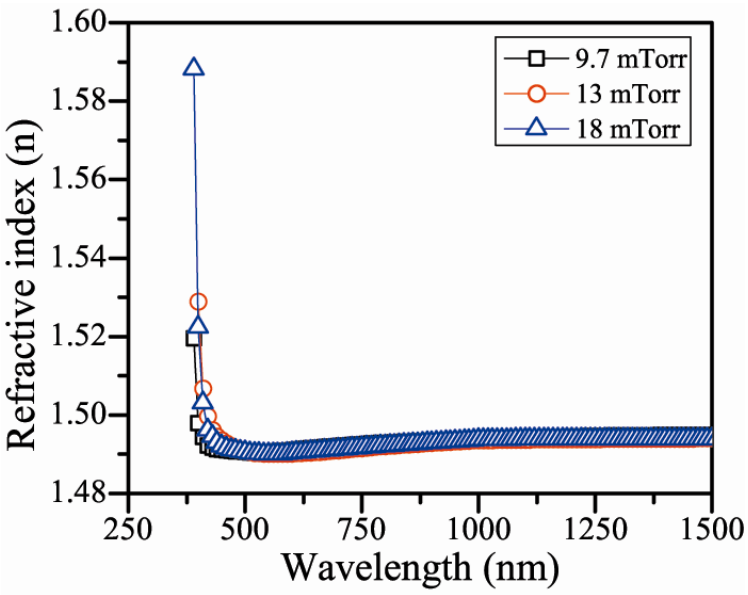

Fig 4.4**:** Refractive index vs wavelength (nm) of un-doped ZnO films at various partial pressures in argon environment.

Figure 4.5 shows the dependence of the extinction coefficient (*k*) on wavelength, λ, for the films. The absorption coefficeint (α) of ZnO films was detemind from transmission measuremnets. Since envelope method is not valid in the strong absorption region, the calculation of absorption coefficeint of the films in this region was calculated using the relation (4.14) [23]. There is no significant change in extinction coefficient with argon working gas pressure. From the plot, it is clear that irrespective of working gas pressure all the films had a lower extinction coefficient (i.e more transmission) could be due to porosity in the films. The extinction coefficient play a singnificant role in optical absoption process. The variation of extinction coefficient can be related to the variation of transmission.

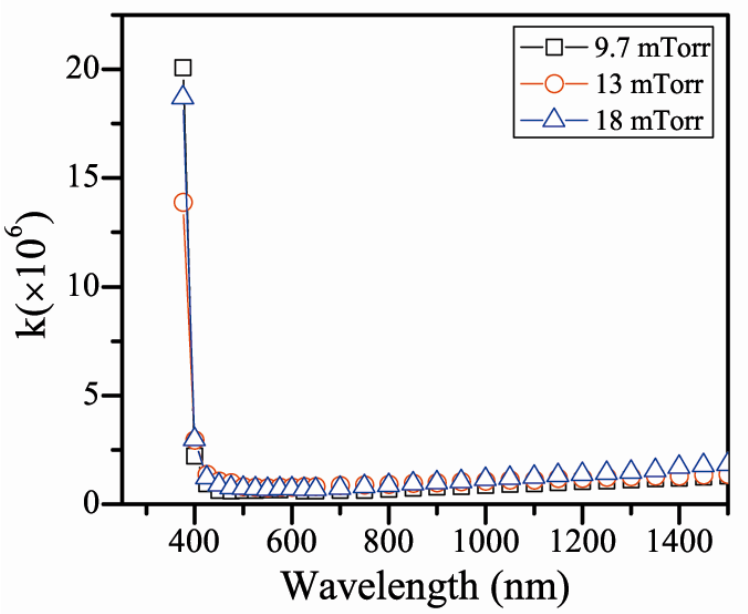

Fig 4.5**:** Extinction coefficient (k) vs wavelength (nm) plot of un-doped ZnO films at various partial pressures in argon gas environment

4.2.1.2 $Zn_{0.95}Mn_{0.05}O$

The RT transmission spectra of Mn5% doped ZnO thin films at various working gas pressures in argon gas are shown figure 4.6. The films show high transmission in the visible range about 90-92 (%),which is slightly above from sol-gel prepared films (80%) [25]. The films thickness for various working pressures ranges from 1003- 807 nm.

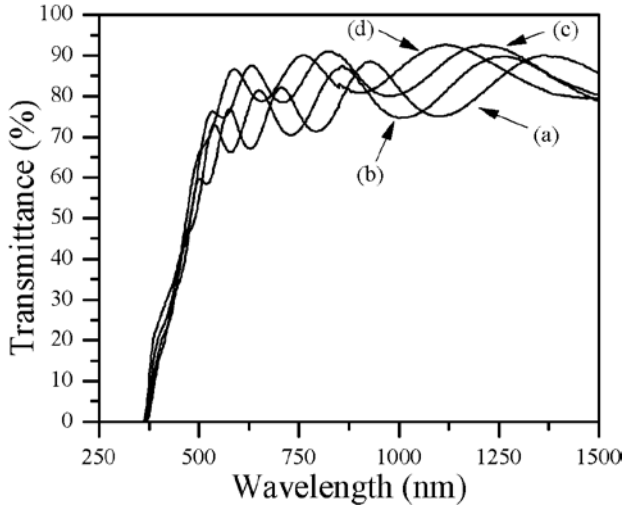

Fig 4.6: RT transmission spectra of $Zn_{0.95}Mn_{0.05}O$ films at various partial pressures (a) 5, (b) 8, (c) 12 and (d) 15 mTorr of argon environment.

The $(\alpha h\nu)^2$ vs hν plot of Mn5% doped ZnO films at different working gas pressure are shown in Fig.4.7. The optical energy gap show red shift with working gas pressure, whereas M.Nirmala et.al [26] reported blue shift with increase in Mn content. The estimated band gap of as deposited films calculated show increase with argon working gas pressure from 3.32 – 3.37 eV.

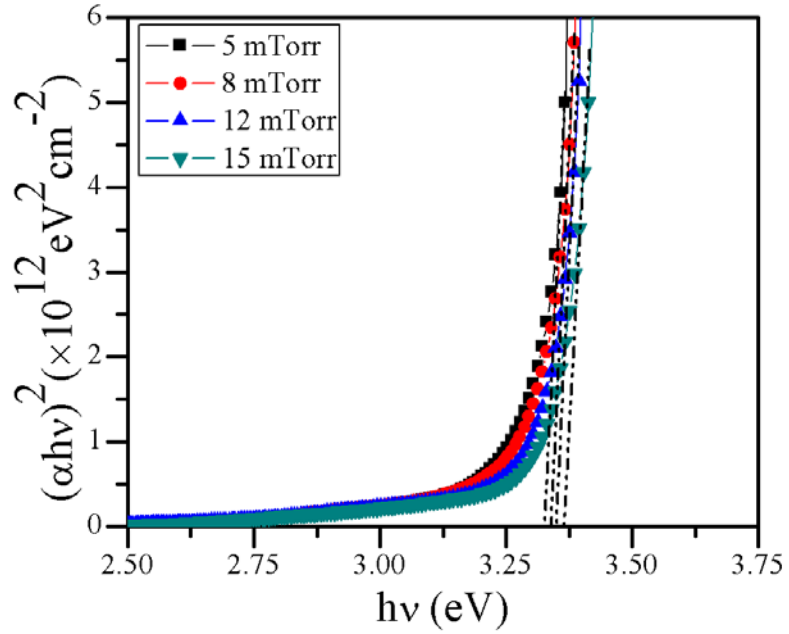

Fig 4.7: Estimated direct band gap of $Zn_{0.95}Mn_{0.05}O$ films at various partial pressures of argon gas environment.

Table 4.2: Optical parameters of $Zn_{0.95}Mn_{0.05}O$ films at various working gas pressure.

Press (mTorr)	Thickness (nm)	T (%)	Band gap (eV)	UE (eV)	RI (n)	β (eV)
5	1003	90	3.32	0.188	1.495	0.073
8	924	89	3.34	0.183	1.493	0.075
12	895	92	3.35	0.145	1.492	0.095
15	807	92	3.37	0.136	1.492	0.101

Fig 4.8 show the ln(α) vs hν plot of Mn5% doped ZnO films at various gas pressures of argon environment. The Urbach energy is decreasing with increase in argon pressure and band gap show increase with working gas pressure, The increase in band gap may be attributed that reduction in Urbach energy. The Urbach energy and stiffness factor of the films arre listed in Table 4.2.

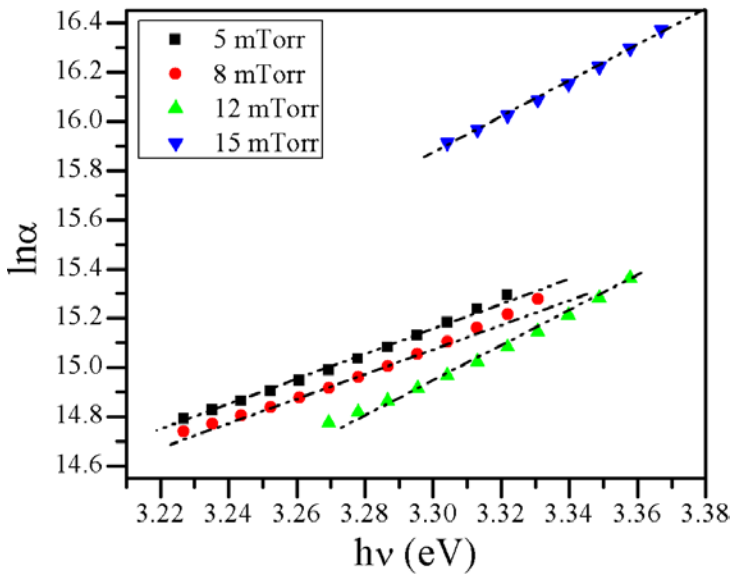

Fig 4.8: ln (α) vs hν of $Zn_{0.95}Mn_{0.05}O$ films at various partial pressures of argon gas environment.

Fig 4.9 show the refractive index (n) as a function of wavelength (nm) of $Zn_{0.95}Mn_{0.05}O$ films at various gas pressures of argon environment. There is no change refractive index with wavelength, the values with working gas pressure ranges from 1.495 – 1.492.

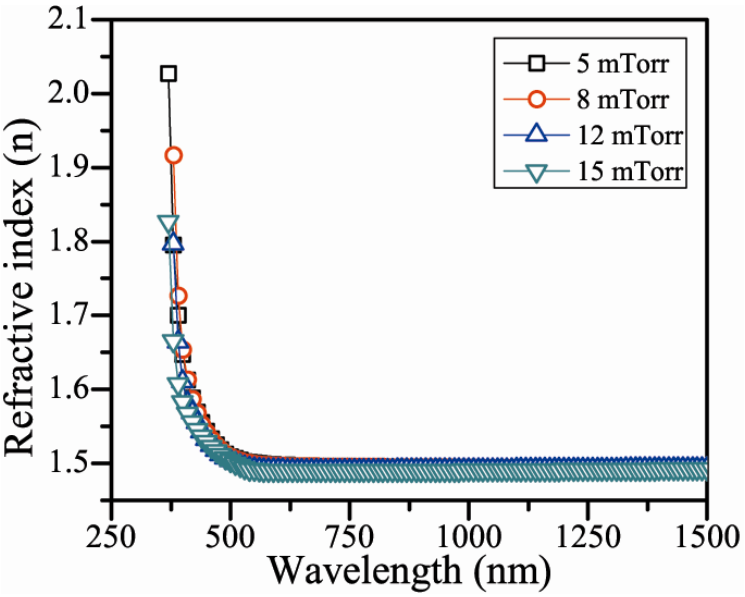

Fig 4.9: Refractive index (n) vs Wavelength (nm) plot of $Zn_{0.95}Mn_{0.05}O$ films at various partial pressures of argon gas environment.

Figure 4.10 shows the dependence of the extinction coefficient (*k*) on wavelength, λ, for the films. There is no significant change in extinction coefficient with argon working gas pressure. From the plot, it is clear that irrespective of working gas pressure all the films had a lower extinction coefficient (i.e more transmission). The extinction coefficient play a singnificant role in optical absoption process. The variation of extinction coefficient can be related to the variation of transmission.

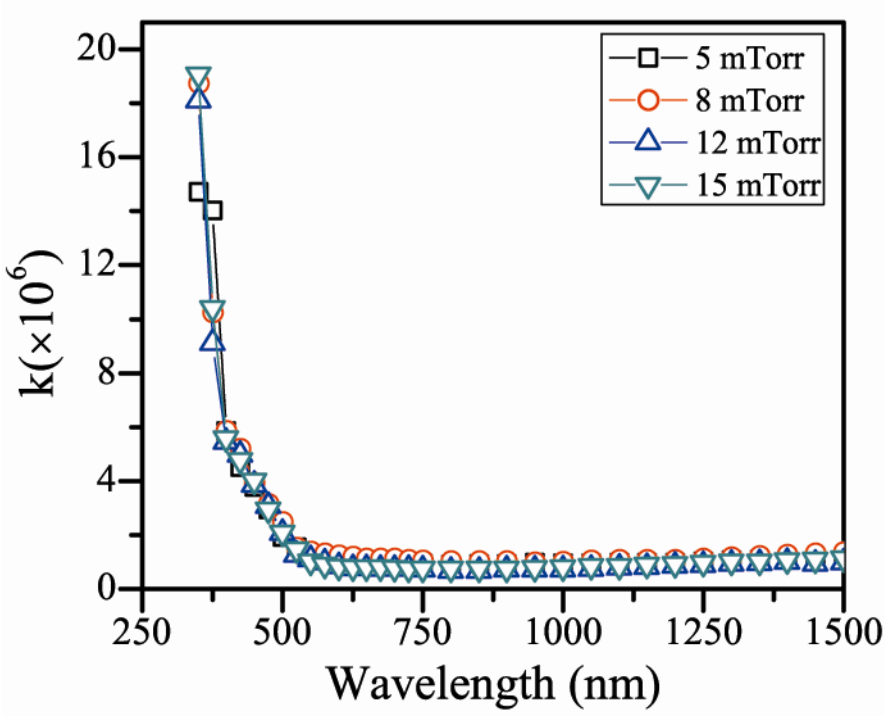

Fig 4.10: Extinction coefficient (k) vs wavelength (nm) of $Zn_{0.95}Mn_{0.05}O$ films at various partial pressures of argon gas environment.

4.2.1.3 $Zn_{0.95}Fe_{0.05}O$

The RT transmission spectra of Fe5% doped ZnO thin films at various working gas pressures in argon gas are shown figure 4.11. The films show high transmission in the visible range about 89-82 (%) is in accordance with reported results of Fe-doped ZnO films [27] is about 80 % in the visible region with argon gas pressure. The film thickness show decrease could be due to nature of dopant present in the film and it vary from 837-705 nm.

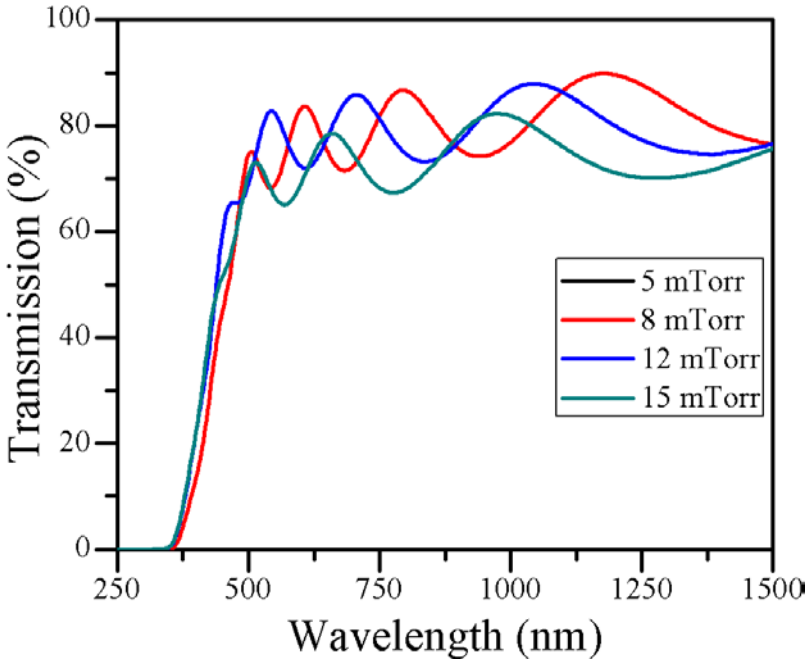

Fig 4.11: RT transmission of $Zn_{0.95}Fe_{0.05}O$ films at various partial pressures of argon gas environment.

The $(\alpha h\nu)^2$ vs $h\nu$ plot of Fe5% doped ZnO films at different working gas pressure are shown in Fig.4.10. The band gap of as deposited films calculated from Tauc[12] relation of transmission spectra show increase with argon working gas pressure from 3.36 – 3.39 eV. Unlike Mn5% doped ZnO films the band gap show high may be due to presence of different ionic radii of $Fe2^+$ or Fe^{3+} in ZnO matrix.

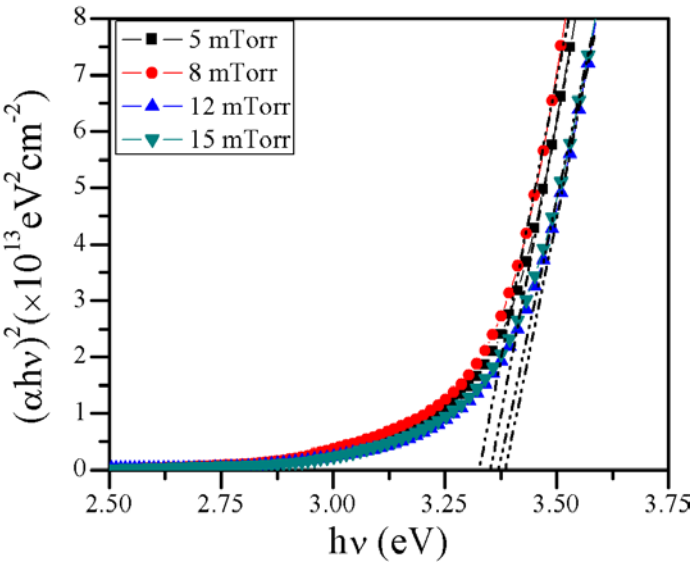

Fig 4.12: Estimated direct band gap of $Zn_{0.95}Fe_{0.05}O$ films at various partial pressures of argon gas environment.

Table 4.3: Optical parameters of $Zn_{0.95}Fe_{0.05}O$ films at various working gas pressure.

Press (mTorr)	Thickness (nm)	T (%)	Band gap (eV)	UE (eV)	RI (n)	β (eV)
5	837	89	3.36	0.466	1.494	0.030
8	785	89	3.33	0.482	1.494	0.028
12	746	87	3.39	0.371	1.495	0.037
15	705	82	3.39	0.037	1.497	0.037

Fig 4.13 show the ln(α) vs hν plot of Fe5% doped ZnO films at various gas pressures of argon environment. The Urbach energy is decreasing with increase in argon pressure and band gap show increase with working gas pressure, The increase in band gap may be attributed that reduction in Urbach energy. The Urbach energy and stiffness factor of the films arre listed in Table 4.3.

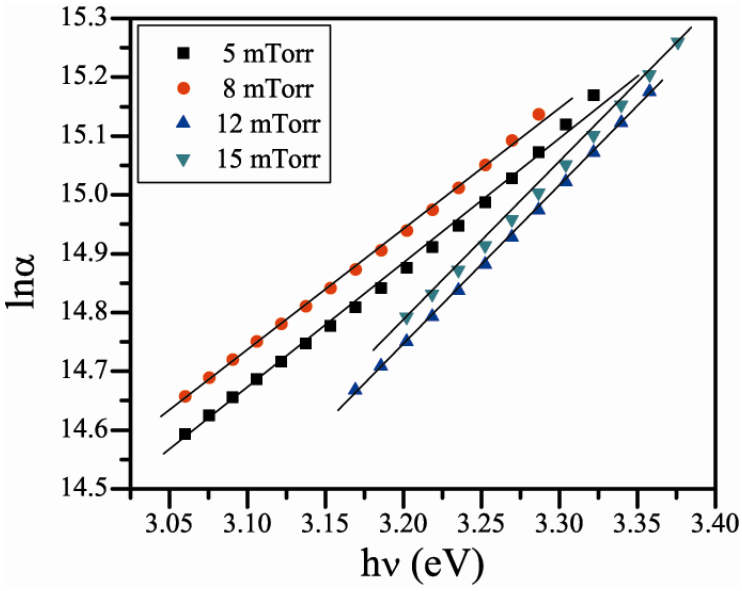

Fig 4.13: Extinction coefficient (k) vs wavelength (nm) of $Zn_{0.95}Fe_{0.05}O$ films at various partial pressures of argon gas environment.

Fig 4.14 show the refractive index (n) as a function of wavelength (nm) of $Zn_{0.95}Fe_{0.05}O$ films at various gas pressures of argon environment. There is no change refractive index with wavelength, the values with working gas pressure ranges from 1.494 – 1.497.

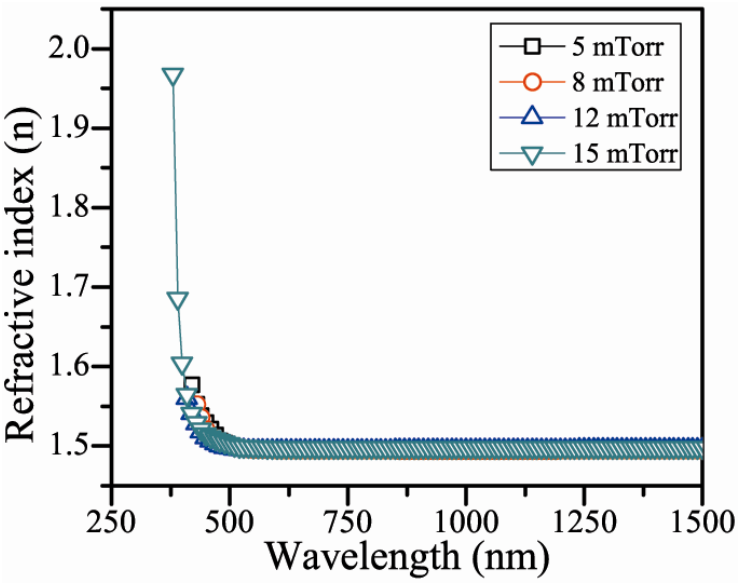

Fig 4.14: Refractive index (n) vs Wavelength (nm) plot of $Zn_{0.95}Fe_{0.05}O$ films at various partial pressures of argon gas environment.

Figure 4.15 shows the dependence of the extinction coefficient (*k*) on wavelength, λ, for the films. There is a slight change in extinction coefficient for films at 15 mTorr oof argon pressure. From the plot, it is clear that except films at 15 mTorr argon gas prressure, films had a lower extinction coefficient (i.e more transmission). The extinction coefficient play a singnificant role in optical absoption process. The variation of extinction coefficient can be related to the variation of transmission.

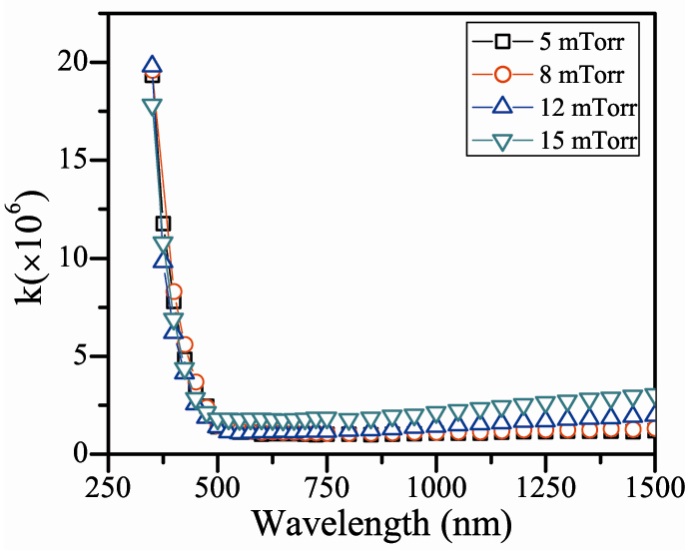

Fig 4.15: Extinction coefficient (k) vs wavelength (nm) of $Zn_{0.95}Fe_{0.05}O$ films at various partial pressures of argon gas environment.

4.2.1.4 $Zn_{0.925}Mn_{0.025}Fe_{0.05}O$

The RT transmission spectra of Mn2.5% and Fe5% doped ZnO thin films at various working gas pressures in argon gas are shown figure 4.16. The films show high transmission in the visible range about 84-86 (%). There is no significant change with working gas pressure and thickness of the films also show inconsistence with pressure are in the range of 1112- 1344 nm.

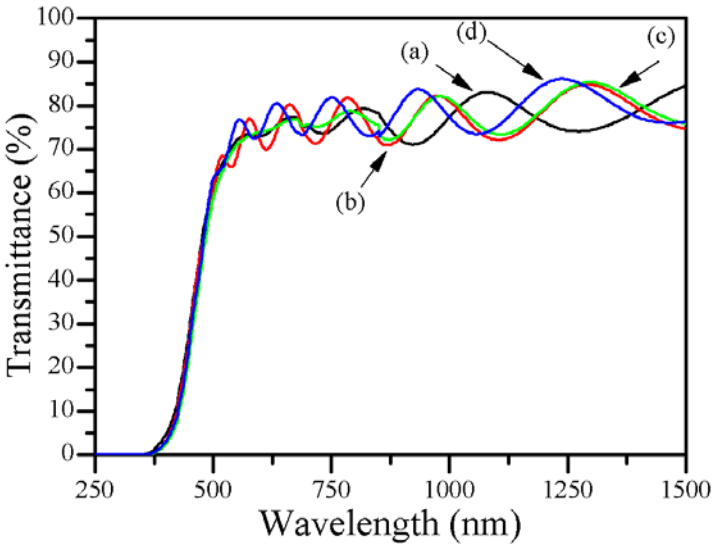

Fig 4.16: RT transmission spectra of $Zn_{0.925}Mn_{0.025}Fe_{0.05}O$ films at various partial pressures of (a) 5, (b) 8, (c) 12 and (d) 15 mTorr of argon gas environment.

Fig 4.17 show the $(\alpha h\nu)^2$ vs $h\nu$ plot of Mn2.5% and Fe5% doped ZnO films at different working gas pressure. The band gap of as deposited films calculated from transmission spectra show increase with argon working gas pressure from 3.23 – 3.27 eV. This behavior may be attributed that variation in ionic radii of Mn and Fe elements presented in ZnO film.

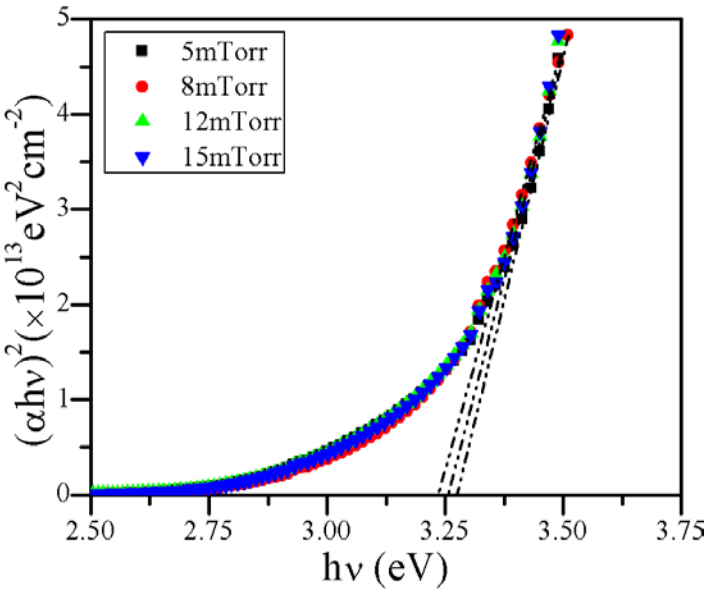

Fig 4.17: Estimated direct band gap of $Zn_{0.925}Mn_{0.025}Fe_{0.05}O$ films at various partial pressures of argon gas environment.

Table 4.4: Optical parameters of $Zn_{0.95}Mn_{0.025}Fe_{0.05}O$ films at various gas pressure.

Press (mTorr)	Thickness (nm)	T (%)	Band gap (eV)	UE (eV)	RI (n)	β (eV)
5	1112	86	3.27	0.582	1.495	0.023
8	1330	84	3.23	0.465	1.496	0.029
12	1344	85	3.25	0.585	1.495	0.024
15	1280	86	3.24	0.507	1.495	0.027

Fig 4.18 show the ln(α) vs hν plot of Mn2.5% and Fe5% doped ZnO films at various gas pressures of argon environment. There is linearity in Urbach energy with working gas pressure. The Urbach energy and stiffness factor (β) values of the films are listed in Table 4.4.

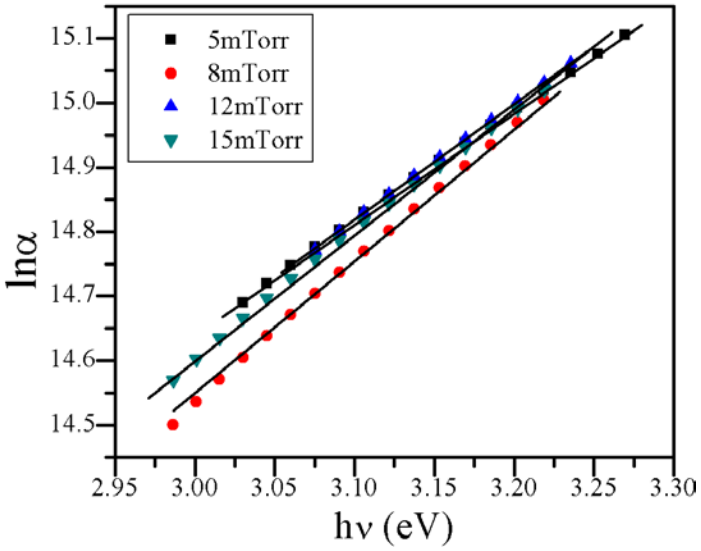

Fig 4.18: ln (α) vs hν of $Zn_{0.925}Mn_{0.025}Fe_{0.05}O$ films at various partial pressures of argon gas environment.

Fig 4.19 show the refractive index (n) as a function of wavelength (nm) of $Zn_{0.925}Mn_{0.025}Fe_{0.05}O$ films at various gas pressures of argon environment. There is no change refractive index with wavelength, the values with working gas pressure ranges from 1.495 – 1.496.

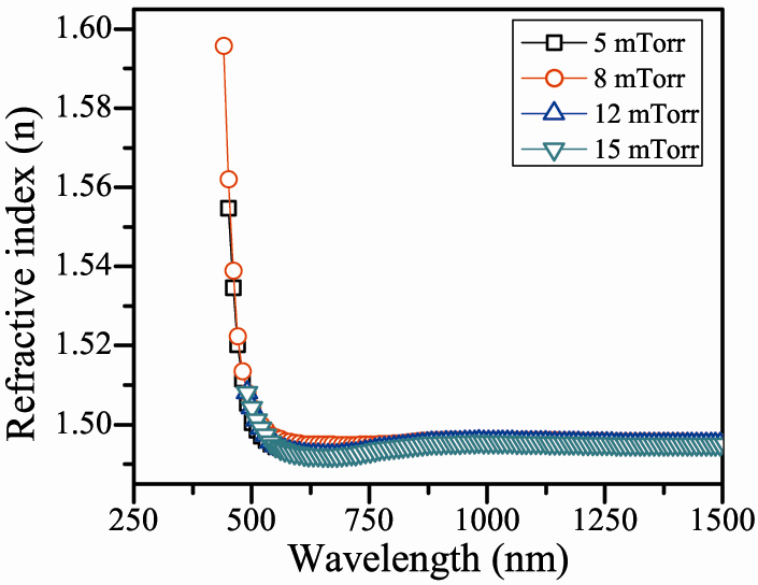

Fig 4.19: Refractive index (n) vs Wavelength (nm) of $Zn_{0.925}Mn_{0.025}Fe_{0.05}O$ films at various partial pressures of argon gas environment.

Figure 4.20 shows the dependence of the extinction coefficient (*k*) on wavelength, λ, for the films. There is no change in extinction coefficient with argon working gas pressure.

From the plot, it is clear that except all the films had a lower extinction coefficient (i.e more transmission). The extinction coefficient play a singnificant role in optical absoption process. The variation of extinction coefficient can be related to the variation of transmission.

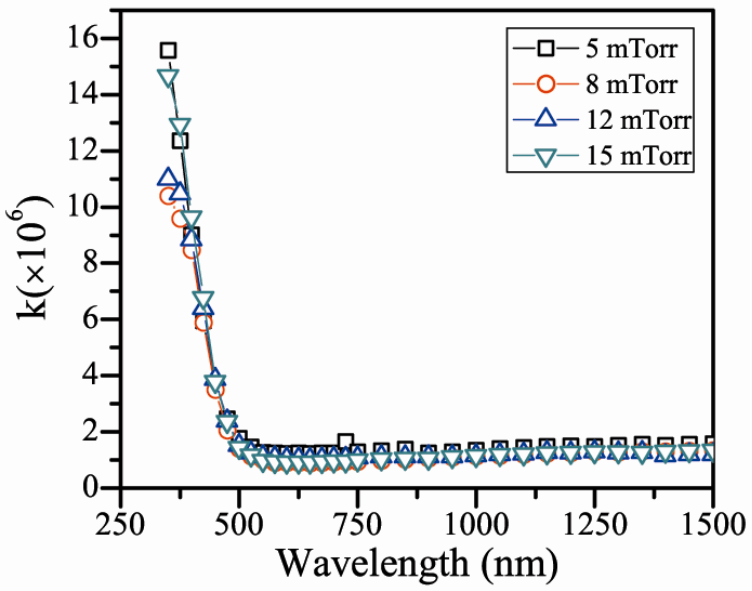

Fig 4.20: Extinction coefficient (k) vs wavelength (nm) of $Zn_{0.925}Mn_{0.025}Fe_{0.05}O$ films at various partial pressures of argon gas environment.

4.2.2 Oxygen environment

The room temperature transmission spectra of un-doped, Mn, Fe individual and co-doped ZnO films deposited quartz substretes by rf sputtering with oxygen partial pressure from 7-18 mTorr. The sputter parametrs i.e RF power, sputter duaration, base pressure and substrate – target diatnce were remain constant expect oxygen gas partial pressure.

4.2.2.1 Un-doped ZnO

The RT transmission spectra of un-doped ZnO thin films at various working gas pressures in oxygen gas are shown figure 4.17. The films show high transmission in the visible range about 88-89 (%). There is no significant change with working gas pressure, unlike argon gas the films show high transmission could be due ro nature processing gas. The films deposited for 9 mTorr of working gas pressure show high thickness than others might be the thresshold pressure give high deposition as we can further increase in prerssure the film thickness decreasing is in the range of 840- 1014 nm.

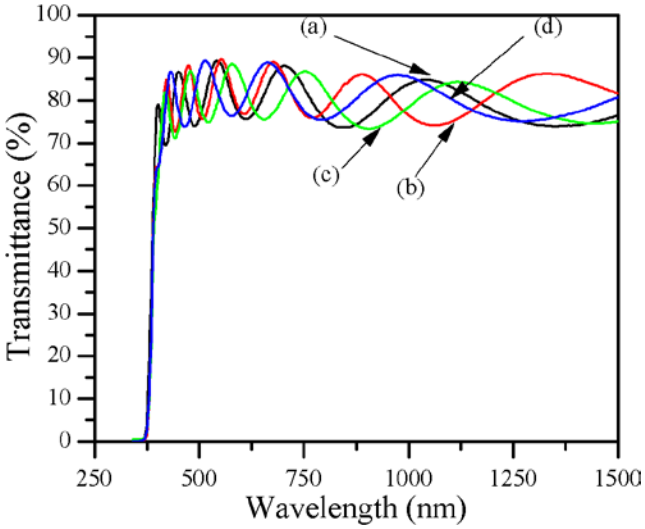

Fig 4.21: RT transmission of un-doped ZnO films at various partial pressures of (a) 7, (b) 9, (c) 13 and (d) 18 mTorr of oxygen gas environment.

Fig 4.22 show the $(\alpha h\nu)^2$ vs $h\nu$ plot of un-doped ZnO films at different working gas pressures in oxygen environment. The band gap of films at various pressures show decrease except films deposited at 18 mTorr working pressure, The optical energy values of ZnO films for different deposition temperatures are also show decrease [28]. The estimated direct band gap varied from 3.30 – 3.25 eV.

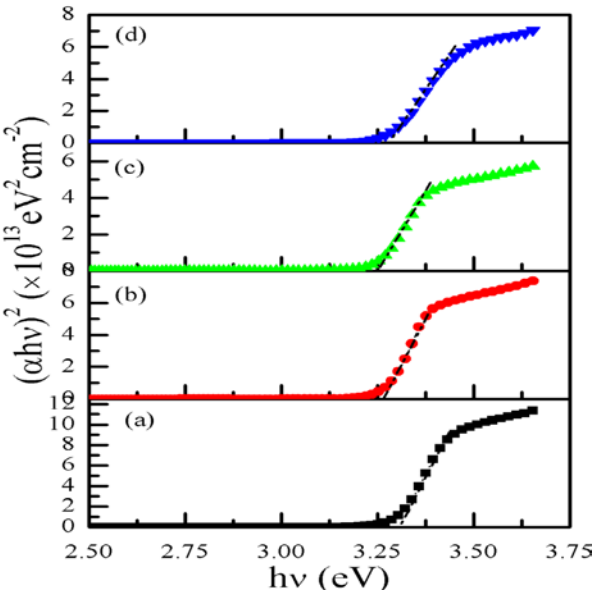

Fig 4.22: Estimated direct band gap of un-doped ZnO films at various partial pressures of (a) 7, (b) 9, (c) 13 and (d) 18 mTorr of oxygen gas environment.

Table 4.5: Optical parameters of un-doped ZnO films at various working gas pressure.

Press (mTorr)	Thickness (nm)	T (%)	Band gap (eV)	UE (eV)	RI (n)	β (eV)
7	840	88	3.30	0.264	1.495	0.052
9	1014	89	3.27	0.444	1.494	0.031
13	842	88	3.25	0.461	1.495	0.029
18	708	89	3.29	0.403	1.495	0.034

Fig 4.23 show the ln(α) vs hν plot of un-doped ZnO films at various gas pressures of oxygen environment. The Urbach energy show increasing with working gas pressure except the films deposited at 18 mTorr of working and inversely related to the optical band gap. The Urbach energy and stiffness factor (β) values of the films are listed in Table 4.5.

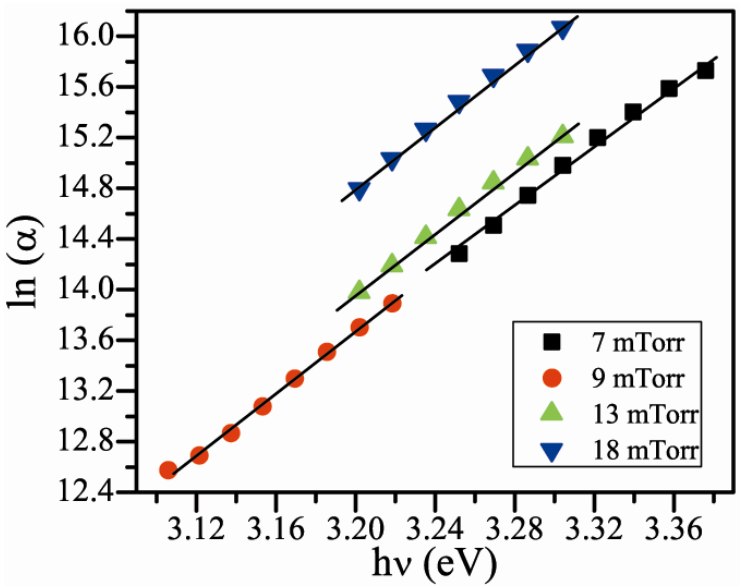

Fig 4.23: ln (α) vs hν plot of un-doped ZnO films at various partial pressures of oxygen gas environment.

Fig 4.24 show the refractive index (n) as a function of wavelength (nm) of un-doped ZnO films at various gas pressures of oxygen environment. There is no change refractive index with wavelength, the values with working gas pressure ranges from 1.494 – 1.495.

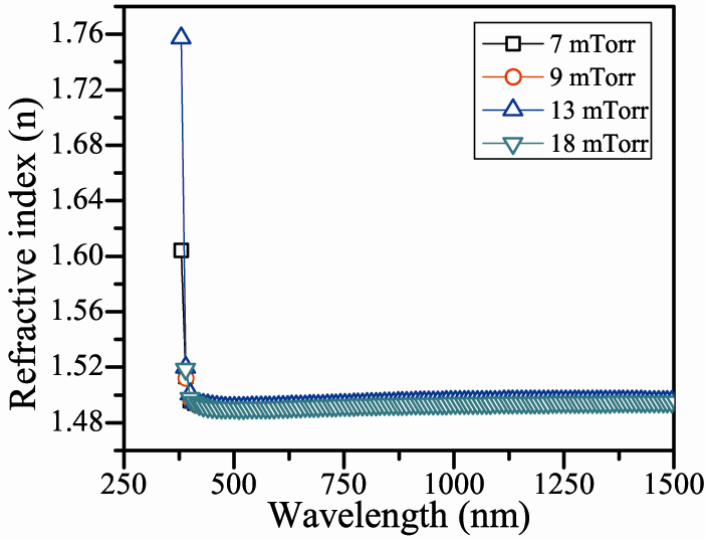

Fig 4.24: Refractive index (n) vs Wavelength (nm) plot of un-doped ZnO films at various partial pressures of oxygen gas environment.

Figure 4.25 shows the dependence of the extinction coefficient (*k*) on wavelength, λ, for the films. There is no change in extinction coefficient with oxygen working gas pressure. From the plot, it is clear that except all the films had a lower extinction coefficient (i.e more transmission). The extinction coefficient play a singnificant role in optical absoption process. The variation of extinction coefficient can be related to the variation of transmission.

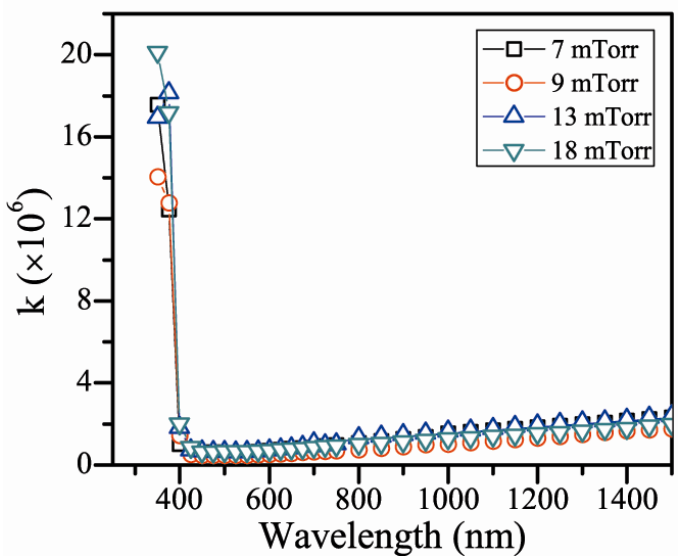

Fig 4.25: Extinction coefficient (k) vs wavelength (λ) of un-doped ZnO films at various partial pressures of oxygen gas environment.

4.2.2.2 $Zn_{0.95}Mn_{0.05}O$

The RT transmission spectra of Mn5% doped ZnO thin films at various working gas pressures in oxygen gas are shown figure 4.26. The films show high transmission in the visible range about 91-84 (%). The transmission of the films decreasing with increase in working gas pressur could be due to increase in the film thickness. The results reported for $Zn_{0.93}Mn_{0.07}O$ deposited on glass substrate by Xue-Yong Li et.al [29] are also show high tramittance for various doping concentrations. The decrease in optical tranmission with working pressure is attributed that excess Mn atoms might act obstacle for transmttance of ZnMnO films [29]. From the plots we can see the interfernce frings very less indicting the films have very thickness than the argon gas deposited films in the range of 398- 450 nm.

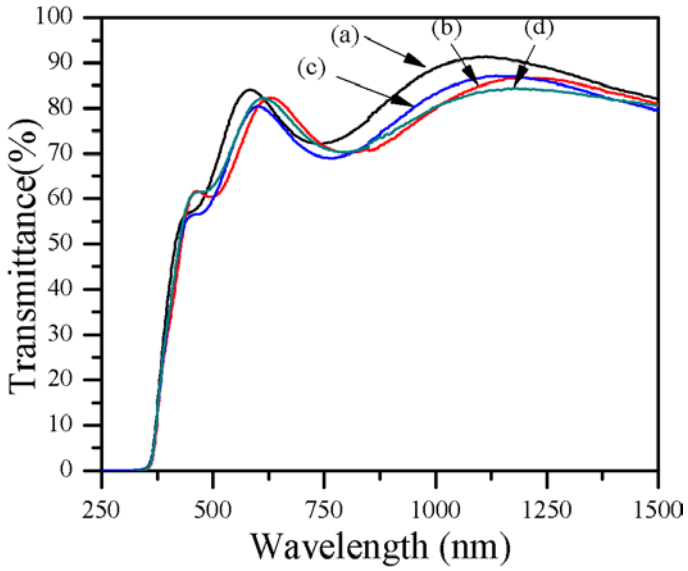

Fig 4.26: RT transmission spectra of $Zn_{0.95}Mn_{0.05}O$ films at various partial pressures of (a) 7, (b) 9, (c) 11 and (d) 13 mTorr of oxygen gas environment.

Fig 4.27 show the $(\alpha h\nu)^2$ vs $h\nu$ plot of Mn5% doped ZnO films at different working gas pressures in oxygen environment. The band gap of films at various pressures show increase except films 9 mTorr working pressure. The energy gap of various working gas pressures of oxygen gas films in support with other reported results [29, 30]. The optical band gap of $Zn_{0.95}Mn_{0.05}O$ films was calculated to be in the range of 3.04 – 2.96 eV.

Obviously, the values for optical band gap of $Zn_{0.95}Mn_{0.05}O$ films smaller than that of bulk ZnO (3.37 eV) due to Mn doping in ZnO.

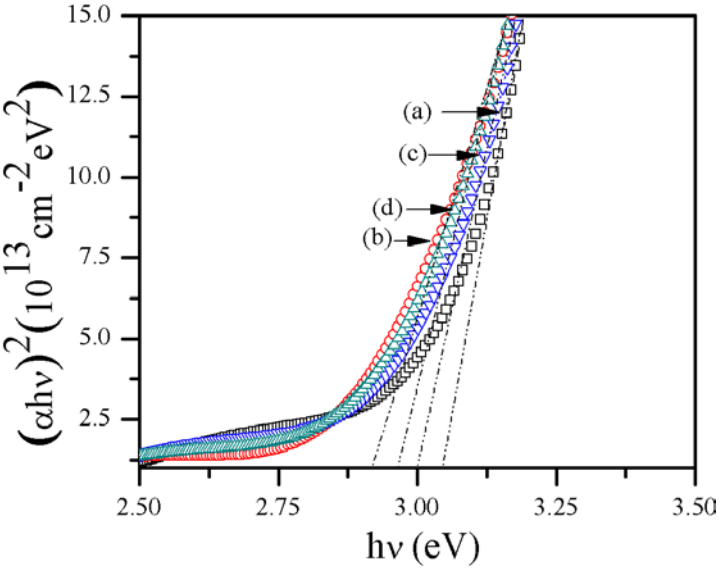

Fig 4.27: Estimate direct band gap of $Zn_{0.95}Mn_{0.05}O$ films at various partial pressures of (a) 7, (b) 9, (c) 11 and (d) 13 mTorr of oxygen gas environment.

Table 4.6: Optical parameters of $Zn_{0.95}Mn_{0.05}O$ films at various working gas pressure.

Press (mTorr)	Thickness (nm)	T (%)	Band gap (eV)	UE (eV)	RI (n)	β (eV)
7	398	91	3.04	0.466	1.494	0.030
9	450	86	2.91	0.482	1.497	0.028
11	405	87	3.00	0.371	1.496	0.037
13	424	84	2.96	0.372	1.496	0.037

Fig 4.28 show the ln(α) vs hν plot of Mn5% doped ZnO films at various gas pressures of oxygen environment. The Urbach energy is decreasing with working gas pressure except the films deposited at 13 mTorr of working and in contrast to Urbach energy of the films. The Urbach energy and stiffness factor (β) values at various working gas pressure are listed in Table 4.6.

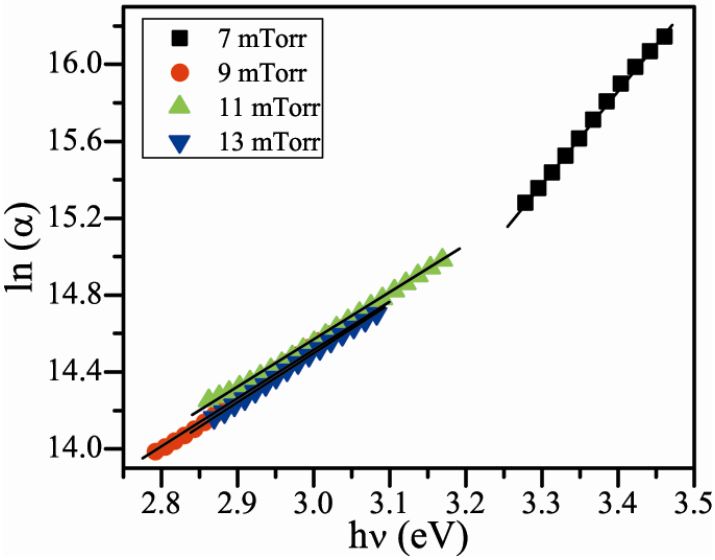

Fig 4.29: ln (α) vs hν plot of $Zn_{0.95}Mn_{0.05}O$ films at various partial pressures of (a) 7, (b) 9, (c) 11 and (d) 13 mTorr of oxygen gas environment.

Fig 4.30 show the refractive index (n) as a function of wavelength (nm) of $Zn_{0.95}Mn_{0.05}O$ films at various gas pressures of argon environment. There is no change refractive index with wavelength, the values with working gas pressure ranges from 1.494 – 1.497.

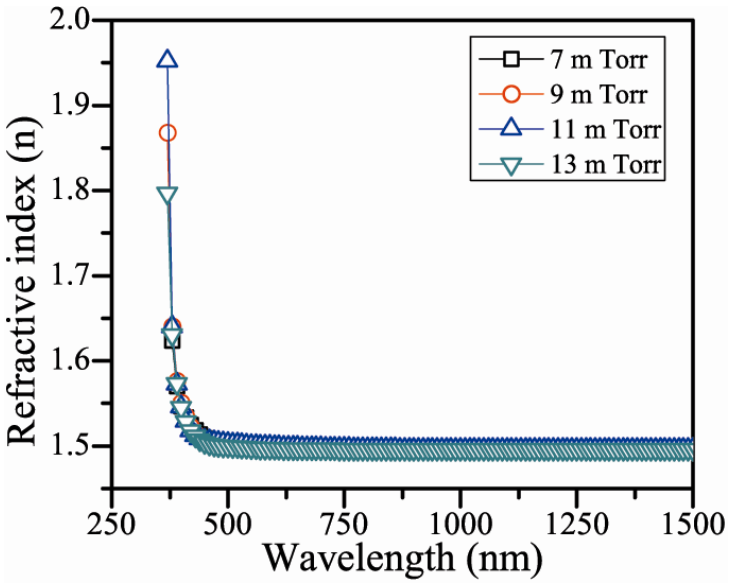

Fig 4.30: Refractive index (n) vs Wavelength (nm) plot of $Zn_{0.95}Mn_{0.05}O$ films at various partial pressures in oxygen gas environment.

Figure 4.31 shows the dependence of the extinction coefficient (*k*) on wavelength, λ, for the films in oxygen environment. There is no change in extinction coefficient with oxygen working gas pressure. From the plot, it is clear that except all the

films had a lower extinction coefficient (i.e more transmission). The extinction coefficient play a singnificant role in optical absoption process. The variation of extinction coefficient can be related to the variation of transmission [31]. As the oxygen pressure is increased the transmittance increases ane results in a decrease in the extinction coefficient.

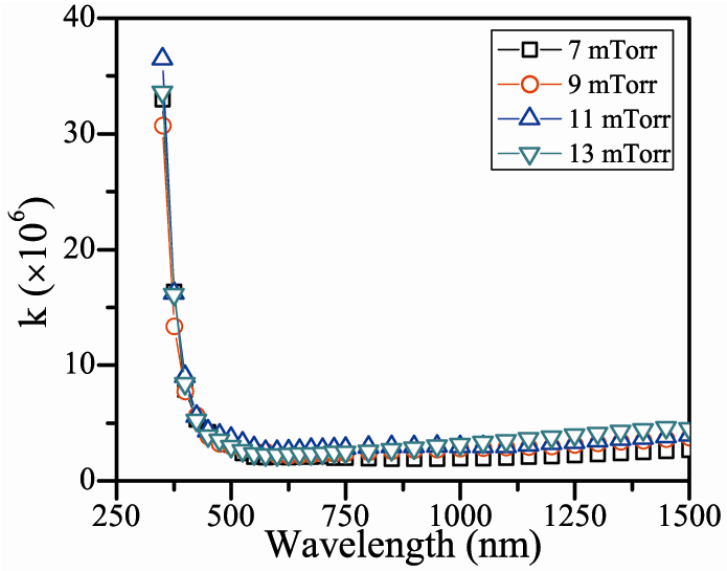

Fig 4.31: Extinction coefficient (k) vs Wavelength (λ) of $Zn_{0.95}Mn_{0.05}O$ films at various partial pressures of (a) 7, (b) 9, (c) 11 and (d) 13 mTorr of oxygen gas environment.

4.2.2.3 $Zn_{0.95}Fe_{0.05}O$

The RT transmission spectra of Fe5% doped ZnO thin films at various working gas pressures in oxygen gas are shown figure 4.32. The films show high transmission in the visible range about 81-89 (%). The transmission of the films increasing with increase in working gas pressure, except the fiilms at 13 mTorr. From the plots we can see the interfernce frings very less indicting the films have very thickness than the argon gas deposited films in the range of 265- 460 nm.

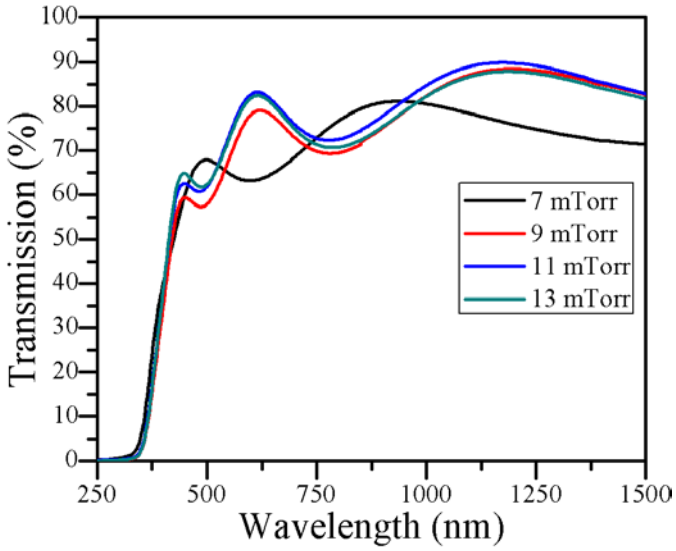

Fig 4.32: Estimate direct band gap of $Zn_{0.95}Fe_{0.05}O$ films at various partial pressures of oxygen gas environment.

Fig 4.33 show the $(\alpha h\nu)^2$ vs $h\nu$ plot of Fe5% doped ZnO films at different working gas pressures in oxygen environment. The band gap of films at various pressures show decrease with increase in working pressure in oxygen gas environment. The direct band gap at various pressures have decreases from 3.38 – 3.35 eV.

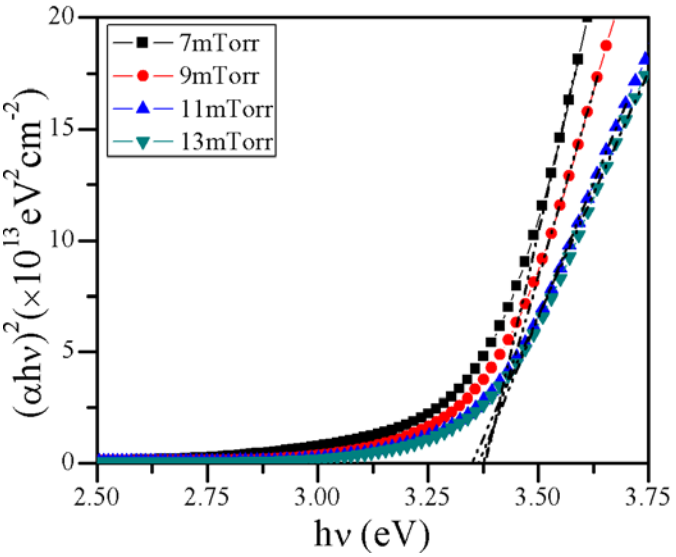

Fig 4.33: Estimate direct band gap of $Zn_{0.95}Fe_{0.05}O$ films at various partial pressures of oxygen gas environment.

Table 4.7: Optical parameters of $Zn_{0.95}Fe_{0.05}O$ films at various working gas pressure.

Press (mTorr)	Thickness (nm)	T (%)	Band gap (eV)	UE (eV)	RI (n)	β (eV)
7	265	81	3.38	0.362	1.499	0.038
9	394	88	3.37	0.364	1.495	0.037
11	430	89	3.36	0.340	1.494	0.040
13	460	87	3.35	0.323	1.495	0.042

Fig 4.34 shows the ln(α) vs hν plot of Fe5% doped ZnO films at various gas pressures of oxygen environment. The Urbach energy at different working gas pressures show decrease with increasing working gas pressure. The Urbach energy and optical band gap of the films show reverse tend as a function of working gas pressure. The Urbach energy and stiffness factor (β) values at various working gas pressure are listed in Table 4.7.

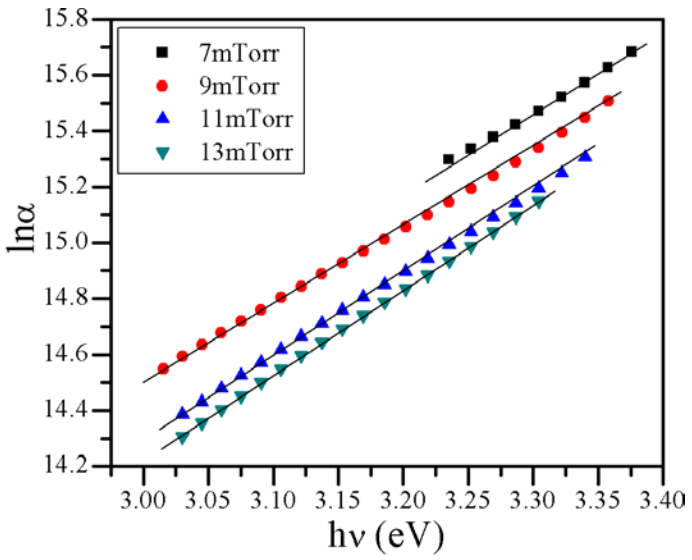

Fig 4.34: ln (α) vs hν of $Zn_{0.95}Fe_{0.05}O$ films at various partial pressures of oxygen gas environment.

Fig 4.35 show the refractive index (n) as a function of wavelength (nm) of $Zn_{0.95}Fe_{0.05}O$ films at various gas pressures of argon environment. There is no change refractive index with wavelength, the values with working gas pressure ranges from 1.499 – 1.494.

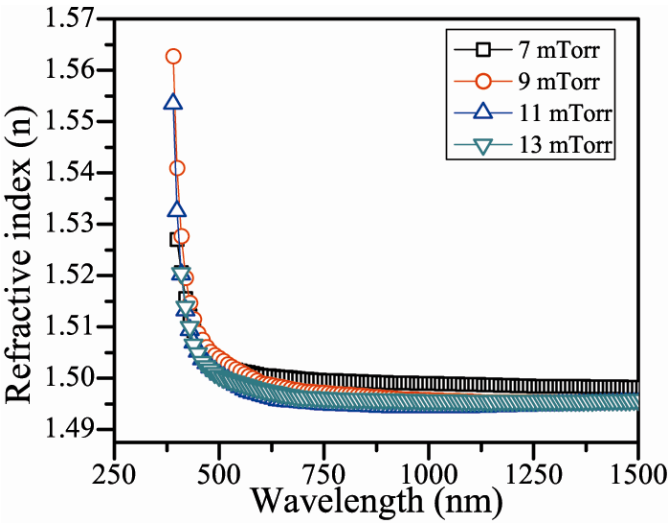

Fig 4.35: Refractive index (n) vs Wavelength (nm) of $Zn_{0.95}Fe_{0.05}O$ films at various partial pressures of oxygen gas environment.

Figure 4.36 shows the dependence of the extinction coefficient (*k*) on wavelength, λ, for the films deposited in oxygen environment. The extinction coefficient sligthly effected by the change in oxygen working gas pressure. From the plot, it is clear that except the films deposited at low oxygen working gas pressure had a lower extinction coefficient (i.e more transmission) than those deposited at high oxygen pressure. This behavior probabily due to lower porasity of the films depositede in oxygen gas atmosphere. This factor plays a singnificant role in optical absoption process. The variation of extinction coefficient can be related to the variation of transmission. As the oxygen pressure is increased the transmittance increases and results in a decrease in the extinction coefficient.

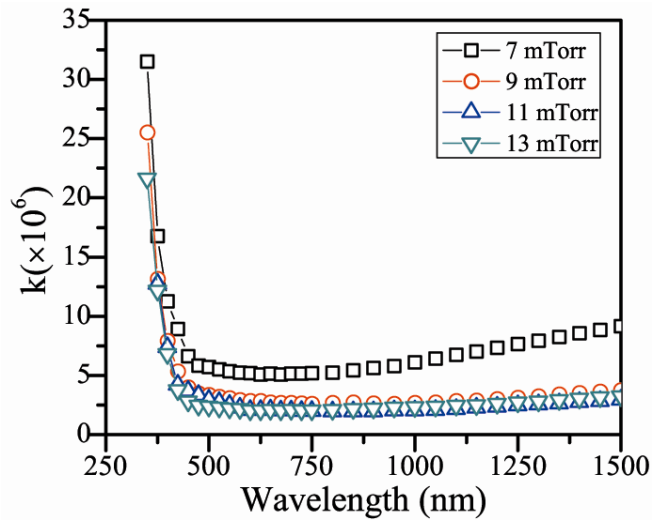

Fig 4.36: Extinction coefficient (k) vs wavelength (nm) of $Zn_{0.95}Fe_{0.05}O$ films at various partial pressures of oxygen gas environment.

4.2.2.4 $Zn_{0.925}Mn_{0.025}Fe_{0.05}O$

The RT transmission spectra of Mn2.5% and Fe5% co-doped ZnO thin films at various working gas pressures in oxygen gas are shown figure 4.37. The films show high transmission in the visible range about 81-89 (%). The transmission of the films increasing with increase in working gas pressure, except the fiilms at 13 mTorr. From the plots we can see the interfernce frings very less indicting the films have very thickness than the argon gas deposited films in the range of 265- 460 nm.

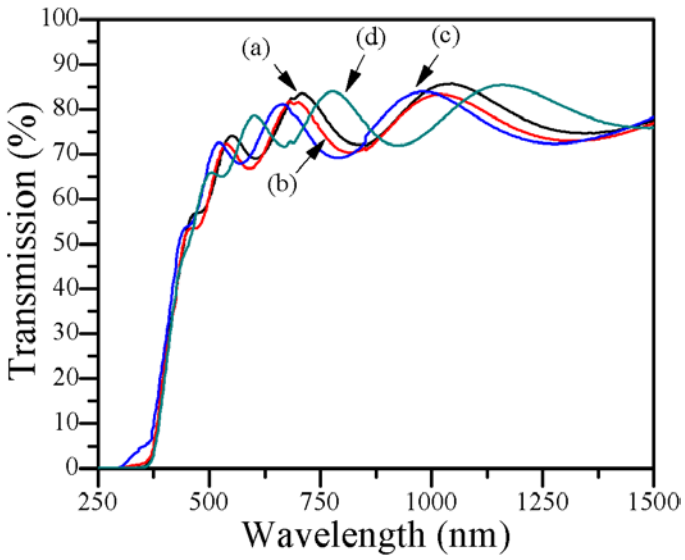

Fig 4.37: Estimate direct band gap of $Zn_{0.925}Mn_{0.025}Fe_{0.05}O$ films at various partial pressures of (a) 7, (b) 9, (c) 11 and (d) 13 mTorr of oxygen gas environment.

Fig 4.38 show the $(\alpha h\nu)^2$ vs $h\nu$ plot of Mn2.5% and Fe5% doped ZnO films at different working gas pressures in oxygen environment. The band gap of films is increasing with increase in working gas pressure except 13 mTorr pressure. The band gap at different pressures are in between from 3.12 – 3.21 eV.

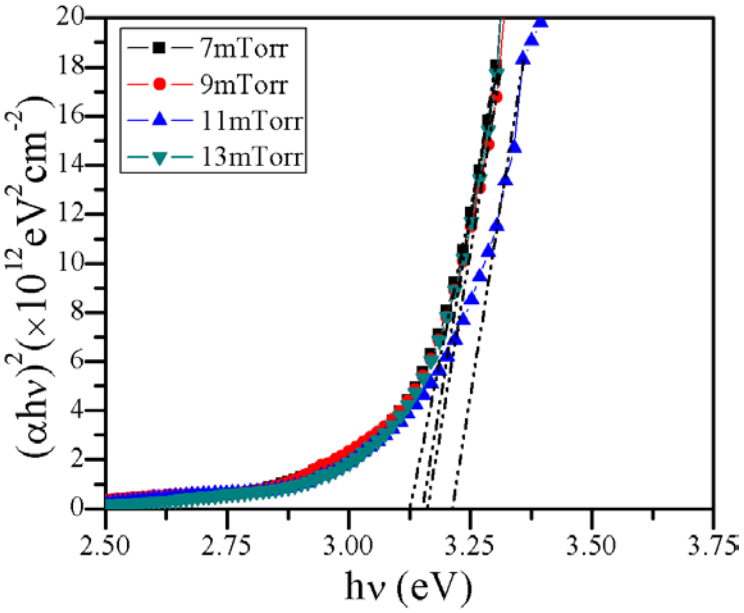

Fig 4.38: Estimated direct band gap of $Zn_{0.925}Mn_{0.025}Fe_{0.05}O$ films at various partial pressures of oxygen gas environment.

Table 4.8: Optical parameters of $Zn_{0.925}Mn_{0.025}Fe_{0.05}O$ films at various gas pressure.

Press (mTorr)	Thickness (nm)	T (%)	Band gap (eV)	UE (eV)	RI (n)	β (eV)
7	726	85	3.15	0.403	1.495	0.034
9	716	83	3.16	0.400	1.496	0.035
11	681	84	3.21	0.367	1.496	0.037
13	801	85	3.12	0.330	1.495	0.042

Fig 4.39 shows the ln(α) vs hν plot of Mn2.5% and Fe5% doped ZnO films at various gas pressures of oxygen environment. The Urbach energy at different working gas pressures show decrease with increasing working gas pressure. The Urbach energy and optical band gap of the films show reverse tend as a function of working gas pressure. The Urbach energy and stiffness factor (β) values at various working gas pressure are listed in Table 4.8.

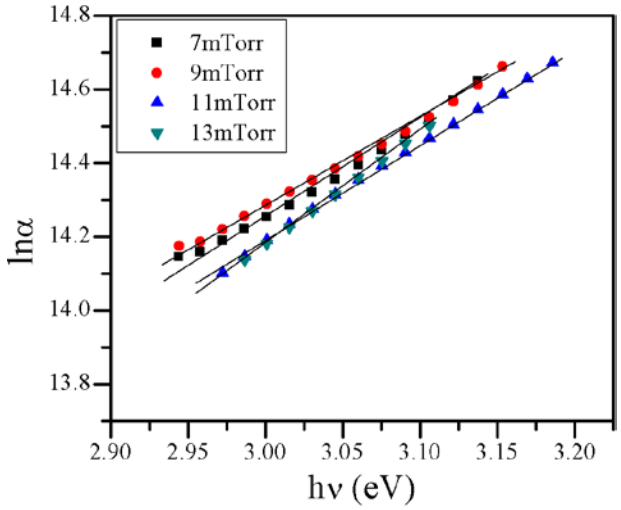

Fig 4.39: ln (α) vs hν plot of $Zn_{0.925}Mn_{0.025}Fe_{0.05}O$ films at various partial pressures of oxygen gas environment.

Fig 4.40 show the refractive index (n) as a function of wavelength (nm) of $Zn_{0.925}Mn_{0.025}Fe_{0.05}O$ films at various gas pressures of argon environment. There is no change refractive index with wavelength, the values with working gas pressure ranges from 1.495 – 1.496.

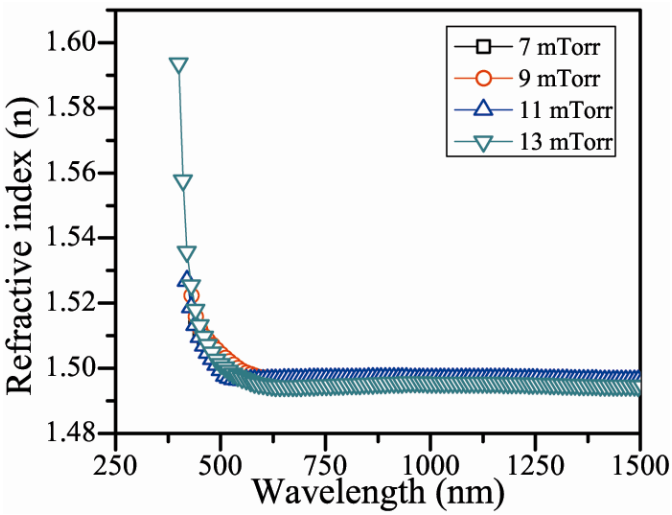

Fig 4.40: Refractive index (n) vs Wavelength (nm) plot of $Zn_{0.925}Mn_{0.025}Fe_{0.05}O$ films at various partial pressures of oxygen gas environment

Figure 4.41 shows the dependence of the extinction coefficient (*k*) on wavelength, λ, for the films deposited in oxygen environment. There is no siginificant change extinction coefficient with working pressure. From the plot, it is clear that all the films had a lower extinction coefficient (i.e more transmission) with change in pressure. The extinction

coefficient plays a singnificant role in optical absoption process. The variation of extinction coefficient can be related to the variation of transmission.

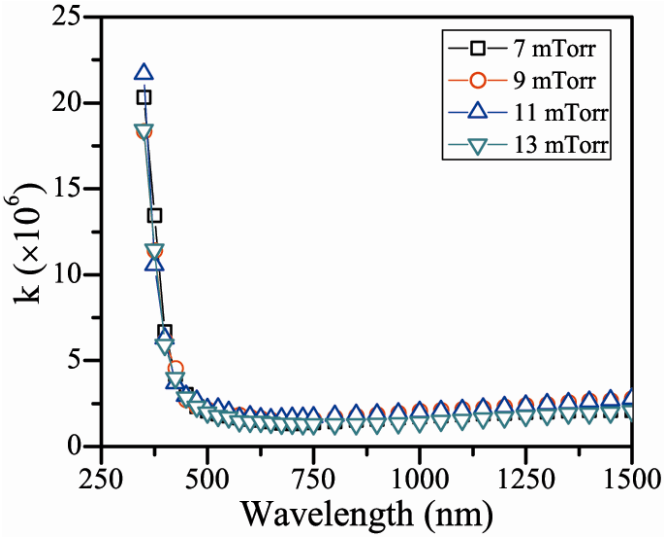

Fig 4.41: Extinction coefficient (k) vs wavelength (nm) of $Zn_{0.925}Mn_{0.025}Fe_{0.05}O$ films at various partial pressures of oxygen gas environment.

4.3 Effect of film thickness

The room temperature tranmission spectra of as deposited films of Mn, Fe and Mn-Fe doped ZnO thin films were depsoited onto quartz substrates by rf-magnetron sputtering with argon and nitrogen gas enviornment for different tie duration varies from 30- 120 min by keeping the other deposition condiction constant i.e rf power 100W, working gas pressure 12 mTorr, sub-target 8 cm and the base pressure was always matined at 1×10^{-6} Torr. The films deposited in argon gas environemnt had high sputter yield (high deposition rate) than nitrogen gas environment. The films deposited in argon gas had thickness high than films deposited in nitrogen atmosphere are in the range of 205 – 2861 nm for argon and 312 – 1650 nm for nitrogen gas environment. The as deposited films show high transmission (70-95%) in the visible region for the both the gases of argon and nitrogen with more fringes indictes that films have constructive interfernce between air-film-substrate-films.

4.3.1 Argon gas environment

The room temperature transmission spectra of un-doped ZnO and Mn, Fe individual and co-doped ZnO films deposited onto quartz substretes by rf sputtering at sputter durations

varied from 30- 120 min at working pressure 12 mTorr, rf power 100W, substrate – target diatnce about 80 mm and base pressure 1×10^{-6} Torr were remained constant for all deposition of the films. The as deposited films have high thickness in could be due to the nature of processing natuarally argon gas gives high rate of depositon than other gases, this enables to thicker films.

4.3.1.1 $Zn_{0.95}Mn_{0.05}O$

The RT transmission spectra (inset envelope method) of Mn5% doped ZnO thin films at various film ticknesses in argon gas are shown figure 4.47. The films show high transmission in the visible range about 50-85 (%). From the plots, we can see the transmittance is decreasing with increase in film thickness and the number of fringes are increasing indicting the films have high thickness less transmittance. The average film thickness of the films varied from 634 – 2861 nm.

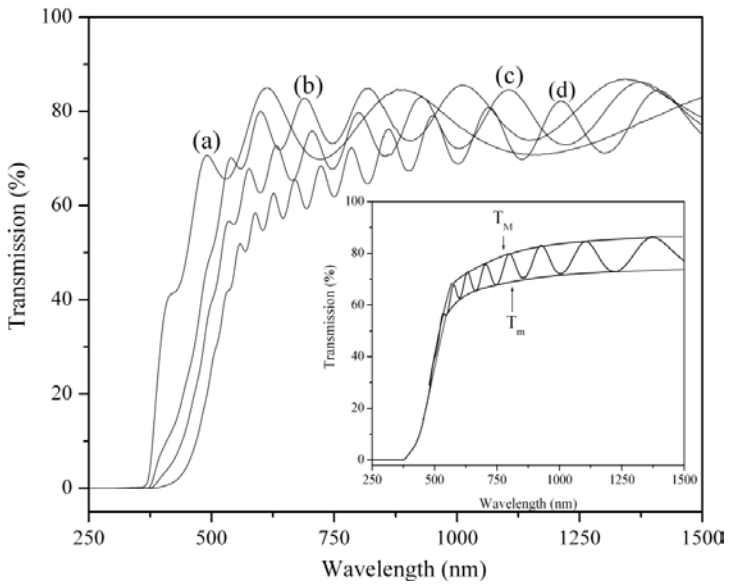

Fig 4.47: RT transmission spectra (inset envelope method) of $Zn_{0.95}Mn_{0.05}O$ films at various film thicknesses of (a) 634, (b) 1404, (c) 1906 and (d) 2861 nm of argon gas environment.

Fig 4.48 shows the $(\alpha h\nu)^2$ vs $h\nu$ plot of Mn5% doped ZnO films at different film thicknesses in argon gas environment. The variation of absorption coefficient with photon energy assumed to exponential for many materials. The band gap is initially decreased and then increased with film thickness are in the range of 3.14 – 3.27 eV.

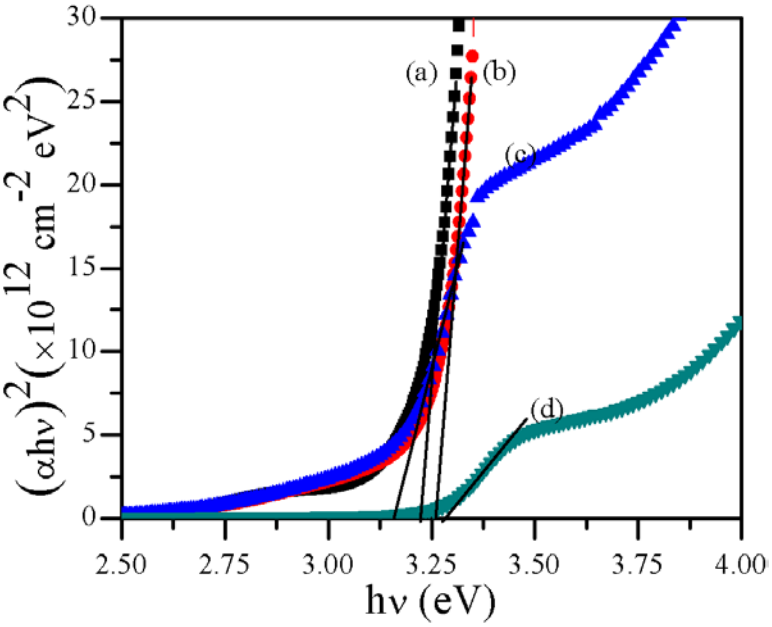

Fig 4.48: Estimated direct band gap of $Zn_{0.95}Mn_{0.05}O$ films at various film thicknesses of (a) 634, (b) 1404, (c) 1906 and (d) 2861 nm of argon gas environment.

Table 4.10: Optical parameters of $Zn_{0.95}Mn_{0.05}O$ films at various thicknesses.

Time (min)	Thickness (nm)	T (%)	Band gap (eV)	UE (eV)	RI (n)	β (eV)
30	634	84	3.22	0.466	1.496	0.030
60	1404	86	3.25	0.482	1.495	0.028
90	1906	88	3.14	0.371	1.495	0.037
120	2861	87	3.27	0.372	1.498	0.037

Fig 4.49 shows the ln(α) vs hν plot of Mn5% doped ZnO films at various film thickness of argon gas environment. At higher wavelengths scattering of light occur for a transparent material of light dominates absorption. The dependence of Urbach energy [34, 35] is calculated from transmittance of the films. The Urbach energy and stiffness factor (β) values at various working gas pressure are listed in Table 4.10.

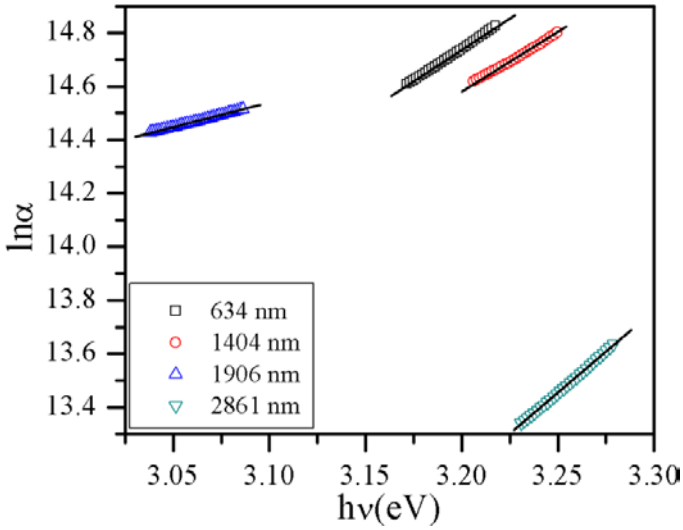

Fig 4.49: ln (α) vs hν plot of $Zn_{0.95}Mn_{0.05}O$ films at various film thicknesses of argon gas environment.

Fig 4.50 show the refractive index (n) as a function of wavelength (nm) of $Zn_{0.95}Mn_{0.05}O$ films at various gas pressures of argon environment. There is no change refractive index with wavelength, the values with working gas pressure ranges from 1.493 – 1.495.

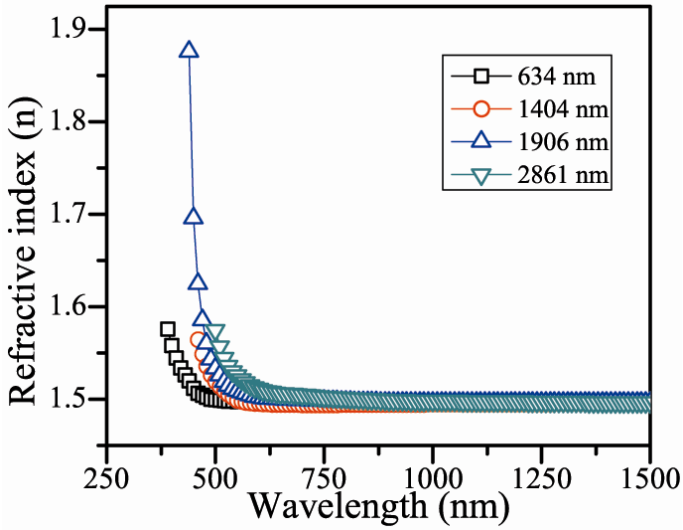

Fig 4.50: Refractive index (n) vs wavelength (nm) of $Zn_{0.95}Mn_{0.05}O$ films at various film thicknesses of argon gas environment.

Figure 4.51 shows the dependence of the extinction coefficient (*k*) on wavelength, λ, for the films deposited with different film thicknesses in argon environment. The extinction coefficient sligthly effected by the change in film thickness. From the plot, it is clear that except the films deposited at low thickness about 634 nm had a lower extinction coefficient (i.e more transmission) than those deposited at high film thicknesses in argon

environment. This behavior probabily due to lower porasity of the films depositede in oxygen gas atmosphere. This factor plays a singnificant role in optical absoption process. The variation of extinction coefficient can be related to the variation of transmission. As the argon pressure is increased the transmittance increases and results in a decrease in the extinction coefficient.

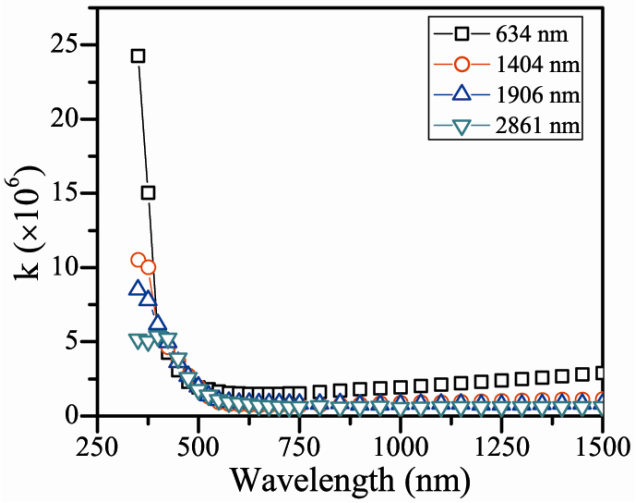

Fig 4.51: Extinction coefficient (k) vs wavelength (nm) of $Zn_{0.95}Mn_{0.05}O$ films at various film thicknesses of argon gas environment.

4.3.1.2 $Zn_{0.95}Fe_{0.05}O$

The RT transmission spectra of Fe5% doped ZnO thin films at various film ticknesses in argon gas are shown figure 4.52. The films show high transmission in the visible range about 93-94 (%). From the plots, we can see the transmittance is decreasing with increase in film thickness and the number of fringes are increasing indicting the films have high thickness less transmittance. The average film thickness of the films varied from 305 – 1234 nm.

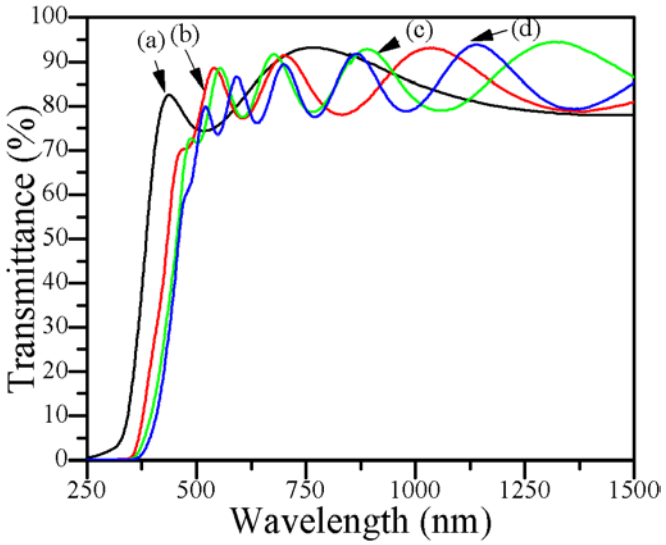

Fig 4.52: RT transmission of $Zn_{0.95}Fe_{0.05}O$ films at various film thicknesses of (a) 305, (b) 737, (c) 940 and (d) 1234 nm of argon gas environment.

Fig 4.53 show the $(\alpha h\nu)^2$ vs $h\nu$ plot of Fe5% ZnO films at different film thicknesses in argon gas environment. The band gap is decreasing with increase in film thickness are in the range of 3.45 – 3.29 eV.

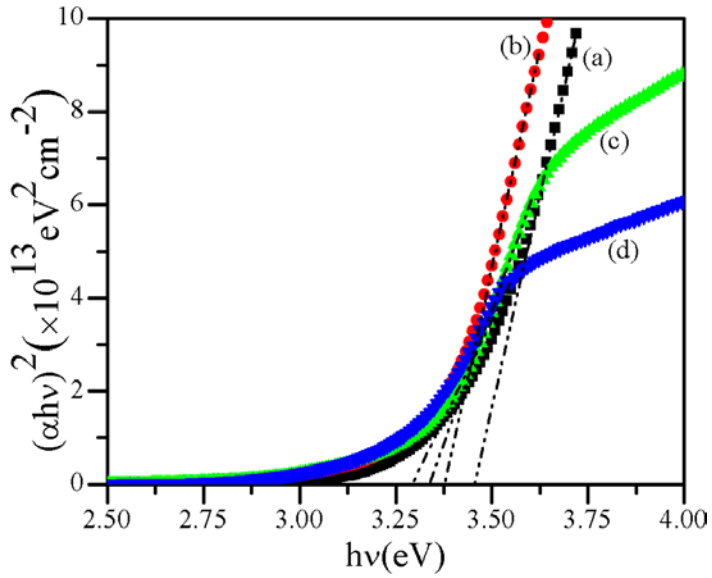

Fig 4.53: Estimated direct band gap of $Zn_{0.95}Fe_{0.05}O$ films at various film thicknesses of (a) 305, (b) 737, (c) 940 and (d) 1234 nm of argon gas environment.

Table 4.11: Optical parameters of $Zn_{0.95}Fe_{0.05}O$ films at various thicknesses.

Time (min)	Thickness (nm)	T (%)	Band gap (eV)	UE (eV)	RI (n)	β (eV)
30	305	93	3.45	0.332	1.492	0.041
60	737	93	3.38	0.350	1.492	0.039
90	940	94	3.33	0.436	1.494	0.032
120	1234	93	3.29	0.422	1.493	0.033

Fig 4.54 shows the ln(α) vs hν plot of Fe5% doped ZnO films at various film thickness of argon gas environment. The Urbach energy is increasing with increase in film thickness. The Urbach energy and stiffness factor (β) values at various working gas pressure are listed in Table 4.10.

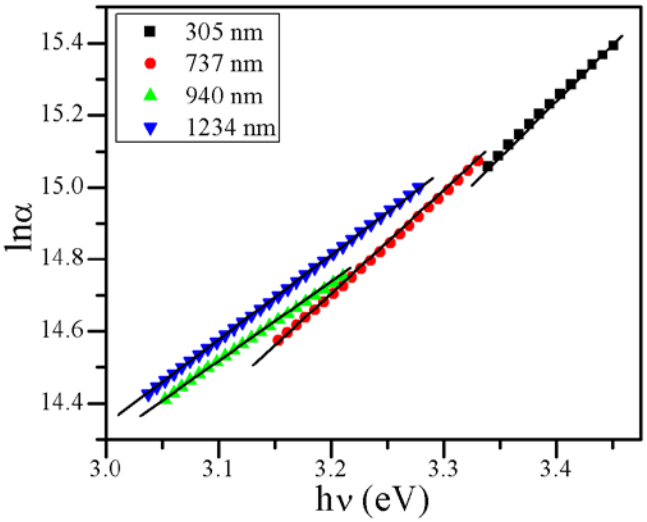

Fig 4.54: ln (α) vs hν plot of $Zn_{0.95}Fe_{0.05}O$ films at various film thicknesses of argon gas environment.

Fig 4.55 show the refractive index (n) as a function of wavelength (nm) of $Zn_{0.95}Fe_{0.05}O$ films at various gas pressures of argon environment. There is no change refractive index with wavelength, the values with working gas pressure ranges from 1.492 – 1.494.

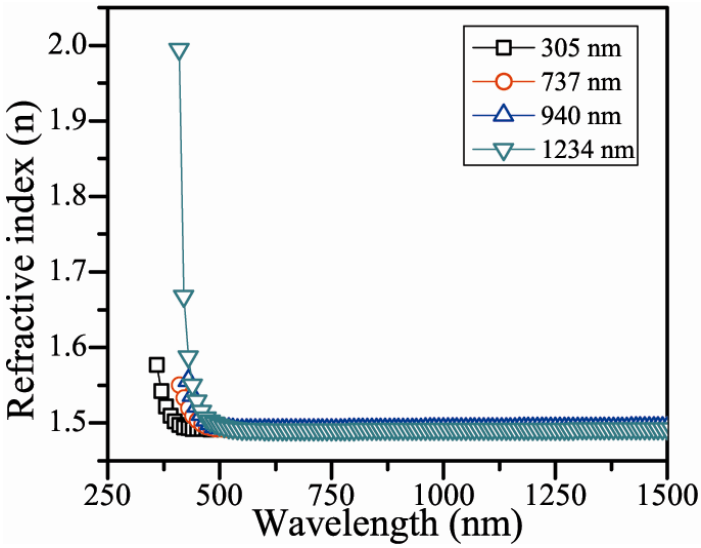

Fig 4.55: Refractive index (n) vs Wavelength (nm) plot of $Zn_{0.95}Fe_{0.05}O$ films at various film thicknesses of argon gas environment.

Figure 4.56 shows the dependence of the extinction coefficient (*k*) on wavelength, λ, for the films deposited with different film thicknesses in argon environment. The extinction coefficient sligthly effected by the change in film thickness. From the plot, it is clear that except the films deposited at low thickness about 305 nm had a lower extinction coefficient (i.e more transmission) than those deposited at high film thicknesses in argon environment. This behavior probabily due to lower porasity of the films depositede in oxygen gas atmosphere. This factor plays a singnificant role in optical absoption process. The variation of extinction coefficient can be related to the variation of transmission. As the argon pressure is increased the transmittance increases and results in a decrease in the extinction coefficient.

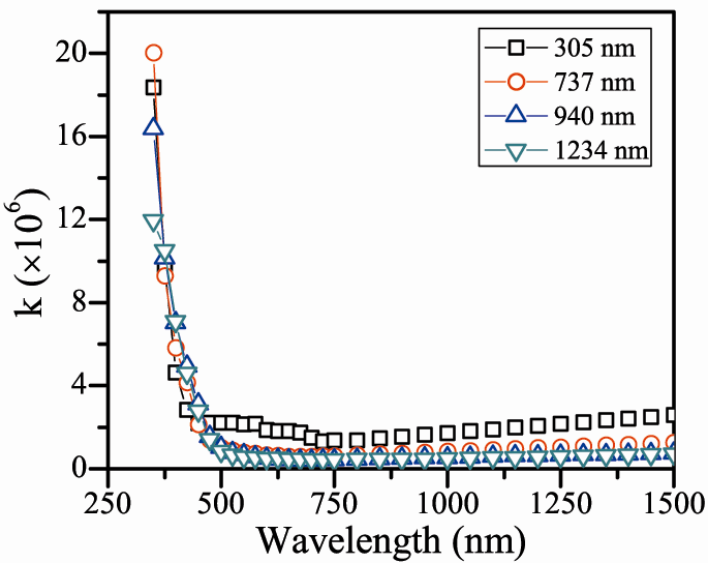

Fig 4.56: Extinction coefficient (k) vs wavelength (nm) plot of $Zn_{0.95}Fe_{0.05}O$ films at various film thicknesses of argon gas environment.

4.3.1.3 $Zn_{0.925}Mn_{0.025}Fe_{0.05}O$

The RT transmission spectra ofMn2.5% and Fe5% doped ZnO thin films at various film ticknesses in argon gas are shown figure 4.57. The films show high transmission in the visible range about 84-93 (%) [36]. From the plots, we can see the transmittance is decreasing with increase in film thickness and the number of fringes are increasing indicting the films have high thickness less transmittance. The average film thickness of the films varied from 365 – 645 nm.

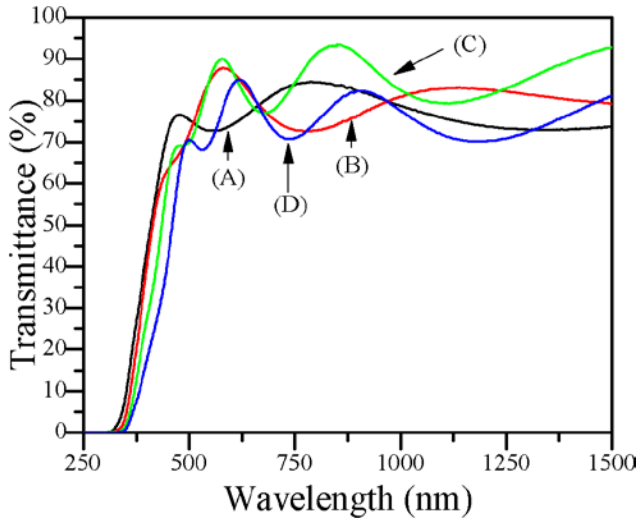

Fig 4.57: RT transmission spectra of $Zn_{0.925}Mn_{0.025}Fe_{0.05}O$ films at various film thicknesses of (a) 365, (b) 385, (c) 595 and (d) 645 nm of argon gas environment.

The plot of $(\alpha h\nu)^2$ vs $h\nu$ of Fe5% ZnO films at different film thicknesses in argon gas environment are shown in figure 4.58. The band gap is decreasing with increase in film thickness are in the range of 3.45 – 3.29 eV [36].

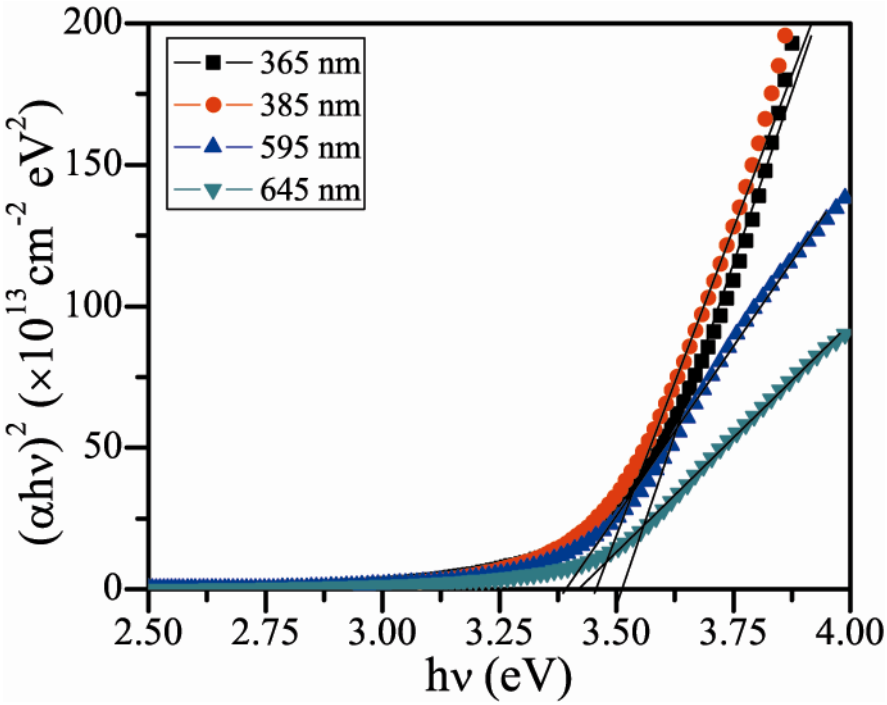

Fig 4.58: Estimated direct band gap of $Zn_{0.925}Mn_{0.025}Fe_{0.05}O$ films at various film thicknesses of (a) 365, (b) 385, (c) 595 and (d) 645 nm of argon gas environment.

Table 4.12: Optical parameters of $Zn_{0.925}Mn_{0.025}Fe_{0.05}O$ film various thicknesses.

Power (Watt)	Thickness (nm)	T (%)	Band gap (eV)	UE (eV)	RI (n)	β (eV)
15	365	84	3.50	0.482	1.496	0.028
20	385	87	3.45	0.334	1.495	0.041
30	595	93	3.39	0.381	1.492	0.036
40	645	84	3.41	0.548	1.498	0.025

Fig 4.59 shows the ln(α) vs hν plot of Fe5% doped ZnO films at various film thickness of argon gas environment. The Urbach energy is increasing with increase in film thickness. The Urbach energy and stiffness factor (β) values at various working gas pressure are listed in Table 4.10.

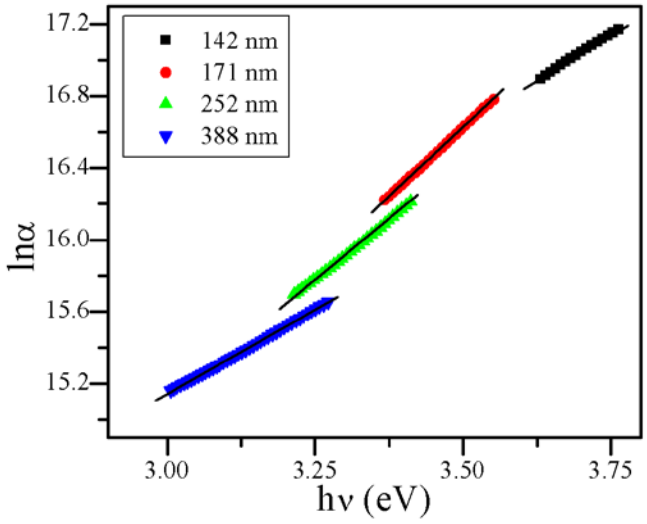

Fig 4.59: ln (α) vs hν plot of $Zn_{0.925}Mn_{0.025}Fe_{0.05}O$ films at various film thicknesses of argon gas environment.

Fig 4.60 show the refractive index (n) as a function of wavelength (nm) of $Zn_{0.95}Fe_{0.05}O$ films at various gas pressures of argon environment. There is no change refractive index with wavelength, the values with working gas pressure ranges from 1.492 – 1.498.

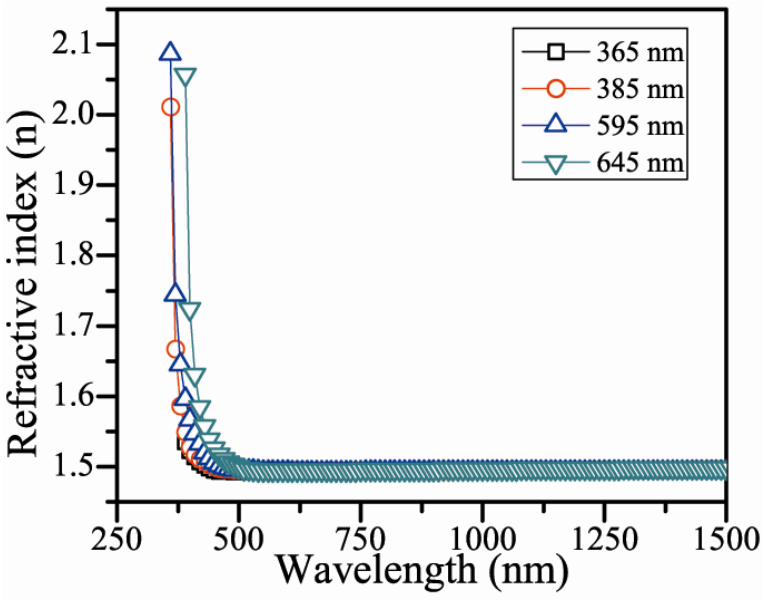

Fig 4.60: Refractive index (n) vs Wavelength (nm) plot of $Zn_{0.925}Mn_{0.025}Fe_{0.05}O$ films at various film thicknesses of argon gas environment.

Figure 4.61 shows the dependence of the extinction coefficient (*k*) on wavelength, λ, for the films deposited with different film thicknesses in argon environment. The extinction

coefficient sligthly effected by the change in film thickness. From the plot, it is clear that except the films deposited at low thicknesses at 365 and 385 nm had a lower extinction coefficient (i.e more transmission) than those deposited at high film thicknesses in argon environment. The extinction coefficient plays a singnificant role in optical absoption process. The variation of extinction coefficient can be related to the variation of transmission [31]. As film thickness increases the transmittance decreases as result the extinction coefficient show decrease.

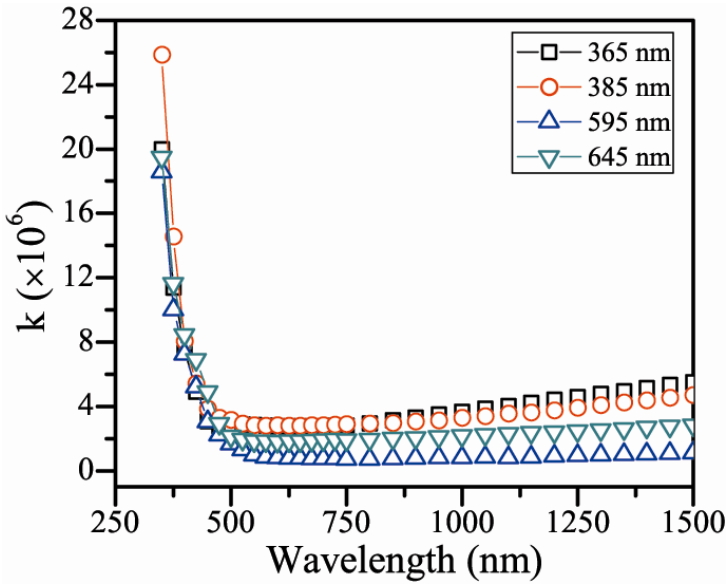

Fig 4.61: Extinction coefficient (k) vs wavelength (nm) of $Zn_{0.925}Mn_{0.025}Fe_{0.05}O$ films at various film thicknesses of argon gas environment.

4.3.2 Nitrogen gas environment

The room temperature transmission spectra of un-doped ZnO and Mn, Fe individual and co-doped ZnO films deposited onto quartz substretes by rf sputtering at sputter duration was varied from 30- 120 min at working pressure 12 mTorr, rf power 100W, substrate – target diatnce about 80 mm and base pressure 1×10^{-6} Torr were remained constant for all deposition of the films. The as deposited films thickness is increasing with time duration .

4.3.2.1 $Zn_{0.95}Mn_{0.05}O$

The RT transmission spectra of Mn5% doped ZnO thin films at various film ticknesses in nitrogen gas are shown figure 4.62. The films have high transmission in the visible range about 84-93 (%). From the plots, we can see the the number of intereference fringes are

increasing with film thickness, indicting the films have high thickness with sputter duration and decease in transmittance. The average film thickness of the films varied from 365 – 645 nm.

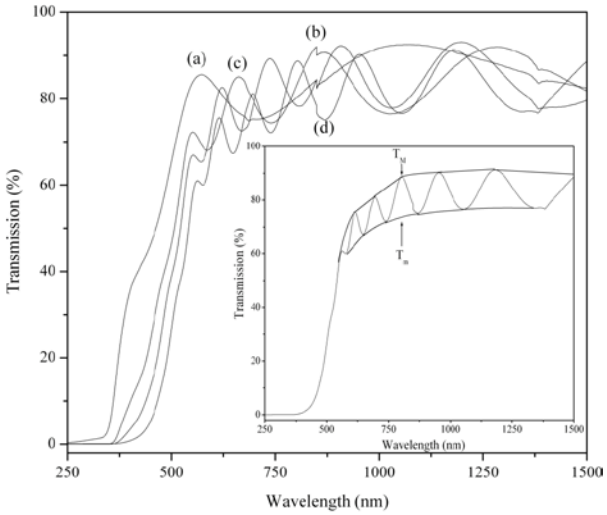

Fig 4.62: RT transmission spectra (Inset envelope method) of $Zn_{0.95}Mn_{0.05}O$ films at various film thicknesses of (a) 398, (b) 957, (c) 1346 and (d) 1650 nm of nitrogen gas environment.

Fig 4.63 shows the $(\alpha h\nu)^2$ vs $h\nu$ plot of Mn5% ZnO films at different film thicknesses in nitrogen gas environment. The band gap of the films marginally decreases with increase in film thickness in the range 3.45 – 3.29 eV.

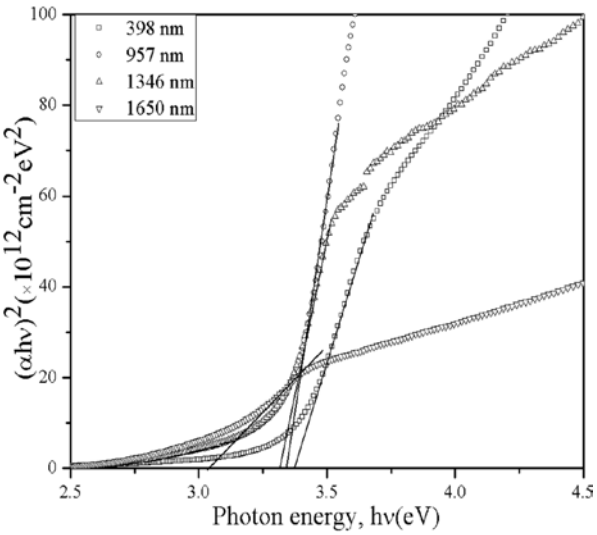

Fig 4.63: Estimated direct band gap of $Zn_{0.95}Mn_{0.05}O$ films at various film thicknesses of nitrogen gas environment.

Table 4.13: Optical parameters of $Zn_{0.95}Mn_{0.05}O$ films of various thicknesses.

Time (min)	Thickness (nm)	T (%)	Band gap (eV)	UE (eV)	RI (n)	β (eV)
30	398	92	3.36	0.466	1.494	0.030
60	957	91	3.33	0.482	1.493	0.028
90	1346	92	3.37	0.371	1.493	0.037
120	1650	91	3.39	0.372	1.494	0.037

Fig 4.64 (A) & (B) shows the ln(α) vs hν plot of Mn5% doped ZnO films at various film thickness of nitrogen gas environment. The estimated Urbach energy as a function of film thickness shows the decrease and optical energy gap show reverse to the Urbach energy. The Urbach energy and stiffness factor (β) values at various working gas pressure are listed in Table 4.13.

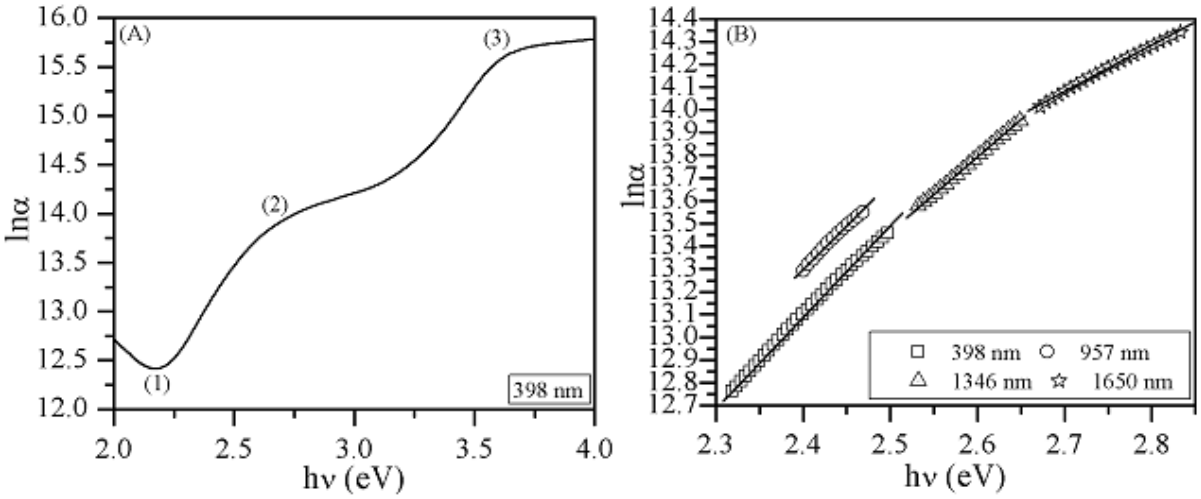

Fig 4.64: ln (α) vs hν plots of (A) 398 and (B) different thicknesses of $Zn_{0.95}Mn_{0.05}O$ films in nitrogen gas environment.

Fig 4.65 show the refractive index (n) as a function of wavelength (nm) of $Zn_{0.925}Mn_{0.05}O$ films at various gas pressures of argon environment. There is no change refractive index with wavelength, the values with working gas pressure ranges from 1.493 – 1.494.

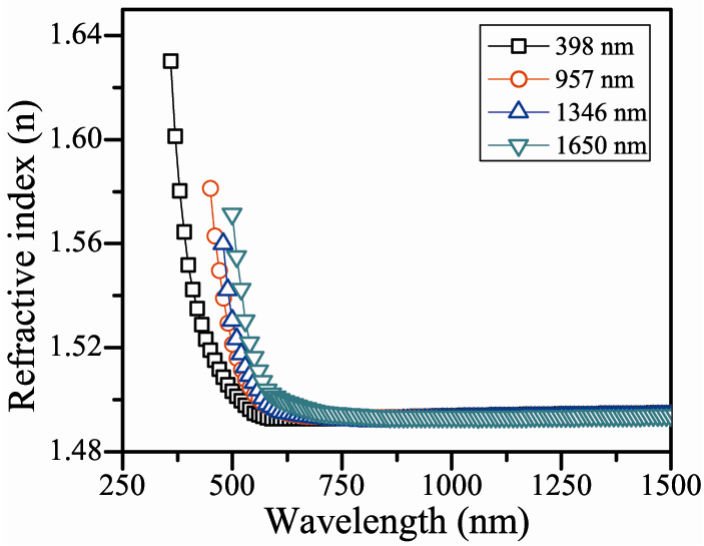

Fig 4.65: Refractive index (n) vs Wavelength (nm) plot of $Zn_{0.925}Mn_{0.05}O$ films at various film thicknesses of argon gas environment.

Figure 4.66 shows the dependence of the extinction coefficient (*k*) on wavelength, λ, for the films deposited with different film thicknesses in argon environment. There is no significant change in extinction coefficient with film thickness. From the plot, it is clear that all the films deposited for different film thicknesses hasd a lower extinction coefficient (i.e more transmission). The extinction coefficient plays a singnificant role in optical absoption process. The variation of extinction coefficient can be related to the variation of transmission.

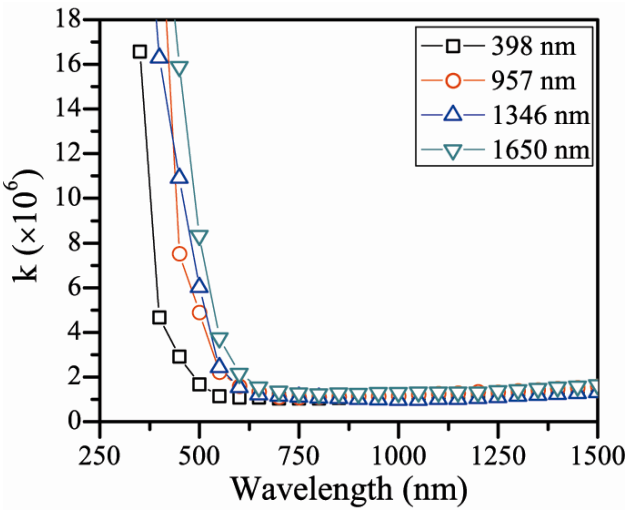

Fig 4.66: Extinction coefficient (k) vs wavelength (nm) of $Zn_{0.95}Mn_{0.05}O$ films at various film thicknesses of (a) 398, (b) 957, (c) 1346 and (d) 1650 nm of nitrogen gas environment.

4.3.2.2 $Zn_{0.95}Fe_{0.05}O$

The RT transmission spectra of Fe5% doped ZnO thin films at various film ticknesses in nitrogen gas atmosphere are shown figure 4.67. The films have high transmittance in the visible region between 86-85 (%). The plots of tramission as a function of wavelength show decrease in transmittance with number of interference fringes increase. This behavior could be due to increase in film thickness with sputter duration. The average thickness of the film from 312 – 850 nm.

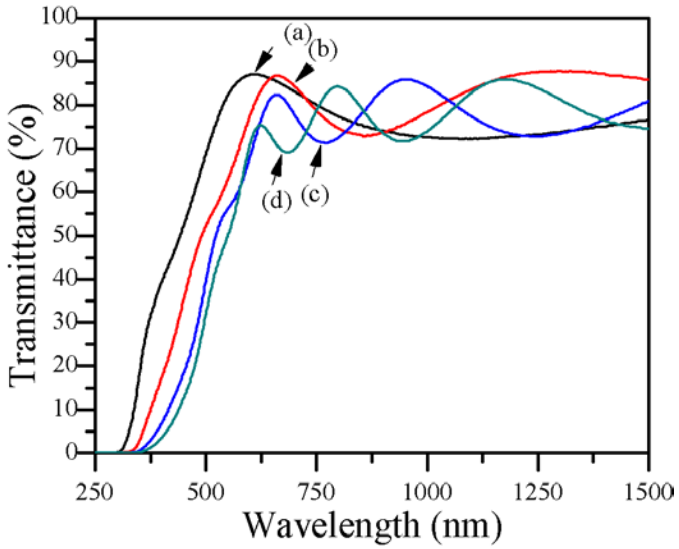

Fig 4.67: RT transmission spectra of $Zn_{0.95}Fe_{0.05}O$ films at various film thicknesses of (a) 312, (b) 588, (c) 684 and (d) 850 nm of nitrogen gas environment.

Fig 4.68 show the $(\alpha h\nu)^2$ vs $h\nu$ plot of Fe5% ZnO films at different film thicknesses in nitrogen gas environment. The direct band gap of the films is decreasing with increase in film thickness in the range of 3.45 – 3.29 eV.

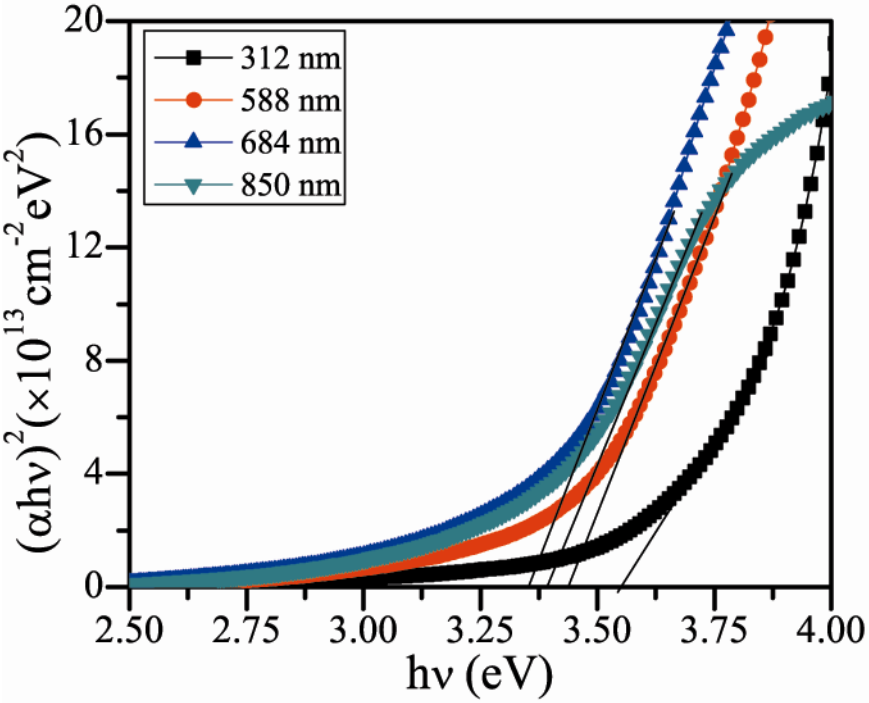

Fig 4.68: Estimated direct band of $Zn_{0.95}Fe_{0.05}O$ films at various film thicknesses of nitrogen gas environment.

Table 4.14: Optical parameters of $Zn_{0.95}Fe_{0.05}O$ films at various film thicknesses.

Time (min)	Thickness (nm)	T (%)	Band gap (eV)	UE (eV)	RI (n)	β (eV)
30	312	86	3.54	0.451	1.497	0.030
60	588	86	3.43	0.707	1.496	0.019
90	684	85	3.39	0.752	1.497	0.018
120	850	85	3.35	0.762	1.496	0.018

Fig 4.69 shows the ln(α) vs hν plot of Fe5% doped ZnO films at various film thickness of nitrogen gas environment. The Urbach energy is increasing with increase in film thickness and the values estimated from ln(α) vs hν plot for different thicknesses are listed in Table 4.14.

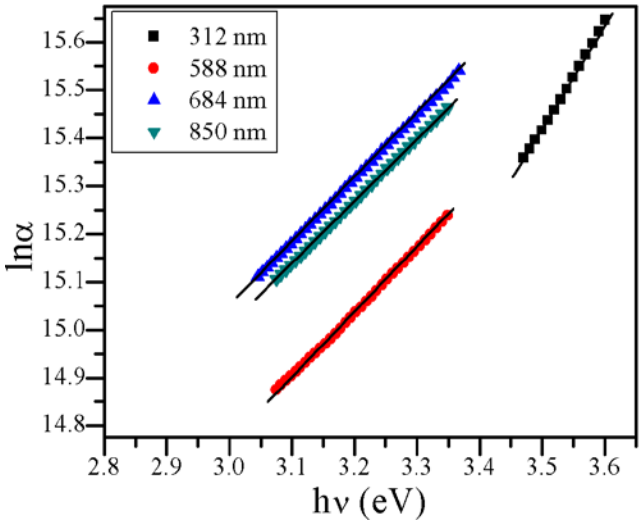

Fig 4.69: ln (α) vs hν plot of $Zn_{0.95}Fe_{0.05}O$ films at various film thicknesses of nitrogen gas environment.

Fig 4.70 show the refractive index (n) as a function of wavelength (nm) of $Zn_{0.925}Mn_{0.05}O$ films at various gas pressures of argon environment. There is no change refractive index with wavelength, the values with working gas pressure ranges from 1.493 – 1.494.

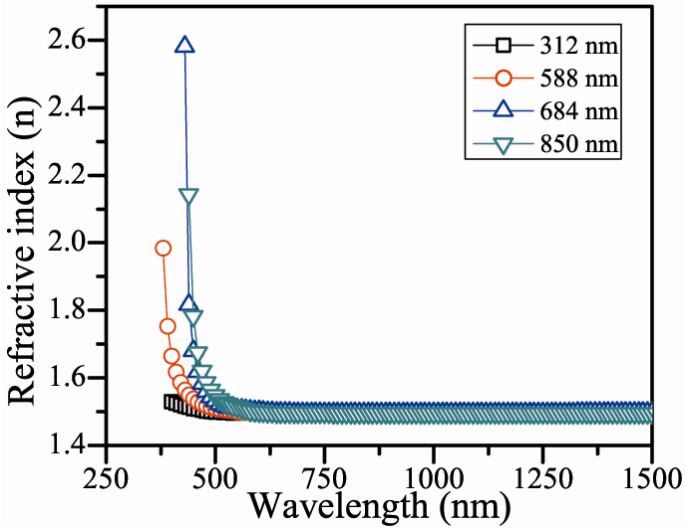

Fig 4.70: Refractive index (n) vs Wavelength (nm) plot of $Zn_{0.95}Fe_{0.05}O$ films at various film thicknesses of nitrogen gas environment.

Figure 4.71 shows the dependence of the extinction coefficient (*k*) on wavelength, λ, for the films deposited with different film thicknesses in nitrgen gas environment. The extinction coefficient sligthly effected by the change in film thickness. From the plot, it is clear that except the films deposited at low thickness about 312 nm had a lower extinction coefficient (i.e more transmission) than those deposited at high film

thicknesses in argon environment. The extinction coefficient plays a singnificant role in optical absoption process. The variation of extinction coefficient can be related to the variation of transmission..

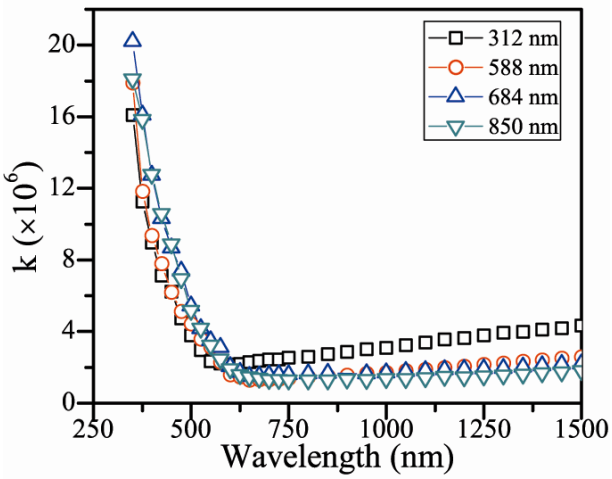

Fig 4.71: Extinction coefficient (k) vs wavelength (nm) of $Zn_{0.95}Fe_{0.05}O$ films at various film thicknesses of nitrogen gas environment.

4.4 Effect of film substrate

The main obejective is study the efffect substrate material on the optical properties of the as deposited films. Thin films of un-doped, Mn, Fe indidual and Mn-Fe co-doped ZnO were deposited on high quality Si (100) substrates in argon and oxygen gas environment. The sputter deposition conditions were kept as for quartz sustrate substrate.

4.4.1 Argon gas environmnet

Figure 4.69 shows the room temperautre reflectance spectra of Mn, Fe and Mn-Fe co-doped ZnO films in argon gas environment. The Mn doped ZnO films show more interference frings and it is decreased for Mn-Fe co-doped ZnO films. The average reflectance of the films was in the range from 0.32 – 0.45.

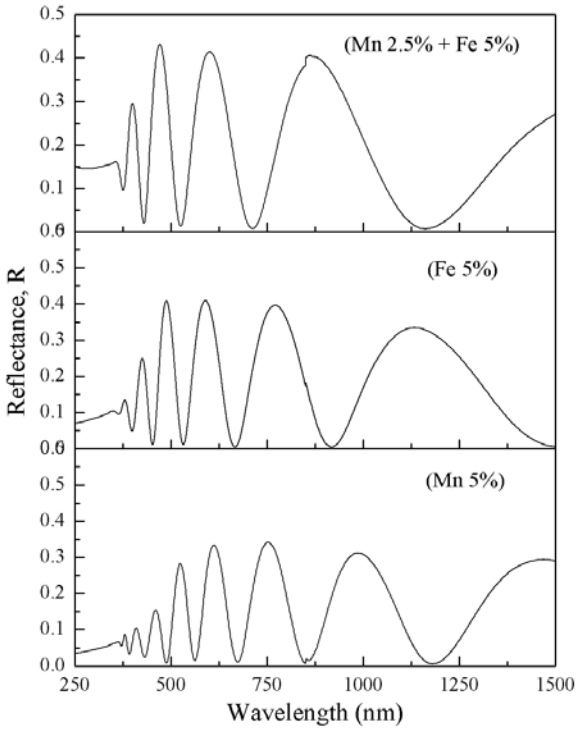

Fig 4.69: RT reflectance spectra of Mn, Fe co-doepd ZnO films on Si (100) substrate in argon gas environment.

The estimated band gap energy from reflectance spectra are shown in Figure 4.70. The energy band gap of as deposited films listed in Table 4.15.

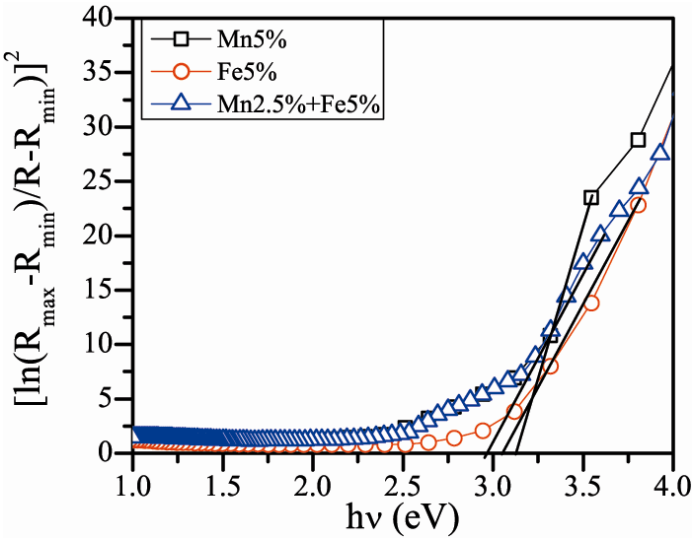

Fig 4.70: Estimated direct band gap of Mn, Fe co-doped ZnO films on Si (100) substrate in argon gas environment.

Table 4.15: Optical energy gap Mn, Fe and Mn-Fe co-doped ZnO films on Si (100) substrate.

Sample	Thickness (nm)	Eg (eV)
$Zn_{0.95}Mn_{0.05}O$	1630	3.21
$Zn_{0.95}Fe_{0.05}O$	1378	3.13
$Zn_{0.95}Mn_{0.025}Fe_{0.05}O$	983	2.98

Conclusions

The conclusions of the study of optical properites of the as deposited films as a function of working gas pressure, thickness and substrate mareial are summarised as follows:

(a) Effect of working gas pressure

- The optical transmission of as deposited un-doped, Mn, Fe doped and Mn-Fe co-doped ZnO thin films have high tansmittance (70 – 93 %) in the visible range of light. The film deposited in oxygen gas show high transmittance (~91-93%) than films in argon gas could be due to oxygen gives less film thickness.

- The direct band gap estimated from transmission spectra of un-doped, Mn, Fe and Mn-Fe co-doped ZnO films was in the range from 3.12 – 3.39 eV. The film deposited in oxygen gas environemnt had higher energy gap than films in argon about 3.04 – 3.39. This behavior might be due to oxygen produces the oxygen difficience or defect concnetration in the film.

- The films with low working gas pressure has high film thckness and it is decreases with increase in gas pressure for Mn, Fe doped ZnO films, whereas for Mn-Fe co-doped it is in reverse direction because of Mn and co-doping hinders the growth of film with variation ioninc radius of dopants in ZnO matrix.

- The Urbach energy of the films have the inverse relation to energy band gap for as deposited films. As band gap decrease the Urbach energy show increase with working gas pressure. This behavior is attributed that presence of impurity bands between valance and conduction bands.

- The refractive index (n) as a function of wavelength has linear beahior, with an average values of refractive index 1.492 – 1.497. Similar kind of behavior was observed for extinction coefficent (k) for Un-doepd, Mn, Fe and Mn-Fe co-doped ZnO films in both argon and oxygen gas environment. The variation of extinction coefficent is realted to transmittance of the films. As the transmittance increases in oxygen gas , the extinction coefficent show decrease.

(b) Effect of films thickness

- The transmittance for un-doped, Mn, Fe and Mn-Fe co-doped ZnO films as a function film thickness is in the range from 84- 94%. The films deposited in nitrogen gas had high transmittance than films in argon gas environment. This phenomina could be due to argon gas gves high rate of depositeion than nitrogen gas in sputtering process.

- There is no significant change in the band gap energy with film thickness with high band gap value for nitrogen gas than films in argon gas environment. The direct band gap of the films with films thickness varied from 3.14 – 3.60 eV.

- The Urbach energy of the films increases with film thickness for all as deopsited films for both in argon and nitrogen gases. The estimated Urbach enrgy of Un-doped, Mn, Fe and Mn-Fe co-doped films is in between 0.144 – 0.762 eV.

- The refractive index (n) with wavelength of as deposited films has no change with film thickness. The extinction coefficent (k) has also show similar behavior as a function of wavlength. The refractive index (n) for un-doped, Mn, Fe and Mn-Fe doped ZnO films with various film thicknesses varies from 1.495 – 1.499 in argon and nitrogen gas environemnt.

(c) Effect of film substrate

- The room temperatur relfetance spectra for Mn, Fe and Mn-Fe co-doped ZnO thin films have multiple interfernece fringes with reflectance 0.32 – 0.52 in the visible range of electromagnetic spectrum. The film deposited in oxygen gas has high refelctance than argon deposited films might be of thcikness difference.

- The energy band gap show decrease with dopant in the films for Mn,Fe and Mn-Fe co-doped ZnO films in argon, but the films in oxygen show increase with dopant in the range of 3.01 – 3.48 eV.

- There is no substrate influence on optical properties of Mn, Fe and Mn-Fe co-doped ZnO films. The best optical proerties acheived for oxygen gas deposited films than argon and nitrogen gas environment and Fe doped ZnO films other dopants of Mn and Mn-Fe co-doped ZnO films in argon and oxygen gases.

Refferences

[1] M.Fox, *Optical properties of solids*, Oxford University press, Great Britain (2001).

[2] J.Singh, *Optical properties of condensed matter and applications*, Wiley, England (2006).

[3] D.Poelman and P.F.Smet, *J.Phys.D:Appl.Phys*. **36** (2003) 1850.

[4] J.C.Manifacier, J.Gasiot and J.P.Fillard, *J.Phys.E:Sci.Instrum*. **9** (1976) 1002.

[5] R.Swanepoel, *J.Phys.E:Sci.Instrum*. **16** (1983) 1214.

[6] E.Marquez, J.R.Malo, P.Villars, R.J.Faray, P.J. S. Ewen, A.E.Owen, *J.Phys.D:Appl.Phys*. **25** (1992) 535.

[7] K.L.Chopra, *Thin film phenomena*, meGrew-Hill, New York (1969).

[8] J. G. E. Gardeniers, Z. M. Rittersma, and G. J. Burger, J. Appl. Phys. **83** (1998) 7844.

[9] S.H.Wemple and M.DiDomenico, *Phys.Rev***23** (1969) 1156.

[10] H.Wemple and M.DiDomenico, *Phys.Rev*.**B3** (1971) 1338.

[11] C. Li, X.C. Li, P.X. Yan, E.M. Chong, Y. Liu, G.H. Yue, X.Y. Fan, Appl. Surf. Sci. **253**
(2007) 4000.

[12] J.Tauc, *Amorphous and liquid semiconductors*, Plenum Press, New York (1972).

[13] A.F.Qasrawi, *Cryst.Res.Technol*. **40** (2005) 610.

[14] F.Wooten, *Optical properties of solids*, Academic Press, New York (1972).

[15] N.Tigau, V.Ciupina and G.Prodan, *J.Crystal Growth*.**277** (2005) 529.

[16] L.Liang, Y.Sheng,Y.Xu, D.Wu, Y.Sun, *Thin Solid Films* **515** (2007) 7765.

[17] Marius Grundmann, *Physics of Semiconductors: An Introduction including Devices and Nanophysics*, Springer, (2006).

[18] C.O.Ayieko, R.J.Musembi, S.M. Waita, B.O. Aduda and P.K. Jain, *International Journal of Energy Engineering* **2(3)** (2012) 67.

[19] Arushanov. E., S. Levcenko, N.Syrbu, V.Tezlevem, M. Merino, M.Leon, *Phys.Sta.Sol (a)* **203** (2006) 2909.

[20] N. Kumar, U.Parihar, R. Kumar, K.J. Patel, C.J. Panchal, N.Padha, *American Journal of Material Science* **2(1)** (2012) 41.

[21] S.Ilican, Y.Caglar and M.Caglar, *J.Optoelectron. Adv. Mater*, **10** (2008) 2578.

[22] Vipin Kumar, Sachin Kr.sharma, T.P.Sharma, Singh, *Optical Materials* **12** (1999) 115.

[23] C. GÜMÜ, O. M. OZKENDIR, H. KAVAK, Y. UFUKTEPE, *J. Opto.Ele. Adv.Mat* **8** (2006) 299.

[24] Lei Zhao, Jianshe Lian, Yuhua Liu, Qing Jiang, *Appl. Surf. Scie* **52** (2006) 8451.

[25] N. Shakti and P.S.Gupta, *Appl.Phys.Res*, **2** (2010) 19.

[26] Xiu-Qin Wang, Jian-Ning Ding, *Proceedings of the IEEE International Conference on Nano/Micro Engineered and Molecular Systems* **5** (2010) 692.

[27] M. Nirmala, A. Anukaliani*, Phot..Lett.Poland* **2(4)** (2010)189.

[28] Ruijin Hong, HeruiWena, CaimingLiu, JinglinChen, JinshengLiao, *Journal of Crystal Growth* **314** (2011) 30.

[29] S. Youssef, ,P. Combette, J. Podlecki,R. Al Asmar and A. Foucaran, *Crystal Growth & Design*, **9** (2009) 1088.

[30] Xue-Yong Li, Hong-Jian Li, Ming Yuana, Zhi-Jun Wanga, Zi-You Zhoua, Ren-Bo Xua, *J. Alloys .Comp* **509** (2011) 3025.

[31] Venkaiah.M, R.Singh, *AIP.Con.Proc*. **1349** (2011) 609.

[32] L. Meng and M. P.Santos, *Appl.Surf.Sci* 68 (1993) 319.

[33] E. S. Tuzemen, Sitki Eker, Hamide Kavak, Ramazan Esen, *Appl.Surf.Sci* **255** (2009) 6195.

[34] E. Marquez, J.R. Malo, P. Villares, R.J. Garay, P.J.S. Ewen, A.E. Owen, J. Phys. D:

Appl. Phys. 25 (1992) 535

[35] J. Sanchez-Gonzalez, A. Diaz-Parralejo, A.L. Ortiz, F. Guiberteau Appl. Surf. Sci.

252

(2006) 6013.

[36] N. Martin, C. Rousselot, C. Savall, F. Palmino, Thin Solid Films 287 (1996) 154

[37] Venkaiah. M, R.Singh, *AIP Conf. Proc*. **1451** (2012) 212.

Chapter 5

Mechanical properties

The mechanical properties like hardness and modulus of elasticity can help in evaluating the reliability of the materials in part and components and to understand the strengthning and deformation mechanism in small scales [1-2]. The design of reliable and functional devices like micro/nano electro mechanical systems (MEMS/ NEMS) relies on the knowledge and understanding of the mechanical behavior of thin film. For mechanical device stability, four material properties of the device components are important: elastic modulus, yield strength, interfacial adhesion and film fracture toughness.

The mechanical proeprties of thin films often differ from those of the bulk materials. Thin films are extremely thermally stable and reasonably hard, but they are fragilie. This can be partially explained by the nanosrutcure of the thin films and the fact that these films are attached to a substrate. Due to typically high yield strength, the thin films can support very high residual stress, this residual stress can be revealed later during processing or in the actual device operation through plastic deformation, thin films fracture or interfacial delamination. Both elastic and plastic properites are important for thin film charecterization [3].

The nanoindentation techniques have been developed for probing mechanical proeprties of thin films[4]. Although, the mechanical properteis of thin films can be measured by tensile tesing of free standing films and by the microbeam cantiliver deflection technique, but the easiest way is by means of nanoindentation.

The nanoindentation is a versatile technique for measuring films mechnaical properties (elasti modulus, hardness, interfacial adhesion and films fracture toughness). During the measurement a sharp diamond indenter is forced into the tested material while continuosly recording both the force and indentation depth. Both elastic modulus and hardness can be readily extracted directly from the nonoindetation curve. Since the depth resolution is on the order of nanometrs, it is possiblie to indent even very thin (100 nm) films. In indentation normally uesd tip is Berkovich triangle tip. Indentation has been

also used to measure the thin films adhesion, where the mechanical energy release rate, or practical work of adhesion is calculated based on the delamination size.

The mechanical and structural properties of fine scale materials are the subject of intense investigations [5]. Both the fundametal and applied problems arise with the decrease in the internal microstructeral length scale to several nanometers. Influence of lengthscale on a variety of physical process such as mechanical strength, work hardning is still not understood. An in-depth knowledge of the microstrucutere is required for its role on mechanical properties of thin films. The fundamental information regarding plasticity in metal thin films on substrates can be obtained by using in-situ transmission electron micorscopy (TEM) [6]. Despite the technical and methodical progress in nanoindentation technique it is still very difficult to obtain accurate values for mechnical properties of coating below 2 μm thickness. To obtain pure film properties the measurement conditions have to be chosen in a way that substrate influence can be minimized.

There are very few nanoindentation studies on ZnO thin films. Mayo et.al. [7] studied the effect of grain size on the hardness strain-rate sensitivity of nanocrystalline bulk ZnO and showed that lower sintering temperatures provide finer grain sizes which tend to promote strain rate sensitivity. Influence of the indentation load, the indentation loading time and the creep behavior during the nanoindentation was studied by Fang et.al.[8] on ZnO. There are no systamatic studies on undoped and 3d TM doped ZnO thin films as a function of working gas atmosphere of argon, oxygen and nitrogen , substrate material , thickness dependence etc. In this chapter the detailed systematic nanoindentation studies on as deposited undoped and doped ZnO thin films (discussed in chapter 3) are presented.

This chapter contains the experimental results of room temperature nanoindetation studies on undoped and TM doped ZnO thin films by rf-magnetron sputtering in argon, oxygen and nitrogen gas environment. This chapter consists three sections i.e (1) effect of indentation load on ZnO thin films, (2) Studies on 3d TM doped ZnO thin films on quartz substrate and (3) Films on Si (100) substrates in argon, oxyegn and nitrogen gas enviornment.

5.1 Analysis

The hardness and Young's modulus as a function of the displacement of the indenter were measured from the laoding- unloading of indenter. A loading –unloading curve is shown in Fig.1. The hardness of a material is defined as resistance to plastic deformation. Thus, hardness H is determained from maximum indentation load P_{max} divided by actual projected contact area A_c and written as:

$$H = \frac{P_{max}}{A_c} \tag{5.1}$$

In depth-sensing nanoindetation, the composite modulus E^* is calculated by [8]:

$$E^* = \frac{\pi S}{2\beta\sqrt{A_c}} \tag{5.2}$$

Where S is the measured stiffenss and β is a shape constant of 1.034 for Berkovich tip. Young's modulus E_m is defined by:

$$E_m = (1 - \nu_m^2)\left(\frac{1}{E^*} - \frac{1-\nu_i^2}{E_i}\right)^{-1} \tag{5.3}$$

Where ν is Poisson ratio, E the Young's modulus, and the subscripts i and m refer to indenter and test material, respectively. Indenter properties used in this study's calculations were E_i = 1141 GPa and ν_i = 0.07 [9] and ν_m is assosiated to be 0.3

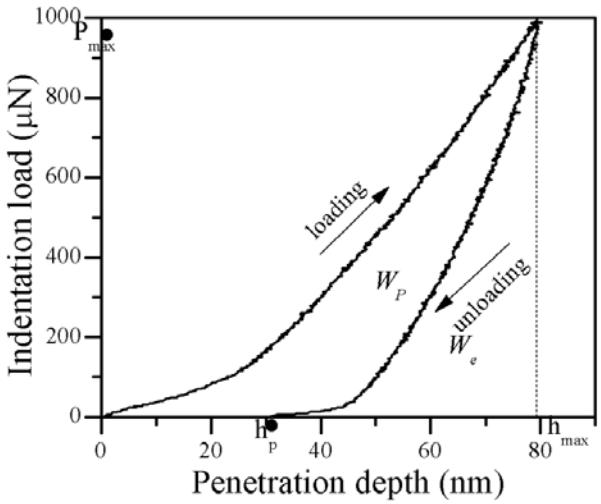

Figure 5.1: The indentation loading –unloading curve at load of 1000 μN in argon gas environment.

In Fig.1 the area under the unloading curve represents the elastic energy deformation and represented by the area designatd as W_e. The area between the loading and unloading curve represents the energy dissipated into the film due to palstic deformation and is represented by the area designated as W_p.

5.2 Effect of indentation load on undoped ZnO thin films

The room temperature mechanical properties of un-doped ZnO as deposited thin films were studied at different indentation loads. The indentation load appiled was in the range 1000μN to 5000 μN. The loading and unloading curves of the films were recorded with maximum indents of 20 for each film. The indentation depths of the film were in the range of 50 - 250 nm, well below the film thickness which is 840 - 1180 nm. The stiffness constant of the films were also extimated from the loading -unloading curves of the nanoindentation data.

5.2.1 Investigation of loading and unloading curve

Figure. 5.2 (a-c) shows the (p-h) curve (penetration depth versus indentation load) for for one indentation on ZnO films deposited under argon, oxygen and nitrogen gas with penetration well below(1/3) the thickness of the films. The films thickness, pentration depth and mechanical properies estimated from loading and unloading curves are listed in table 5.1 – 5.3 for the films indented at indentation loads of 1000 μN, 3000 μN and 5000 μN. In the current study, a continuous loading curve was observed for the films unlike the previous studies on ZnO thin films where a " pop in" (didscontinuous) loading curve is reported [2, 9-10]. In Fig. 5.2, it can be seen that the oxygen gas deposited films show less indentation depth and plastic deformation W_p than the films deposited in argon and nitrogen gas environment. The penetration depth, plastic deformation (W_p) is high for the films deposited in argon and nitrogen gas. The deepest plastic depth was produced for films deposited in argon gas. The overlapping loading curves of argon and nitrogen gas deposited films show that the ZnO film surface properties were similar [8].

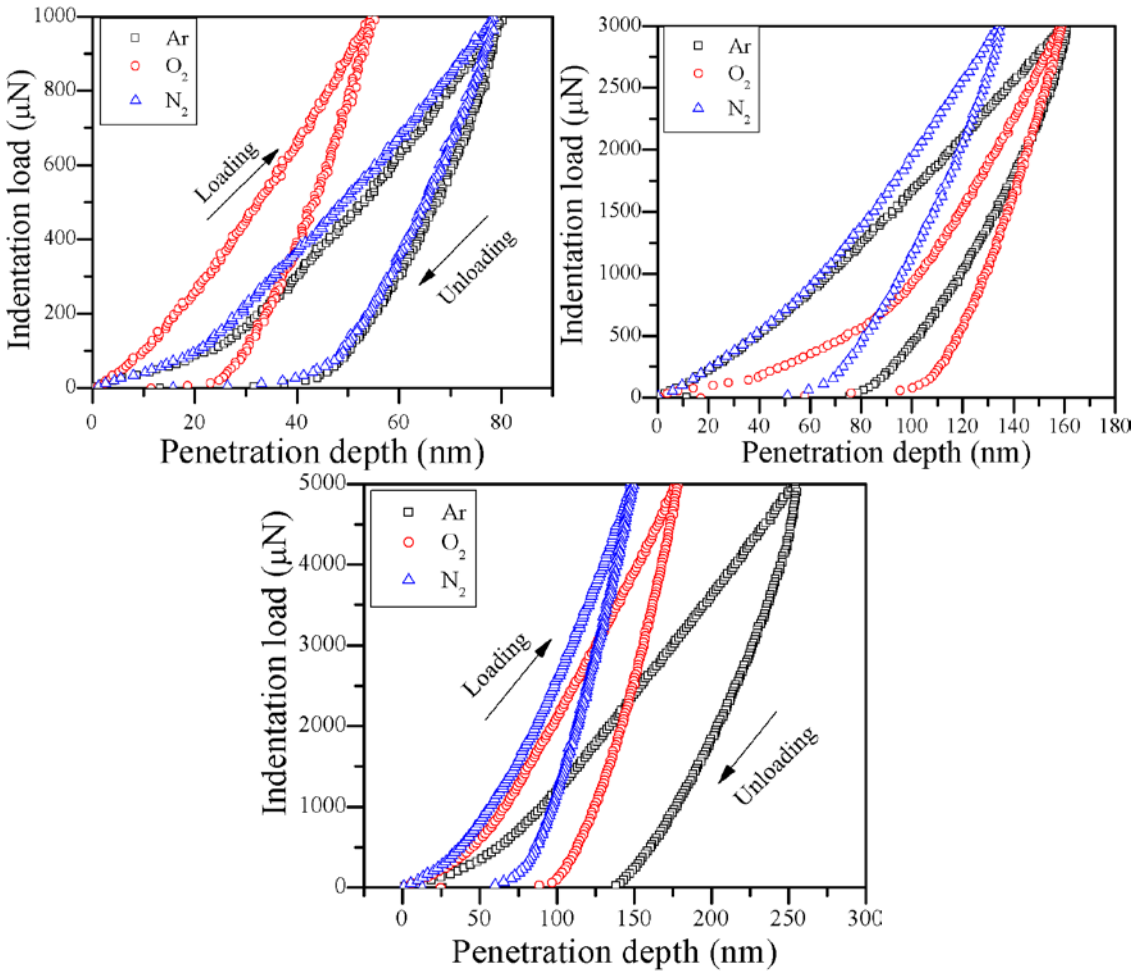

Figure 5.2 (a-c): loading-unloading curves for undoped ZnO thin film at indentation load of 1000μN, 3000μN and 5000μN in (□) Ar, (○) O_2 and (Δ) N_2 working gas environment.

Table 5.1 Mechanical parameters of films at indentation load 1000μN.

	Ar	O2	N2
Thickness(nm)	1067	842	983
Penetration depth (nm)	74-92	51-80	62-70
Young's modulus (GPa)	136-87	233-133	182-127
Hardness (GPa)	11-6	31-8	19-12
Stiffness (μN/nm)	45-39	53-42	49-38

Table 5.2 Mechanical parameters of films at indentation load 3000μN.

	Ar	O2	N2
Thickness(nm)	1067	842	983
Penetration depth (nm)	158-172	113-142	131-141
Young's modulus (GPa)	85-75	166-123	119-102
Hardness (GPa)	8-6	16-9	13-10
Stiffness (μN/nm)	61-57	83-71	64-59

Table 5.3 Mechanical parameters of films at indentation load 5000μN.

	Ar	O2	N2
Thickness(nm)	1067	842	983
Penetration depth (nm)	234-247	175-192	162-145
Young's modulus (GPa)	66-62	136-112	158-137
Hardness (GPa)	6-5	11-8	13-18
Stiffness (μN/nm)	69-67	103-94	96-90

The penetration depth strogly depends on the the maximum indentation load. For a given load highest penetration depth is observed for film deposited in argon gas. The penetration depth is lower for films deposited in oxygen and nitrogen gas. From the loading and unloading curves we can see that the films deposited in argon gas environment have more *plastic deformation*. It is also noticed that at high indentation load the material shows the high plastic nature rather at lower indentation loads.

5.2.2 Young's modulus and hardness

The elastic modulus and hardness of the films at different indentaion loads in argon, oxygen and nitrogen deopsited films as a function of penetration depth are shown in figure 5.3 (a-c).

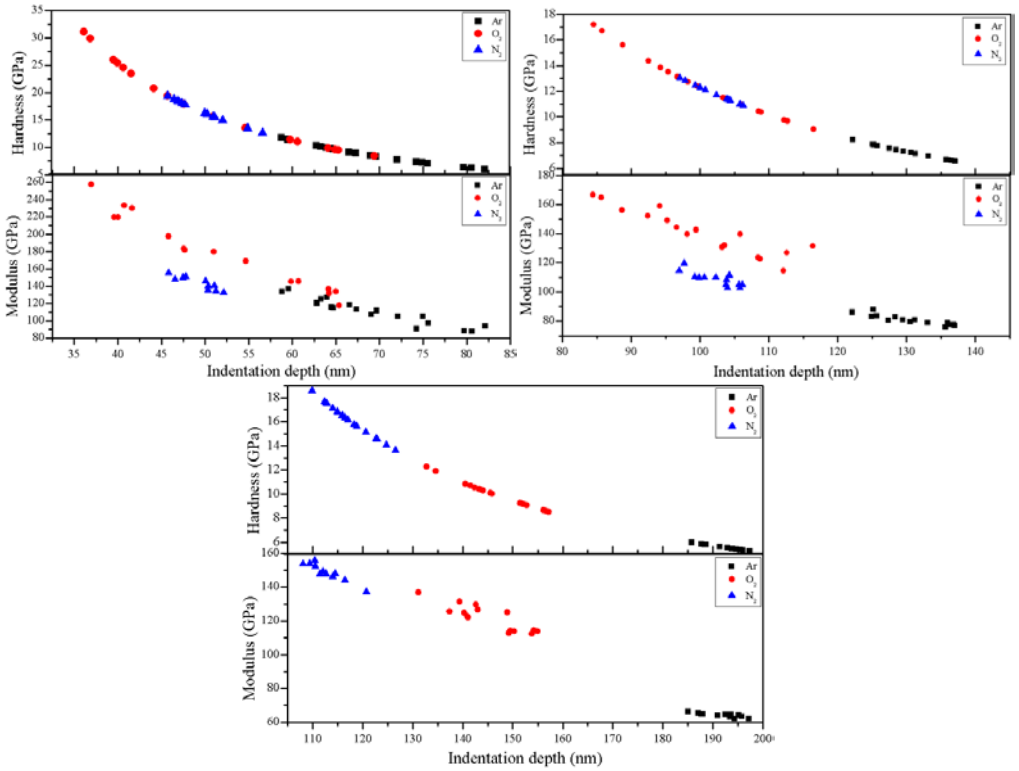

Figure 5.3 (a-c): Young's modulus and hardness of undoped ZnO thin film at indentation load of 1000µN, 3000µN and 5000µN in (■) Ar, (●) O_2 and (▲) N_2 argon, oxygen and nitrogen gas.

At lower load the variation in elastic parametrs is large between the indentation locations. This may be because of film surface morphology. This variation is reduced as the indentation load is increased indicating a more uniform internal stucture of films.

The elastic parameter values decrease with the increase in indentation load (penetration depth) for all the films. These values are strongly dependent on indentation load and the preparation conditions of the films. The decrease in elastic parameters with increase in penetration depth on single crystal of ZnO are reported by Lucca et al. [11] and klopfstein et al.[12]. They have reported the values of elastic modulus and hardness in the range 104 - 134 GPa and 2- 7 GPa, respectivly.

In the present study the maximum value of elastic modulus and hardness in the range 133-233GPa, 8-31 GPa respectively are obtained for the films deposited in oxygen gas under an indentation load of 1000µN. The stiffness of the films for oxygen deposited is

also than that of films deposited in argon and nitrogen gas environment. This may be due to disordered nature of the oxygen deposited thin films.

5.3 Studies on 3d TM doped ZnO thin films on quartz substrate.

Nanoindentation tests were performed for Mn5%, Fe5% and Mn-Fe doped ZnO thin films deposited on fused quartz substrates by rf magnetron sputtering in argon, oxygen and nitrogen gas environment. The room temprature loading and unloading behavior was examined at indentation load of 5000μN for the as deposited films of Mn, Fe and Mn-Fe doped ZnO films. To get best data each film was indented for 20 indents.

5.3.1 Argon environment

The loading and unloading curve for Mn5%, Fe5% and Fe-Mn co-doped ZnO films are shown in figure.5.4. The penetration depth is well below the film thickness for all the films.The loading and unloading curves for individual dopants of Mn and Fe doped ZnO films have close and similar profile than Mn-Fe doped ZnO films. The is no "pop-in" behavior for loading and unloading curve for the films. The mechanical parameters estimated from loading and unloading curves are listed in table 5.4. The Young's modulus and hardness as a function of indentation depth are presented in figure 5.5.

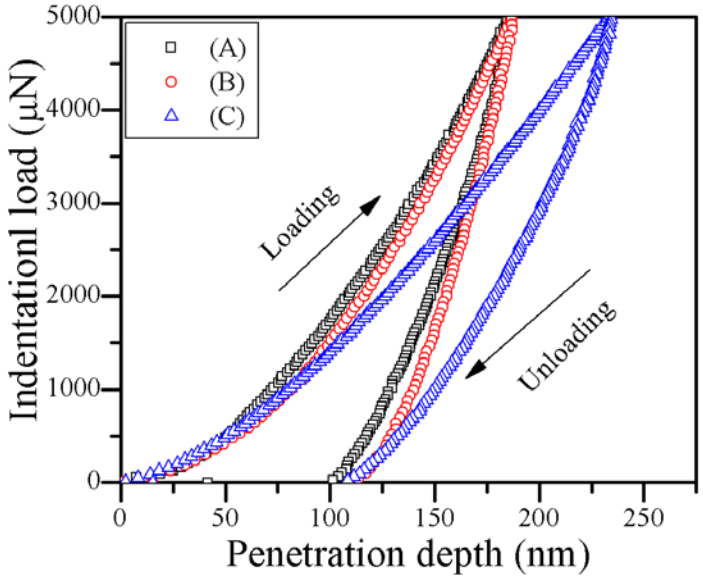

Figure 5.4: Loading-unloading curves at indentation load 5000μN of A(□) Mn5%, B(○) Fe5% and C(Δ) Mn2.5%+Fe5% films in argon environmnet.

Table 5.4: Mechanical parameters of as deposited films of Mn, Fe co -doepd ZnO in argon gas environement.

	Mn5%	Fe5%	Mn2.5%+Fe5%
Thickness (nm)	2861	1234	1280
Penetration depth (nm)	175-205	180-191	225-234
Young's modulus (GPa)	96-114	122-134	61-70
Hardness (GPa)	7-11	8-9	6-7
Stiffness (μN/nm)	82-96	108-110	61-69

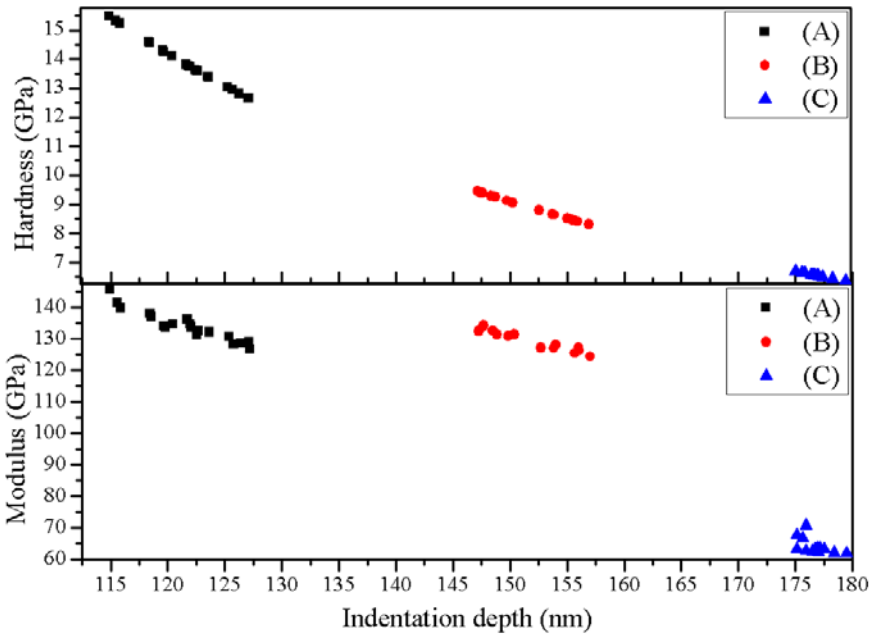

Figure 5.5: Young's modulus and hardness at 5000μN of (■) Mn5%, (●) Fe5 and (▲) Mn2.5%+Fe5% in argon environment.

The higher values of Young's moduls and hardness for Mn doped ZnO thin films could be due to nature of dopant present in the film. The stiffness of the films variation is in the range 82-96 μN/nm, 108 – 110 μN/nm and 61 – 69 μN/nm for Mn, Fe and Mn-Fe doped ZnO films respectively. The Young's modulus and hardness for Fe doped ZnO films has high value in the range of 122 -134 GPa and 8- 9 GPa respectively compared to Mn-Fe and Mn doped ZnO films.

5.3.2 Oxygen environment

The loading and unloading curve for Mn5%, Fe5% and Mn-Fe ZnO films are shown in figure.5.6. The films deposited for Fe doped ZnO has high indentation depth than Mn and Mn-Fe doped ZnO films is about 189-204 No pop-in behavior in loading-unloading curves noticed for any film. The indentation depth and plastic deformation is high for Mn-Fe doped ZnO films than individual dopant of Mn and Fe in the range of 175 – 234 nm.

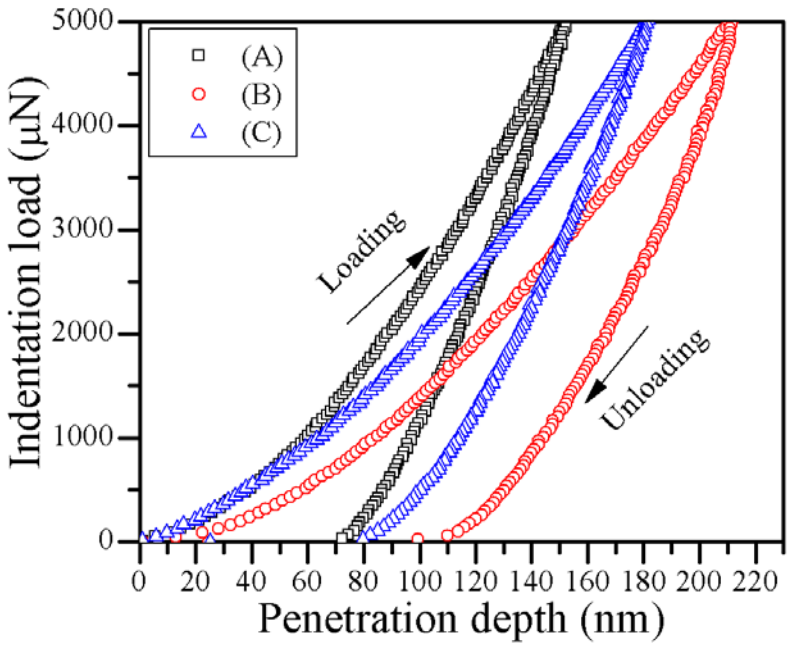

Figure 5.6: Loading-unloading curves at indentation load 5000μN of (□) Mn5%, (○) Fe5% and (Δ) Mn2.5%+Fe5% films in oxygen environment.

Table 5.5: Mechanical parameters of as deposited films of Mn, Fe co -doped ZnO in oxygen gas environment

	Mn5%	Fe5%	Mn2.5%+Fe5%
Thickness(nm)	424	1234	801
Penetration depth (nm)	148-159	204-189	180-183
Young's modulus (GPa)	132-150	90-150	98-101
Hardness (GPa)	15-19	8-9	11-12
Stiffness (μN/nm)	84-87	75-80	72-74

The Young's modulus and hardness as a function of pentration depth are show in the figure 5.7. The mechanical parameters estimated from loading and unloading curves are listed in table 5.5. The Fe doped ZnO films show similar trend as observed in argon gas deposited films. The stiffness varies in the range 84 -87 µN/nm, 75-80 µN/nm and 72 – 74 µN/nm for Mn, Fe and Mn-Fe doped ZnO films.

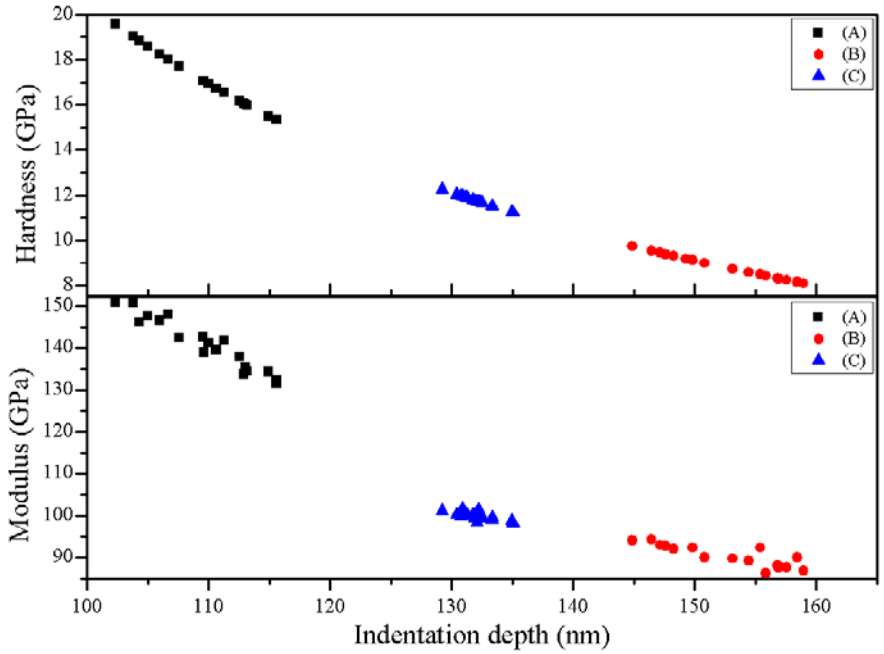

Figure 5.7: Young's modulus and hardness at 5000µN of (■) Mn5%, (●) Fe5 and (▲) Mn2.5%+Fe5% in oxygen environment.

The Young's modulus and hardness is high for Mn doped ZnO than Fe and Mn-Fe doped ZnO films is about 132 -150 GPa and 15- 19 GPa respectively.

5.3.3 Nitrogen environment

The loading and unloading curve for Mn, Fe and Mn-Fe doped ZnO films are shown in figure.5.8. The indentation depth and plastic deformation is high for Mn doped ZnO films compared to Fe and Mn-Fe doped ZnO films. The loading and unloading curve behavior is same for Fe and Mn-Fe doped ZnO films with average penetration depth about 155 – 175 nm .

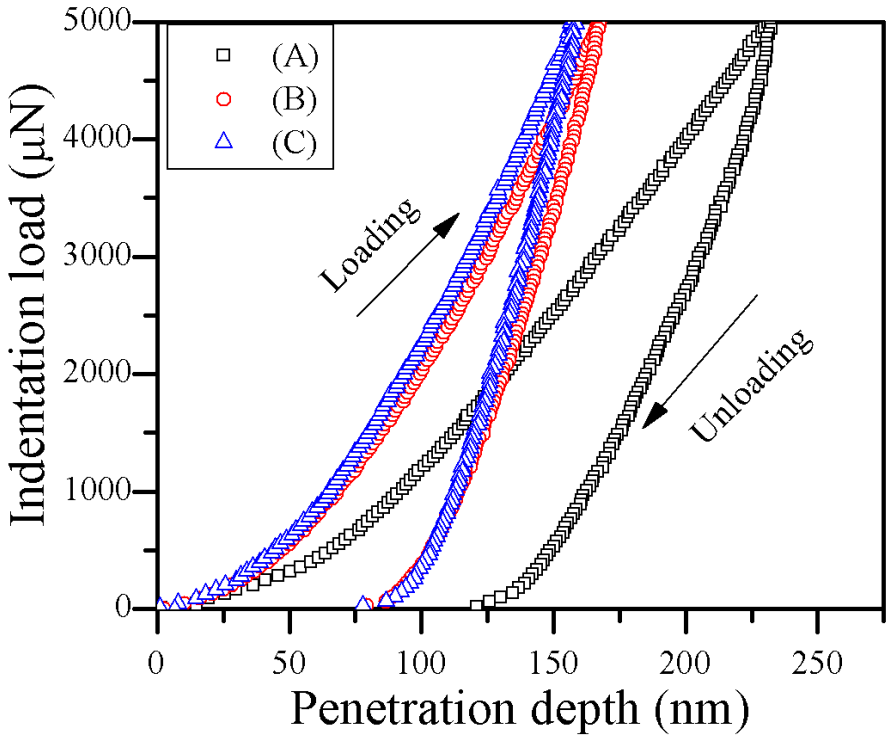

Figure 5.8: Loading-unloading curves at indentation load 5000μN of (□) Mn5%, (○) Fe5% and (Δ) Mn2.5%+Fe5% films in nitrogen environmnet.

Table 5.6: Mechanical parameters of as deposited films of Mn, Fe co -doepd ZnO in nitrogen gas environement.

	Mn5%	Fe5%	Mn2.5%+Fe5%
Thickness(nm)	1650	850	1836
Penetration depth (nm)	204-217	164-175	155-166
Young's modulus (GPa)	71-78	126-134	139-164
Hardness (GPa)	7-8	11-12	10-14
Stiffness (μN/nm)	64-67	93-97	107-114

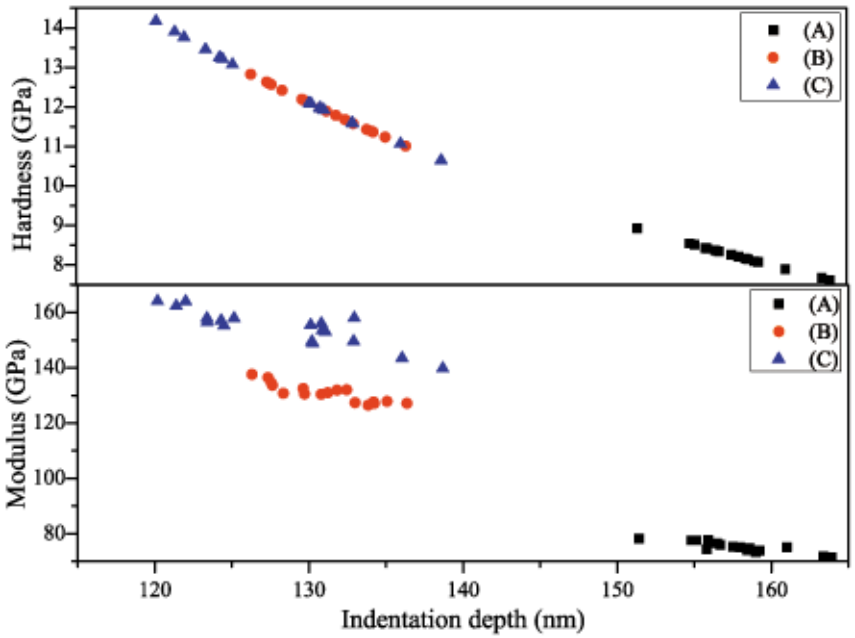

Figure 5.9: Young's modulus and hardness at 5000μN of (■) Mn5%, (●) Fe5 and (▲) Mn2.5%+Fe5% in nitrogen environment.

The stiffness is high for Mn-Fe doped ZnO films about 107 – 114 μN/nm compared to Mn and Fe doped films. Unlike argon and oxygen gas deposited films, the nitrogen deposited films have low hardness values in the range of 10 – 14 GPa.

5.4 Films on silicon substrates

Nanoindentation studies were carried out for Mn, Fe and Mn-Fe doped ZnO thin films deposited on Si (100) substrates in argon, oxygen and nitrogen environment. The room temprature loading and unloading curves were recorded at indentation load of 5000μN. The objective is to study the effect of Si (100) substrate on mechanical properties of thin fims.

5.4.1 Argon gas environment

The loading and unloading curve for Mn, Fe and Mn-Fe doped ZnO films are shown in figure.5.10. There is no indication of *pop-in* for these curves. The mechanical parameters estimated from loading and unloading curves are listed in table 5.7.

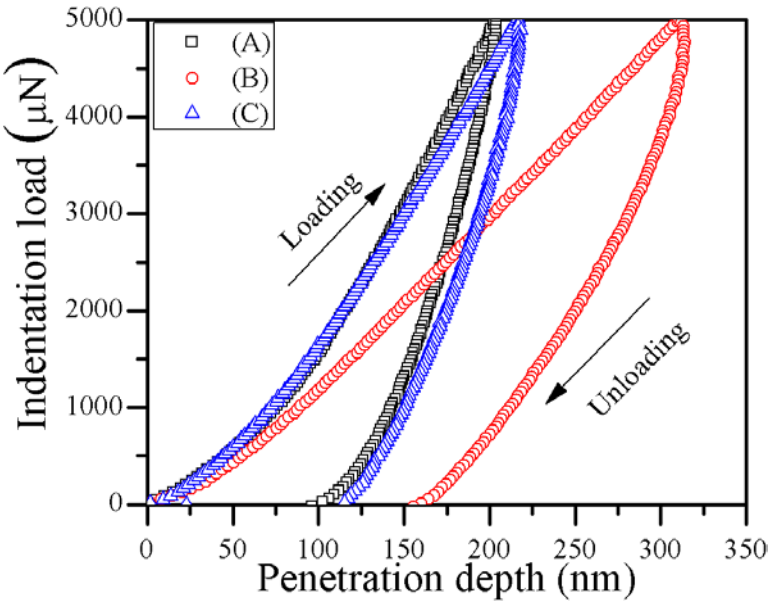

Figure 5.10: Loading-unloading curves at indentation load 5000μN of (□) Mn5%, (○) Fe5% and (Δ) Mn2.5%+Fe5% films in argon environmnet.

Table 5.7: Mechanical propetrties of as deposited of Mn, Fe and co-doepd ZnO thin films in argon environment.

	(A)	(B)	(C)
Thickness(nm)	510	458	521
Penetration depth (nm)	207-213	304-320	218-223
Young's modulus (GPa)	91-96	36-39	78-80
Hardness (GPa)	6-7	2-3	6-7
Stiffness (μN/nm)	87-90	52-54	79-80

The Young's modulus and hardness as a function of penetration depth are show in the figure 5.11. The average modulus values is high for Mn doped ZnO films than Fe and Mn-Fe doped ZnO films in between 91 -96 GPa but the hardness is comparable with that of Mn-Fe doped films . The dopant play significant role in getting the moduls and harndness of the films. The stiffness for Mn, Fe and Mn-Fe doped ZnO films varied from 87 -90 μN/nm, 52-54 μN/nm and 79 – 80 μN/nm respectively.

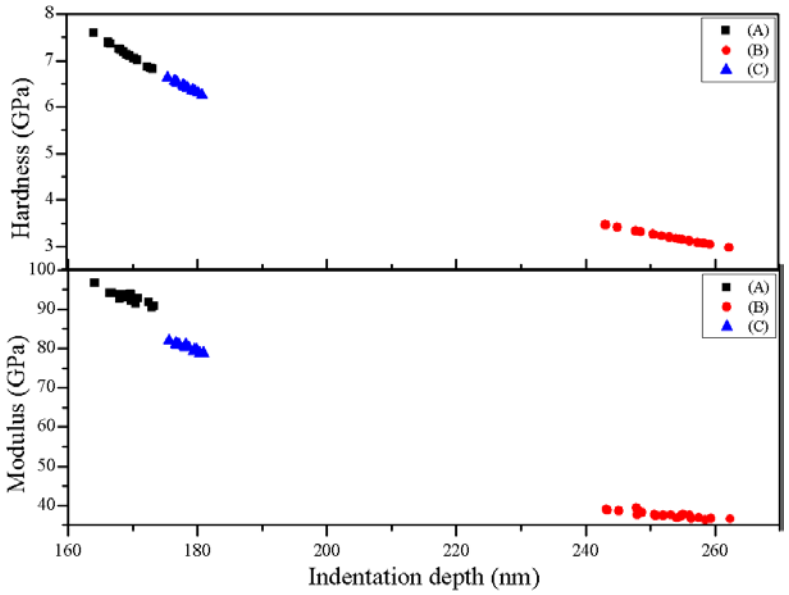

Figure 5.11: Young's modulus and hardness at 5000μN of (■) Mn5%, (●) Fe5 and (▲) Mn2.5%+Fe5% in Argon environment.

5.4.2 Oxygen gas environment

The loading and unloading curve for Mn, Fe and Mn-Fe doped ZnO films are shown in figure.5.12. From the loading and unloading curve we can see irrespective of dopant all the films shown similar behavior of loading and unloading curve. There is no *pop-in* in the indentation curves. The mechanical prameters estimated from loading and unloading curves are listed in table 5.8.

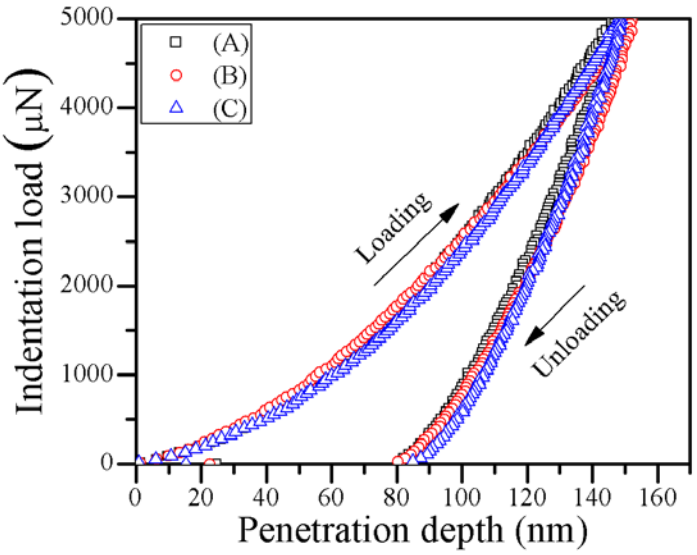

Figure 5.12: Loading-unloading curves at indentation load 5000μN of (□) Mn5%, (○) Fe5% and (Δ) Mn2.5%+Fe5% films in oxygen environmnet.

Table 5.8: Mechanical propetrties of as deposited of Mn, Fe and co-doepd ZnO thin films in oxygen environment.

	Mn5%	Fe5%	Mn2.5%+Fe5%
Thickness(nm)	386	435	410
Penetration depth (nm)	146-151	150-155	152-148
Young's modulus (GPa)	177-166	158-152	184-172
Hardness (GPa)	15-14	15-14	15-13
Stiffness (μN/nm)	112-106	103-99	121-117

The Young's modulus and hardness as a function of pentration depth are show in the figure 5.13. The modulus is high for Mn-Fe doped ZnO films than Mn and Fe individual doped in ZnO films. The hardness values are same for all the doped films.

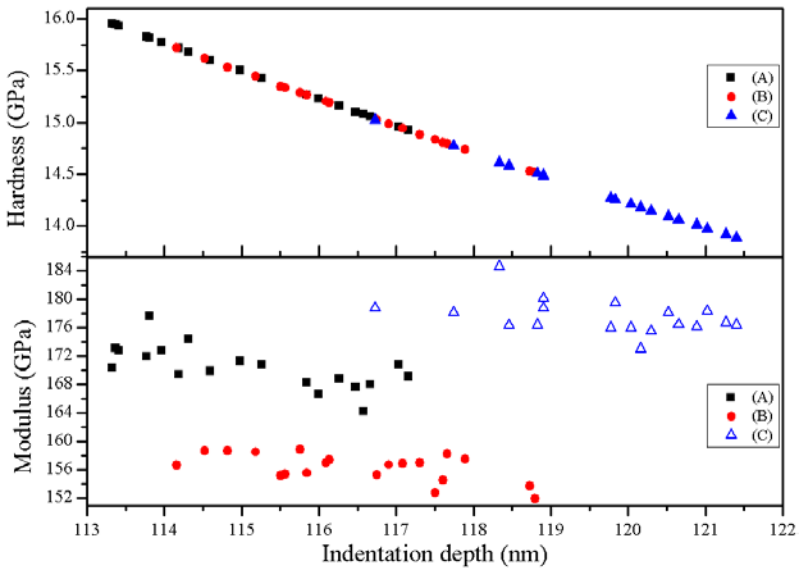

Figure 5.13: Young's modulus and hardness at 5000μN of (■) Mn5%, (●) Fe5 and (▲) Mn2.5%+Fe5% in oxygen environment.

5.4.3 Nitrogen gas environment

The loading and unloading curve for Mn, Fe and Mn-Fe doped ZnO films are shown in figure.5.14. The films indented for Fe doped ZnO had high indentation depth than Mn and Mn-Fe doped ZnO films. The plastic deformation (W_p) is higher for Fe doped ZnO films compared with other doped films.

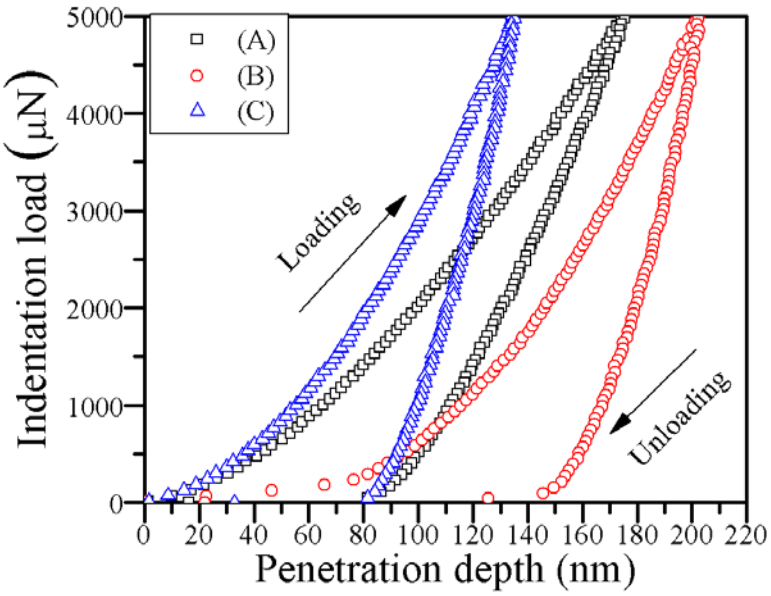

Figure 5.14: Loading-unloading curves at indentation load 5000μN of (□) Mn5%, (○) Fe5% and (Δ) Mn2.5%+Fe5% films in argon environmnet.

Table 5.9: Mechanical propetrties of as deposited of Mn, Fe and co-doepd ZnO thin films in oxygen environment

	Mn5%	Fe5%	Mn2.5%+Fe5%
Thickness(nm)	424	585	453
Penetration depth (nm)	170-175	149-160	105-110
Young's modulus (GPa)	109-104	201-172	241-216
Hardness (GPa)	14-13	13-11	19-18
Stiffness (μN/nm)	73-71	135-122	59-56

The Young's modulus and hardness as a function of pentration depth are show in the figure 5.15. The modulus and hardness for Mn-Fe doped ZnO films is higher than Mn and Fe individual doped films. The Young's modulus and hardness show decrease trend with increase in indentation depth. The stiffness for Fe doped ZnO films had higher values than Mn and Mn-Fe doped ZnO films.

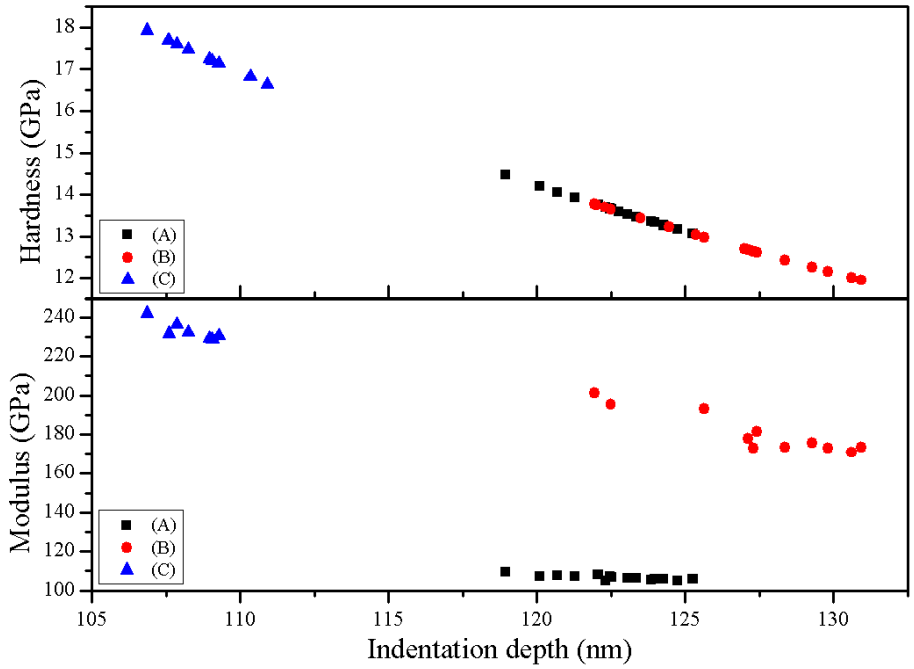

Figure 5.15: Young's modulus and hardness at 5000μN of (■) Mn5%, (●) Fe5 and (▲) Mn2.5%+Fe5% in nitrogen environment.

Conclusions

The summary and conclusions of this chapter are as follows:

- The loading and unloading curves of un-doped and Mn, Fe doped ZnO thin films have no *pop-in* (discontinious) behavior for different indention loads of 1000 µN, 3000 µN and 5000 µN indicating the films are smooth and have homogenious internal structure.

- The penetration depth strogly depends on the the maximum indentation load. For a given load highest penetration depth is observed for film deposited in argon gas. The penetration depth is lower for films deposited in oxygen and nitrogen gas. From the loading and unloading curves we can see that the films deposited in argon gas environment have more *plastic deformation*. It is also noticed that at high indentation load the material shows the high plastic nature rather at lower indentation loads.

- The ZnO films deposited in oxygen gas atmosphere show high mechanical strength than argon and nitrogen which may be due to the disordered nature of the films..

- At lower load the variation in elastic parametrs is large between the indentation locations. This may be because of film surface morphology. This variation is reduced as the indentation load is increased indicating a more uniform internal stucture of films.

- The elastic parameter values decrease with the increase in indentation load (penetration depth) for all the films. These values are strongly dependent on indentation load and the preparation conditions of the films.

- The Mn, Fe and Mn-Fe co-doped ZnO films show elastic modulus which depend on the preparation conditions and indentation load.

- The Mn, Fe co-doepd ZnO films in oxygen gas had high mechancal stability than other gases of argon and nitrogen gases.
- The mechanical parametrs of Mn.Fe and Mn-Fe doped films on Si (100) substrate have higher values compared to the films on fused quartz substrates.

References

[1] P.Parakala, R.A. Mishams, S,Nasrazadani, K.Lian *Effect of thickness and indenter geometry in nanoindetation of Nickel thin films*. University of North Texas, Denton, TX

[2] C.Fischer-Cripps, *Nanoindentation* New York Springer, 2002 P.1-9.

[3] S.Bull. *Mechanical characterization of very thin films*, Newcastle University, UK

[4] R.Bhal, A.Kumar, M.Vedawyas, D.Patel, Appl.Phys.A69 (1999) S643.

[5] E.Arzt, O.Kraft, *Mechanical properties of thin films*, Max-planck-institute for Metallforschung.

[6] M.J.Mayo, R.W.Siegel, Y.X.Liao, W.D.Nix, J.Mater.Res 7(4) (1992) 973.

[7] Te-Hua Fang, Win-Jin Chang, Chao-Ming Lin, Mater.Sci.Eng A 452 (2007) 715.

[8] W.C.Oliver, G.M.Pharr, *J.Mater.Res.* 7 (1992) 1564.

[9] R.Navamathavan et.al, Materials Characterization **59** (2008) 359.

[10] R.Navamathavan et.al Appl.Surf.Sci. **253** (2006) 464.

[11] D.A. Lucca, M.J.Klopfstein, R.Ghisleni, G.Cantwell, *Ann. CIRP* 51 (2002) 483.

[12] M.J.Klopfstein, D.A. Lucca, G.Cantwell, *Phys.Status Solidi* (a) **196** (2003) R1.

Chapter 6

Magnetic studies

This chapter contains the magnetic studies on undoped and 3d transition metal (Mn, Fe) doped ZnO rf-sputtered thin films at room temperature. The main objective of the study is to understand the influence of working gas pressure, film thickness and substrate material on the room temperature magnetic properties of the rf-sputtered films.

6.1 Effect of working gas pressure

The room temperature magnetic properties of undoped and Mn5%, Fe5% and Mn2.5%+Fe5% doped ZnO thin films described in chapter 3 were carried out using a Vibrating Sample Magnetometer (VSM). The magnetic measuremetns were carried out with applied field of ±10 kG in the film plane direction. The diamagnetic contribution from substrate (quartz) was substracted from the raw data for all the samples. The sample dimensions of ~ 1 cm length and 0.5 cm breadth were kept for all the films.

6.1.1 Argon environment

6.1.1.1 Undoped ZnO

Several samples of the undoped ZnO were studied. Only one sample showed significant paramagnetic magnetic moment at room temperature. All other thin film samples showed diamagnetic behaviour. Fig 6.1 shows *M-H* plots for the film deposited at 9.7 mTorr of argon gas pressure.

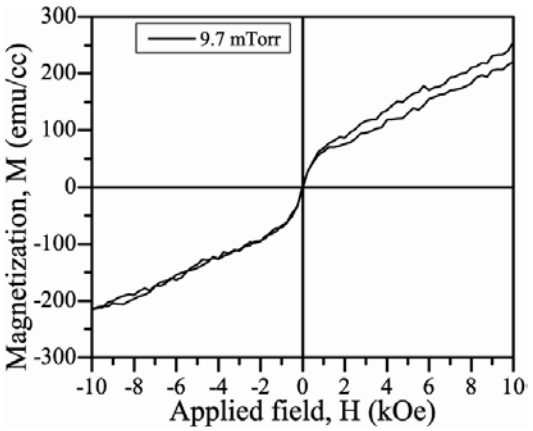

Figure 6.1: Room temperature curves of M-H curves of ZnO thin films deposited at of different working gas pressure in argon environment.

There are reports of ferromagneitsm in ZnO films not due to interface effects [2]. Ferromagetic singnature in ZnO films [3, 4] is dominated by diamagnetic signals from the sample because this behavior is not coming from the presence of exchange interactions but from the host ZnO matrix. There are reports on ZnO exibiting paramagnetic [6] behaviour as well as room teperature ferromagetism [7].The films prepared by spraypyrolysis donot show clear hystersis loops [8]. The ZnO films deposited on suphhire show ferromagetism by PLD show ferromagnetism [10,11]. The superparamangetic behavior observed for this sample could be due to the oxygen defects in the films created during the deposition process.

6.1.1.2 $Zn_{0.95}Mn_{0.5}O$

Figure 6.2 shows the magnetic hysteresis loops of $Zn_{0.95}Mn_{0.5}O$ films coated at different gas pressures after subtracting the diamagnetic contribution from quartz substrate. The hysteresis curves show weak ferromagnetic for the films deposited upto 12 mTorr of argon gas pressure. The films deposited at 15 mTorr of argon working gas pressure show paramagnetic behavior. The films show saturation magnetization (M) and coercive field (H) in the range of 4-8 (emu/cc) and 226 – 387 Oe respectively. The film deposited at 12 mTorr pressure has coercive field of 387 Oe and magnetization ~ 5 (emu/cc). The magnetic parameters extracted from hysteresis loops are listed in table 6.1

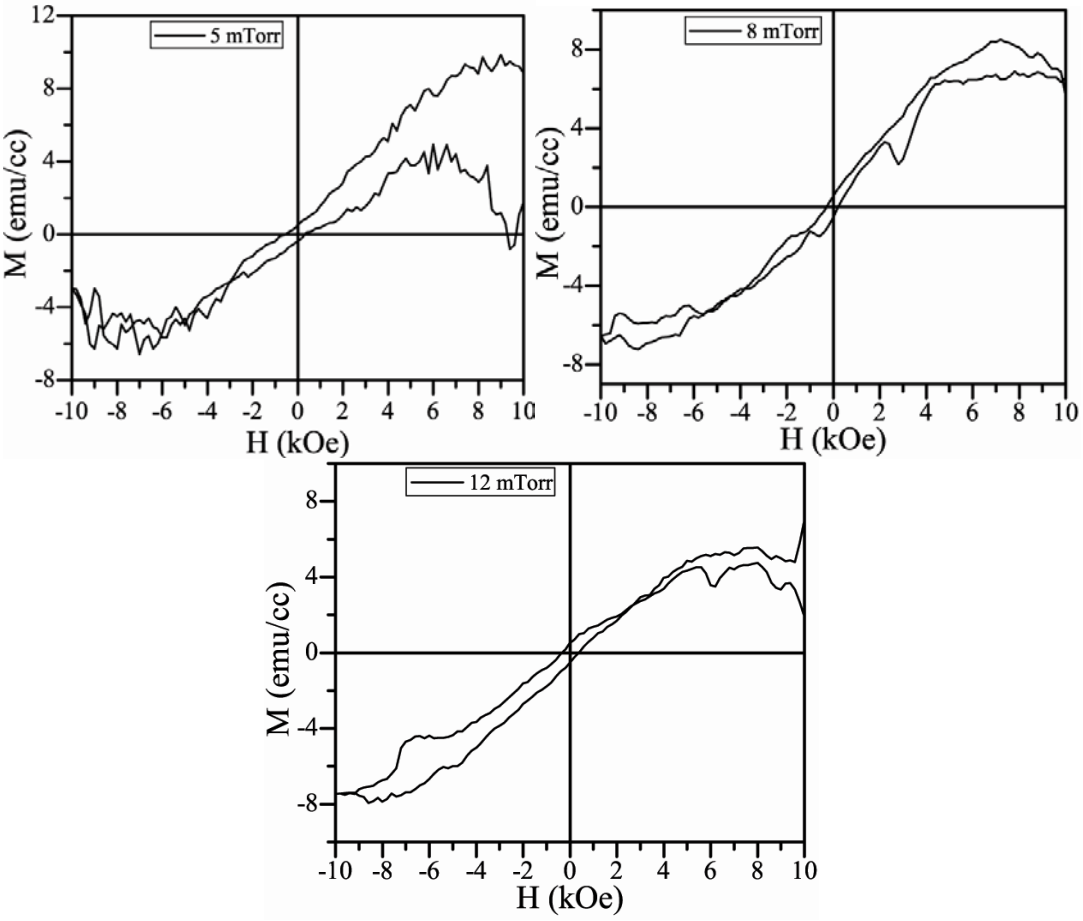

Figure 6.2: M-H curves of $Zn_{0.95}Mn_{0.05}O$ thin films coated different working gas pressure in argon environment.

Table 6.1 The estimated magnetic parameters from M-H curves of $Zn_{0.95}Mn_{0.05}O$ thin films.

P (mTorr)	**t (nm)**	**M_S (emu/cc)**	**H_C (Oe)**
5	1003	4	337
8	924	8	226
12	895	5	387

The Mn doped ZnO sample shows clear ferromagetism [9]. The obeservation of room temeprature ferromagnetism present in ZnMnO hollow spehrical system is related only to the incorporation of Mn^{2+} ion into the host lattice. The films deposited in the mixture of argon +oxygen show ferromagetism [12,13]. The Room tempearature ferromagnetism in ZnMnO nanorods has also been reported [14]. The growth process and role of lattice

defects have to be taken into account in the films. The possible extrinsic source for the observed ferromagnetism may be Mn-based oxides. An exception is ferromagnetic Mn_3O_4 [5]. However, Mn_3O_4 phase has not been detected by XRD and hence cannot cause the observed ferromagnetism. Among the Mn oxides, MnO is antiferrromagnetic with a Neel temperature 96 K while Mn_3O_4 is ferromagnetic with Curie temperature of 43 K. The formation of these oxides are unlikely to give rise to RT ferromagnetism. The presence of ferromagnetic nature can be attributed to the Mn^{2+} ions replacing the Zn^{2+} ions in the host ZnO matrix or another possible reason could be grain boundary scattering in the films.

6.1.1.3 $Zn_{0.9}Fe_{0.5}O$ thin films

The (M-H) plots for $Zn_{0.9}Fe_{0.5}O$ thin films deposited at different working pressures of Ar at room temperature are shown in figure 6.3. The magnetic parameters extracted from hysteresis loops are listed in the table 6.2. The films deposited at 12 mTorr of argon gas pressure show diamagnetism.

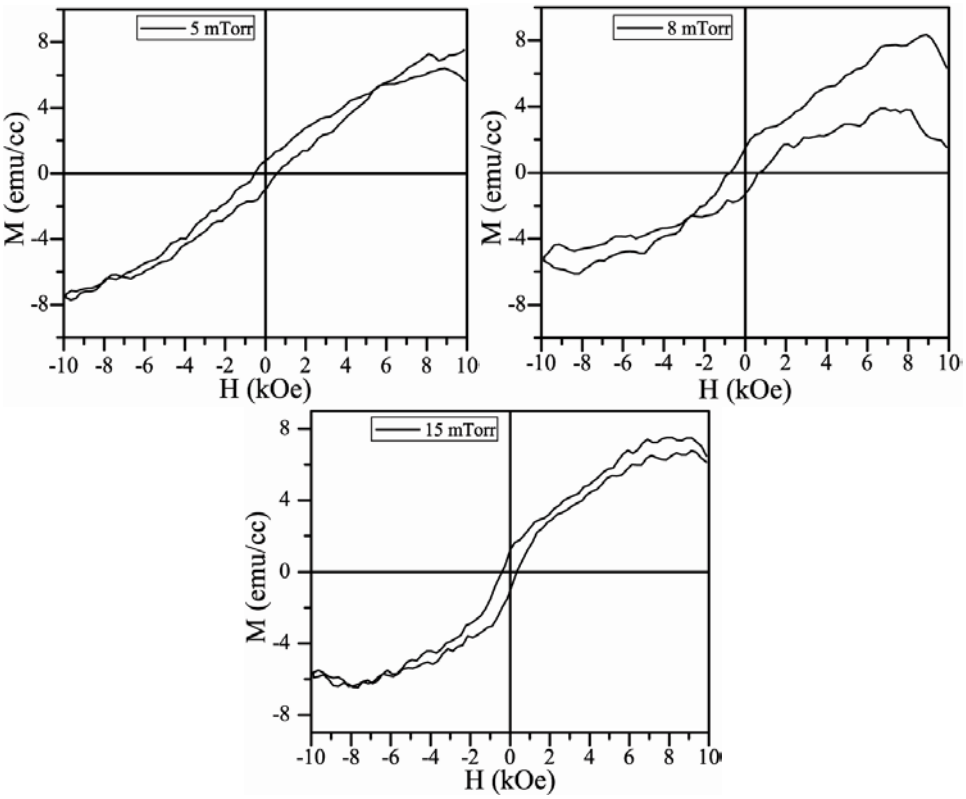

Figure 6.3: M-H curves of $Zn_{0.95}Fe_{0.05}O$ thin films of different working gas pressure in argon environment.

Table 6.2 magetic prarameters of undoped $Zn_{0.95}Fe_{0.05}O$ thin films.

P (mTorr)	t (nm)	M_S (emu/cc)	H_C (Oe)	M_R (emu/cc)
5	837	7	600	0.7
8	785	6	644	1.4
15	705	8	349	1.1

The absence of room tempeerature ferromageitsm in Fe implanted ZnO hydrothermally grown films is reported by D.Wanga *et.al* [15]. The dominent paramagnetism is obeserved in ZnFeO films deposited by sprapyrolysis [16]. The observed room temperature ferromagetism in these films could arise from a number of possiblilties [17]. The existence of secondary phase such as Fe metal, FeO and Fe_3O_4 in the films have been ruled out. Therefeore, ferromagnetism is expected to arise from the intrinsic exchange interaction of magetic moments in the doped films. As for as Fe-doped ZnO films concerned the magnetic properties have some discrepancies. Hong et.al [18] revealed that the origin of magetic properties was due to the defects on Zn site and Fe doping did not play any role in introducing magnetism in ZnO. Lin et.al [19] disclosed that Fe atoms get dissolved in the ZnO lattice in Fe^{2+} and Fe^{3+} state which was beneficial for the magetic origin in Fe-doped ZnO films. In addition Chen [20] discovered that Fe elements formed Fe^{2+} only which played a key role in the magnetic origin. Electronic structure calculation suggest by Karmakar et.al [21] showed that the hole doping (Zn vacancy) is more effective in stabilizing ferromagetism in Fe-doped ZnO. Ferromagnetism in Fe doped nanocrystalline ZnO sample is ascribed to presence of oxygen vacancies [22]. The magnetic origin in Fe doped ZnO films still remains to be understood and needs more studies to be carried out.

6.1.1.4 $Zn_{0.925}Mn_{0.025}Fe_{0.05}O$

Figure 6.4 shows the M-H curves for $Zn_{0.925}Mn_{0.025}Fe_{0.05}O$ films at room temperature with working gas pressure 5-15 mTorr. The M-H curves for 5 and 12 mTorr samples are linear with zero coerscive field (Hc) typical of paramagnetic sample. For 8 and 15 mTorr films, the signature of ferromagetism have been observed.

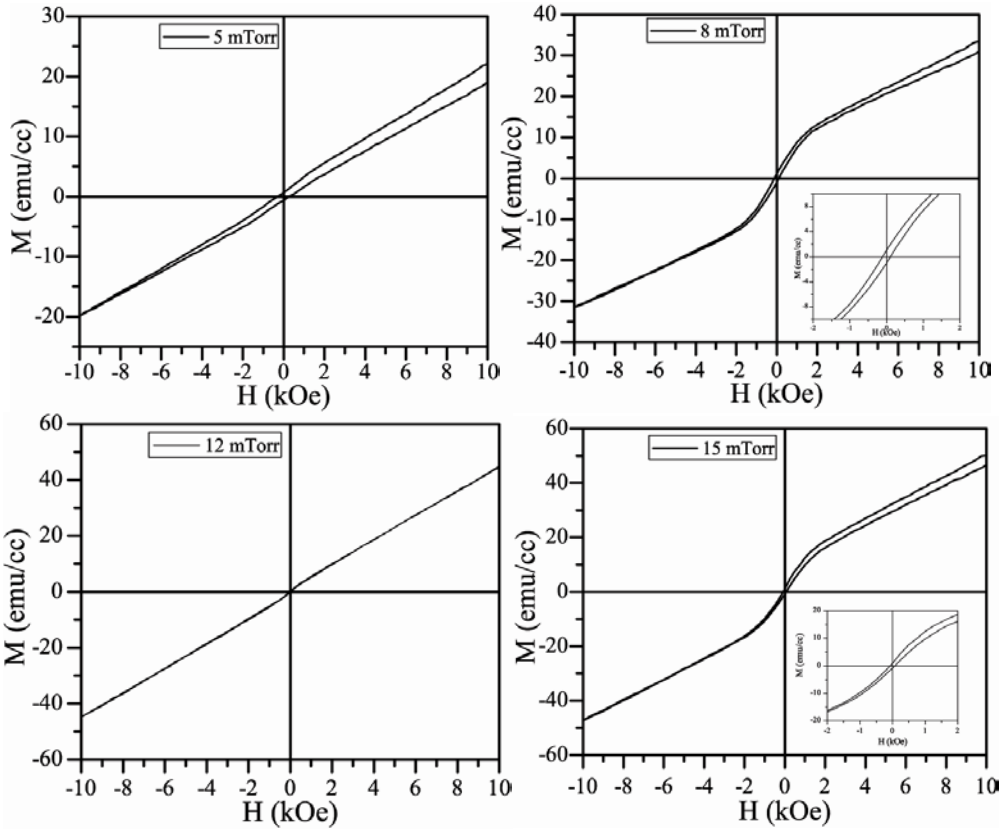

Figure 6.4: M-H curves of $Zn_{0.925}Mn_{0.025}Fe_{0.05}O$ thin films of working gas pressure from 5-15 mTorr in argon environment.

The films deposited at 15 mTorr gas pressure shows superparagnetic behaviour arising due to the existance of ferromagnetic clustrs with (Ms) of ~8 emu/cm^3 and coercivity (Hc) of 71 Oe. The ferromagnetism in these films can be ascribed to several factors as discussed in earlier section.

6.1.2 Oxygen environment

The room temperature magnetization studies were carried on undoped, Mn, Fe and co-doped ZnO thin films deposited by rf-magnetron sputtering in oxygen gas environment pressure of 7-18 mTorr.

6.1.2.1 Un doped ZnO

The (*M-H*) curves for undoped ZnO films are shown figure 6.5. Both the as deposited films show superparamgnetic behavior because of FM clusters. These results are similar to reported by Mal *et al* [23].

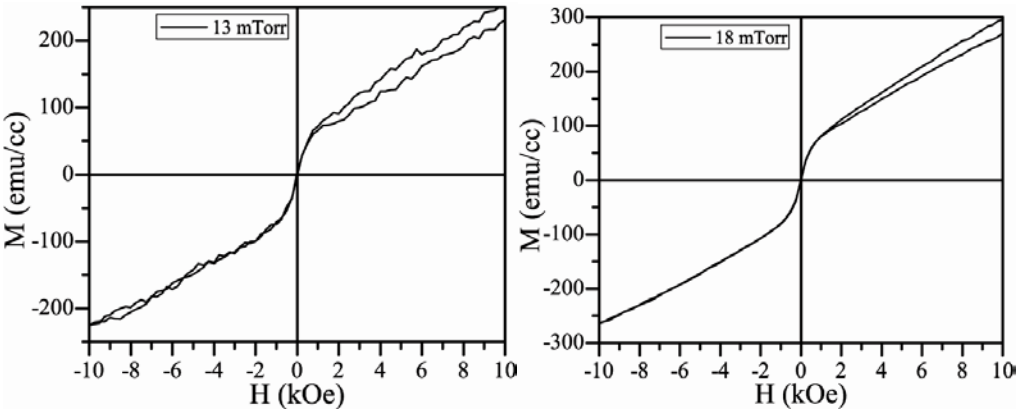

Figure 6.5: M-H curves of ZnO thin films of working gas pressure varies from 7-18 mTorr in oxygen environment.

6.1.2.2 $Zn_{0.95}Mn_{0.05}O$

Magnetic measurements on as-deposited $Zn_{0.95}Mn_{0.05}O$ thin film samples prepared under different working gas pressures are shown in figure 6.6. The estimated magnetic parameters obtained from hysteresis loops are listed in table 6.3.

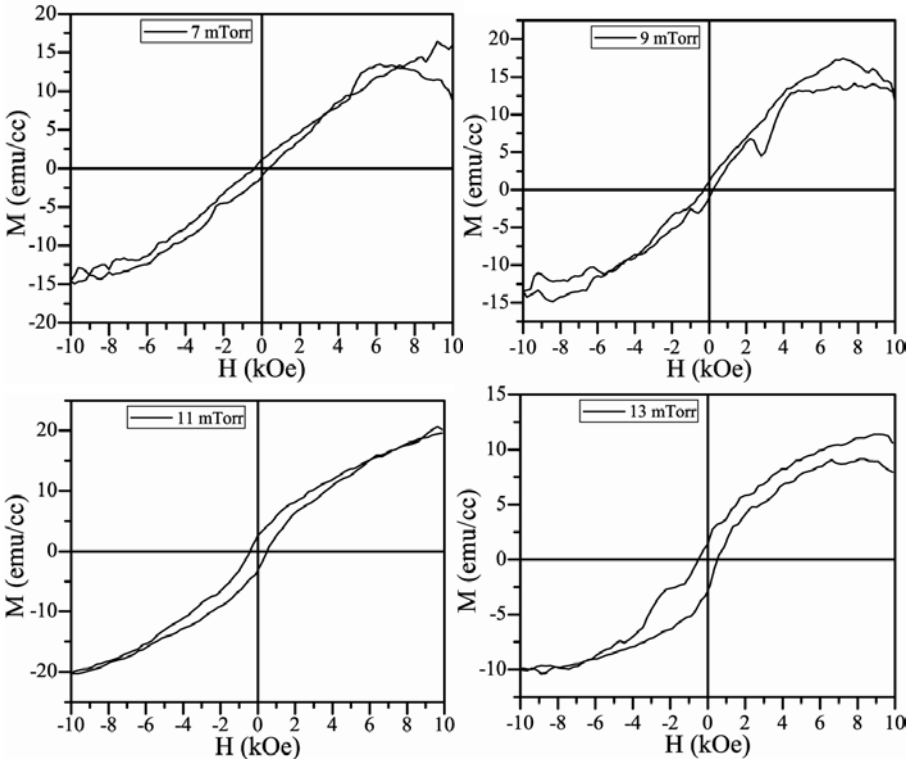

Figure 6.6: M-H curves of $Zn_{0.95}Mn_{0.05}O$ thin films of working gas pressure varies from 7-13 mTorr in oxygen environment.

Table 6.3 The estimated magnetic prarmeters of $Zn_{0.95}Mn_{0.05}O$ thin films in oxygen environment.

P (mTorr)	t (nm)	M_S (emu/cc)	H_C (Oe)	M_R (emu/cc)
7	398	13	369	1.09
9	450	17	221	1.06
11	405	20	516	2.56
13	424	10	534	1.43

6.1.2.3 $Zn_{0.95}Fe_{0.05}O$

The room temperature magnetic hysteresis loops of $Zn_{0.95}Fe_{0.05}O$ thin films are shown in figure 6.7. The films show ferromagnetism for different working gas partial pressure except the films deposited at 13 mTorr of oxygen gas pressure. The estimated magnetic parameters are summarized in table 6.4.

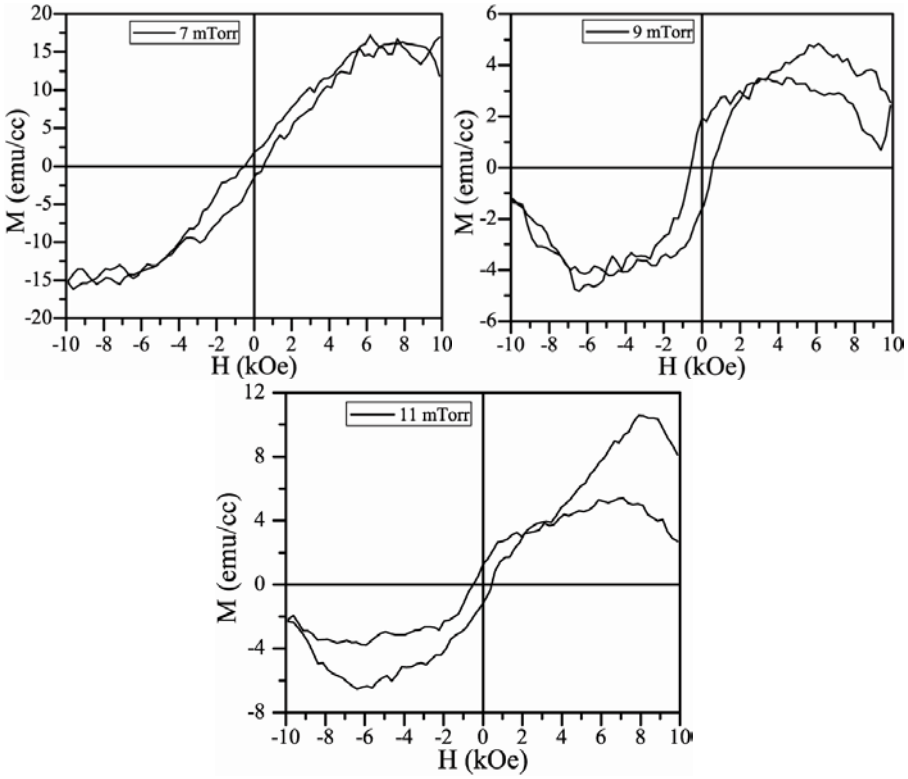

Figure 6.7: M-H curves of $Zn_{0.95}Fe_{0.05}O$ thin films of working gas pressure from 7-13 mTorr in oxygen environment.

Table 6.4 The estimated magnetic prarmertets of $Zn_{0.95}Fe_{0.05}O$ thin films.

P (mTorr)	t (nm)	M_S (emu/cc)	H_C (Oe)	M_R (emu/cc)
7	265	16	510	1.7
9	394	5	557	2
11	430	6	441	1.2

6.1.2.4 $Zn_{0.925}Mn_{0.025}Fe_{0.05}O$

The *M-H* loops of $Zn_{0.925}Mn_{0.025}Fe_{0.05}O$ thin films for different working gas pressures of oxygen are shown in figure 6.8. These plots indicate the paramagnetic behavior of the films deposited in oxygen gas environment.

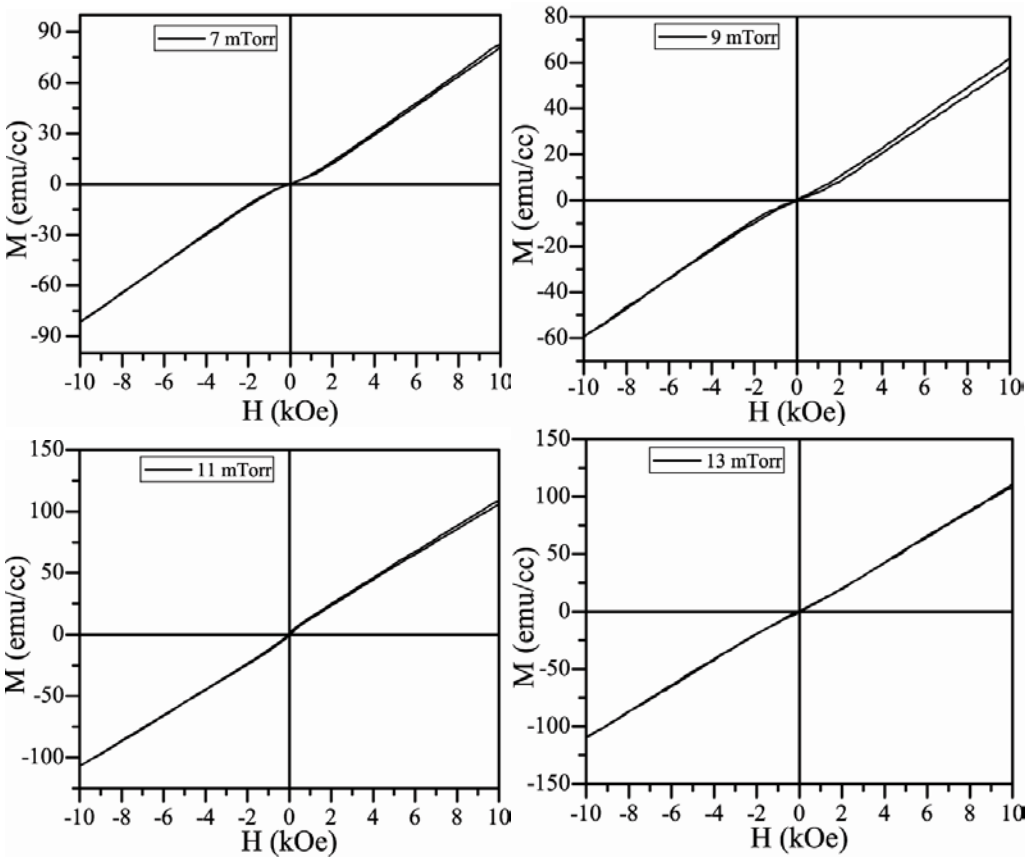

Figure 6.8: M-H curves of $Zn_{0.925}Mn_{0.025}Fe_{0.05}O$ thin films working gas pressure from 7-13 mTorr in oxygen environment.

6.2 Effect of film thickness

The room temperature (RT) magnetization studies were conducted for Mn, Fe doped ZnO thin films as a function of film thickness in argon and nitrogen gas environment. The magnetization versus magnetic field (*M-H*) hysteresis loops were recorded at room temperature in applied field of ± 10 kG in the film plane. The main objective is to study the effect of film thickness on the room temperature magnetic properties.

6.2.1 Argon environment

The RT magnetization studies on Mn, Fe doped ZnO films as a function of film thickness in argon gas environment were recorded in plane to the applied magnetic field. The diamagnetic contribution of quartz substrate was subtracted from raw data. The Fe doped ZnO films show higher magnetization than the Mn doped ZnO films might be due to nature of dopnat element. The films thickness doesn't have any influence on magnetic properties of the as deposited films.

6.2.1.1 $Zn_{0.95}Mn_{0.05}O$

The magnetization versus magnetic field (*M-H*) curves for $Zn_{0.95}Mn_{0.05}O$ films as a function of film thickness are shown in the figure 6.9. The substrate background signal is subtracted from the raw data. The paramagnetic behavior is observed for thicker films.

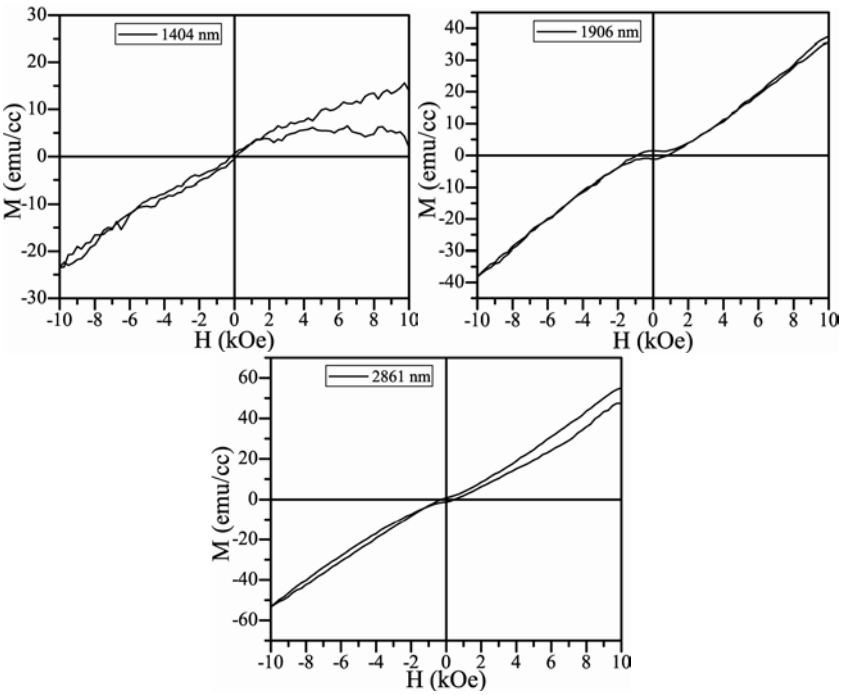

Figure 6.9: M-H curves of $Zn_{0.95}Mn_{0.05}O$ thin films of different film thickness in argon environment.

6.2.1.2 $Zn_{0.95}Fe_{0.05}O$

Figure 6.10 show the *M-H* plots of $Zn_{0.95}Fe_{0.05}O$ thin films for different thickness at an applied magnetic field of ±1 Tesla in the plane of the thin film. The as deposited films show paramagnetic behavior with increase in film thickness. The M-H plots show hysteresis with no saturation.

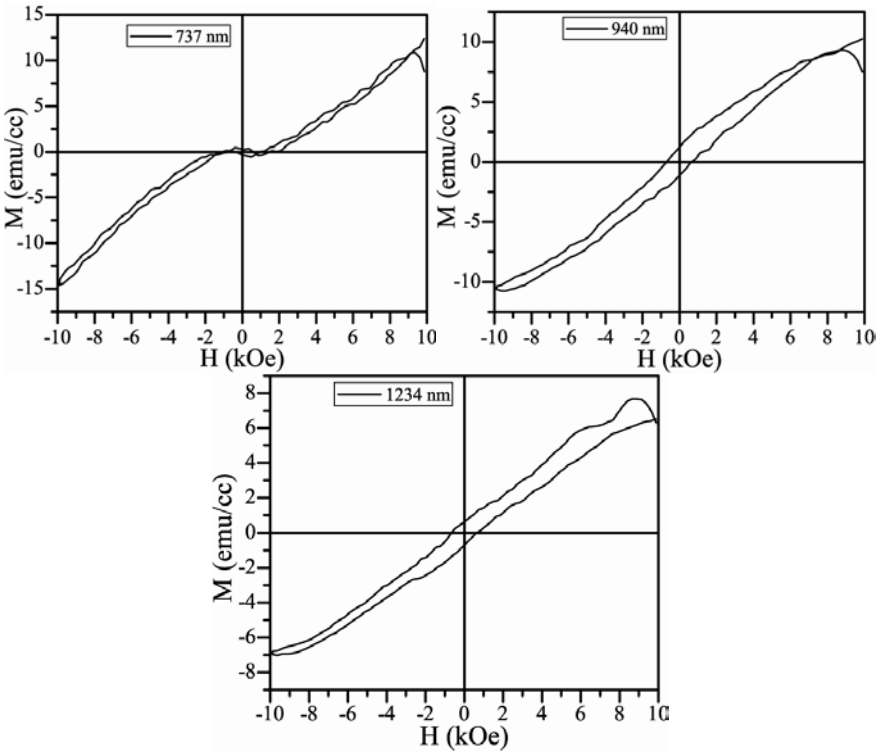

Figure 6.10: M-H curves of $Zn_{0.95}Fe_{0.05}O$ thin films of different film thickness in argon environment.

6.2.2 Nitrogen environment

The RT magnetic properties of Mn, Fe doped ZnO films deposited in nitrogen gas environment are recorded as a function of films thickness. The magnetic field of ±1tesla was applied in the plane of the film.

6.2.2.1 $Zn_{0.95}Mn_{0.05}O$

The magnetization versus applied magnetic field (*M-H*) curves of $Zn_{0.95}Mn_{0.05}O$ thin films as a function of film thickness are shown in figure 6.11. The as deposited films show ferromagnetic signature for all films with increase in film thickness. The magnetization and coercivity is the range of 2.2 to 9 emu/cm^3 and 544 to 1016 Oe respectively. For various thickness of the films the remnant magnetization varies from 0.69 to 2.54 emu/cm^3. The magnetic parameters estimated from hysteresis curves are listed in table 6.6.

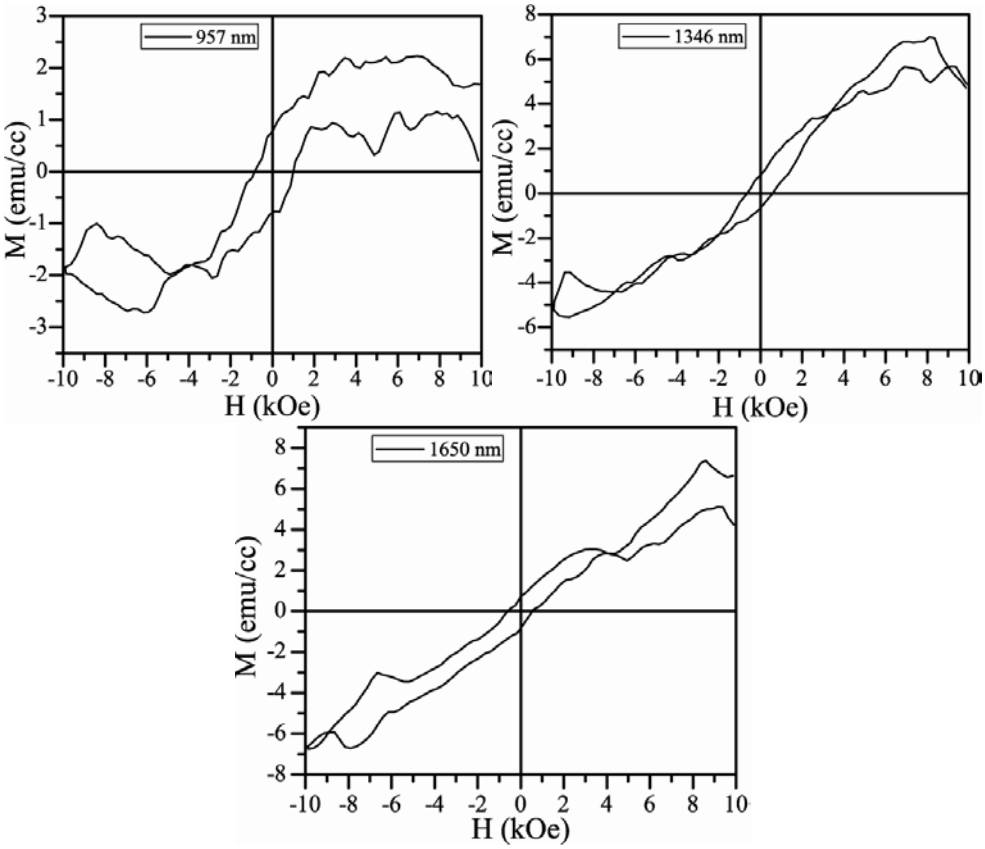

Figure 6.11: M-H curves of $Zn_{0.95}Mn_{0.05}O$ thin films of different film thickness in nitrogen environment.

The present results are in agreement with reports on Mn and N_2 co-doped ZnO thin films deposited on sapphire [24] and silica [25] substrates. The dopant N_2 will produce the donar vacanicies in ZnO matrix and also enhances the defect concentration in the films.

Table 6.6 The estimated magnetic prarmertets of $Zn_{0.95}Mn_{0.05}O$ thin films.

t (nm)	M_S (emu/cc)	H_C (Oe)	M_R (emu/cc)
957	2	1016	0.7
1346	7	593	0.8
1650	7	544	0.6

6.2.2.2 $Zn_{0.95}Fe_{0.05}O$

Figure 6.12 shows the room temperature magnetic hysteresis loops of $Zn_{0.95}Fe_{0.05}O$ thin films of various thicknesses. The saturated magnetization (Ms) and coercive field estimated from M-H plot has 1.74 (emu/cc) and 734 Oe respectively.

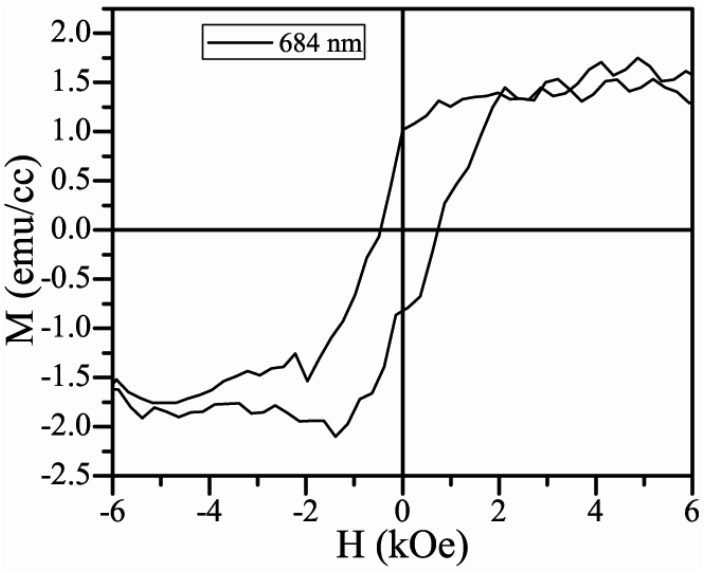

Figure 6.12: M-H curves of different film thickness of $Zn_{0.95}Fe_{0.05}O$ thin films in nitrogen environment.

6.3 Films on silicon substrates

The effect of Si (100) substrate on magnetic properties of Mn, Fe doped ZnO thin films in argon and oxygen gas environment were studied. The diamagnetic contribution of Si (100) substrate has been subtracted from raw data.

6.3.1 Argon environment

The magnetization versus magnetic field (*M-H*) of Mn5%, Fe5% and co-doped ZnO thin films in argon gas environment are shown in the figure 6.13. The hysteresis curves show the clear indication of ferromagnetism with magnetization and coercivity values in the range of 3 to 11 emu/cm^3 and 447 to 605 Oe respectively. The highest magnetization values of 11 emu/cm^3, coercive field 487 Oe and remnant magnetization of 1.34 emu/cm^3 are achieved for Fe doped ZnO thin films. The enhanced magnetic properties could be due to the presence of multi valence ionic states of Fe ion (Fe^{2+} or Fe^{3+}) in the host ZnO matrix. The magnetic parameters estimated from magnetic hysteresis loops are summarized in table 6.7.

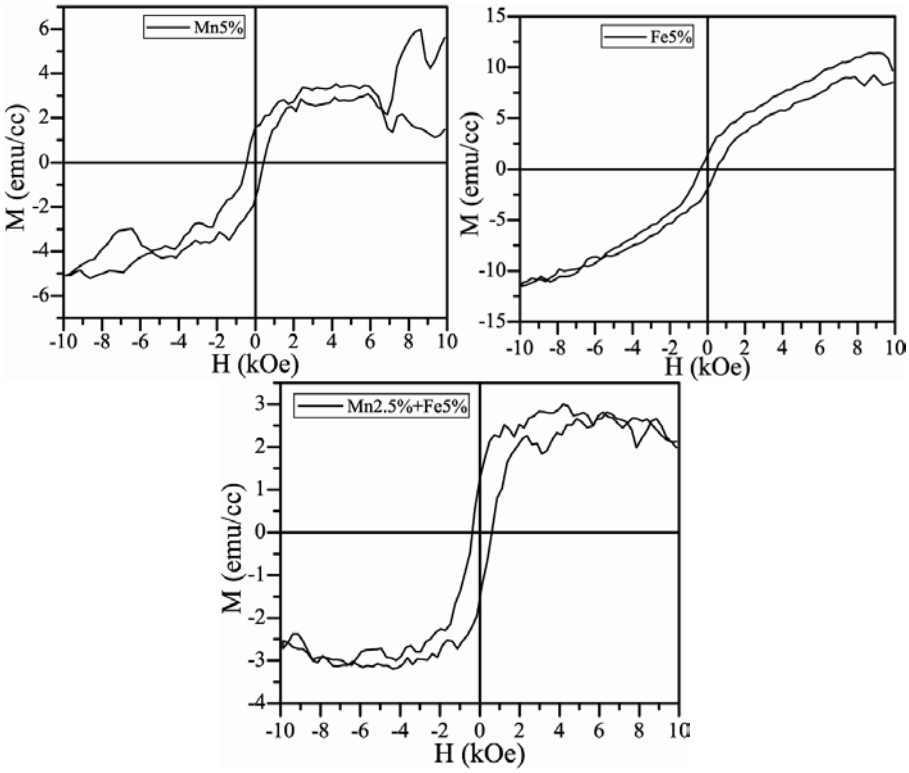

Figure 6.13: Room temperature M-H curves of (A) Mn5% , (B) Fe 5% and (C) Mn2.5% + Fe5% co-doped ZnO thin films argon environment.

The clear hystersis, indicates that $Zn_{0.95}Fe_{0.05}O$ display strong ferromagnetic properties in agreement with other reports [26,27]. From the magnetization data we can conclude that the substrate has a significant role in getting the ferromagnetic proeprties in the doped ZnO films.. This may be due to the substrates surface effects , lattice mismatch of the Si (100) and ZnO and lower substrate contribtion compared to glass and quartz.

Table 6.7 The estimated magnetic prarmertets of Mn, Fe and co-doped ZnO thin films.

Sample	t (nm)	M_S (emu/cc)	H_C (Oe)	M_R (emu/cc)
Mn5%	510	5	447	1.5
Fe5%	458	11	487	1.3
Mn2.5%+Fe5%	521	3	605	1.2

6.3.2 Oxygen environment

The magnetization versus magnetic field (*M-H*) loops of Mn5%, Fe% and co-doed ZnO thin films fabricated in oxygen gas environment are shown in the figure 6.13. The as

deposited films show saturation magnetization and corecivity in the range of 1.01 to 2.56 emu/cm^3 and 438 to 555 Oe, respectively. The Fe5% doped ZnO thin films show strong magnetic properties as in the case of argon gas environment deposited films with magnetization and coercivity of ~ 2.56 emu/cm^3 and 555 Oe respectively. The magnetic parameters estimated from magnetic hysteresis loops are summarized in table 6.8.

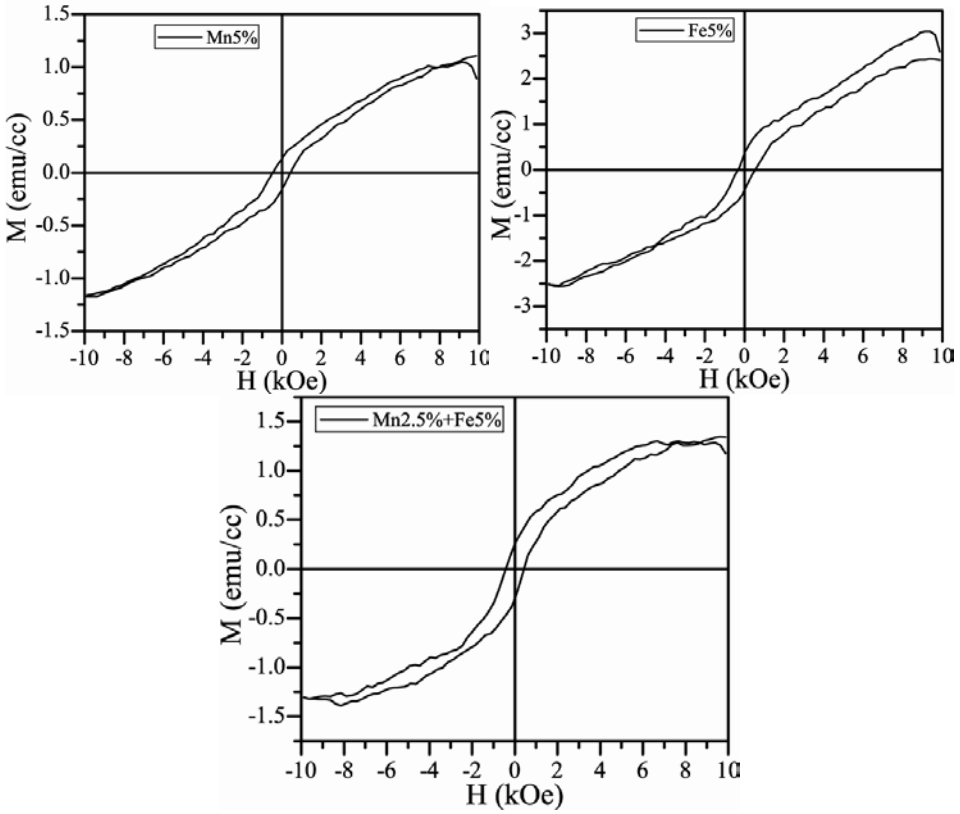

Figure 6.14: M-H curves of (A) Mn5% , (B) Fe 5% and (C) Mn2.5% + Fe5% co-doped ZnO thin films oxygen environment.

The clear and evident hystersis, indicates that $Zn_{0.95}Fe_{0.05}O$ exhibits ferromagetic behavior in agreement with literature [18,26].

Table 6.8 The magnetic prarmertets of Mn, Fe and co-doed ZnO thin films.

Sample	t (nm)	M_S (emu/cc)	H_C (Oe)	M_R (emu/cc)
Mn5%	680	1	454	1.1
Fe5%	218	2	555	0.3
Mn2.5%+Fe5%	405	3	438	0.2

Conclusions:

Some of the basic conclusions drawn from this chapter as follows:

- The magnetization studies using vibrating sample magnetometer (VSM) were carried out for the undoped and 3d doped ZnO thin films prepared under different gas environment conditions with the objective of understanding the origin of magnetic order in these films.
- The signature of ferromagnetism in the as deposited undoped, Mn, Fe doped ZnO films have been observed
- The M-H plots as a function of film thickness of Mn, Fe and co-doped ZnO thin films deposited in nitrogen gas environment show ferromagnetism.
- The films deposited on Si (100) substrate show clear hysteresis of ferromagnetism than films on quartz substrate in argon and oxygen gas environment.
- The Mn, Fe co-doped ZnO films deposited on Si (100) in oxygen gas environment show room temperature ferromagnetism with saturation magnetization (M_S) 8 -15 (emu/cc) and coercive field (H_C) 567- 1060 Oe.
- The present study has helped in identifying the deposition conditions for observing room temperature ferromagnetism in undoped and 3d TM doped ZnO thin films.

References

[1] K. Wasa, M. Kitabatake, and H. Adachi, *Thin Films Material Technology: Sputtering of Compound Materials,* William Andrew, USA, (2004).

[2] M. Khalid et al, *Phy. Rev . B* **80** (2009) 035331.

[3] M. A. Gracia et.al, *Nano Lett*. **7** (2007) 1489.

[4] X. G. Chen, Y.B. Yang, R. Wu, R. Liu, X. D. Kong, L. Han, Y. C. Yang and J. B. Yang, *Physica B* 1341 (2011) 1344.

[5] H. Y. Xu, Y. C. Liu, C. S. Xu, Y. X. Liu, C. L. Shao, and R. Mu, *Appl. Phys. Lett.* **88** (2006) 242502.

[6] Liu Xue-Chao, Zhang Hua-Wei, Zhang Tao, Chen Bo-Yuan, Chen Zhi-Zhan Song Li-Xin and Shi Er-Wei, *Chinese Physics B* **17** (2008) 1674.

[7] R. K. Singhala, M.S. Dhawana, S. K. Gaura, S. N. Doliaa, Sudhish Kumarb, T. Shripathi,
U. P. Deshpandec, Y.T. Xingd, Elisa Saitovitchd and K.B. Gargа, *J. Alloy. Comp* **477** (2009) 379.

[8] Preetam Singh, Ajay Kaushal and Davinder Kaur, *J. Alloy. Comp* **471** (2009) 11.

[9] Z.F. Wu, X.M. Wu, L.J. Zhuge, B. Hong, X. M. Yang, X.M. Chen and Q. Chen, *Matt. Lett*. **64** (2010) 472.

[10] D. Mukherjee, T. Dhakal, H. Srikanth, P. Mukherjee, and S. Witanachchi, *Phy .Rev. B* **48** (2010) 205202.
[11] A. Di Trolio, C. Veroli, A. M. Testa and D. Fiorani *Superlattices and Microstructures* **46** (2009) 101.

[12] Li-wei Wang, Zheng Xu, Fu-jun Zhang, Su-ling Zhao, and Li-fang Lu *International Journal of Minerals, Metallurgy and Materials* **17**(2010) 475.

[13] J. Elanchezhiyan, K.P. Bhuvana, N. Gopalakrishnan and T. Balasubramanian *Superlattices and Microstructures* **62** (2008) 3379.

[14] Mingxia Yuan, Wuyou Fu, Haibin Yang, Qingjiang Yu, Shikai Liu, Qiang Zhao, Yongming Sui, Dong Ma, Peng Sun, Yanyan Zhang and Baomin Luo *Matt. Lett* **63** (2009) 1574.

[15] D. Wanga, Z.Q. Chen a, F. Zhou, W. Lub, M. Maekawa, and A. Kawasuso *Appl. Surf. Sci*. **255** (2009) 9371.

[16] I. Soumahoro, R. Moubah, G. Schmerber, S. Colis, M. Ait Aouaj, M. Abd-lefdil, N. Hassanain, A. Berrada, and A. Dinia *Thin. Solid. Films* **518** (2010) 4593.

[17] Wei-Guang Zhang, Bin Lu, Li-Qiang Zhang, Jian- Guo Lu, Min Fang, Ke-Wei Wu, Bing-Hui Zhao and Zhi-Zhen Ye *Thin. Solid. Films* **519** (2011) 4593.

[18] N.H. Hong, J. Sakai, V. Brize, *J. Phys.: Condens. Matter* **19** (2007) 036219.

[19] Y. Lin, D.M. Jiang, F. Lin, W.Z. Shi, X.M. Ma, *J. Alloys. Compd*. **436** (2007) 30.

[20] Z.C. Chen, L.J. Zhug, X.M. Wu, Y.D. Meng, Thin. Solid. Films **515** (2007) 5462.

[21] Debjani Karmakar, S. K. Mandal, R. M. Kadam, P. L. Paulose, A. K. Rajarajan, T. K. Nath, A. K. Das, I. Dasgupta and G. P. Das *Phys. Rev. B* **75** (2007) 144404.

[22] M. Chakrabarti, S. Dechoudhury, D. Sanyal,T. Kundu Roy, D. Bhowmick and A.Chakrabarti *J. Appl. Phys.D* **41** (2008) 135006.

[23] Siddhartha Mal, Sudhakar Nori, Chunming Jin, J. Narayan, S. Nellutla, A. I. Smirnov and J. T. Prater *J. Appl. Phys.* **108** (2010) 0753510.

[24] Zheng-Bin Gu, Ming-Hui Lu, Jing Wang, Di Wu, Shan-Tao Zhang, Xiang-Kang Meng, Yong-Yuan Zhu, Shi-Ning Zhu, Yan-Feng Chen, and Xiao-Qing Pan *Appl. Phys. Lett* **88** (2006) 082111.

[25] Z L Lu, Z R Mo, W Q Zou, S Wang, G Q Yan, X C Liu, Y B Lin, J P Xu, L Y Lv, X M Wu, Z H Xia, M X Xu, F M Zhang and Y W Du *J.Phys. D: Appl. Phys*. **41** (2008) 115008.

[26] D. Karmakar, S.K. Mandal, R.M. Kadam, P.L. Paulose, A.K. Rajarajan, T.K. Nath, A.K.
Das, I. Dasgupta, G.P. Das, *Phys. Rev. B* **75** (2007) 144404.

Summary and Conclusions

ZnO based oxide semiconductors are very important material in the family of oxide semiconductors with stable phase of wurtzite structure. ZnO based semiconductors have wide range of application from light emitting diodes to solar cells, flat panel displays and transparent electrodes etc. The technological importance of ZnO based semiconductors have increased as many discoveries required the use of spintronic materials. Nanoscale ZnO based semiconductors have found enormous potential applications in medicine and lubricants. Thin films of ZnO based semiconductors are potential candidates for integrated device applications.

In this thesis, the system of un-doped and 3d Tm doped ZnO thin films with general formula $Zn_{1-x}M_xO$ (x= Mn and Fe) were synthesized. The sputter target was prepared by solid state reaction and thin films were synthesized by RF – magnetron sputtering. The RF – magnetron sputtering can offer way to deposit nanocrystalline un-doped and 3d TM doped ZnO thin films with highly reproducible properties. Mn and Fe doped ZnO thin films are very interesting for their textural, structural, optical mechanical and magnetic properties. It is shown that film deposition environment (Ar, O_2 and N_2) and film thickness play a vital role in controlling the morphology and properties of ZnO thin films.

The main conclusions and summary of the thesis work as follows:

Structural and morphological studies

- The detailed structural and morphological studies conducted on Mn, Fe and Mn and Fe co-doped ZnO thin films has revealed that the microstructure and preferential orientation of the as-deposited films strongly depend on the deposition gas environment , gas pressure , duration of deposition (thickness) , dopant nature and type of substrate.

- All the as- deposited films show hexagonal wurtzite structure.

- The as- deposited films in argon and nitrogen gas environment show the hexagonal wurtzite structure with highly oriented with (002) plane along *c* – axis.

- The preferential orientation of the as –deposited film can be controlled by adjusting the gas pressure and doping with Mn or Fe. The (002) orientation can be improved for the undoped films and Mn-Fe codoped films by increasing the gas pressure. Whereas for the Mn and Fe doped films highly oriented films along (002) direction can be obtained at low gas pressure.

- The increase in gas pressure leads to decrease in thin film thickness because of back sputtering process.

- The films deposited in oxygen gas environment are disordered in nature and are not found to be stable.

- The average grain size increases with films thickness from 40- 80 nm in argon gas compared to nitrogen gas deposited films

- The films deposited in argon gas show bigger grain size compared to films deposited in oxygen or nitrogen gas atmosphere. This could be due high rate of deposition in argon gas.

- Thin films of un-doped and Mn, Fe doped ZnO show films have compressive (negative) stress for both argon and oxygen gases.

- The crystal structure of the films improved as a function of film thickness for Mn and Fe doped ZnO films with preferred orientation in (002) plane along *c*-axis perpendicular to substrate base plane.

- The Mn doped ZnO films have tensile (positive) stress, where as un-doped and Fe doped films show compressive (negative) stress.

- The films deposited in argon gas for different dopants have high values of residual stress (σ) in the range of – 4.525 – 2.184 GPa than films in oxygen gas.

- The films deposited on Si (100) show higher lattice paramerters (*c*) than the films on quartz substrate.

- The crystallite (D) size is lower (2 – 21 nm) for films on Si (100) substrate. Whereas for films on quartz substrate it is in the range 15- 45 nm. This could be due to lattice mismatch and surface properties of substrate material.

- The residual stress (σ) of the films is compressive (negative) for all the as deposited films.

Optical properties

- The optical transmission of as deposited un-doped, Mn, Fe doped and Mn-Fe co-doped ZnO thin films have high tansmittance (70 – 93 %) in the visible range of light. The film deposited in oxygen gas show high transmittance (~91-93%) than films in argon gas could be due to oxygen gives less film thickness.

- The direct band gap estimated from transmission spectra of un-doped, Mn, Fe and Mn-Fe co-doped ZnO films was in the range from 3.12 – 3.39 eV. The film deposited in oxygen gas environemnt had higher energy gap than films in argon about 3.04 – 3.39. This behavior might be due to oxygen produces the oxygen difficience or defect concnetration in the film.

- The films with low working gas pressure has high film thckness and it is decreases with increase in gas pressure for Mn, Fe doped ZnO films, whereas for Mn-Fe co-doped it is in reverse direction because of Mn and co-doping hinders the growth of film with variation ioninc radius of dopants in ZnO matrix.

- The Urbach energy of the films have the inverse relation to energy band gap for as deposited films. As band gap decrease the Urbach energy show increase with working gas pressure. This behavior is attributed that presence of impurity bands between valance and conduction bands.

- The refractive index (n) as a function of wavelength has linear beahior, with an average values of refractive index 1.492 – 1.497. Similar kind of behavior was observed for extinction coefficent (k) for Un-doepd, Mn, Fe and Mn-Fe co-doped ZnO films in both argon and oxygen gas environment. The variation of extinction coefficent is realted to transmittance of the films. As the transmittance increases in oxygen gas , the extinction coefficent show decrease.

- *Effect of films thickness*

- The transmittance for un-doped, Mn, Fe and Mn-Fe co-doped ZnO films as a function film thickness is in the range from 84- 94%. The films deposited in

nitrogen gas had high transmittance than films in argon gas environment. This phenomina could be due to argon gas gves high rate of depositeion than nitrogen gas in sputtering process.

- There is no significant change in the band gap energy with film thickness with high band gap value for nitrogen gas than films in argon gas environment. The direct band gap of the films with films thickness varied from 3.14 – 3.60 eV.

- The Urbach energy of the films increases with film thickness for all as deopsited films for both in argon and nitrogen gases. The estimated Urbach enrgy of Un-doped, Mn, Fe and Mn-Fe co-doped films is in between 0.144 – 0.762 eV.

- The refractive index (n) with wavelength of as deposited films has no change with film thickness. The extinction coefficent (k) has also show similar behavior as a function of wavlength. The refractive index (n) for un-doped, Mn, Fe and Mn-Fe doped ZnO films with various film thicknesses varies from 1.495 – 1.499 in argon and nitrogen gas environemnt.

- *Effect of film substrate*

- The room temperatur relfetance spectra for Mn, Fe and Mn-Fe co-doped ZnO thin films have multiple interfernece fringes with reflectance 0.32 – 0.52 in the visible range of electromagnetic spectrum. The film deposited in oxygen gas has high refelctance than argon deposited films might be of thcikness difference.

- The energy band gap show decrease with dopant in the films for Mn,Fe and Mn-Fe co-doped ZnO films in argon, but the films in oxygen show increase with dopant in the range of 3.01 – 3.48 eV.

- There is no substrate influence on optical properties of Mn, Fe and Mn-Fe co-doped ZnO films. The best optical proerties acheived for oxygen gas deposited films than argon and nitrogen gas environment and Fe doped ZnO films other dopants of Mn and Mn-Fe co-doped ZnO films in argon and oxygen gases.

Mechanical properties

- The loading and unloading curves of un-doped and Mn, Fe doped ZnO thin films have no *pop-in* (discontinious) behavior for different indention loads of 1000 μN, 3000 μN and 5000 μN indicating the films are smooth and have homogenious internal structure.

- The penetration depth strogly depends on the the maximum indentation load. For a given load highest penetration depth is observed for film deposited in argon gas. The penetration depth is lower for films deposited in oxygen and nitrogen gas. From the loading and unloading curves we can see that the films deposited in argon gas environment have more *plastic deformation*. It is also noticed that at high indentation load the material shows the high plastic nature rather at lower indentation loads.

- The ZnO films deposited in oxygen gas atmosphere show high mechanical strength than argon and nitrogen which may be due to the disordered nature of the films.

- At lower load the variation in elastic parametrs is large between the indentation locations. This may be because of film surface morphology. This variation is reduced as the indentation load is increased indicating a more uniform internal stucture of films.

- The elastic parameter values decrease with the increase in indentation load (penetration depth) for all the films. These values are strongly dependent on indentation load and the preparation conditions of the films.

- The Mn, Fe and Mn-Fe co-doped ZnO films show elastic modulus which depend on the preparation conditions and indentation load.

- The Mn, Fe co-doepd ZnO films in oxygen gas had high mechancal stability than other gases of argon and nitrogen gases.

The mechanical parametrs of Mn.Fe and Mn-Fe doped films on Si (100) substrate have higher values compared to the films on fused quartz substrates.

Magnetic properties

- The magnetization studies using vibrating sample magnetometer (VSM) were carried out for the undoped and 3d doped ZnO thin films prepared under different gas environment conditions with the objective of understanding the origin of magnetic order in these films.

- The signature of ferromagnetism in the as deposited undoped, Mn, Fe doped ZnO films have been observed

- The M-H plots as a function of film thickness of Mn, Fe and co-doped ZnO thin films deposited in nitrogen gas environment show ferromagnetism.

- The films deposited on Si (100) substrate show clear hysteresis of ferromagnetism than films on quartz substrate in argon and oxygen gas environment.

- The Mn, Fe co-doped ZnO films deposited on Si (100) in oxygen gas environment show room temperature ferromagnetism with saturation magnetization (M_S) 8 -15 (emu/cc) and coercive field (H_C) 567- 1060 Oe.

- The present study has helped in identifying the deposition conditions for observing room temperature ferromagnetism in undoped and 3d TM doped ZnO thin films.

PUBLICATIONS

1. Structure and optical properties of RF-sputtered Mn-ZnO Nanocrystalline thin films.
   Venkaiah. M, and R.Singh, *AIP.Con.Proc* **1349** 609 (2011)

2. Effect of thickness on structure and optical properties of RF-sputtered $Zn_{0.925}Mn_{0.025}Fe_{0.05}O$ thin films**.**
   Venkaiah. M, and R.Singh *AIP.Con.Proc* **1451** 212 (2012)

3. **Venkaiah. M** and R.Singh., Structure, optical and mechanical properties of rf-sputtered thin films of $Zn_{0.95}Mn_{0.05}O$ in nitrogen gas environment (communicated to *Physica B*)

4. Crystal Structure and Magnetic properties of $Zn_{0.9}Cu_{0.1}O_y$ rf-sputterd thin films.
   Venkaiah.M, Kiran Kumar U and R.Singh, (Accepted in *AIP.Con.Proc*.)

5. Effect of argon gas on structure and mechanical properties of rf-sputtered thin films of $Zn_{0.95}Mn_{0.05}O$.
   Venkaiah. M, and R.Singh, (under preparation)

6. Room temperature ferromagnetism in $Zn_{0.925}Mn_{0.025}Fe_{0.05}O$ rf-sputted thin films.
   Venkaiah. M, and R.Singh, (under preparation)

7. Effect of working gas environment on structure and mechanical properties of rf-sputterd thin films on silicon substrates
   Venkaiah. M, and R.Singh, (under preparation)

Presentations at Conferences:

1. Nanocrystalline ZnO thin films,
   Venkaiah. M, Joji Kuarian and R.Singh, ICONSAT-2012 January 20 -23 Hyderabad, India (2012).

2. Structure and properties of RF-sputtered Mn-ZnO nanocrystalline thin films, **Venkaiah. M**, and R.Singh, Physics at small scales, March 18 19 Hyderabad, India 18 -19 March (2011).

3. Effect of thickness on structure and optical properties of RF-sputtered $Zn_{0.925}Mn_{0.025}Fe_{0.05}O$ thin films**.**
   Venkaiah. M, and R.Singh, IVS Symposium on Thin Films: Science & Technology, November 9 -12 Mumbai, India (2011).

4. Structure and Magnetic properties of nanocrystalline Mn-Fe dopedZnO thin films, **Venkaiah. M**, and R.Singh, ISJP Symposium February 19-21, Hyderabad, India (2010).

5. Structure and optical properties of RF-sputtered Mn-ZnO Nanocrystalline thin films. **Venkaiah. M**, and R.Singh, DAE SSP Symposium, December 26-30 Manipal, India (2010).

6. Structure and properties nanocrystalline pure and Mn-Fe doped ZnO thin films, **Venkaiah. M**, and R.Singh, DAE SSP symposium, December 14 -18 Vadodara, India (2009).